Multi-Scale Study of All-Optically Induced Magnetization Dynamics in Co/Pt Multilayers utilizing TR-mSAXS at FEL Sources

Dissertation zur Erlangung des akademischen Grades
Doktor der Naturwissenschaften
– Dr. rer. nat. –

an der Fakultät für Mathematik, Informatik und Naturwissenschaften
Fachbereich Physik der Universität Hamburg

vorgelegt von
Matthias Riepp
aus Prien am Chiemsee

Hamburg, 2021

Gutachter/innen der Dissertation:	Prof. Dr. G. Grübel Prof. Dr. R. Röhlsberger
Zusammensetzung der Prüfungskommission:	Prof. Dr. G. Grübel Prof. Dr. R. Röhlsberger Prof. Dr. B. Ziaja-Motyka Prof. Dr. K. Rossnagel
Vorsitzende/r der Prüfungskommission:	Prof. Dr. M. Potthoff
Datum der Disputation:	16.09.2021
Vorsitzender Fach-Promotionsausschusses PHYSIK:	Prof. Dr. Wolfgang Hansen
Leiter des Fachbereichs PHYSIK:	Prof. Dr. Günter H. W. Sigl
Dekan der Fakultät MIN:	Prof. Dr. Heinrich Graener

Meiner Familie

Abstract

This thesis deals with the impact of ultrashort near-infrared (nIR) and extreme ultraviolet (XUV) laser pulses on the magnetic multi-domain states of particularly thin Co/Pt multilayers. The laser induced magnetization dynamics are investigated with femtosecond time and nanometer spatial resolution utilizing time-resolved magnetic small-angle X-ray scattering (TR-mSAXS) at the free-electron lasers (FEL) FLASH in Hamburg and FERMI@Elettra in Trieste.

One part of the thesis deals with ultrafast demagnetization in three different Co/Pt-multilayer samples with total film thicknesses in the range of the attenuation length of nIR radiation in Co and Pt. For excitation of the magnetic states, nIR-laser pulses of different fluence, pulse duration and polarization are used, addressing important aspects of ultrafast demagnetization in such optically thin Co/Pt multilayers, for the first time, by resonant magnetic scattering. In particular, a model that accounts for both the low-temperature behavior of the remagnetization dynamics and its drastic slowing down at high temperatures is proposed, taking into account recent theoretical predictions. Within this model, the remagnetization dynamics are described via energy exchange between a strongly coupled electron–spin system and the phonon system.

Another part of the thesis addresses the influence of nIR and XUV-laser (FEL) pulses on the lateral configuration of nanoscopic multi-domain states. Different multi-domain states are generated in a selected Co/Pt multilayer by using out-of-plane (OOP) magnetic fields. Aside from ultrafast demagnetization, that behaves similar for the different multi-domain states, permanent lateral domain modifications forming on longer time scales are observed, that do depend on the underlying multi-domain state. Moreover, the permanent modifications only occur if nIR and XUV-laser pulses temporally overlap. Since the action of the combined (pump/probe) peak intensity alone cannot explain the observed effects, it is concluded that the permanent modifications also depend on the photon energies of the laser pulses. In particular, the permanent modifications in the close-to single-domain state point at laser induced nucleation processes and thus a novel all-optical switching (AOS) like mechanism that is based on the interplay of two different laser excitations.

Zusammenfassung

Diese Arbeit befasst sich mit dem Einfluss ultrakurzer Nahinfrarot (nIR) und Extrem-Ultraviolett (XUV) Laserpulse auf Multi-Domänenzustände in besonders dünnen Co/Pt Multilagen. Die laserinduzierten Magnetisierungsdynamiken wurden mit Femtosekunden Zeitauflösung und Nanometer Ortsauflösung, unter Verwendung von zeitaufgelöster magnetischer Kleinwinkelstreuung (TR-mSAXS) an den Freie-Elektronen Lasern (FEL) FLASH in Hamburg und FERMI@Elettra in Trieste, untersucht.

Ein Teil der Arbeit befasst sich mit ultraschneller Demagnetisierung in drei verschiedenen Co/Pt Multilagen mit Gesamtschichtdicken im Bereich der Absorptionslänge von nIR-Strahlung in Co und Pt. Zur Anregung der magnetischen Zustände wurden nIR-Laserpulse unterschiedlicher Fluenz, Pulslänge und Polarisierung verwendet, wodurch wichtige Aspekte ultraschneller Demagnetisierung in solch optisch dünnen Co/Pt Multilagen zum ersten Mal anhand von resonanter magnetischer Streuung gemessen wurden. Insbesondere wird ein Modell vorgeschlagen welches, unter Berücksichtigung theoretischer Vorhersagen, sowohl das Niedrigtemperaturverhalten der Remagnetisierungsdynamik, als auch deren drastische Verlangsamung bei hohen Temperaturen beschreibt. Darin wird die Remagnetisierungsdynamik über den Energieaustausch zwischen einem stark gekoppelten Elektronen–Spinsystem und dem Phononensystem beschrieben.

Ein weiterer Teil der Arbeit beschäftigt sich mit dem Einfluss von nIR und XUV-Laserpulsen auf die laterale Konfiguration der nanoskopischen Multidomänenzustände. Externe Magnetfelder senkrecht zur Filmebene (OOP) wurden verwendet, um verschiedene Multidomänenzustände in einer ausgewählten Co/Pt Multilage zu erzeugen. Neben ultraschneller Demagnetisierung, welche unabhängig vom Multidomänenzustand abläuft, treten vergleichsweise langsame, permanente Änderungen im Domänensystem auf, die wiederum vom zugrundeliegenden Multidomänenzustand abhängen. Die permanenten Änderungen werden außerdem nur dann beobachtet, wenn die nIR und XUV-Laserpulse die Probe gleichzeitig anregen. Da die beobachteten Effekte nicht durch das alleinige Wirken der kombinierten (pump/probe) Peakintensität beschrieben werden können, wird der Schluss gezogen, dass die permanenten Änderungen auch von den Photonenenergien der Laserpulse abhängen. Inbesondere deuten die dauerhaften Änderungen nahe des eindomänigen Zustandes auf laserinduzierte Nukleationsprozesse hin, und somit auf einen neuartigen Mechanismus optisch induzierten Schaltens (AOS), der auf dem Zusammenspiel zweier unterschiedlicher Laseranregungen beruht.

Contents

List of Figures

List of Tables

1 Introduction

Magnetism has already been described 2500 years ago and has historically been applied for ritual purposes and later for navigation [1]. Today, magnetism has its place in everyday life in many different and maybe unexpected ways. Beyond the most commonly known "fridge magnet", magnets and magnetism are used, e. g., in electric motors, transformers and generators, safety switches and sensors, micro wave ovens, compasses, magnet resonance tomography imaging, medical implants, data storage and more. Hence magnetism impacts life on virtually every sector, ranging from power generation via transport and navigation to health and "modern life" including convenience applications and in particular mass data storage.

Scientifically, a wide variety of magnetic phenomena are studied including the interaction of light with magnetism, a field that this thesis contributes to. Light–magnetism interactions were first found and described by M. Faraday and J. Kerr in the mid 19th century [2, 3]. The field of *femtomagnetism* has emerged with the possibility to produce light pulses that possess a pulse duration shorter than 100 fs in the mid 1980s [4]. For the first time, magnetization dynamics could be studied on sub-picosecond time scales with the surprising result that magnetization can be quenched within a few 100 fs, much faster than previously deemed possible. This seminal finding of E. Beaurepaire *et al.* in 1996 [5] has sparked many investigations of the phenomenon that has been called *ultrafast demagnetization* leading to currently more than 2200 citations of the original paper including a number of reviews, e. g., Refs. [6–11], summarizing the developments in the field. Typically in ultrafast demagnetization, time scales of ≈ 100 fs [12–15] down to sub-50 fs [16, 17] are found, mediated by a variety of microscopic mechanisms including electron–phonon spin-flip scattering and superdiffusive spin currents. Very recently, however, reports on so-called optically induced spin transfer (OISTR) suggest that the ultimate time scale of manipulating spins by light might, in principle, only be limited by the pulse duration of the excitation pulse, opening the new field of *attomagnetism* [18–21].

In 2007, another phenomenon induced by a sub 100 fs-short laser pulse, namely *all-optical switching* (AOS) of magnetization, was found in ferrimagnetic alloys consisting of $3d$ and $4f$ elements [22]. Originally, AOS in ferrimagnets was believed to be a helicity-dependent effect induced by the inverse Faraday effect. Today, AOS in ferrimagnets is known to be largely independent from helicity but is due to the different demagnetization times of the $3d$ and $4f$ constituents, mediating AOS on femto to picosecond time scales [23]. Therefore, it came as a surprise when in 2014, C.-H. Lambert *et al.* found AOS also in ferromagnetic systems

with only one magnetic constituent, e. g., cobalt in particularly thin cobalt-platinum (Co/Pt) multilayers [24]. Obviously, a different mechanism has to be responsible for the *helicity-dependent* AOS (HD-AOS) in ferromagnets. In a lively discussion both inverse Faraday effect and magnetic circular dichroism are put forward to account for the helicity dependence of AOS in ferromagnets [25, 26].

The manipulation of a magnetic state on ultrafast time scales by all-optical means is especially interesting for future data storage applications. As a first step towards AOS-based recording media, today, optical laser pulses are used to heat up a "bit" of the medium, allowing the information to be written with a smaller magnetic field than would be needed for the cold medium, which thus is called *heat-assisted magnetic recording* (HAMR) [27, 28]. While an increase in recording speed is not achieved by HAMR, it allows for the use of magnetically harder materials an thus for a further increase in recording density.

For the development of future all-optical magnetic recording devices, however, a fundamental understanding of laser induced magnetization dynamics on femtosecond time and nanometer length scales is required. Free-electron lasers (FELs), that provide sub 100 fs-short light pulses in the XUV to hard X-ray regime, ideal for investigating magnetization dynamics element-selectively, have been contributing to that task over the past ten years [29–42].

In this thesis, the impact of ultrashort near-infrared (nIR) laser pulses on magnetic multi-domain states of three specifically designed Co/Pt multilayers with total film thicknesses in the range of the attenuation length of nIR radiation was investigated. The magnetization dynamics were studied with femtosecond time and nanometer spatial resolution, utilizing time-resolved resonant magnetic small-angle X-ray scattering (TR-mSAXS) at the FEL facilities FLASH in Hamburg and FERMI@Elettra in Trieste.

In the experiment at FLASH (chapter 5), ultrafast demagnetization in the three different samples was studied, varying the fluence, pulse duration and polarization of the nIR-laser pulses. In the experiment at FERMI, the impact of nIR and XUV-laser heating on the lateral configuration of nanoscopic multi-domain states in the presence of out-of-plane magnetic fields was investigated in a selected Co/Pt multilayer (chapter 6). Before describing the experiments and their outcome, the fundamentals of ferromagnetism as well as the interactions of polarized light with magnetic matter are introduced in chapter 2. Details on the fabrication process and the magnetic properties of the Co/Pt-multilayer samples are given in chapter 3. The experimental methods, i. e., time-resolved magnetic small-angle X-ray scattering (TR-mSAXS) at the FELs FLASH and FERMI and imaging of nanoscopic multi-domain states via Fourier-transform holography at the synchrotron PETRA III, are presented in chapter 4. Final conclusions and an outlook to future experiments are given in chapter 7.

2 Fundamentals of Ferromagnetism and Light–Matter-Interactions

The 3*d* transition metals Fe, Co and Ni have since long been a subject of scientific research, due to their manifold electron correlation effects that are the basis for numerous technological applications. Of particular interest in fundamental research is their unique electronic band structure which shows an imbalance in spin-up and spin-down states at the Fermi level and thus a net magnetic moment, i. e., a ferromagnetic order. An introduction to the fundamentals of ferromagnetism in 3*d* elements is given in section 2.1.

The possibility to engineer magnetic materials, e. g., by layering thin sheets (or also alloying) of 3*d* transition-metal elements with heavy-metal or rare-earth elements, prompted a series of technological breakthroughs including perpendicular magnetic recording (PMR) [43, 44] or highly sensitive magnetic sensors based on the giant magneto-resistance (GMR) effect [45–47]. Current sate-of-the-art fabrication processes allow for preparing nanoscopic magnetic structures, including thin films (2D) that may even be further processed, e. g., by lithography methods, to create wires (1D) or quasi-0D magnetic nanodots in periodic structures. Interesting ideas for future technological applications, such as bit-patterned media (BPM) [48, 49] or skyrmion race-track memories [50, 51], are still depending on a better understanding of magnetization dynamics in low-dimensional systems. For an understanding of the formation of nanoscopic magnetic multi-domain states in the here investigated magnetic thin films consisting of Co/Pt multilayers (section 2.3), the relevant contributions to the total magnetic free energy are introduced in section 2.2.

In this thesis, the nanoscopic multi-domain states were excited by femto to picosecond short polarized nIR-laser pulses and subsequently probed by means of mSAXS utilizing XUV pulses produced by the FLASH and FERMI FEL sources. The basics of the interactions of polarized light with magnetic matter and the principle of mSAXS are introduced in section 2.4.

When excited by ultrashort nIR-laser pulses, the long-range order in a ferromagnetic thin film gets (partially) lost within a few hundreds of femtoseconds. Aside from this so-called ultrafast demagnetization, which gives insight in fundamental electron (de-)correlation effects on femtosecond time scales, under certain conditions, a ferromagnetic state can also be switched from a magnetization pointing up to a magnetization pointing down (and vice versa) using circularly polarized laser pulses, known as helicity-dependent all-optical switching (HD-

AOS). The focus of this work is on studying these laser induced magnetization dynamics with femtosecond time and nanoscopic spatial resolution. The two mechanisms are described in detail in the final section of this chapter (section 2.5).

2.1. Ferromagnetism in $3d$ Metals

Up to date a unified model that captures both the localized and delocalized character of ferromagnetism in $3d$ transition metal elements is still lacking. Instead, our present-day understanding of magnetism is based on two models, each describing parts of their magnetic properties: the Stoner model and the Heisenberg model [1, 52]. The former considers itinerant (delocalized) electrons that form energy bands in the presence of the periodic potential of the crystal lattice. The latter treats the electrons as to be localized on atomic sites, interacting with each other via inter-atomic exchange.

The Stoner model correctly predicts the non-integer atomic moment values of the ferromagnetic $3d$ elements of $2.2\,\mu_B$ for Fe, $1.7\,\mu_B$ for Co and $0.6\,\mu_B$ for Ni [52, 53]. Today, precise knowledge about the electronic band structure of materials is either obtained from experiments, using angle-resolved photoemission spectroscopy (ARPES) [54–57], or from first-principles calculations, e. g., density functional theory (DFT) [58–60]. A characteristic of the $3d$ ferromagnets is a spin-split electronic band structure that originates from a spin-dependent dispersion relation in 3-dimensional k-space, $E_n^{\uparrow\downarrow}(\mathbf{k})$ ($\uparrow$ denotes spin-up, $\downarrow$ denotes spin-down), where n is the band index. From this dispersion relation, the total (spin-resolved) density of states, $D_{\uparrow\downarrow}(E)$, is obtained by counting available electronic states per unit volume in an energy interval $[E; E + \mathrm{d}E]$. Mathematically, this is expressed as an integral over surfaces of constant energy (e. g., the Fermi surface) in k-space [61, 62]

$$D_{\uparrow\downarrow}(E) = \frac{1}{(2\pi)^3} \sum_n \int \frac{1}{\left|\nabla_{\vec{k}} E_n^{\uparrow\downarrow}\right|} \mathrm{d}S_{\vec{k}}, \tag{2.1}$$

where $\mathrm{d}S_{\vec{k}}$ is a surface element. The spin-resolved density of states of fcc Co is shown in Fig. 2.1 a). The spin-up band is shifted in energy with respect to the spin-down band by $E_{ex} \approx (1\text{–}2)\,\mathrm{eV}$, which is called the exchange splitting or exchange energy. In the Stoner model, E_{ex} is also called spin-flip energy and corresponds to the reversal of a single electron-spin in the sea of all other electron-spins. As two electrons cannot occupy the same state (Pauli exclusion principle), a spin flip is associated with an energy cost determined by E_{ex}. As a consequence of the exchange splitting, there exists an imbalance in the number of occupied spin-up (red-shaded area) and spin-down states (blue-shaded area), which are named the *majority* and the *minority-spin* band, respectively.[1] The difference in the number of majority

[1] The choice of up and down is arbitrary, but it is important that the spin-orientation is opposite in the two bands.

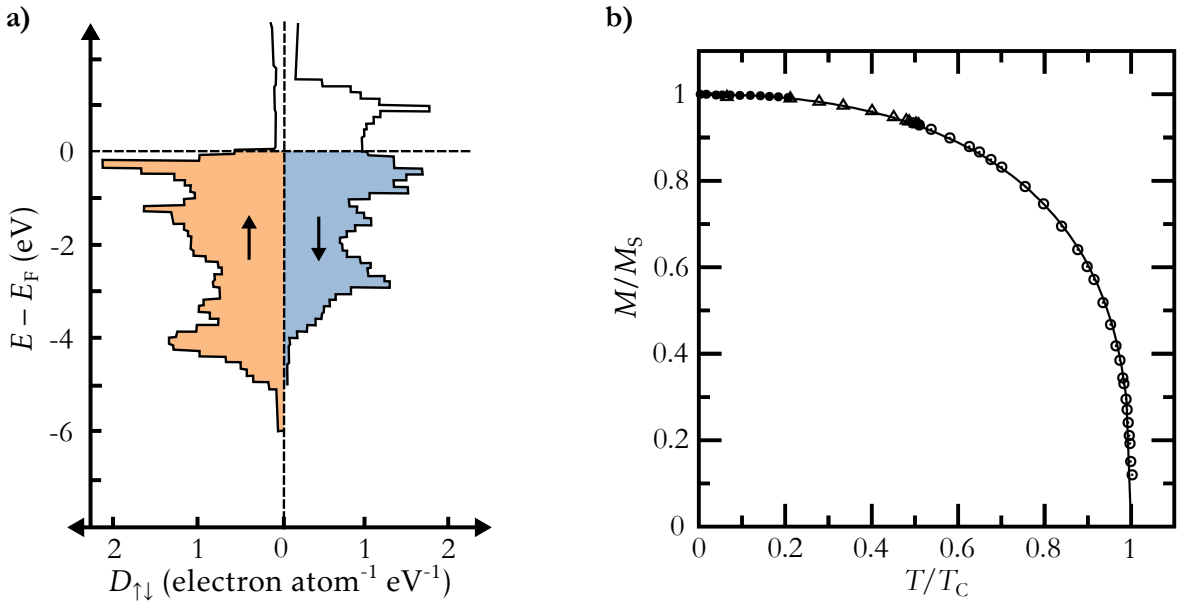

Figure 2.1.: a) Calculated spin-dependent density of states, $D_{\uparrow\downarrow}(E)$, in fcc Co consistent with the results from UV and X-ray photoelectron spectra (taken from Ref. [63] with minor modifications). In fcc Co, majority (red) and minority band (blue) are shifted in energy by $E_{ex} \approx 1\,\text{eV}$ [59]. The exchange-split valence band results in an imbalance in the number of occupied majority-spin ($D_{\uparrow}(E_F) = 0.65\,\text{electron/(atom eV)}$) and minority-spin states ($D_{\downarrow}(E_F) = 0.99\,\text{electron/(atom eV)}$), with E_F the Fermi energy. b) Reduced magnetization, M/M_S, versus reduced temperature, T/T_C, in Co with $T_C = 1394\,\text{K}$ and $M_S = 1.4 \cdot 10^6\,\text{A/m}$ [64] (taken from Ref. [65] with minor modifications).

and minority-spin electrons gives rise to an uncompensated magnetic moment [1, 62]

$$m = \frac{\hbar}{2}\gamma_e \int \big(D_{\uparrow}(E) - D_{\downarrow}(E)\big) f(E,T)\,\mathrm{d}E, \tag{2.2}$$

where γ_e is the (electron) gyromagnetic ratio and $f(E,T) = \exp\left(((E-\mu)/k_B T) + 1\right)^{-1}$ is the Fermi-Dirac distribution with the chemical potential, μ. Using calculated values for $D_{\uparrow\downarrow}(E)$, eq. (2.2) predicts well the experimentally observed fractional magnetic moments for the 3*d* ferromagnets given above. The Stoner model furthermore predicts ferromagnetic order for materials that fulfill the so-called Stoner criterion, $I(E_F)D(E_F) > 1$, where I describes the exchange energy savings when shifting the spin sub-bands with respect to each other [52]. Correctly, the Stoner criterion is only fulfilled by the 3*d* elements Fe, Co and Ni, which are the only ferromagnetic elements at room temperature.[2]

Even though the magnetic properties of the 3*d* transition metals are essentially defined by itinerant electrons, the Stoner model fails in accurately describing thermodynamic properties, e. g., the temperature dependence of the magnetization. The full loss of magnetic order in the

[2] Note that some elements are close to $I(E_F)D(E_F) = 1$, such as Pd, which are therefore easily magnetized. Further note that rare earth elements like Gd are ferromagnetic only at temperatures below room temperature.

Stoner model would require to overcome the exchange energy of $E_{\mathrm{ex}} \approx (1\text{–}2)\,\mathrm{eV}$, i. e., a Curie temperature on the order of $T_{\mathrm{C}} = E_{\mathrm{ex}}/(3k_{\mathrm{B}}) \approx (0.5\text{–}1) \cdot 10^4\,\mathrm{K}$, which is about a factor of five to ten larger than the experimentally observed values [1].

A more accurate description of the temperature dependence of the magnetization, shown for Co in Fig. 2.1 b), is given by the Weiss-Heisenberg model. Based on the descriptions by P.-E. Weiss, long-range magnetic ordering is due to a molecular field that is proportional to the magnetization [1]. From this approach, also known as *mean field theory*, follows the spontaneous magnetic saturation at low temperatures and the phase transition to a paramagnetic material at the Curie temperature, T_{C}. However, large molecular fields on the order of $\mu_0 H_{\mathrm{W}} \approx 1000\,\mathrm{T}$ would be required to account for a $T_{\mathrm{C}} \approx 1000\,\mathrm{K}$ in the $3d$ ferromagnets [1]. If this was an actual magnetic field in the classical sense, it would require the presence of charge current densities that exceed the damage threshold of the material itself.

In the Weiss-Heisenberg model, the Weiss molecular field is connected to the strong quantum mechanical exchange interaction [1]. The exchange interaction can be described by the Heisenberg Hamiltonian, which considers magnetic moments that are localized on atomic sites and interact with each other by means of a quantum mechanical (inter-atomic) exchange [1]

$$\mathcal{H}_{\mathrm{ex}} = -\sum_{i \neq j} J_{ij} \mathbf{s}_i \cdot \mathbf{s}_j, \tag{2.3}$$

where $\mathbf{s}_i$ and $\mathbf{s}_j$ are the spins of the electrons at lattice sites i and j, respectively, and J_{ij} is the exchange constant, or exchange integral. The (inter-atomic) exchange interaction originates from the repulsive Coulomb interaction between the electrons under consideration of the Pauli exclusion principle, which states that the total wavefunction of the electron system has to be antisymmetric when interchanging any two (indistinguishable) electrons [1]. The total wavefunction can be expressed as the product of space, ψ, and spin wave function, χ, so that for a symmetric ψ (electrons tend to be close to each other), the Pauli principle leads to an antisymmetric χ (electrons have opposite spins), whereas for an antisymmetric ψ (electrons tend to avoid each other), a symmetric χ (electrons have parallel spins) is required. A collective spin arrangement is preferred for a non-zero exchange integral, J_{ij}. For $J_{ij} > 0$ a parallel alignment is preferred, i. e., the material is a ferromagnet, whereas for $J_{ij} < 0$ an antiparallel alignment is preferred and the material is characterized as an antiferromagnet.

Today, information on the inter-atomic exchange in materials (and its temperature dependence) can be obtained by mapping the results from DFT on an effective Heisenberg Hamiltonian [62, 66]. The idea of this approach is to use the results from DFT for the magnetic ground state ($T = 0$) and to use the Heisenberg model for the description of the magnetic properties at finite temperatures. This is done through spin-wave-like excitations of the magnetization, which not only allows to describe the low-temperature behavior but also yields

an expression for the Curie temperature [1, 60, 66, 67]

$$T_C = \frac{2\langle \mathbf{s} \rangle^2 J}{3k_B}, \tag{2.4}$$

where $\langle \mathbf{s} \rangle$ is the expectation value of the atomic spin and $J = \sum_j J_{ij}$. When deriving eq. (2.4) it is assumed that all atomic spins, $\mathbf{s}$, are identical and consist of a mean constant component, $\langle \mathbf{s} \rangle$, and a component that is responsible for temperature dependent effects, $\mathbf{s} - \langle \mathbf{s} \rangle$. In the Weiss-Heisenberg-DFT theory, the Curie temperature is directly proportional to the exchange coupling constant and the expectation value of the atomic spin moments. With $\langle \mathbf{s} \rangle^2 J \approx 200\,\mathrm{meV}$ (dimensionless $\mathbf{s}$), eq. (2.4) yields a $T_C \approx 1500\,\mathrm{K}$ for fcc Co in good agreement with experimental observations [1]. Compared to the Co bulk value of $T_C = 1394\,\mathrm{K}$ [64], the Curie temperature is significantly reduced in ultrathin Co films. In general, T_C increases with total Co content in the sample, i. e., from $T_C = 216\,\mathrm{K}$ to $T_C = 300\,\mathrm{K}$ in sub-nanometer thin Co layers with increasing Co-layer thickness from $d_{Co} = 0.35\,\mathrm{nm}$ to $d_{Co} = 0.45\,\mathrm{nm}$ [68]. The Curie temperature further increases to $T_C \approx 900\,\mathrm{K}$ in a Co layer that consists of three atomic planes [69]. In Co/Pt multilayers, the Curie temperature was found to be reduced with increasing Pt-layer thickness, i. e., a reduction of T_C by $\approx 100\,\mathrm{K}$ can be expected for an increasing $d_{Pt} = (0.8\text{–}1.4)\,\mathrm{nm}$ [70]. From investigations of T_C on the total Co content, a $T_C \gtrsim 1000\,\mathrm{K}$ can be expected in the here investigated samples with total Co contents between 57% and 83% [71].

The exchange interaction is strong and falls off rapidly with inter-atomic distance, i. e., it is short-range in nature. It is thus feasible to consider only next-nearest neighbor interactions as well as only small angle deviations between adjacent spins. The scalar product in eq. (2.3) can then be expanded into a Taylor series up to first order. A transition from the atomistic to the so-called micromagnetic approximation is a transition to continuous variables, e. g., replacing the summation by an integration, and the spin (magnetic moment) by an averaged density of magnetic moments, i. e., the saturation magnetization, M_S. The exchange energy density is then given by [72]

$$\frac{E_{ex}}{V} = A_{ex}\left[\left(\nabla m_x\right)^2 + \left(\nabla m_y\right)^2 + \left(\nabla m_z\right)^2\right], \tag{2.5}$$

where A_{ex} is a material specific parameter (on the order of 10 pJ/m in Co thin films [71]), the so-called exchange stiffness, and $m_i = M_i/M_S$ is the reduced magnetization component along direction i. With an energy density on the order of $10^3\,\mathrm{MJ/m^3}$, the (inter-atomic) exchange interaction is the strongest magnetic interaction and leads to the long-range order of magnetic moments in ferromagnetic materials. In order to understand the complex micro and nanostructure of magnetic thin films, however, further energy contributions have to be considered which are briefly introduced in the following section.

2.2. Magnetic Energies in Multilayers

Aside from the exchange energy, further energy terms have to be considered for the total free energy E_{tot}: the magnetostatic energy, E_{ms}, containing the Zeeman energy, E_{zee}, and the stray-field or demagnetization energy, E_{d}, and the magnetocrystalline anisotropy energy, E_{mca}

$$E_{\mathrm{tot}} = E_{\mathrm{ex}} + E_{\mathrm{ms}} + E_{\mathrm{mca}}, \tag{2.6}$$

which are obtained by integrating the individual energy density contributions over the sample volume, V.[3] In equilibrium, the magnetic material will develop a magnetic domain structure for which the total free energy is at a global or local minimum. Different equilibrium domain configurations can be generated in magnetic materials, such as the here investigated $[\mathrm{Co/Pt}]_x$ multilayers, due to the tunability of the individual energy contributions.

2.2.1. Magnetostatic Energy

The magnetostatic energy, E_{ms}, is given by the sum of the Zeeman energy, E_{zee}, which is an energy due to the interaction of the magnetization, $\mathbf{M}$, with an external magnetic field, $\mathbf{H}_{\mathrm{ext}}$, and the stray-field or demagnetization energy, E_{d}, which is a self-energy generated by the magnetization itself. The latter is a consequence of the second Maxwell equation in matter, i. e., a consequence of the demagnetizing field, $\mathbf{H}_{\mathrm{d}}$, that arises if sinks and sources of magnetization are generated ($\nabla \cdot \mathbf{M} \neq 0$). For a ferromagnetic material in an external magnetic field the magnetostatic energy is [78]

$$E_{\mathrm{ms}} = -\frac{\mu_0}{2} \int_V \mathbf{M} \cdot \mathbf{H}_{\mathrm{d}} \, \mathrm{d}V - \mu_0 \int_V \mathbf{M} \cdot \mathbf{H}_{\mathrm{ext}} \, \mathrm{d}V. \tag{2.7}$$

The stray-field energy (first integral) is always positive semi-definite so that the existence of $\mathbf{H}_{\mathrm{d}}$ always enhances the total free energy. Hence, due to the stray-field energy a magnetic system will try to develop a domain pattern with as little magnetic volume ($\rho_{\mathrm{m}} = -\nabla \cdot \mathbf{M}$) and surface charges ($\sigma = \mathbf{M} \cdot \mathbf{n}$, $\mathbf{n}$: film normal) as possible [72]. For the case of a homogeneously magnetized thin film with main axis $a = b \to \infty$ and $c \ll a$, that are aligned with the coordinate system ($c \parallel z$),

[3] Note that in general, further energy terms such as the Dzyaloshinskii-Moriya interaction (DMI) or interlayer exchange coupling (IEC) have to be considered when determining the total free energy of magnetic multilayers. While the former is small for symmetrically stacked Co/Pt multilayers (order of $0.1\,\mathrm{mJ/m^2}$) [73–75], the latter was found to yield an antiferromagnetic coupling across Pt-interlayers only for $d_{\mathrm{Pt}} > 2.4\,\mathrm{nm}$ [76, 77], which is not realized within this work.

the demagnetizing field is uniform and depends linearly on the magnetization [78]

$$\mathbf{H}_\mathrm{d} = -\hat{N}_\mathrm{film} \cdot \mathbf{M} \quad \text{with} \quad \hat{N}_\mathrm{film} = \begin{pmatrix} 0 & 0 & 0 \\ 0 & 0 & 0 \\ 0 & 0 & 1 \end{pmatrix}, \tag{2.8}$$

where $\hat{N}_\mathrm{film}$ is the demagnetizing factor. The stray-field energy density can thus be calculated for thin films as

$$\frac{E_\mathrm{d}}{V} = \frac{\mu_0}{2}\left(\hat{N}_\mathrm{film} \cdot \mathbf{M}\right) \cdot \mathbf{M} = \frac{\mu_0}{2} M_z^2 = \frac{\mu_0}{2} M_\mathrm{S}^2 \cos^2\Theta, \tag{2.9}$$

where Θ is the angle between the magnetization, $\mathbf{M}$, and the film normal, $\mathbf{n}$. The demagnetization energy is thus at maximum for the out-of-plane direction ($\mathbf{M} \parallel \mathbf{n}$, $\Theta = 0°$) and minimum for the in-plane direction ($\mathbf{M} \perp \mathbf{n}$, $\Theta = 90°$). The difference in energy density between the direction of easiest and hardest magnetizability is called shape anisotropy

$$\frac{E_\mathrm{d}}{V} = K_\mathrm{d} = \frac{\mu_0}{2} M_\mathrm{S}^2. \tag{2.10}$$

The shape anisotropy for Co thin films at room temperature with $M_\mathrm{S} = 1.4 \cdot 10^6\,\mathrm{A/m}$ [64] is $K_\mathrm{d} = 1.23\,\mathrm{MJ/m^3}$, which is about three orders of magnitude smaller than the exchange energy density.

2.2.2. Magnetocrystalline Anisotropy Energy

Besides the stray-field energy, another anisotropic energy to E_tot in magnetic thin films arises from the crystal structure. The magnetocrystalline anisotropy (MCA) has a volume ($E_\mathrm{mca,V}$) and a surface ($E_\mathrm{mca,S}$) contribution which dictate the crystallographic direction of easiest and hardest magnetizability. A uniaxial anisotropy can be induced, e. g., in systems with distorted crystal lattices such as in $L1_0$-ordered FePt(Cu) thin films [79], but also in multilayer thin films, where the translational symmetry of the crystal structure is broken along the out-of-plane direction.

Magnetocrystalline Volume Anisotropy The magnetocrystalline volume anisotropy arises from the spin–orbit interaction (SOI) which is given by the spin–orbit Hamiltonian $\mathcal{H}_\mathrm{SOI} = A\mathbf{L}\cdot\mathbf{S}$, with A the spin–orbit parameter that describes the strength of the interaction [1]. The orbital momentum, $\mathbf{L}$, is linked to the crystal lattice so that due to the SOI, the energy density related with MCA depends on the orientation of the spin, $\mathbf{S}$, relative to the crystal lattice. For crystal lattices with a single preferred direction of magnetization (uniaxial), the energy density is only a function of the angle, Θ, between this direction and the magnetization, $\mathbf{M}$ [71]. For fcc Co the easy axes of magnetization are the $\langle 111 \rangle$ directions [80]. The uniaxial energy density can

then be expanded into a power series [52]

$$\frac{E_{\mathrm{mca,V}}}{V} = K_{1\mathrm{V}} \sin^2\Theta + K_{2\mathrm{V}} \sin^4\Theta + \mathcal{O}(\sin^6\Theta), \tag{2.11}$$

where $K_{1\mathrm{V}}$ and $K_{2\mathrm{V}}$ are the uniaxial anisotropy constants of first and second order, respectively. The power-series expansion, in a good approximation, can by terminated after the second order term, as $K_{i\mathrm{V}} \gg K_{(i+1)\mathrm{V}}$. Due to the high symmetry of cubic lattices, $K_{1\mathrm{V}}$ and $K_{2\mathrm{V}}$ are small as compared to the shape anisotropy in fcc Co(111), i. e., on the order of $10^{-2}\,\mathrm{MJ/m^3}$ [80]. Hence, the magnetocrystalline volume anisotropy cannot be sufficient to induce a perpendicular easy axis of magnetization.

Magnetocrystalline Surface Anisotropy L. Néel first predicted that the magnetic anisotropy is substantially enhanced at the surface of a ferromagnet compared to the bulk, owing to missing bonds and an incompletely quenched orbital moment [81]. Surfaces and interfaces interrupt the translational symmetry of the crystal lattice which yields a surface contribution, K_{S}, to the MCA with

$$\frac{E_{\mathrm{mca,S}}}{V} = \frac{2K_{\mathrm{S}} \sin^2\Theta}{d}, \tag{2.12}$$

where d is the thickness and the factor two accounts for the two surfaces of the thin film. The surface contribution to MCA is inversely proportional to the thin-film thickness. Note that deviations from this inverse proportionality can be found due to film roughness, interdiffusion or strain [82]. By layering few-monolayer thin sheets of ferromagnetic Co with heavy metals Pd or Pt, thin films with an overall perpendicular magnetic anisotropy could be fabricated for the first time in the mid 1980's [83, 84]. For such Co/Pt-based multilayers, typical values for the surface (or interface) anisotropy were found to be in the range of $K_{\mathrm{S}} = (0.27\text{–}1.29)\,\mathrm{mJ/m^2}$ [85, 86], which is on the order of $10^{-3}\,\mathrm{eV}$ per interface atom.

The here investigated Co/Pt multilayer thin films are polycrystalline but exhibit a pronounced (111) texture along the out-of-plane direction and thus uniaxial shape and magnetocrystalline volume and surface anisotropy which add up to the total or effective anisotropy which can be expressed as

$$K_{1,\mathrm{eff}} = \underbrace{K_{1\mathrm{V}} - \frac{\mu_0}{2} M_{\mathrm{S}}^2}_{K_{1\mathrm{V,eff}}} + \frac{2K_{1\mathrm{S}}}{d}. \tag{2.13}$$

The second order magnetic anisotropy was found to be always positive ($K_2 \approx 0.07\,\mathrm{MJ/m^3}$) in Co/Pt multilayers, independent from the individual Co and Pt-layer thicknesses or the substrate [87–89], so that a perpendicular magnetic anisotropy (PMA) is obtained for samples with $K_{1,\mathrm{eff}} > 0$.

The first-order effective magnetic anisotropy, $K_{1,\mathrm{eff}}$, of the here investigated Co/Pt multilayers, was determined by measuring the magnetic field dependence of the magnetization via magneto-optical Kerr-effect (MOKE) measurements in both in-plane and out-of-plane direction (section 3.2.2). Under consideration of the Zeeman energy density, $E_{\mathrm{zee}}/V = -\mu_0 \mathbf{M} \cdot \mathbf{H}_{\mathrm{ext}} = -\mu_0 M_{\mathrm{S}} H_{\mathrm{ext}} \cos\Phi$, with Φ the angle between $\mathbf{M}$ and $\mathbf{H}$, the total free energy density in second order approximation is given by

$$\frac{E_{\mathrm{tot}}}{V} = K_{1,\mathrm{eff}} \sin^2\Theta + K_2 \sin^4\Theta - \mu_0 M_{\mathrm{S}} H_{\mathrm{ext}} \cos\Phi. \tag{2.14}$$

For a thin film with easy axis of magnetization along the surface normal, $K_{1,\mathrm{eff}}$ is determined from the hard-axis hysteresis loop, by applying H_{ext} in any in-plane direction ($\Phi = 90° - \Theta$). Then, the equilibrium zero-torque condition, $\partial(E_{\mathrm{tot}}/V)/\partial\Theta = 0$, yields

$$\begin{aligned} &2K_{1,\mathrm{eff}} \sin\Theta + 4K_2 \sin^3\Theta - \mu_0 M_{\mathrm{S}} H_{\mathrm{ext}} = 0 \\ &\Leftrightarrow \frac{2K_{1,\mathrm{eff}}}{M_{\mathrm{S}}} m_{\parallel} + \frac{4K_2}{M_{\mathrm{S}}} m_{\parallel}^3 = \mu_0 H_{\mathrm{ext}}(m_{\parallel}), \end{aligned} \tag{2.15}$$

with $m_{\parallel} = M_{\parallel}/M_{\mathrm{S}} = \sin\Theta$ the reduced magnetization component parallel to the external field direction (in-plane component).

2.3. Magnetic Domains and Domain-Walls

Up to this point, only homogeneous magnetization distributions were regarded. In general, the total free energy in magnetic thin films can be significantly reduced through the formation of an inhomogeneous magnetization distribution, i. e., a magnetic multi-domain pattern, as described in detail in Ref. [90]. The formation of such an inhomogeneous magnetization distribution often occurs in thin films with PMA, due to the large number of surface charges in the single-domain configuration and the associated large stray-field energy density of $E_{\mathrm{d}}/V = \mu_0 M_{\mathrm{S}}^2/2$ (section 2.2.1). Thus it is often energetically preferred to reduce E_{d} at the expense of exchange, E_{ex}, and magnetocrystalline anisotropy energy, E_{mca}, via the formation of alternating up and down-magnetized domains, as illustrated in Fig. 2.2 a).[4] Inside the individual domains, however, the magnetization distribution remains homogeneous so that E_{ex} and E_{mca} are minimized. The (average) width and shape of the domains in such a multi-domain pattern depends on the size of the individual energy terms that contribute to E_{tot}. Different equilibrium configurations are realized by tuning the individual Co and Pt-layer thicknesses, and thus $E_{\mathrm{mca,S}}$ (eq. (2.12)), as well as by altering the number of multilayer repetitions, i. e., the

[4] Note that more complex multi-domain configurations may occur in different materials, e. g., the formation of flux-closure domains in ferroelectric $Pb(Zr,Ti)O_3$ [92].

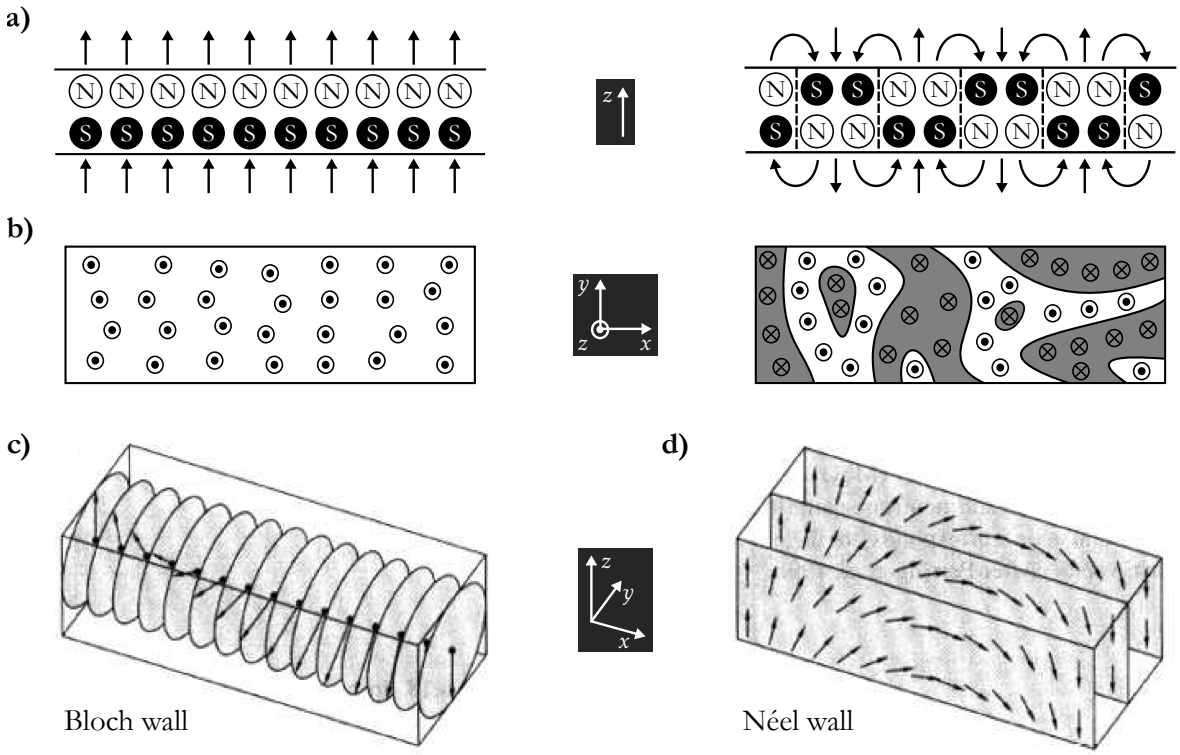

Figure 2.2.: Illustration of the multi-domain formation in magnetic thin films: a) side view and b) top view. The large stray-field energy of a homogeneously magnetized thin film (single-domain state on the left), may be reduced through the formation of alternating up and down-magnetized domains (multi-domain state on the right). The exact configuration of domains in the local or global energetic minimum depends on structural details of the thin film. Up and down-magnetized domains are connected via either c) a Bloch wall, or d) a Néel wall (taken from Ref. [91]).

total Co amount, and thus E_d (eq. (2.12)). On nanoscopic length scales, however, the shape of the domain configuration depends on local energetic minima, e. g., structural defects like lattice missmatches or vacancies, which act as pinning sites for the magnetic domains [90]. Consequently, after out-of-plane demagnetization cycles as described in section 3.2.3, the maze-domain ground state, on the one hand, can be characterized by an *average* domain size, D_{av}, with a certain degree of short-range order, i. e., a certain lateral correlation length, ξ. On the other hand, it may show differences on the nanoscopic length scale when repeating the demagnetization cycles, i. e., the exact nanostructure cannot be fully controlled.

The up and a down-magnetized domains in a multi-domain pattern are connected via a gradual rotation of the magnetization over a distance δ_w, i. e., the domain-wall width. The formation of a domain wall is associated with an energy cost γ_w determined by E_{ex} and E_{mca}. In equilibrium, the domain configuration is a result of minimizing the total free energy associated with both γ_w and E_d, i. e., a multi-domain pattern with a large number of domains is obtained for $\gamma_w < E_d$, whereas a domain pattern with a small number of domains is formed

for $E_d < \gamma_w$. Note that in the here investigated Co/Pt multilayers, that possess a Co content of only $d_{Co}^{tot} < 5\,nm$, the stray-field energy contribution is rather small so that also the single-domain configuration is an energetically stable equilibrium state, i. e., the samples exhibit full remanence (see Fig. 3.3 on page 59).

In general, there exist two possibilities for the rotation of magnetization within a domain wall, namely a rotation in the wall plane (Bloch wall) or a rotation perpendicular to the wall plane (Néel wall), as shown in Fig. 2.2 c) and d), respectively. An important property of Bloch walls in thin films with PMA is that the magnetization distribution is free of divergence and thus free of volume charges $\rho_m = -\nabla \cdot \mathbf{M}$. As this is not the case for Néel walls, Bloch walls are lower in energy and thus are typically the preferred kind. The domain-wall energy per area and the domain-wall width of such Bloch walls in first order approximation of the effective anisotropy, $K_{1,eff}$, is given by [93]

$$\gamma_{Bloch} \approx 4\sqrt{A_{ex} K_{1,eff}} \quad , \quad \delta_{Bloch} \approx \pi \sqrt{\frac{A_{ex}}{K_{1,eff}}}. \tag{2.16}$$

A magnetic multi-domain pattern can be seen as a disordered magnetic grating, that can be investigated by sccattering experiments, provided that a contrast exists between up and down-magnetized domains (section 2.4.4). Within this work, information on changes of the average domain periodicity, $T_{av} = 2D_{av}$, and the lateral correlation length, ξ, in nanoscopic multi-domain states were obtained by using coherent XUV pulses ($\lambda = 20.8\,nm$) from a free-electron laser (FEL) in a time-resolved resonant magnetic small-angle X-ray scattering (TR-mSAXS) experiment (chapter 6). As a pre-study for these time-resolved investigations, the nanoscopic multi-domain states were imaged in real space by Fourier-transform holography (FTH) using coherent synchrotron radiation. Details on the experimental methods are given in chapter 4. By combining time-resolved scattering experiments with imaging of multi-domain structures allows for a detailed understanding of nIR-laser induced modifications in nanoscopic magnetic structures.

2.4. Interactions of Polarized Light with Magnetic Matter

The interaction of polarized light with condensed matter has been studied in the mid 19th century by Michael Faraday who "[...] *succeeded in magnetizing and electrifying a ray of light, and in illuminating a magnetic line of force*" [2]. In his groundbreaking experiments M. Faraday demonstrated that the plane of polarization of linearly polarized light is rotated when light is *transmitted* through lead-borosilicate glass in a magnetic field that exhibits a non-zero component in the direction of the light beam. In changing the polarity of the electromagnet, and hence the direction of the magnetic field, the direction of the rotation of polarization was

reversed. The discovery of the *magneto-optical Faraday effect* (MOFE) was the first experimental observation of an interaction between light and magnetism. In 1877, John Kerr found a rotation of polarization of linearly polarized light upon *reflection* from the polished surface of the pole of an iron electromagnet [3]. The so-called polar *magneto-optical Kerr effect* (MOKE) thus is the analogy to the MOFE in reflection geometry. Both MOFE and MOKE originate from off-diagonal components of the dielectric tensor, $\hat{\varepsilon}$, which give the material an anisotropic permittivity and thus left-circular (LCP) and right-circular (RCP) polarized light waves propagate in the medium with different phase velocities. As linearly polarized light can be seen as a superposition of LCP and RCP components of equal amplitudes, the different phase velocities lead to a phase shift and hence to the observed rotation of the polarization plane. The discovery of the magneto-optical effects by M. Faraday and J. Kerr prompted to think of light as electromagnetic (EM) radiation and played a central role in the development of James Clerk Maxwell's theory of electromagnetism [94].

In the here investigated ferromagnetic metals, another polarization dependent magneto-optical phenomenon occurs, which is known as *magnetic circular dichroism* (MCD) [1, 95]. The name "dichroic" means "two-colors" and refers to the different absorption of LCP and RCP light in magnetized absorbing media.

In this work, polarized light was used to both excite and probe the magnetic multi-domain states in about 10 nm-thin ferromagnetic Co/Pt multilayers in transmission geometry. They were excited by femto to picosecond-short linearly (LP) and circularly (CP) polarized optical laser pulses with a central wavelength in the near infrared (nIR) regime ($\lambda = 800\,\mathrm{nm}$). The transmission of polarized light through a homogeneously magnetized medium is described classically in section 2.4.1. Limitations of the classical picture arise when the photon energy matches a core to valence band excitation in the magnetic material, i. e., a resonance energy. The quantum mechanical picture of resonant X-ray interactions with magnetic materials is introduced in section 2.4.2. The optically excited multi-domain states were probed by means of resonant magnetic small-angle X-ray scattering (mSAXS), utilizing the strongly enhanced magneto-optical effects in the extreme ultraviolet (XUV) regime at the dichroic Co $M_{2,3}$ resonance ($\lambda = 20.8\,\mathrm{nm}$) to obtain a large magnetic scattering intensity. The scattering formalism of mSAXS is introduced in section 2.4.3. The influence of different domain configurations on the magnetic scattering intensity is simulated in section 2.4.4 and an expression for the expected (maximum) transmitted intensity in mSAXS for the here investigated Co/Pt multilayers is given in section 2.4.5.

2.4.1. Transmission of EM Waves through Ferromagnetic Thin Films with Perpendicular Magnetic Anisotropy

In this section, the polarization-dependent transmission of an EM wave through a thin magnetic film with perpendicular magnetic anisotropy is described classically by electrodynamics, following the formalisms given by D. J. Griffiths [96], J. D. Jackson [97] and P. Oppeneer [98].

The propagation of a polarized EM wave through a ferromagnetic thin film is governed by the Maxwell equations in matter [94, 97]

$$\nabla \cdot \mathbf{D} = \rho, \tag{2.17}$$

$$\nabla \cdot \mathbf{B} = 0, \tag{2.18}$$

$$\nabla \times \mathbf{H} = \mathbf{j} + \frac{\partial \mathbf{D}}{\partial t}, \tag{2.19}$$

$$\nabla \times \mathbf{E} = -\frac{\partial \mathbf{B}}{\partial t}, \tag{2.20}$$

with $\mathbf{E}$ the electric field, $\mathbf{H}$ the magnetic field, $\mathbf{D} = \hat{\varepsilon}\mathbf{E}$ the electric displacement, $\mathbf{B} = \hat{\mu}\mathbf{H}$ the magnetic induction and ρ and $\mathbf{j}$ the charge and current density, respectively. In the following, a homogeneous medium is assumed, i. e., the permittivity or dielectric tensor, $\hat{\varepsilon} = \varepsilon_0 \hat{\varepsilon}_\mathrm{r}$, and the magnetic permeability tensor, $\hat{\mu} = \mu_0 \hat{\mu}_\mathrm{r}$, do not vary inside the medium. Here, $\hat{\varepsilon}_\mathrm{r}$ and $\hat{\mu}_\mathrm{r}$ are the material's relative permittivity and permeability tensors and ε_0 and μ_0 are the vacuum permittivity and permeability, respectively. In general, $\hat{\varepsilon}(\mathbf{k}, \omega)$ and $\hat{\mu}(\mathbf{k}, \omega)$ depend on the wavevector, $\mathbf{k}$, and the frequency, ω, of the EM field. For the here used nIR ($\lambda = 800\,\mathrm{nm}$) and XUV ($\lambda \approx 20\,\mathrm{nm}$) radiation, the wavelength is much larger than the lattice parameters of Co and Pt with $a_\mathrm{Co} = 0.353\,\mathrm{nm}$ and $a_\mathrm{Pt} = 0.392\,\mathrm{nm}$, respectively [99]. Thus, the $\mathbf{k}$-dependence of the permittivity and permeability tensors can be neglected [98].

Taking the partial time derivative of eq. (2.19) and combining it with eq. (2.20), allows to derive the homogeneous ($\partial \mathbf{j}/\partial t = 0$)[5] continuity equation of a light wave's electric field inside a material

$$\boldsymbol{\nabla} \times (\boldsymbol{\nabla} \times \mathbf{E}) = \hat{\mu}\hat{\varepsilon}\frac{\partial^2 \mathbf{E}}{\partial t^2}. \tag{2.21}$$

Importantly, even in ferromagnetic materials the relative permeability can be approximated by the unit tensor, $\hat{\mu}_\mathrm{r} = \hat{1}$. This is because the direct response of the electron-spin is too slow to follow the EM field of nIR and shorter wavelength radiation, that oscillate with frequencies up to a factor of 10^6 higher than the ferromagnetic resonance (gigahertz regime). Hence, the

[5] Note that in general $\partial \mathbf{j}/\partial t \neq 0$ in conducting materials such as ferromagnetic metals. The solution of the homogeneous wave equation, however, is a good approximation to describe the polarization dependent transmission of a light wave through a magnetic material.

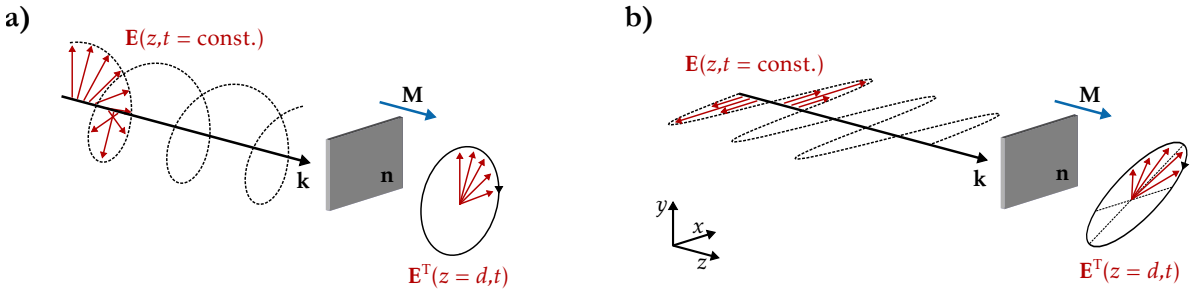

Figure 2.3.: Illustration of the incoming and transmitted **E**-field through a homogeneously magnetized material of thickness d with refractive index $\mathbf{n} = n\mathbf{e}_z$, for parallel alignment between the wavevector $\mathbf{k} = k\mathbf{e}_z$ and the magnetization $\mathbf{M} = M_z\mathbf{e}_z$ along the z-direction. a) The polarization state of a circular polarized wave is preserved upon transmission through the magnetic material. b) An initially LP wave gets elliptically polarized and the axis of the ellipse is rotated (Faraday effect).

propagation of an EM wave inside a magnetic material is dominated by the electric response, described by the dielectric tensor, $\hat{\varepsilon}$ [98].

The dielectric tensor of a magnetized medium adopts a particular form, which is related to the crystal symmetry and the direction of the magnetization with respect to the crystal axes [100]. The here investigated Co/Pt multilayers have a fcc crystal structure with a pronounced (111)-texture [82] and thus a 3-fold rotational symmetry with respect to the sample surface normal (z-direction). They furthermore possess a perpendicular magnetic anisotropy, i. e., a magnetization direction that is aligned with the sample's surface normal ($\mathbf{M} = M_z\mathbf{e}_z$). In that case, the dielectric tensor adopts the following form [98, 101]

$$\hat{\varepsilon}_\mathrm{r} = \begin{pmatrix} \varepsilon_{xx} & \varepsilon_{xy} & 0 \\ -\varepsilon_{xy} & \varepsilon_{xx} & 0 \\ 0 & 0 & \varepsilon_{zz} \end{pmatrix}. \tag{2.22}$$

Note that only for non-magnetic materials the dielectric tensor is diagonal, i. e., $\varepsilon_{xy} = 0$, and only for the case of an isotropic medium becomes $\hat{\varepsilon}_\mathrm{r} = \hat{1}$. The off-diagonal elements are a result of the magnetization and give rise to polarization-dependent magneto-optical phenomena. The geometry for the transmission of polarized light that propagates along the z-direction ($\mathbf{k} = k_z\mathbf{e}_z$) through a homogeneously magnetized thin film ($\mathbf{n} = n\mathbf{e}_z$) is illustrated in Fig. 2.3.

An ansatz to solve eq. (2.21) are plane EM waves that undergo absorption and dispersion in the magnetic medium according to the dispersion relation $n(\omega) = k_z c/\omega$

$$\mathbf{E}(z,t) = \mathbf{E}_0 \exp\left(i\omega\left(\frac{nz}{c} - t\right)\right). \tag{2.23}$$

The complex refractive index, $n(\omega)$, given by the quotient of the velocity of light in vacuum, c, and the phase velocity of light in the thin film, ω/k_z, is evaluated in the following. For that, the

plane-wave ansatz is inserted in the continuity eq. (2.21)

$$\begin{pmatrix} \partial^2/\partial z^2 \\ \partial^2/\partial z^2 \\ 0 \end{pmatrix} \mathbf{E}_0 \exp\left(i\omega\left(\frac{nz}{c} - t\right)\right) - \frac{1}{c^2}\hat{\varepsilon}_r \begin{pmatrix} \partial^2/\partial t^2 \\ \partial^2/\partial t^2 \\ 0 \end{pmatrix} \mathbf{E}_0 \exp\left(i\omega\left(\frac{nz}{c} - t\right)\right) = 0, \tag{2.24}$$

using the definition of the speed of light in vacuum, $c^2 = 1/\mu_0\varepsilon_0$. Executing the partial derivatives leads to an eigenvalue problem, which, in its general form is known as the Fresnel equation

$$\begin{pmatrix} n^2 - \varepsilon_{xx} & -\varepsilon_{xy} & 0 \\ \varepsilon_{xy} & n^2 - \varepsilon_{xx} & 0 \\ 0 & 0 & \varepsilon_{xx} \end{pmatrix} \mathbf{E}(z,t) = 0. \tag{2.25}$$

The non-trivial solution of eq. (2.25) is obtained by calculating its determinant, which yields two eigenvalues for the complex refractive index, n_+^2 and n_-^2, given by $n_\pm^2 = \varepsilon_{xx} \pm i\varepsilon_{xy}$. The two solutions can be viewed as different refractive indices either for LCP and RCP light at a fixed magnetization direction, or for a fixed helicity at opposite magnetization directions. Taking the square root and using the Taylor series expansion up to first order in ε_{xy} allows to separate $n_\pm$ into a non-magnetic part, $n_0 = \sqrt{\varepsilon_{xx}}$, and its magnetic variation, $\Delta n = i\varepsilon_{xy}/\sqrt{\varepsilon_{xx}}$. The latter can be expressed by [62]

$$\Delta n = -\Delta\delta + i\Delta\beta, \tag{2.26}$$

with $\Delta\beta$ and $\Delta\delta$ being the magnetic variations to absorption and dispersion, known as the *magnetic circular dichroism* (MCD) and the *magneto-optical Faraday* (MOFE) effect, respectively. Due to these magnetic variations of the refractive index, $n_\pm = n_0 \pm \Delta n$, the amplitudes and phases of the transmitted fields differ for LCP and RCP light. The corresponding eigenmodes for circularly (CP) and linearly polarized (LP) plane waves, that describe the **E**-field upon transmission through a magnetic thin film are given in the following.

Circular Polarization (CP): For right-circularly (RCP,−) and left-circularly polarized (LCP,+) incident light with $\mathbf{E}_0^\pm = E_0/\sqrt{2}\left(\mathbf{e}_x \pm i\mathbf{e}_y\right)$, the transmitted electric field, $\mathbf{E}_\mathrm{T}^\pm$, through a thin magnetic film of thickness d is [62]

$$\mathbf{E}_\mathrm{T}^\pm = \mathbf{E}_0^\pm \exp(in_0k_zd)\exp(\mp\Delta\beta k_zd)\exp(\mp i\Delta\delta k_zd). \tag{2.27}$$

For CP incident light, the polarization remains unchanged upon transmission through a thin magnetic film, as illustrated in Fig. 2.3 a). Considering either LCP or RCP light, incident on a thin magnetic film that possesses a *multi-domain* state, the solutions $\mathbf{E}_\mathrm{T}^+$ and $\mathbf{E}_\mathrm{T}^-$ correspond to the fields transmitted through the up-magnetized and down-magnetized domains, respectively. The difference in the phase is $2k_z\Delta\delta d$ and the difference in the amplitude is

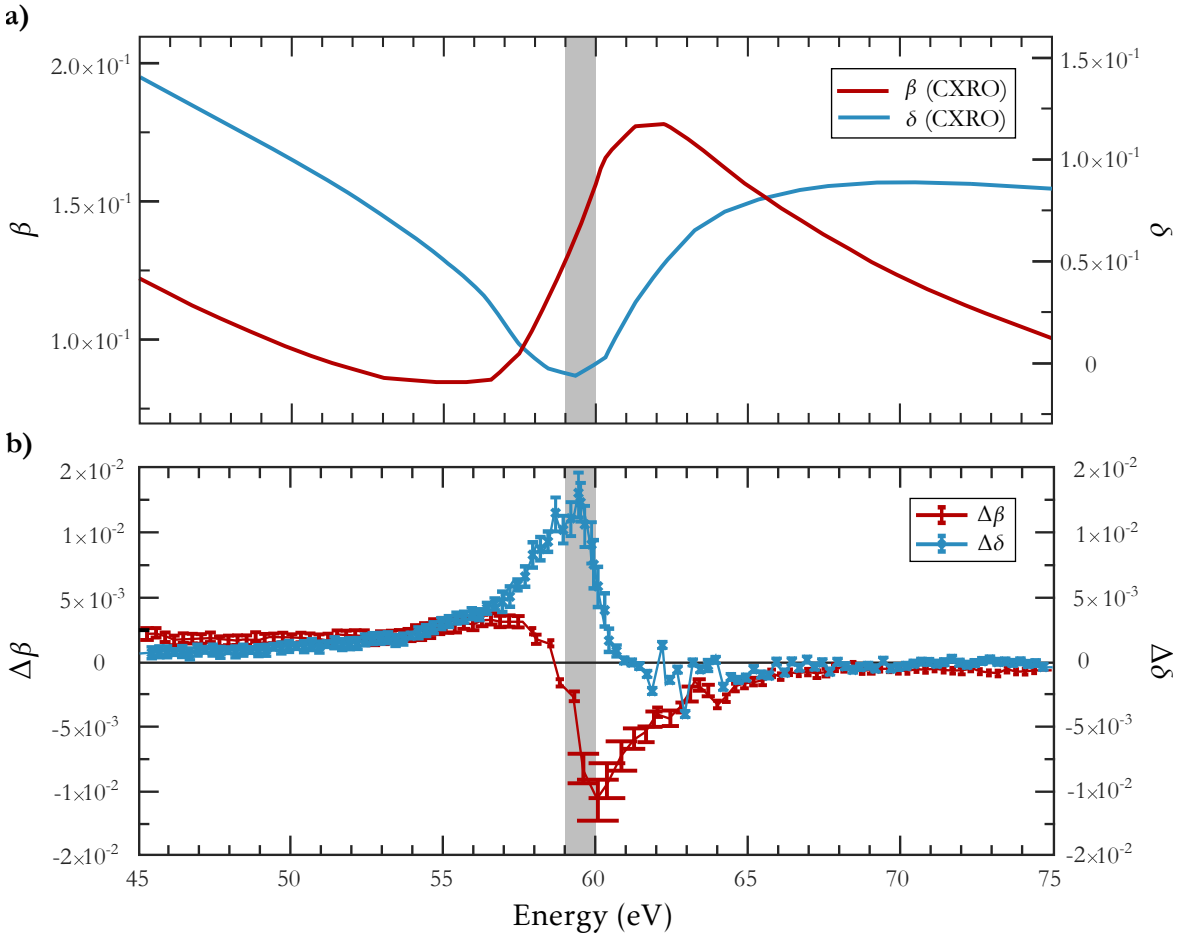

Figure 2.4.: Energy dependence of the complex refractive index, $n_{\pm} = n_0 \pm \Delta n = 1 - (\delta \pm \Delta\delta) + i(\beta \pm \Delta\beta)$ in the vicinity of the Co M edge at $E_{\mathrm{ph}} \approx 60\,\mathrm{eV}$ (gray area): a) absorption, β, and dispersion, δ,[6] and b) their magnetic variations, $\Delta\beta$ and $\Delta\delta$ (taken from Ref. [102]). Note that XMCD and X-ray Faraday effect are connected via the Kramers-Kronig relations [1]. The magnetic variations, $\Delta\beta$ and $\Delta\delta$, vanish afar from the resonance energy and are at least one order of magnitude smaller than their non-magnetic counterparts.

approximately $2k_z\Delta\beta d$ [62]. Importantly, the preservation of the state of polarization for CP incident light allows for imaging of nanoscopic multi-domain patterns via Fourier transform holography (FTH), which requires interference of an unchanged reference wave with the transmitted wave (section 4.3). For that, the two fields need to have identical polarization states, which is the case only for CP light.

Linear Polarization (LP): A LP incident light wave can be seen as the superposition of RCP and LCP light fields of equal amplitude, $\mathbf{E}_0^s = 1/\sqrt{2}\left(\mathbf{E}_0^+ + \mathbf{E}_0^-\right) = E_0\mathbf{e}_x$.[7] The transmitted field

[6] CXRO database: http://henke.lbl.gov.

[7] Note that s-polarization is chosen here, the electric field vector for p-polarization is $\mathbf{E}_0^p = E_0\mathbf{e}_y$.

through an up-magnetized (+) or a down-magnetized (−) thin film of thickness d is given by [62]

$$\begin{aligned}\mathbf{E}_{\mathrm{T}}^{\pm} = &\frac{1}{2}\mathbf{E}_0^s\left[1+\exp\left(-2\Delta\beta k_z d\right)\exp\left(-2i\Delta\delta k_z d\right)\right]\exp\left(in\_k_z d\right)\\ &\mp\frac{i}{2}\mathbf{E}_0^p\left[1-\exp\left(-2\Delta\beta k_z d\right)\exp\left(-2i\Delta\delta k_z d\right)\right]\exp\left(in\_k_z d\right).\end{aligned} \tag{2.28}$$

For LP incident light, the state of polarization is *not* preserved upon transmission through a homogeneously magnetized medium. The initially s-polarized **E**-field is elliptically polarized and the axis of the ellipse is rotated (MOFE), as illustrated in Fig. 2.3 b).[8] The transmitted fields for the two magnetization directions (±) have the same $\mathbf{E}_0^s$ component and an $\mathbf{E}_0^p$ component of the same magnitude but opposite sign, resulting in a phase shift of π between them [62].

Several scattering and spectroscopy methods utilize the fact that $\Delta\beta$ and $\Delta\delta$ are increased by orders of magnitude at specific energies in the XUV and X-ray regime, i. e., at atomic resonance energies. In the X-ray regime, these are known as the *X-ray magnetic circular dichroism* (XMCD) and the *X-ray Faraday* effect, respectively, shown in Fig. 2.4 b) for a photon-energy range that includes the atomic $3p$–$3d$ transitions (M edge) in Co ($E_{\mathrm{ph}} = 59.8\,\mathrm{eV}$) [102]. The contributions to the non-magnetic refractive index, n_0, i. e., absorption β and dispersion δ, are shown in Fig. 2.4 a). The strongly increased $\Delta\beta$ and $\Delta\delta$ at atomic resonance energies can not be explained within the classical formalism. An introduction to the quantum mechanical picture of resonant magnetic scattering is given in the following.

2.4.2. Resonant X-ray Interactions

Within the quantum-mechanical formalism of resonant X-ray interactions with a magnetic medium, the material is considered to be built from atoms in a lattice, where electrons occupy quantized states. Resonant excitations are induced when the energy of the incident EM field matches the energy difference between an atomic core level and unoccupied valence-band states at and above the Fermi energy. In the here conducted experiments, the photon energy was tuned to $E_{\mathrm{ph}} = 59.8\,\mathrm{eV}$, which is in resonance with the Co M edge ($3p$–$3d$ transitions). Through that, the magnetic properties of the Co/Pt multilayers are probed with elemental sensitivity to the ferromagnetic Co, where the $3d$ valence band is exchange split by $E_{\mathrm{ex}} \approx 1\,\mathrm{eV}$ (section 2.1). Using polarized X-ray radiation with a photon energy of 59.8 eV to induce resonant excitations, the

[8] Note that, in general, the transmitted **E**-field component through a non-homogeneous, e. g., a Co/Pt-multilayer sample, can differ from the here derived solution. By stacking thin films of different materials on top of each other, the crystallographic symmetry gets broken along the z-direction, giving $\varepsilon_{zz} \neq \varepsilon_{xx}$. Under the given experimental geometry, i. e., under normal incidence, the broken symmetry along the z-direction does not affect the eigenvalues and eigenmodes, which are independent of the ε_{zz}-component of the dielectric tensor. A formalism to describe $\mathbf{E}^{\mathrm{T}}$ in the optical regime under consideration of the different refractive indexes n_i in multilayer systems under oblique incidence can be found in Refs. [62, 103].

difference in (un-)occupied states in the $3d$ valence band is probed. In the following, resonant X-ray interactions in magnetism, namely the XMCD effect and resonant magnetic scattering, are introduced, following the descriptions given by S. W. Lovesey and S. P. Collins [104] as well as J. Stöhr and H. C. Siegmann [1].

In a quantum mechanical picture all interactions of polarized photons with magnetic matter can be described in terms of a scattering problem. A polarized EM wave either gets absorbed or scattered by the electrons in the magnetic material. The probability for polarization-dependent resonant absorption and scattering can be described with time-dependent perturbation theory, where a time-dependent EM field induces transitions between an initial state $|i'\rangle$ and a final state $|f'\rangle$. The transition probability per unit time, $T_{i'f'}$, up to second order perturbation was originally derived by H. A. Kramers and W. Heisenberg [105] and P. A. M. Dirac [106]

$$T_{i'f'} = \frac{2\pi}{\hbar}\left|\underbrace{\left\langle f'\middle|\mathcal{H}_{\mathrm{int}}\middle|i'\right\rangle}_{T^{\mathrm{abs}}} + \underbrace{\sum_{n'}\frac{\left\langle f'\middle|\mathcal{H}_{\mathrm{int}}\middle|n'\right\rangle\left\langle n'\middle|\mathcal{H}_{\mathrm{int}}\middle|i'\right\rangle}{\epsilon_{i'}-\epsilon_{n'}}}_{T^{\mathrm{scat}}}\right|^2 \delta(\epsilon_{i'}-\epsilon_{f'})\rho(\epsilon_{f'}), \tag{2.29}$$

where $\mathcal{H}_{\mathrm{int}}$ is the interaction Hamiltonian, $\epsilon_{i'}$, $\epsilon_{n'}$ and $\epsilon_{f'}$ are initial, intermediate and final state energies and $\rho(\epsilon_{f'})$ is the density of final states per energy.[9] The first-order perturbation in eq. (2.29) describes resonant absorption (T^{abs}), i. e, the XMCD effect, the second-order perturbation describes resonant X-ray scattering (T^{scat}). The last expression, $\delta(\epsilon_{i'}-\epsilon_{f'})\rho(\epsilon_{f'})$, accounts for the resonance condition, allowing transitions only for resonant photons with an energy $\hbar\omega = \epsilon_{f'} - \epsilon_{i'}$, weighed by the density of available final states $\rho(\epsilon_{f'})$.

Within the dipole approximation, considering CP X-rays with $\mathbf{k} \parallel \mathbf{e}_z$, the interaction Hamiltonian can be expressed by the polarization dependent dipole operators $\mathcal{H}_{\mathrm{int}} = \mathcal{P}_{\pm} = \mathbf{r}\cdot\boldsymbol{\varepsilon}_{\pm}$, with the electron position vector $\mathbf{r} = x\mathbf{e}_x + y\mathbf{e}_y + z\mathbf{e}_z$ and the unit photon polarization vector $\boldsymbol{\varepsilon}_{\pm} = \mathbf{e}_{z,\pm} = \mp 1/\sqrt{2}(\mathbf{e}_x \pm i\mathbf{e}_y)$. In the dipole approximation, it is assumed that the size of the absorbing atomic shell ($\approx 0.01\,\mathrm{nm}$) is small compared to photon wavelength, which is well met for XUV radiation with $\lambda = 20.8\,\mathrm{nm}$, so that the electric field can be considered constant over the atomic volume. Furthermore, transitions between pure electronic initial and final states of the form $|i\rangle = |n,l,m_l,s,m_s\rangle$ and $|f\rangle = |n^*,l^*,m_l^*,s^*,m_s^*\rangle$ are restricted according to the dipole selection rules, that allow transitions only between initial and final states with $\Delta l = l^* - l = \pm 1$ ($\Delta m_l = m_l^* - m_l = \pm 1$), like the p–d transitions, under preservation of the photoelectron spin, $\Delta s = s^* - s = 0$ ($\Delta m_s = m_s^* - m_s = 0$) [1].

[9] The states and energies in eq. (2.29) reflect those of the combined electron and photon system.

2.4.2.1. X-ray Magnetic Circular Dichroism (XMCD) Effect

The XMCD effect was predicted theoretically in 1975 for the p–d transitions (M edge) in Ni [107] and experimentally observed for the first time in 1987 at the storage ring DORIS at DESY for s–p transitions (K edge) in Fe [108]. It describes the polarization-dependent absorption of resonant X-rays in magnetic materials, given by the first-order perturbation term, T^{abs}, in eq. (2.29). In the dipole approximation the transition rate, T^{abs}, can be expressed as [1]

$$T^{\mathrm{abs}} \propto I_{\pm}^{\mathrm{abs}} = C^{\mathrm{abs}} \left| \langle f \left| \boldsymbol{\varepsilon}_{\pm} \cdot \mathbf{r} \right| i \rangle \right|^2 , \tag{2.30}$$

where $C^{\mathrm{abs}} = 4\pi^2 \hbar \omega \alpha_{\mathrm{f}}$ and $\alpha_{\mathrm{f}} = e^2/4\pi\varepsilon_0 \hbar c$ is the fine structure constant. In the following, the XMCD effect is shortly outlined for the here relevant $3p$–$3d$ (M edge) transitions in ferromagnetic Fe, Co and Ni in the range of $E_{\mathrm{ph}} = (50\text{–}70)\,\mathrm{eV}$, which can be understood from a simple two-step model [1, 95].

In the first step, the incident CP radiation excites spin-polarized photoelectrons from a spin-orbit split core level, like the $3p_{3/2}$ level (M_3 edge). The spin polarization is opposite, both, for LCP and RCP incident radiation, and for the $3p_{3/2}$ (M_3) and $3p_{1/2}$ (M_2) core levels [1]. In the second step, the exchange-split $3d$ valence band ($E_{\mathrm{ex}} \approx 1\,\mathrm{eV}$ [102]), with unequal occupancy of spin-up and spin-down electrons, acts as a detector for the spin of the excited photoelectrons ($\Delta s = 0$ in the dipole approximation).[10] The so-called XMCD asymmetry, which is the normalized difference of the transition intensities for antiparallel and parallel orientations of the magnetization and the photon polarization, is shown for the $M_{2,3}$ edges of the $3d$ ferromagnets in Fig. 2.5 a). In contrast to, e. g., the L_3 and L_2 edges, the M_3 and M_2 edges are spin-orbit split by only $E_{\mathrm{SOC}} \approx 1\,\mathrm{eV}$ in the $3d$ ferromagnets, which is about the same size as the width, $\Delta_n \approx 1\,\mathrm{eV}$ [110], of the edges. As a consequence, the M_2 and M_3 edges are not clearly distinguishable in energy but form one broad $M_{2,3}$ edge [111]. Firstly, this makes it difficult to calculate their respective transition probabilities. Secondly, the maximum XMCD asymmetry is not necessarily obtained *at* the edges, but slightly above or below, e. g., a maximum value of 10% is measured at 60 eV in Co [109].

2.4.2.2. Resonant X-ray Scattering

Resonant X-ray scattering can be described in second-order perturbation theory, by the transition probability denoted with T^{scat} in eq. (2.29), which, in the dipole approximation can

[10] For a d band with equal spin-up and spin-down occupancy, e. g., non-ferromagnetic $3d$ elements, there is no XMCD effect since the total (summed) transition intensities for RCP and LCP are identical.

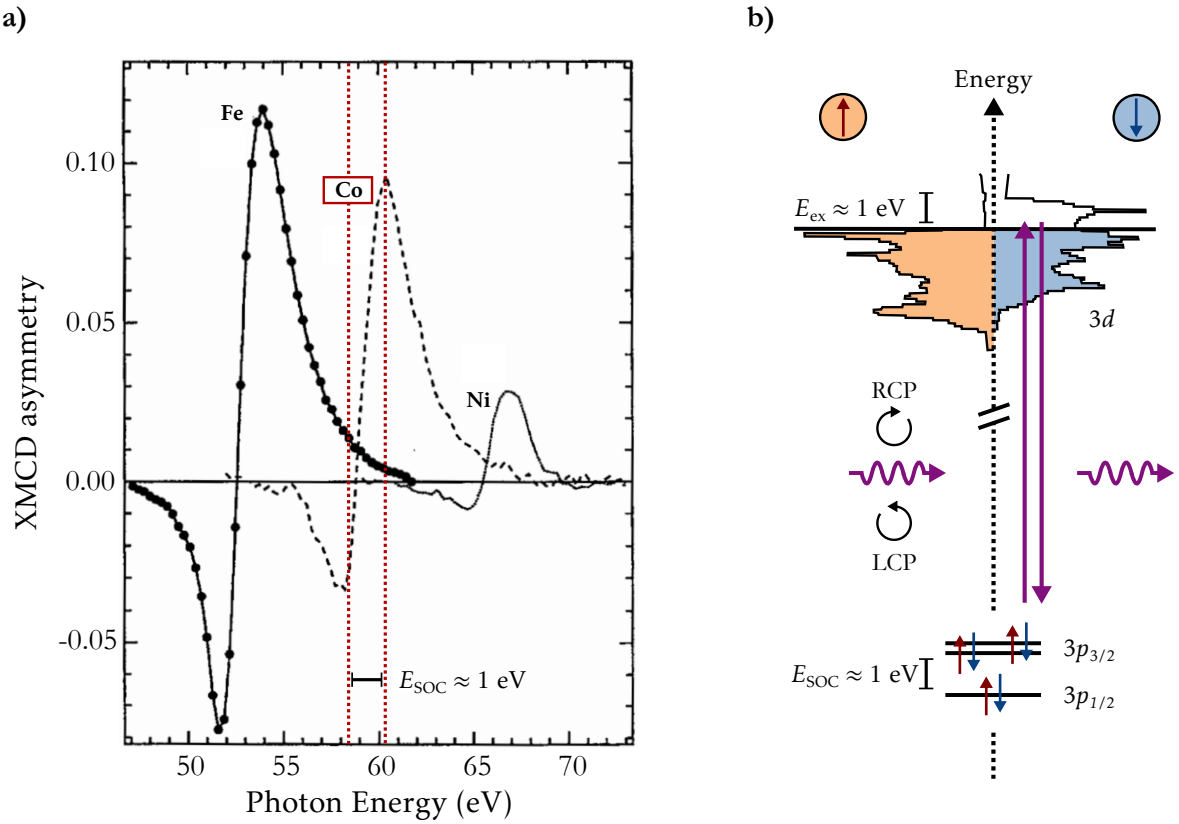

Figure 2.5.: a) X-ray magnetic circular dichroism (XMCD) at the M edges of Fe, Co and Ni, i. e., corresponding to the $3p$–$3d$ transitions, measured in reflection geometry under an incident angle of $\theta_i \approx 65°$ (reproduced with modifications from Ref. [109]). The negative and positive sign in the XMCD asymmetries correspond to the M_3 and M_2 edge, respectively. b) Illustration of resonant X-ray scattering at the Co $M_{2,3}$ edge. Circularly polarized photons with $E_{ph} \approx 59.8$ eV excite electrons from the spin-orbit split $3p_{3/2}$ and $3p_{1/2}$ core states to empty intermediate (virtual) states, $|n\rangle$, in the exchange split $3d$ band ($E_{ex} \approx 1$ eV), followed by a de-excitation to its initial state, $|i\rangle$, through emission of a photon with the same energy (elastic scattering). As the number of empty $3d$ states in the majority band (red) is small, resonant (de-)excitations in Co are mainly mediated in the minority band (blue).

be written as [1]

$$T^{\mathrm{scat}} \propto \int \left(\frac{\mathrm{d}\sigma}{\mathrm{d}\Omega}\right)^{\mathrm{scat}} \mathrm{d}\Omega = C^{\mathrm{scat}} \int \left| \sum_n \frac{\langle i|\boldsymbol{\varepsilon}_2^* \cdot \mathbf{r}|n\rangle\langle n|\boldsymbol{\varepsilon}_1 \cdot \mathbf{r}|i\rangle}{(E - E_n) + i(\Delta_n/2)} \right|^2 \mathrm{d}\Omega, \tag{2.31}$$

where $C^{\mathrm{scat}} = \hbar^2\omega^4\alpha_f^2/c^2$ and $\boldsymbol{\varepsilon}_1$ and $\boldsymbol{\varepsilon}_2$ are the unit photon polarization vectors of the incident and scattered radiation, respectively. The transition probability for resonant X-ray scattering is proportional to the differential resonant X-ray scattering cross section, $\mathrm{d}\sigma/\mathrm{d}\Omega$, integrated over the solid angle, $\mathrm{d}\Omega$. Apart from the constant C^{scat}, the transition probability for resonant scattering, T^{scat}, contains two important terms.

The squared matrix element in the numerator determines the weight of the transitions. For resonant scattering, the polarization-dependent dipole operator, $\mathbf{r} \cdot \boldsymbol{\varepsilon}_{\pm}$, acts on the electronic states twice. First, an electron is excited out of the spin-orbit split $3p_{3/2}$ or $3p_{1/2}$ core level into an empty intermediate (or virtual) state, $|n\rangle$, in the conduction band through polarization-dependent absorption of a resonant photon. Second, the (virtual) excitation is followed by a de-excitation back to the initial state, $|i\rangle$, through the creation of a photon with the same energy as the incident one (elastic scattering). The resonant scattering process is illustrated in Fig. 2.5 b). It is about a factor of 10^3 less probable than resonant absorption, however, also about a factor of 10^4 more probable than non-resonant Thomson scattering [1].

The denominator in eq. (2.31) determines the energy, $E - E_n$, and width, $i(\Delta_n/2)$, of the resonance process. As mentioned above, the resonance widths of the M_2 and M_3 edges is of comparable size as the spin-orbit splitting in the $3d$ ferromagnets, forming one broad absorption edge. In order to find the optimum magnetic scattering signal in resonant X-ray scattering experiments, the photon energy typically has to be slightly tuned around the $M_{2,3}$ edge.

2.4.3. Magnetic Small-Angle X-ray Scattering (mSAXS)

The nanoscopic multi-domain states were probed by means of resonant magnetic small-angle X-ray scattering (mSAXS) using XUV pulses with a photon energy of $E_{\mathrm{ph}} = 59.8\,\mathrm{eV}$, tuned to resonance with the Co $M_{2,3}$ edge (see previous sections). The experiments were conducted in transmission geometry so that, for the here investigated Co/Pt multilayers with PMA, the magnetization in the domain pattern is parallel or antiparallel to the light wave's propagation direction, i. e., the z-direction is the quantization axis ($\mathbf{m}(\mathbf{r}) \parallel \mathbf{k} \parallel \mathbf{e}_z$). The geometry of mSAXS in transmission is illustrated in Fig. 2.6 a). In the chosen experimental geometry, the XUV pulses impinge on the sample under normal incidence. Apart from a small portion that is reflected from the surface, the main portion of the incident XUV-pulse intensity is transmitted through the magnetic thin film, which results in a very intense direct beam ($\mathbf{Q} = 0$) on the detector that has to be blocked by a beam stop. Moreover, the polarization dependent interactions of X-rays with magnetic matter, i. e., the XMCD effect and the X-ray Faraday effect, give rise to magnetic scattering as outlined in the previous sections. The momentum transfer $\mathbf{Q} = \mathbf{k}' - \mathbf{k}$ is given by the difference between incident and scattered wavevectors, $\mathbf{k}$ and $\mathbf{k}'$, respectively, which, for elastic scattering have the same length, $|\mathbf{k}| = |\mathbf{k}'| = 2\pi/\lambda$, as illustrated in Fig. 2.6 b).

$\mathbf{Q}$ is also called the scattering vector and its length is expressed by [112]

$$|\mathbf{Q}| = \frac{4\pi}{\lambda} \sin\Theta = \frac{4\pi}{\lambda} \sin\left(\frac{1}{2} \arctan\left(\frac{R}{L}\right)\right), \tag{2.32}$$

where 2Θ is the scattering angle between $\mathbf{k}$ and $\mathbf{k}'$. Q can be calculated by taking into account

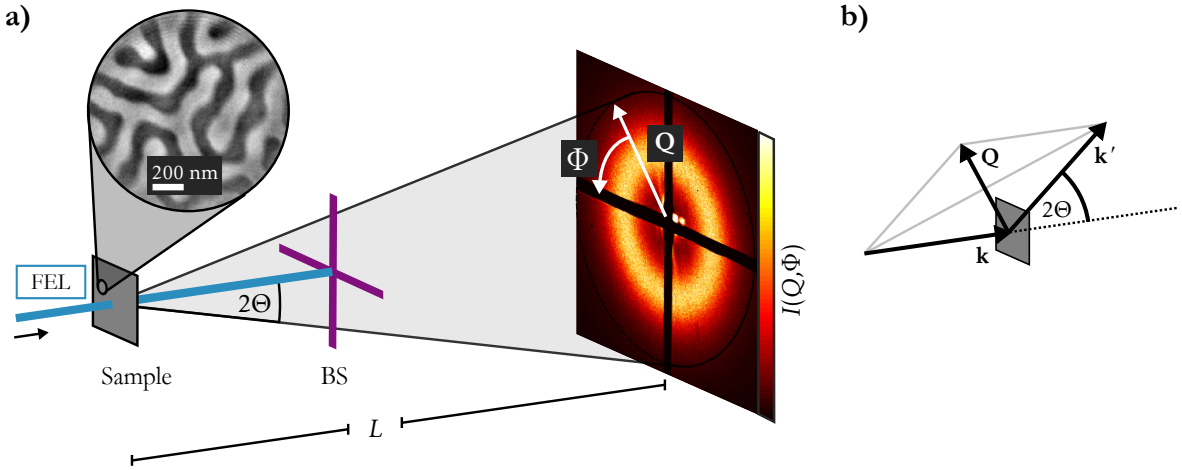

Figure 2.6.: a) Illustration of resonant magnetic small-angle X-ray scattering (mSAXS) in transmission geometry. The magnetic scattering intensity, $I(Q,\Phi)$, is recorded by a CCD camera at a distance L from the sample. The direct FEL beam is blocked by a beam stop (BS). Due to the disordered nature of the maze-domain state with an average domain size, D_{av}, the magnetic scattering intensity, $I(Q,\Phi)$, is distributed in the shape of a ring with radius, Q_{peak}. b) Geometry of resonant (elastic) scattering. The momentum transfer $\mathbf{Q}$ is given by the difference between incident ($\mathbf{k}$) and scattered ($\mathbf{k}'$) wavevectors, $\mathbf{Q} = \mathbf{k}' - \mathbf{k}$.

the experimental geometry, $\tan 2\Theta = R/L$, where R is the radial distance to the transmitted beam and L is the sample-detector distance. Hence, in mSAXS experiments the sample-detector distance, L, has to be chosen appropriately in order to detect the (first-order) magnetic scattering intensity from the multi-domain patterns. For the case of a disordered maze-domain state with a predominating length scale or average domain size, D_{av}, the magnetic scattering intensity, $I(\mathbf{Q}) \equiv I(Q,\Phi)$, has the shape of a ring. The shape and intensity of the magnetic scattering ring, however, changes if the domain configuration is changed, e. g., by external magnetic fields. The dependence of $I(Q,\Phi)$ on the underlying domain configuration is outlined in section 2.4.4.

The scattering intensity, $I(\mathbf{Q})$, obtained by mSAXS on magnetic multi-domain states, is proportional to the modulus squared of the Fourier transform of the total scattering amplitude, $f_j^{\mathrm{tot}}(\mathbf{r}_j)$, from the lattice sites j with position vector $\mathbf{r}_j$ [112–114]

$$I(\mathbf{Q}) \propto \left| \sum_j f_j^{\mathrm{tot}}(\mathbf{r}_j) \exp\left(i\mathbf{Q}\cdot\mathbf{r}_j\right) \right|^2 = \left| \int_V f^{\mathrm{tot}}(\mathbf{r}) \exp\left(i\mathbf{Q}\cdot\mathbf{r}\right) \mathrm{d}\mathbf{r} \right|^2 . \tag{2.33}$$

All lattice sites within a magnetic domain give the same scattering amplitude and thus, the sum in the first expression of eq. (2.33) runs over effective domains rather than single (atomic) scatterers [113]. The integral in the second expression of eq. (2.33) ranges over the illuminated

sample volume, V. Considering dipole transitions only, an expansion of the total scattering amplitude, $f^{\mathrm{tot}}(\mathbf{r})$, up to second order provides the fundamental description of the distinct charge and magnetic scattering amplitudes [104, 115, 116]

$$f^{\mathrm{tot}}(\mathbf{r}) = (\boldsymbol{\varepsilon}' \cdot \boldsymbol{\varepsilon}) f_{\mathrm{c}}(\mathbf{r}) + i(\boldsymbol{\varepsilon}' \times \boldsymbol{\varepsilon}) \cdot \mathbf{m}(\mathbf{r}) f_{\mathrm{m1}} + (\boldsymbol{\varepsilon}' \cdot \mathbf{m}(\mathbf{r}))(\boldsymbol{\varepsilon} \cdot \mathbf{m}(\mathbf{r})) f_{\mathrm{m2}}, \tag{2.34}$$

where $\mathbf{m}(\mathbf{r})$ is the unit vector along the axis of the local magnetization and the terms $f_{\mathrm{c}}(\mathbf{r})$, f_{m1}, f_{m2} describe distinct linear combinations of matrix elements between initial and resonant intermediate states (see eq. (2.31)). The term $f_{\mathrm{c}}(\mathbf{r})$ is composed of both the non-resonant (approximately the atomic number Z) and the resonant charge scattering contribution. The first-order magnetic term, f_{m1}, scaling linearly with the magnetization, describes the contribution to magnetic scattering due to the XMCD effect (section 2.4.2.1) and the second-order magnetic term, f_{m2}, scaling quadratically with the magnetization, accounts for the XMLD effect [116].

At normal incidence of the X-ray pulses and samples with PMA, the XMLD effect is negligibly small ($\boldsymbol{\varepsilon} \cdot \mathbf{m}(\mathbf{r}) \approx 0$) and eq. (2.34) simplifies to

$$f^{\mathrm{tot}}(\mathbf{r}) = (\boldsymbol{\varepsilon}' \cdot \boldsymbol{\varepsilon}) f_{\mathrm{c}}(\mathbf{r}) + i(\boldsymbol{\varepsilon}' \times \boldsymbol{\varepsilon}) \cdot \mathbf{m}(\mathbf{r}) f_{\mathrm{m1}}. \tag{2.35}$$

The remaining contributions to the total scattering amplitude are charge scattering, e. g., from the inhomogeneous granular structure of the thin film, as well as (first-order) magnetic scattering, originating from the spin-dependent charge-density distribution in magnetic materials, i. e., the magnetic domain pattern.

As the scattering intensity, $I(\mathbf{Q})$, is proportional to the squared modulus of the total scattering amplitude, it contains a charge-magnetic cross term aside from pure-charge and pure-magnetic contributions. The resonant magnetic scattering intensity might be affected by charge scattering, if both show inhomogeneities on the same length scale and thus coincide in reciprocal space [116, 117]. The Co/Pt multilayers in this work, fabricated by sputtering techniques, have a granular structure with grain sizes on the order of 10 nm [82, 118], whereas they form magnetic domain networks with an average domain size of $D_{\mathrm{av}} > 100\,\mathrm{nm}$ (see Fig. 2.6 a)). Hence, charge and magnetic-scattering contributions are naturally well separated in reciprocal space for the here used samples.

Finally taking into account the experimental geometry, the expression for the total scattering amplitude further simplifies. The polarization vectors of the incident and scattered light wave, $\boldsymbol{\varepsilon}$ and $\boldsymbol{\varepsilon}'$, are orthogonal to their respective wavevectors, $\mathbf{k}$ and $\mathbf{k}'$. For small scattering angles, the cross product $\boldsymbol{\varepsilon}' \times \boldsymbol{\varepsilon}$ is thus parallel to the light wave's propagation direction and the scalar product $(\boldsymbol{\varepsilon}' \times \boldsymbol{\varepsilon}) \cdot \mathbf{m}(\mathbf{r})$ in eq. (2.35) only gives non-zero contributions for $\mathbf{m}(\mathbf{r}) = m_z(\mathbf{r})$. Hence, the resonant magnetic scattering intensity in the absence of the XMLD effect and charge

scattering is given by

$$I(\mathbf{Q}) \propto |f_{\mathrm{m1}}|^2 \left| \int_A m_z(\mathbf{r}) \exp\left(i\mathbf{Q}\cdot\mathbf{r}\right) \mathrm{d}\mathbf{r} \right|^2 \propto \left|\mathcal{F}\left(m_z(\mathbf{r})\right)\right|^2, \tag{2.36}$$

where A is the illuminated area. It follows from eq. (2.36) that the resonant magnetic scattering intensity, $I(\mathbf{Q})$, is proportional to the modulus squared of the Fourier transform of the sample's magnetization distribution $m_z(\mathbf{r})$.

2.4.4. Lateral Domain Configuration and Magnetic Scattering Intensity

In the following, the dependence of $I(\mathbf{Q})$ on the configuration of the magnetic domains, $m_z(\mathbf{r})$, is discussed. Within this work three different Co/Pt multilayers were investigated by mSAXS, each possessing a different $m_z(\mathbf{r})$. Moreover applying OOP or IP magnetic fields, different multi-domain patterns, e. g., the disordered maze-domain pattern or the well-ordered stripe-domain pattern, with symmetric or asymmetric filling ratios of up and down-magnetized domains can be generated.

To illustrate the influence of a varying $m_z(\mathbf{r})$ on $I(\mathbf{Q})$, several magnetic multi-domain patterns were simulated, assuming a binary magnetization distribution, as shown in Fig. 2.7 a)–c). The simplest case is a perfectly ordered, symmetric magnetic stripe-domain pattern, which can be seen as a one-dimensional magnetic grating [119], shown together with its 2D Fourier transform in Fig. 2.7 a). Its $I(\mathbf{Q})$ shows the same characteristics, i. e., higher-order scattering peaks, as the diffracted intensity of coherent optical light from a non-magnetic multi-slit. The position of the n-th order scattering peak in reciprocal space is given by [112]

$$Q_n = n \cdot \frac{2\pi}{T_{\mathrm{av}}}, \tag{2.37}$$

where T_{av} is the (average) domain periodicity. For an equal area filling of up and down-magnetized domains, the position of the first-order scattering peak relates to the average domain size, $T_{\mathrm{av}} = 2D_{\mathrm{av}} \Rightarrow Q_1 \equiv Q_{\mathrm{peak}} = \pi/D_{\mathrm{av}}$.

A measure for the degree of order in the multi-domain pattern is given by the width, w, of the scattering peaks which relates to the lateral correlation length, ξ, as [119, 120]

$$w = \frac{2\pi}{\xi}. \tag{2.38}$$

The perfectly ordered stripe-domain pattern in Fig. 2.7 a) shows scattering peaks that are directed perpendicular to the stripe-domain orientation (quasi-1D). It produces narrow scattering peaks with a finite width, due to the finite size of the simulated area, which

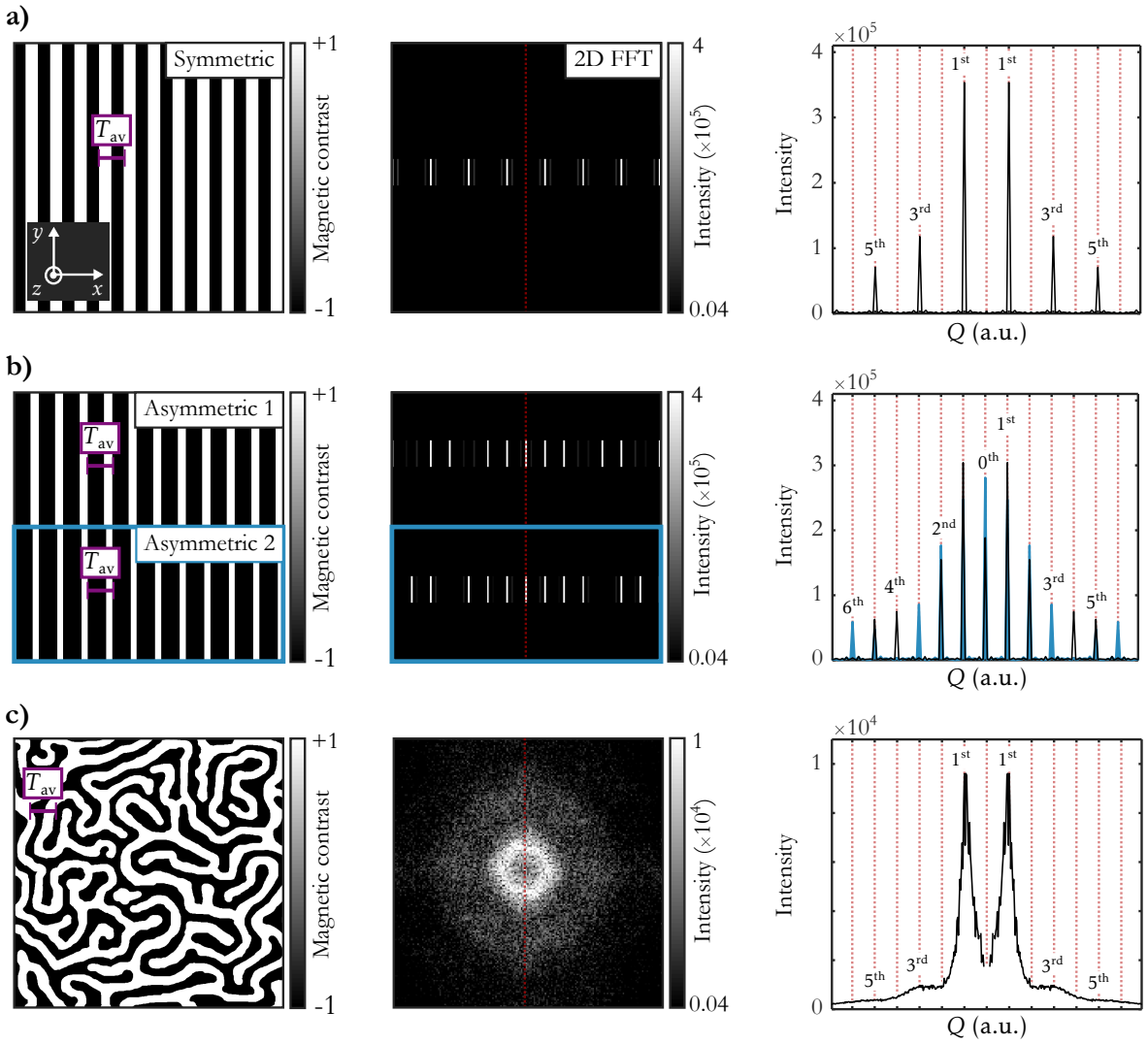

Figure 2.7.: Simulation of the scattering intensity, $I(\mathbf{Q})$, from binary magnetic multi-domain patterns, i. e., $m_z(\mathbf{r}) = -1$ (down-magnetized) and $m_z(\mathbf{r}) = +1$ (up-magnetized), obtained by 2D Fourier transformation. All magnetic domain configurations possess the same average domain periodicity, T_{av}, but different area fillings of up and down-magnetized domains: a) symmetric stripe-domain pattern (filling ratio 1:1), b) two asymmetric stripe-domain patterns with filling ratios of 2:1 and 3:1 and c) symmetric maze-domain pattern (filling ratio about 1:1). The 1D intensity distributions, $I(Q)$, are obtained by drawing line cuts along the direction of the scattering maxima in a) and in b) and by azimuthal averaging around the image center in c).

resembles its (almost) infinite lateral correlation length. In contrast, the maze-domain pattern in Fig. 2.7 c) produces a ring-shaped intensity distribution with reduced maximum intensity (intensity is distributed in 2D) and broadened width (increased disorder and thus reduced lateral correlation length). In contrast to a non-magnetic multi-slit, the unit cell of a magnetic multi-domain pattern is composed of an up–down domain pair with $m_{\uparrow}(\mathbf{r}_j) = +1$ for an up-magnetized domain and $m_{\downarrow}(\mathbf{r}_j) = -1$ for a down-magnetized domain that is shifted by half of the domain period T_{av}. For a better understanding of the scattered intensity in the n-th order scattering peak Q_n from magnetic multi-domain states, eq. (2.36) can be split into contributions from up and down-magnetized domains

$$I(Q_n) \propto |f_{\mathrm{m1}}|^2 \left| \sum_{j=1}^{N/2} m_{\uparrow}(\mathbf{r}_j) \exp\left(iQ_n T_{\mathrm{av}}\right) + \sum_{j'=1}^{N/2} m_{\downarrow}(\mathbf{r}_{j'}) \exp\left(iQ_n \frac{T_{\mathrm{av}}}{2}\right) \right|^2, \tag{2.39}$$

where N is the total number of domains. The magnetic scattering intensity in the 0^{th}, 1^{st} and 2^{nd}-order scattering peak from a stripe-domain pattern thereafter scales as

$$\begin{aligned}
\mathbf{n = 0}: \quad I(Q_0) &\propto |f_{\mathrm{m1}}|^2 \left| \sum_{j=1}^{N/2} m_{\uparrow}(\mathbf{r}_j) + \sum_{j'=1}^{N/2} m_{\downarrow}(\mathbf{r}_{j'}) \right|^2 = |f_{\mathrm{m1}}|^2 \left| \sum_{j=1}^{N/2} 1 + \sum_{j'=1}^{N/2} -1 \right|^2 = 0, \\
\mathbf{n = 1}: \quad I(Q_1) &\propto |f_{\mathrm{m1}}|^2 \left| \sum_{j=1}^{N/2} m_{\uparrow}(\mathbf{r}_j) \exp(i2\pi) + \sum_{j'=1}^{N/2} m_{\downarrow}(\mathbf{r}_{j'}) \exp(i\pi) \right|^2 \\
&= |f_{\mathrm{m1}}|^2 \left| \sum_{j=1}^{N/2} 1 + \sum_{j'=1}^{N/2} 1 \right|^2 = |f_{\mathrm{m1}}|^2 N^2, \\
\mathbf{n = 2}: \quad I(Q_2) &\propto |f_{\mathrm{m1}}|^2 \left| \sum_{j=1}^{N/2} m_{\uparrow}(\mathbf{r}_j) \exp(i4\pi) + \sum_{j'=1}^{N/2} m_{\downarrow}(\mathbf{r}_{j'}) \exp(i2\pi) \right|^2 \\
&= |f_{\mathrm{m1}}|^2 \left| \sum_{j=1}^{N/2} 1 + \sum_{j'=1}^{N/2} -1 \right|^2 = 0.
\end{aligned} \tag{2.40}$$

The intensity in the odd-order scattering peaks is seen as the sum of the scattering contributions from up and down-magnetized domains, which scales with $I(Q) \propto |f_{\mathrm{m1}}|^2 N^2$. In contrast, the intensity in the even-order scattering peaks is seen as the difference of the scattering contributions from up and down-magnetized domains and thus is strongly suppressed for the symmetric case, i. e., for a filling ratio of up to down-magnetized domains of 1:1 (Fig. 2.7 a) and Fig. 2.7 c)). The suppression of the intensity in the even-order scattering peaks is uplifted when

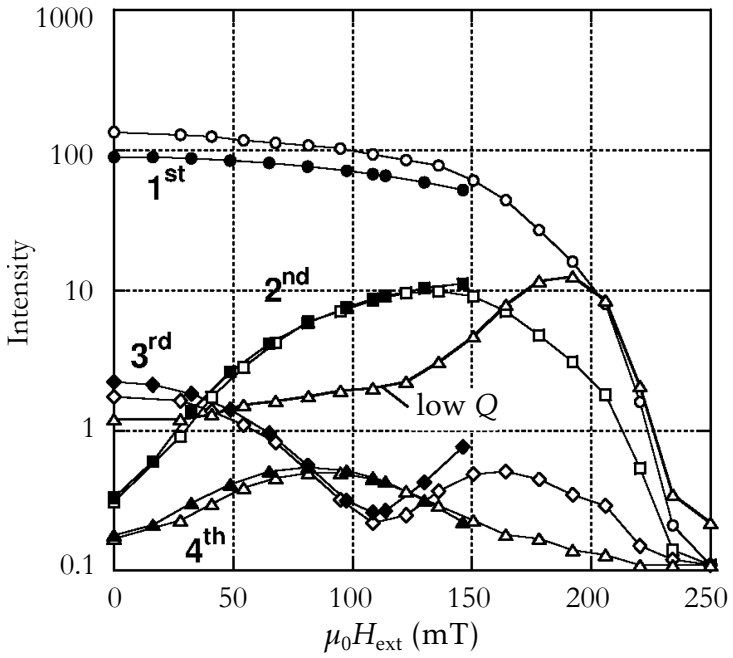

Figure 2.8.: Intensity evolution in the n-th order scattering peak up to $n = 4$ versus increasing OOP magnetic fields, i. e., for an increasing asymmetry in the area filling of up and down-magnetized domains (taken from Ref. [119] with minor modifications). Open symbols show experimental data obtained by mSAXS from the stripe-domain pattern of a $[CoO(1.0)]\{[Co(0.4)/Pt(0.7)]_4Co(0.6)\ CoO(1.0)\}_{10}$ multilayer. Filled symbols show calculated values.

an asymmetry between up and down-magnetized domains is induced, e. g., by OOP magnetic fields. The scattering situation from stripe-domain patterns with asymmetric filling ratios of 2:1 (black) and 3:1 (blue) is shown in Fig. 2.7 b). In these cases destructive interference occurs in the 3rd-order and 4th-order scattering peaks and multiples of that, respectively.

The result from simulating the magnetic scattering intensity from a disordered maze-domain pattern is presented in Fig. 2.7 c). For the simulation, the same average domain periodicity, T_{av}, as for the stripe-domain case, as well as an equal area filling of up and down-magnetized domains was used. Due to the disordered nature of the maze-domain pattern, its corresponding $I(\mathbf{Q})$ in reciprocal space is an isotropic ring-shaped intensity distribution with its center at $Q = 0$. The 2D intensity distribution is reduced to 1D by azimuthally averaging $I(\mathbf{Q})$ around the image center. Analogue to the symmetric stripe-domain pattern even-order scattering peaks are strongly suppressed (filling ratio of about 1:1). A broadening of the scattering peaks compared to the ones from the stripe-domain pattern, is due to the increased disorder, i. e., the maze-domain pattern consists of a broad distribution of magnetic length scales with an average domain size, D_{av}, and not a single well-defined domain size. A more detailed approach of modeling the disordered maze-domain pattern by a 1D chain of alternating up- and down-magnetized domains is given in Ref. [121]. Instead of using an average domain size D_{av} for the whole domain pattern, size variations are taken into account by modeling the domain sizes via gamma distributed random numbers and assigning them to local magnetic elements with opposite magnetization directions. An improved resemblance with experimental data could furthermore be found by including the domain walls in the model.

The fall-off of the intensity in the higher-order scattering peaks for all the shown multi-domain states in Fig. 2.7 is due to the fact that, aside from their absolute value of ±1, $m_{\uparrow}(\mathbf{r}_j)$ and $m_{\downarrow}(\mathbf{r}_j)$ have a size and a shape, described by their form factor, $F(Q)$. In the idealized case of a rectangular-shaped magnetic domain, i. e., neglecting the domain walls, the form factor can be modeled by [113]

$$F(Q) = N_s \frac{\sin(QD_{\mathrm{av}}/2)}{QD_{\mathrm{av}}/2}, \tag{2.41}$$

where N_s is the number of scatterers inside the domain. As the form factor $F(Q = 0) = 1$, the intensity in the 0^{th}-order scattering peak, given as the difference of $m_{\uparrow} - m_{\downarrow}$, shows the macroscopic magnetization in the sample. Note that the magnetic scattering intensity at $Q = 0$ is not accessible in mSAXS experiments in transmission geometry, as it coincides with the position of the direct beam.

The evolution of the intensity in the n-th order scattering peak versus increasing OOP magnetic field was studied by O. Hellwig *et al.* in Ref. [119], using magnetic X-ray scattering on the stripe-domain pattern of a $[\mathrm{CoO}(1.0)]\{[\mathrm{Co}(0.4)/\mathrm{Pt}(0.7)]_4\ \mathrm{Co}(0.6)\mathrm{CoO}(1.0)\}_{10}$ multilayer (Fig. 2.8). Their results were complemented by X-ray resonant microscopy, allowing to link the reciprocal-space information to real space. In good agreement with the simulations, their results show only a slight decrease of the intensity in the 1^{st}-order scattering peak with increasing asymmetric area filling of up and down-magnetized domains, i. e., with increasing external magnetic field up to a field strength close to the saturation field. The higher-order scattering peaks were found to have much stronger field dependencies. On the one hand, the 2^{nd} and 4^{th}-order scattering peaks, that are suppressed in the symmetric case ($\mu_0 H_{\mathrm{ext}} = 0\,\mathrm{mT}$), monotonically increase with increasing magnetic field. On the other hand, the intensity in the 3^{rd}-order scattering peak monotonically decreases, reaching close to zero for a filling ratio of 2:1 at $\mu_0 H_{\mathrm{ext}} \approx 110\,\mathrm{mT}$. A strong suppression of the 3^{rd}-order scattering peak for a filling ratio of 2:1 is confirmed by the here conducted simulations (Asymmetric 1 in Fig. 2.7 b)). When further increasing the external field, the stripe-domain pattern was found to slowly disappear eventually reaching the single-domain state, which resulted in a superposition of the well-defined scattering peaks as well as an intensity increase towards low Q values.

In general, the dependence of $I(\mathbf{Q})$ on increasing OOP magnetic fields is expected to be similar to the one of the stripe-domain pattern shown in Fig. 2.8. Within this thesis, disordered multi-domain states with both symmetric and asymmetric area filling of up and down-magnetized domains set by OOP magnetic fields were investigated (chapter 6). Prior to investigating the time evolution of $I(\mathbf{Q})$ upon laser excitation, the magnetic field dependence of the disordered maze-domain pattern was studied in both reciprocal and real space, combining mSAXS with imaging via Fourier-transform holography (section 6.1).

2.4.5. Thickness Dependence of Resonant Magnetic Scattering

The shape and intensity of the first-order magnetic scattering peak, $I(\mathbf{Q})$, depends on the configuration of the magnetic domains as outlined in the previous section. The investigated Co/Pt multilayers not only differ in their domain configurations but also in their total film thicknesses. An expression for the thickness dependence of the total magnetic scattering intensity, I_{tot}, with respect to the incident intensity, I_{in}, was derived in Ref. [62]. From eq. (2.28) the magnetic scattering intensity from a magnetic thin film of thickness d and homogeneous magnetization throughout the sample can be expressed as

$$\begin{aligned} I_{\mathrm{tot}} &= \varepsilon_0 c \left| \frac{i}{2} \mathbf{E}_0^p \left[1 - \exp\left(-2\Delta\beta k_z d\right) \exp\left(-2i\Delta\delta k_z d\right)\right] \exp\left(i n_- k_z d\right) \right|^2 \\ &= \frac{I_{\mathrm{in}}}{4} \Big| \underbrace{\Big[\exp\left(\Delta\beta k_z d\right) \exp\left(i\Delta\delta k_z d\right) - \exp\left(-\Delta\beta k_z d\right) \exp\left(-i\Delta\delta k_z d\right) \Big]}_{\text{magnetic scattering}} \underbrace{\exp\left(i n_0 k_z d\right)}_{\text{attenuation}} \Big|^2 , \end{aligned} \tag{2.42}$$

where the non-magnetic part of the complex refractive index in the X-ray regime is defined as $n_0 = 1 - \delta + i\beta$ [1]. Equation (2.42) can be simplified, by Taylor expanding the exponents of the *magnetic scattering contribution* in powers of $\Delta\beta$ and $\Delta\delta$ up to first order, which yields an estimate for the resonant magnetic scattering (RMS) efficiency ρ_{RMS} [62]

$$\begin{aligned} \rho_{\mathrm{RMS}} = \frac{I_{\mathrm{tot}}}{I_{\mathrm{in}}} &= \frac{1}{4} \left| \left(2\Delta\beta k_z d + 2i\Delta\delta k_z d\right) \right|^2 \exp\left(-2\beta k_z d\right) \\ &= \left(\frac{2\pi d}{\lambda} \right)^2 \left(\Delta\beta^2 + \Delta\delta^2 \right) \exp\left(-4\pi\beta d/\lambda\right). \end{aligned} \tag{2.43}$$

Here, $k_z = 2\pi/\lambda$ has been used. The $[\mathrm{Co}(d_{\mathrm{Co}})/\mathrm{Pt}(d_{\mathrm{Pt}})]_x$-multilayer samples that were used in this work consist of x Co and $(x-1)$ Pt layers of thickness d_{Co} and d_{Pt}, respectively. The magnetic scattering intensity is furthermore attenuated in the Pt-cap (final Pt layer) and Pt-seed layers with thickness $d_{\mathrm{cap}} = 2.0\,\mathrm{nm}$ and $d_{\mathrm{seed}} = 4.0\,\mathrm{nm}$, respectively, as well as the Si_3N_4 membrane with a thickness of $d_{\mathrm{SiN}} = 50\,\mathrm{nm}$. Consequently, the layer-dependent $\rho_{\mathrm{RMS}}(x)$ in the $[\mathrm{Co}(d_{\mathrm{Co}})/\mathrm{Pt}(d_{\mathrm{Pt}})]_x$-multilayer samples is given by

$$\begin{aligned} \rho_{\mathrm{RMS}}(x) = \left(\frac{2\pi x d_{\mathrm{Co}}}{\lambda} \right)^2 \left(\Delta\beta^2 + \Delta\delta^2 \right) &\cdot \exp\left(-4\pi\beta_{\mathrm{Co}} x d_{\mathrm{Co}}/\lambda\right) \cdot \exp\left(-4\pi\beta_{\mathrm{Pt}}(x-1) d_{\mathrm{Pt}}/\lambda\right) \\ &\cdot \exp\left(-4\pi\beta_{\mathrm{Pt}} d_{\mathrm{cap}}/\lambda\right) \cdot \exp\left(-4\pi\beta_{\mathrm{Pt}} d_{\mathrm{seed}}/\lambda\right) \cdot \exp\left(-4\pi\beta_{\mathrm{SiN}} d_{\mathrm{SiN}}/\lambda\right). \end{aligned} \tag{2.44}$$

The calculated layer dependent resonant magnetic scattering efficiency, $\rho_{\mathrm{RMS}}(x)$, at the Co $M_{2,3}$ edge ($\lambda = 20.8\,\mathrm{nm}$) is shown in Fig. 2.9 for the three Co/Pt-multilayer compositions, i. e., $[\mathrm{Co}(1.0)/\mathrm{Pt}(1.2)]_x$, $[\mathrm{Co}(0.8)/\mathrm{Pt}(1.4)]_x$ and $[\mathrm{Co}(0.6)/\mathrm{Pt}(0.8)]_x$. For the calculations, tabulated

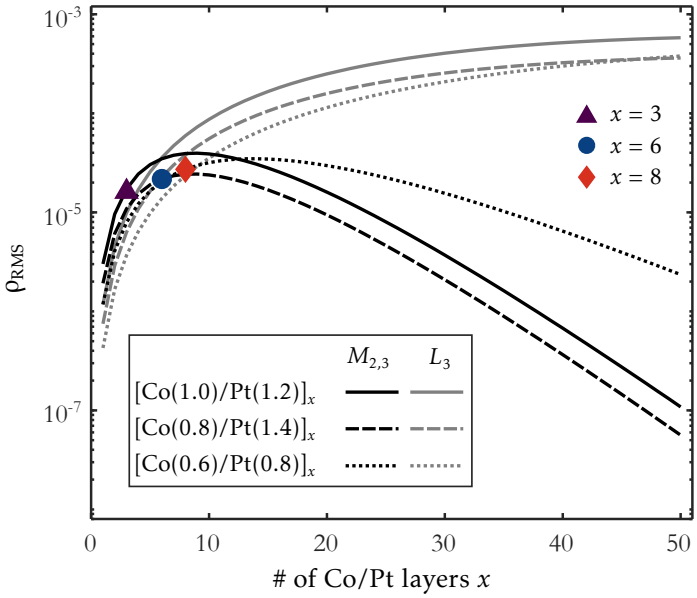

Figure 2.9.: Layer dependent resonant magnetic scattering efficiency, $\rho_{RMS}(x)$, of the three $[Co(d_{Co})/Pt(d_{Pt})]_x$-multilayer compositions at the Co $M_{2,3}$ edge (λ = 20.8 nm), calculated according to eq. (2.44). Filled data points show the Co/Pt-multilayer compositions used in this work. The $\rho_{RMS}(x)$ behavior for the three compositions at the Co L_3 edge (λ = 1.6 nm) is included for comparison.

values for absorption, β,[11] and measured values of $\Delta\beta \approx -1.1 \cdot 10^{-2}$ and $\Delta\delta \approx 1.1 \cdot 10^{-2}$ from Fig. 2.4 are used. Despite their different individual layer compositions, comparable resonant magnetic scattering efficiencies within 40%, i. e., $\rho_{RMS} \approx (1.7\text{–}2.7) \cdot 10^{-5}$, can be expected in the three samples. The increase in scattering intensity with Co-layer thickness is smaller than might be expected, as simultaneously also absorption increases in both Co and Pt. Note that the calculated values of ρ_{RMS} have to be regarded as maximum estimates, as $\Delta\beta$ and $\Delta\delta$ might be reduced in reality through, e. g., the layering of Co and Pt in Co/Pt multilayers, or the non-uniform magnetization distribution in multi-domain states (domain walls).

In the here conducted TR-mSAXS experiments the small ρ_{RMS} of the thin Co/Pt multilayers is compensated by using highly brilliant FEL pulses with about (10^{10}–10^{12}) photons/pulse, which, typically, allows to acquire scattering images with sufficient photon statistics by accumulating the magnetic scattering intensity from approximately 100 FEL-pulse exposures. To check for the comparability of the results from the different samples with different shape and intensity of $I(\mathbf{Q})$, ρ_{RMS} is determined and compared to the estimated values from eq. (2.44) (section 5.3.2). Furthermore the ρ_{RMS} of the very same sample is measured at the FEL facilities FLASH and FERMI. Differences in ρ_{RMS} at the two facilities are briefly addressed in section 6.3.1.

2.5. Laser-Induced Magnetization Dynamics

A particularly interesting aspect of today's research in magnetism is the *dynamics* of the magnetic states upon excitation by ultrashort laser pulses. For excitation or *pumping* of the magnetic states, most commonly, laser light with a wavelength in the near-infrared (nIR)

[11] CXRO data base: http://henke.lbl.gov

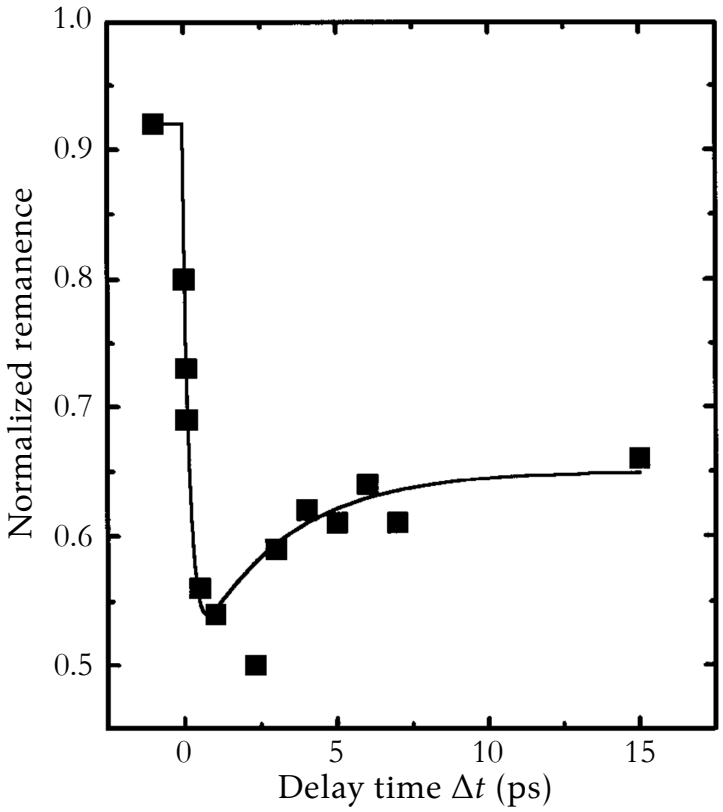

Figure 2.10.: First time observation of ultrafast demagnetization by E. Beaurepaire *et al.* in 1996 (taken from Ref. [5] with minor modifications). Upon excitation of a 20 nm Ni thin film by 60 fs-short laser pulses ($\lambda = 620$ nm) with a fluence of $F = 7\,\mathrm{mJ/cm^2}$, the remanent magnetization was found to be lost within an, at that time, unprecedented short time scale of $\tau_M < 1$ ps. The line is a guide to the eye.

regime is used ($\lambda = 800$ nm), which mainly gets absorbed (polarization independent) in the magnetic material generating an excited electron population within approximately 1.6 eV around the Fermi energy.

Among the most exciting discoveries in magnetization dynamics in the past three decades is *ultrafast demagnetization* (section 2.5.1), which describes the sub-picosecond quenching of magnetization upon excitation by a sub 100 fs-short laser pulse (Fig. 2.10). Originally discovered in Ni by E. Beaurepaire *et al.* in 1996 [5], ultrafast demagnetization has been extensively studied in a variety of magnetic materials, including the remaining ferromagnetic 3*d* elements Fe [122, 123] and Co [124–129], alloys like NiFe [130], $CoPt_3$ [131] and CoPd [132], chemically ordered FePt [133], as well as multilayered structures like CoNi/Pt [134], Co/Pd [135] and Co/Pt [15, 135–137].[12] Depending on, e.,g., the sample thickness or the sample structure in composite materials such as Co/Pt multilayers, different dominating driving mechanisms for ultrafast demagnetization are discussed, which are introduced in section 2.5.1. In this work, ultrafast demagnetization in three different Co/Pt multilayers is modeled by a phenomenological fit function, that is based on the well-established three-temperature model (3TM). The 3TM as

[12] Note that also other magnetic materials, like the technologically relevant ferrimagnetic GdFeCo or TbFe alloys, undergo ultrafast demagnetization. Here, ultrafast demagnetization is outlined for the 3*d* transition metal ferromagnets, as only such samples are studied.

well as the fluence and thickness dependence of ultrafast demagnetization are outlined in section 2.5.1 as well.

Apart from polarization independent absorption, nIR light undergoes polarization dependent absorption in magnetic materials, known as the MCD effect (section 2.4.1). As the plane of polarization of an incident EM field is moreover rotated upon transmission through a magnetic material (MOFE), also the inverse effect has to be considered, i. e., the rotation of the plane of polarization induces an effective opto-magnetic field, H_{OM}, via the so-called *inverse Faraday effect* (IFE) [138–140]. MCD and IFE are put forward to describe another fascinating opto-magnetic phenomenon, namely deterministic *all-optical switching* (AOS) of a magnetic state from an up to a down-direction (or vice versa) depending on the helicity of the circularly polarized laser pulses used for excitation (section 2.5.2).

2.5.1. Ultrafast Demagnetization

It was understood up to the mid 1990s that laser induced demagnetization proceeds on a 100 ps to nanosecond time scale via spin–lattice relaxation. A. Vaterlaus *et al.* determined the spin-lattice relaxation time in Fe and Gd via time-resolved spin-polarized photoemission, finding $\tau_{s\ell} = 30\,\mathrm{ps}$–$20\,\mathrm{ns}$ in Fe and $\tau_{s\ell} = (100 \pm 80)\,\mathrm{ps}$ in Gd [141]. The results could be well described by a microscopic theory that connects $\tau_{s\ell}$ to the static magnetocrystalline anisotropy in Gd, yielding a spin–lattice relaxation time of 48 ps [142]. At the same time, laser systems that produce ultrashort and intense laser pulses with pulse durations below 100 fs and pulse energies of several (10–100) mJ became available [143, 144], which allowed, for the first time, to study laser induced magnetization dynamics on a sub-picosecond time scale.[13] Utilizing such 60 fs-short laser pulses in a time-resolved MOKE experiment, E. Beaurepaire *et al.* discovered that laser induced demagnetization in a Ni thin film proceeds well within the first picosecond after excitation, which is at least two to three orders of magnitudes faster than previously deemed possible (see Fig. 2.10). This sub-picosecond loss of magnetization has become known as *ultrafast demagnetization* [5].

2.5.1.1. Phenomenological Description of Ultrafast Demagnetization: The Three Temperature Model (3TM)

Within the pioneering work of E. Beaurepaire *et al.* a phenomenological model is proposed which describes the loss of magnetization within the first picosecond in terms of exchanging energy between three (internally) thermalized reservoirs, the electron, spin and lattice (phonon system) at temperature T_{e}, T_{s} and T_{ℓ}, respectively (Fig. 2.11 a)).

[13] In 2018, part of the Nobel Prize in physics was awarded to Donna Strickland and Gérard Mourou for inventing the method of chirped pulse amplification (CPA) to generate high-intensity, ultra-short (femtosecond) optical laser pulses [4].

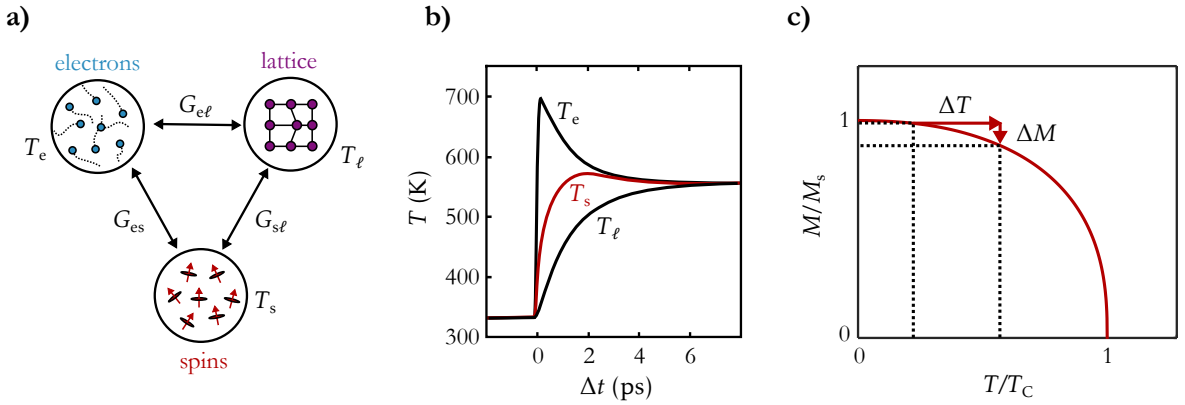

Figure 2.11.: a) Schematic representation of the three temperature model (3TM), providing a phenomenological description of ultrafast demagnetization via three interacting temperature reservoirs: the nIR-laser power is initially absorbed by the electrons and subsequently redistributed to the lattice and the spins according to eqs. (2.45)–(2.47). b) Evolution of electron, T_e, lattice, T_ℓ and spin temperature, T_s, according to the 3TM (taken from Ref. [5]). c) The final net increase of spin temperature leads to a reduction of the total magnetization according to the well known $M(T)$ curve (taken from Ref. [147]).

Note that within the duration of a typically sub 100 fs-short laser pulse, first, a hot electron population that is out of thermal equilibrium is generated that subsequently thermalizes to a Fermi distribution via electron–electron interactions [145]. In 3*d* transition metal ferromagnets, thermalization times of only $\tau_T \approx 10$ fs are due to the large density of states at the Fermi level and the related short hot-electron lifetimes. Electron–electron thermalization is not included in the original 3TM, but the electron system is considered to be in thermal equilibrium from the start, hence assuming $\tau_T = 0$ [145].[14]

Thus, from the start on ($t = 0$), temperatures can be assigned to the electron (T_e) as well as the spin system (T_s), both showing a sharp rise upon laser excitation, followed by an exponential decay towards a plateau within a decay time of approximately 1 ps (Fig. 2.11 b)). A slight temporal delay between the peak values of T_e and T_s can be qualitatively understood, considering that the spin is conserved ($\Delta s = 0$, $\Delta m_s = 0$) during optical excitations (dipole approximation). Hence, the non-thermal electron distribution, at first, has the same spin polarization as the ground state. Subsequent local spin-flip scattering processes and/or non-local spin-dependent electron transport lead to a homogenization of spin-up and spin-down occupancy, described by an increase of T_s. An increasing spin temperature can be directly related to a decreasing magnetization, via the well known relation between M and T [145], illustrated in Fig. 2.11 c). The maximum spin temperature and hence the maximum degree of demagnetization is established after the first few 100 fs, i. e., when electron and spin system reach thermal equilibrium. The subsequent cooling down of the spin (and electron) system via

[14] Note that the effect of an initially non-thermal electron distribution on ultrafast demagnetization is included in the so-called extended 3TM (E3TM) (see, e. g., Ref. [146]).

energy transfer to the lattice leads to the recovery of magnetization on a pico to nanosecond time scale. The temporal evolutions of the respective temperatures are described via three coupled differential equations [5]

$$C_\mathrm{e}(T_\mathrm{e})\frac{\mathrm{d}T_\mathrm{e}}{\mathrm{d}t} = -G_{\mathrm{e}\ell}(T_\mathrm{e} - T_\ell) - G_\mathrm{es}(T_\mathrm{e} - T_\mathrm{s}) + P(t), \tag{2.45}$$

$$C_\mathrm{s}(T_\mathrm{s})\frac{\mathrm{d}T_\mathrm{s}}{\mathrm{d}t} = -G_\mathrm{es}(T_\mathrm{s} - T_\mathrm{e}) - G_{\mathrm{s}\ell}(T_\mathrm{s} - T_\ell), \tag{2.46}$$

$$C_\ell(T_\ell)\frac{\mathrm{d}T_\ell}{\mathrm{d}t} = -G_{\mathrm{e}\ell}(T_\ell - T_\mathrm{e}) - G_{\mathrm{s}\ell}(T_\ell - T_\mathrm{s}), \tag{2.47}$$

where $P(t)$ is the initially absorbed laser power in the electron system, C_i are the specific heats and G_{ij} are the coupling constants between the individual sub-systems, denoted with subscripts e, s and ℓ for the electron, spin and lattice subsystem, respectively. Note that the 3TM only accounts for energy conservation whereas angular momentum conservation is not considered. Different local and non-local processes that may account for angular momentum conservation during ultrafast demagnetization are introduced later in this section.

2.5.1.2. Analytical solution of the 3TM

In order to determine a characteristic time scale for the sub-picosecond demagnetization (τ_M) as well as the picosecond remagnetization (τ_E) from experimentally observed magnetization transients (see Fig. 2.10), an analytical solution of eqs. (2.45)–(2.47) was derived by B. Koopmans *et al.* for the case of low laser fluences, as briefly outlined in the following [145].

At low temperatures, C_e and C_ℓ are assumed to be temperature independent and the spin specific heat, at first, is neglected ($C_\mathrm{s} = 0$). This reduces the problem to an effective 2TM (see Refs. [148–150]), which yields exponentially converging electron and lattice temperatures with a time constant [145]

$$\tau_\mathrm{E} = \frac{C_\mathrm{e}C_\ell}{C_\mathrm{e} + C_\ell}\frac{1}{G_{\mathrm{e}\ell}} \approx \frac{C_\mathrm{e}}{G_{\mathrm{e}\ell}}. \tag{2.48}$$

The subscript E denotes “Energy” equilibration. Energy equilibration with the lattice governs the remagnetization dynamics which proceeds on a time scale of $\tau_\mathrm{E} \lesssim 0.5\,\mathrm{ps}$ at low temperatures in the 3*d* ferromagnets [151]. The electron-temperature transient is introduced by the empirical relation [151, 152]

$$\Delta T_\mathrm{e}(t) = \Delta T_1\left[1 - \exp\left(-\frac{t}{\tau_\mathrm{T}}\right)\right]\exp\left(-\frac{t}{\tau_\mathrm{E}}\right) + \Delta T_2\left[1 - \exp\left(-\frac{t}{\tau_\mathrm{E}}\right)\right], \tag{2.49}$$

where $\Delta T_1 \geq \Delta T_2$ is the initial temperature rise in the electron system, thermalizing within the thermalization time, τ_T, and ΔT_2 is the final temperature to which T_e and T_ℓ converge. Hence, ΔT_2 describes a temperature rise after thermal equilibrium between the electron, spin and

lattice systems is established. Neglecting the initial thermalization within the electron system, allows to identify electron and phonon-related temperature transients [145]

$$\begin{aligned}\Delta T_\mathrm{e}(t) &= T_1 \exp\left(-\frac{t}{\tau_\mathrm{E}}\right) + T_2\left[1-\exp\left(-\frac{t}{\tau_\mathrm{E}}\right)\right]\\ \Delta T_\ell(t) &= T_2\left[1-\exp\left(-\frac{t}{\tau_\mathrm{E}}\right)\right].\end{aligned} \tag{2.50}$$

The transient spin temperature, ΔT_s, is finally represented through the exchange of energy between the electron and phonon system by the rate equation [145]

$$\frac{\mathrm{d}T_\mathrm{s}}{\mathrm{d}t} = \frac{(T_\mathrm{e}-T_\mathrm{s})}{\tau_\mathrm{M,e}} + \frac{(T_\ell - T_\mathrm{s})}{\tau_\mathrm{M},\ell}, \tag{2.51}$$

which, under consideration of eqs. (2.50) has the general solution [145]

$$\Delta T_\mathrm{s}(t) = \Delta T_2 + \frac{(\tau_\mathrm{E}\Delta T_1' - \tau_\mathrm{M}\Delta T_2)}{\tau_\mathrm{E}-\tau_\mathrm{M}}\exp\left(-\frac{t}{\tau_\mathrm{M}}\right) + \frac{\tau_\mathrm{E}(\Delta T_2 - \Delta T_1')}{\tau_\mathrm{E}-\tau_\mathrm{M}}\exp\left(-\frac{t}{\tau_\mathrm{E}}\right), \tag{2.52}$$

with $\tau_\mathrm{M}^{-1} = \tau_\mathrm{M,e}^{-1} + \tau_\mathrm{M},\ell^{-1}$ being the demagnetization time composed of spin-electron and spin-phonon contributions and $\Delta T_1' = \Delta T_1 \frac{\tau_\mathrm{M}}{\tau_\mathrm{M,e}}$. Equation (2.52) allows to determine a demagnetization time, τ_M, from experimentally obtained magnetization transients without prior knowledge about which one of the two channels, $\tau_\mathrm{M,e}$ or $\tau_\mathrm{M,p}$, dominates. The temperature rises, $\Delta T_1'$ and ΔT_2, are consequently interpreted as *effective* spin-temperature rises after reaching thermal equilibrium in the electron and spin ($\approx 100\,\mathrm{fs}$) and the electron, spin and phonon systems ($\approx 1\,\mathrm{ps}$), respectively.

For low-fluence excitations, i. e., at low temperatures, the spin temperature rise, ΔT_s, in a good approximation, scales linearly with the degree of demagnetization, ΔM, as illustrated in Fig. 2.11 c). Hence, eq. (2.52) can be used for fitting experimentally obtained magnetization transients, as shown in section 5.4.2.1. It is emphasized that the assumption of $M \propto T_\mathrm{s}$ is justified only for sufficiently small temperature rises (low nIR-laser fluences). Within this thesis, temperature rises close to T_C were induced in the Co/Pt multilayers by nIR-laser pulses with fluences in the range of $F_\mathrm{nIR} = (9.6\text{–}18.9)\,\mathrm{mJ/cm^2}$, i. e., far away from a low-fluence excitation. Any calculated absolute temperature rises therefore have to be regarded with care. However, the analytical solution of the 3TM, as well as comparable phenomenological approaches, have been shown to reliably fit the characteristic time scales, τ_M and τ_E, in magnetization transients with degrees of demagnetization ranging from a few per cent ($F_\mathrm{nIR} \approx 10\,\mathrm{\mu J/cm^2}$) [133], a few 10% ($F_\mathrm{nIR} \approx (1\text{–}10)\,\mathrm{mJ/cm^2}$) [37, 135, 137], up to $\approx 70\%$ ($F_\mathrm{nIR} \approx (10\text{–}20)\,\mathrm{mJ/cm^2}$) [32]. For further details on the analytical solution of the 3TM, it is referred to Refs. [145, 147, 151].

2.5.1.3. Microscopic Mechanisms in Ultrafast Demagnetization

On a sub-picosecond timescale, the three interacting temperature reservoirs can be considered to be well-isolated from the environment. In such a closed system, not only the total energy, but also the total angular momentum, $\mathbf{J}$, is conserved, which is not treated within the conventional 3TM. The different microscopic mechanisms, that take total angular momentum conservation during ultrafast demagnetization into account, are introduced in the following.

Direct transfer of Angular Momentum Originally, it was proposed by G. P. Zhang *et al.* that ultrafast demagnetization can be coherently induced within the duration of the laser field, exciting the spin-polarized ground state to a spin-unpolarized excited state in the presence of SOC [16], which was supported later on by experimental findings [153]. As within early interpretations of laser induced demagnetization interactions with the lattice were understood to proceed on a time scale of about 100 ps [141, 142], it has been argued that an ultrafast demagnetization within a few 100 fs has to be mediated within the electron system. Only regarding the electron system with a magnetic moment $\boldsymbol{\mu} = \mu_\mathrm{B}(\mathbf{L}_\mathrm{e} + g\mathbf{S}_\mathrm{e})$, where $g \approx 2$ is the gyromagnetic ratio, a reduction of $\boldsymbol{\mu}$ would have to be mediated between $\mathbf{S}_\mathrm{e}$ and $\mathbf{L}_\mathrm{e}$ via SOC [145]. In the ground state, the magnetization in 3*d* ferromagnets is dominated by spin angular momentum due to a quenching of the orbital momentum by the surrounding crystal field ($\mathbf{L}_\mathrm{e} \approx 0$) yielding $\boldsymbol{\mu} \approx g\mathbf{S}_\mathrm{e}\mu_\mathrm{B}$ [1]. Thus, a complete transfer of spin-angular to orbital momentum could, theoretically, only result in a maximum reduction of μ by a factor of 2. This is in contradiction to the experimentally observed full demagnetization at high laser fluences, as observed, e. g., in Refs. [131, 154], and also in this work (section 5.4.1). Employing time-resolved XMCD measurements on Ni thin films, C. Stamm *et al.* could narrow down the contribution of a coherent coupling between the EM field and the spin system to ultrafast demagnetization to be $\lesssim 10\%$, leaving only dissipation of angular momentum into the lattice on an ultrafast time scale as a viable explanation [155].

Electron–Phonon Scattering and the Microscopic 3TM (M3TM) Dissipation of the electrons' spin angular momentum to the lattice on a 100 fs time scale was addressed by B. Koopmans *et al.* in a microscopic implementation of the 3TM, referred to as M3TM [156, 157]. Within this model, spin relaxation is mediated by Elliott–Yafet-like processes, with a spin-flip probability, a_sf, for electron–phonon momentum scattering events. In the M3TM, the magnetization dynamics are described by [157]

$$\frac{\mathrm{d}m}{\mathrm{d}t} = Rm\frac{T_\ell}{T_\mathrm{C}}\left(1 - \coth\left(\frac{mT_\mathrm{C}}{T_\mathrm{e}}\right)\right), \tag{2.53}$$

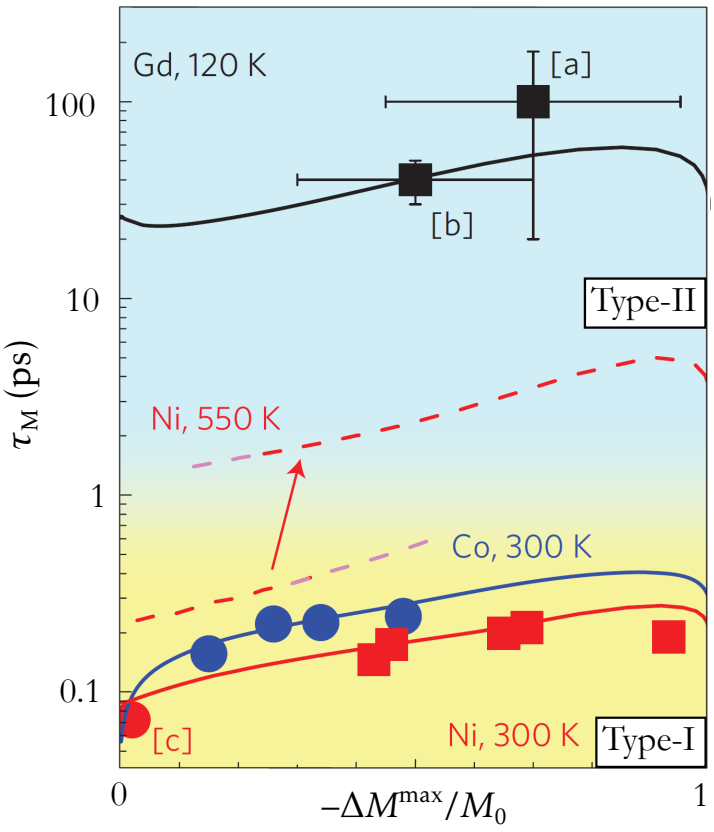

Figure 2.12.: Classification of type-I and type-II demagnetization dynamics (taken from Ref. [157]). Shown is the dependence of the demagnetization time, τ_M, on the maximum degree of demagnetization, $-\Delta M_z^{max}/M_{z,0}$, in the $3d$ elements Ni ([c] Ref. [12]) and Co, and the $4f$ element Gd ([a], Ref. [158]; [b], Ref. [159]). The τ_M versus $-\Delta M_z^{max}/M_{z,0}$ behavior for both the one-step (Ni and Co) and the two-step (Gd) demagnetization dynamics can be described via the M3TM (solid lines). All simulations are for infinitesimally thin, free-standing films, using a_{sf} of 0.185 (Ni), 0.150 (Co) and 0.090 (Gd). At elevated temperatures the M3TM predicts a transition from type-I to type-II dynamics for the $3d$ elements, which was confirmed in experiments [133, 160].

where $m = M/M_s$ is the magnetization relative to its value at zero temperature. Note that in order to fit experimental data, also the temperature transients for the electron (eq. (2.45)) and lattice (eq. (2.47)) subsystems have to be solved.[15] The prefactor, R (unit s^{-1}), is a material-specific scaling factor for the demagnetization rate [157]

$$R = \frac{4a_{sf}G_{e\ell}k_B T_C^2 V_{at}}{(\mu_{at}/\mu_B)E_D^2}, \tag{2.54}$$

where k_B is the Boltzmann constant, μ_{at} is the atomic magnetic moment, V_{at} is the atomic volume and E_D is the Debye energy (see supplementary information to Ref. [157]). For the analysis of experimentally obtained magnetization transients, a_{sf} (determining the initial slope of ultrafast demagnetization), $G_{e\ell}$ (determining the cooling down of the electron gas), T_C (if not measured) as well as the ratio C_ℓ/γ (determining the magnitude of the initial peak and the final degree of demagnetization with γ as a material-specific parameter) are remaining fit parameters.

The M3TM is of particular relevance, as it is capable of describing different types of ultrafast demagnetization in $3d$ and $4f$ elements, denoted as type-I and type-II demagnetization dynam-

[15] In analogy to the derivation of the analytical solution of the 3TM, the spin-specific heat, C_s, is neglected.

ics, respectively. Materials with large values of R, e. g., $R = 17.2\,\mathrm{ps}^{-1}$ in Ni and $R = 25.3\,\mathrm{ps}^{-1}$ in Co [157], undergo type-I demagnetization dynamics, characterized by a one-step demagnetization within $\tau_M \approx (100\text{–}300)\,\mathrm{fs}$, followed by a pronounced recovery of magnetization within the energy equilibration time, $\tau_E \approx (0.5\text{–}1)\,\mathrm{ps}$. In this regime, demagnetization is completed before electron–phonon equilibration is achieved. In contrast, materials with small values of R, e. g., $R = 0.092\,\mathrm{ps}^{-1}$ in Gd, are found to undergo type-II demagnetization dynamics, characterized by a two-step demagnetization. After an initial rapid decay on a 100 fs time scale, demagnetization continues at a lower demagnetization rate that can extend over several 10 ps. In this regime, the demagnetization efficiency is too low to establish a full thermal equilibrium in the spin system during electron–phonon equilibration [157]. Experimental results on Ni, Co and Gd as well as the corresponding calculations via the M3TM from Ref. [157], are shown for increasing maximum degrees of demagnetization (increasing laser fluences) in Fig. 2.12.

It is argued that the large values of R in 3d transition metal ferromagnets originate from surprisingly large $a_{sf} = 0.185 \pm 0.015$ in Ni and $a_{sf} = 0.150 \pm 0.015$ in Co [157], supported by numerical evaluations [161], which is due to so-called *spin hot spots* in the valence band structure [162].[16] Remarkably, this means that about every tenth momentum scattering event would be accompanied by a spin-flip process in 3d transition metal ferromagnets, mediating the ultrafast decay of magnetic order within only (100–300) fs with involvement of the lattice. Notably, a smaller $a_{sf} = 0.025 \pm 0.005$ in elemental Co was reported in Ref. [136]. Such large differences might stem from the fact that the model depends on the above mentioned microscopic material-specific parameters, which have to be determined simultaneously with a_{sf}. An about twice as low spin-flip probability of $a_{sf} = 0.08$ in Ref. [160], as compared to $a_{sf} = 0.185$ in Ref. [157], e. g., was explained by different values for the electronic heat capacity. Despite discrepancies in the reported values for a_{sf}, the importance of electron–phonon scattering as a main driving force for ultrafast demagnetization was confirmed in various experiments [155, 164, 165].

A faster demagnetization time of $\tau_M \approx (70\text{–}150)\,\mathrm{fs}$ is observed in Co/Pd and Co/Pt multilayers [15, 135, 137]. Reduced values of τ_M by a factor of two in multilayered structures as compared to elemental Co was proposed to stem from the enhanced spin–orbit coupling (SOC) [136], which scales with Z^4 [166] (Z: atomic number). By layering of the 3d transition metal Co ($Z = 27$) with a heavy metal like Pt ($Z = 78$), however, only the interface-near Co atoms are in close vicinity to the Pt atoms so that an increase of τ_M with an effective Z and not a direct scaling of $\tau_M \propto 1/Z^4$ should be expected. Within the M3TM also the spin-flip probability scales with SOC [157], i. e., with the effective Z. It describes the reduction of τ_M by a factor of two in Co/Pt multilayers compared to elemental Co by an increase in the spin-flip probability by a factor of four from $a_{sf} = 0.025 \pm 0.005$ to $a_{sf} = 0.105 \pm 0.005$ [136].

[16] Note that this is about two orders of magnitude larger than in non-magnetic 3d elements like Cu [163].

Electron–Electron Scattering Another mechanism that might contribute to ultrafast demagnetization is electron–electron spin-flip scattering, conserving angular momentum via collective spin excitations (magnons) [13, 167, 168]. It has been confirmed that the emission of magnons, induced by scattering of hot electrons, takes place on a femtosecond time scale and can act as an efficient microscopic mechanism to describe ultrafast demagnetization [123]. Results have to be regarded with care, as it is pointed out that the efficiency of magnon generation is material specific and therefore not necessarily holds as a unified explanation for ultrafast demagnetization. By combining different experimental approaches, M. Cinchetti *et al.* could give a deeper insight in the demagnetization dynamics involving magnons [129]. It was concluded that microscopically, spin-wave excitations play an important role for ultrafast spin dynamics, but the ultrafast demagnetization in Co is mainly due to Elliott–Yafet-type of spin-flip scattering, as proposed in Refs. [156, 157]. Recent findings, however, suggest that the generation of magnons might become the dominating contribution to ultrafast demagnetization in the regime of strong demagnetization [169].

2.5.1.4. Superdiffusive Spin Currents

An alternative mechanism to describe ultrafast demagnetization is proposed by M. Battiato *et al.* within the concept of superdiffusive spin-currents [170]. Through laser heating, electrons get excited from the quasi-localized d-band to sp-bands above the Fermi level where they become highly mobile, reaching velocities of $\approx 1\,\mathrm{nm/fs}$ [32]. The electron motion is described by superdiffusive transport which means that the variance of the displacement of a particle distribution, $\sigma^2 \propto t^\gamma$, does not grow linearly in time and γ moreover is time dependent, taking values from $\gamma = 2$ (ballistic) at small times to $\gamma = 1$ (Brownian) at long times [170]. The superdiffusive spin-current may give rise to ultrafast demagnetization due to the different inelastic lifetimes of majority and minority-spin electrons and associated different mean free paths in $3d$ ferromagnets [170]. By utilizing time and spin-resolved photoemission spectroscopy, distinct differences for the lifetimes of minority and majority-spin electrons have been found in Co, with $\tau_{\mathrm{maj}} \approx 20\,\mathrm{fs}$ and $\tau_{\mathrm{min}} \approx 17\,\mathrm{fs}$ at an energy of about 0.6 eV above the Fermi level and $\tau_{\mathrm{maj}} \approx 8\,\mathrm{fs}$ and $\tau_{\mathrm{min}} \approx 4\,\mathrm{fs}$ at an energy of about 1 eV above the Fermi level [171]. From that, a mean free path on the order of a few (1–10) nm can be expected [172].

Using XUV TR-MOKE, to study the *indirectly* induced change of magnetization in Ni/S/Fe heterostructures (S = Ru (spin conductor), S = Ta (spin scatterer) and $S = \mathrm{Si_3N_4}$ (insulator)), it was shown that superdiffusive spin currents may contribute to ultrafast demagnetization with equal strength as local spin-flip scattering [164, 173]. However, when using spacer layers, S, with a short spin-lifetime like Ta (or also Pt), the spin current between adjacent layers was found to be suppressed [174]. From that, no significant contribution to ultrafast demagnetization from superdiffusive spin currents in transverse direction, i. e., across Co/Pt

interfaces, is expected in the here investigated Co/Pt multilayers with individual Co and Pt-layer thicknesses on the order of 1 nm.

In lateral directions, superdiffusive spin currents across domain boundaries could, however, contribute to ultrafast demagnetization in magnetic multi-domain systems. Due to their overall short mean free path on the order of a few (1–10) nm, only electrons close to the domain boundaries are expected to be involved in a spin-current induced ultrafast demagnetization. In a previous collaborative TR-mSAXS experiment at FLASH, indications for such superdiffusive spin currents along lateral directions were found [32] (see also appendix C). Using the nIR-pump–XUV-probe mode, the ultrafast loss of the magnetic-scattering intensity from the multi-domain state of a $[Co/Pt]_{16}$ multilayer, indicative of ultrafast demagnetization, was found to be accompanied by transient changes in the position, Q_{peak}, of the magnetic scattering peak, $I(Q)$. The observed transient Q_{peak}-shift was explained by a broadening of the domain-wall profile due to superdiffusive spin currents that lead to an accumulation of minority-spin electrons at the domain boundaries. The effect of ultrafast laser heating on transient and permanent lateral modifications in magnetic multi-domain states was further investigated here, in the TR-mSAXS experiment at FERMI (chapter 6). In magnetic multi-domain states with an average domain size of ≈ 100 nm and a domain-wall broadening on the order of ≈ 10 nm, the change in the area filling of the domain walls relative to the domains accounts for only $\approx 1\%$. Hence, the contribution from a transiently broadened domain wall profile to the overall demagnetization is also expected to be small.

2.5.1.5. Fluence Dependence of Ultrafast Magnetization Dynamics

In the 3*d* ferromagnets, Fe, Co and Ni, a fluence dependent increase of the demagnetization time has been reported, taking values of $\tau_M \lesssim 200$ fs for low fluences and reaching up to $\tau_M \approx 300$ fs for high fluences [13, 136, 157, 175]. In general, reported literature values on the demagnetization time, τ_M, in the 3*d* ferromagnets, or composite materials like Co/Pt multilayers, are difficult to compare, as usually thin films of different thicknesses, or multilayers with different layer compositions, are investigated and the demagnetization time depends on the film thickness (section 2.5.1.6). Moreover, information on the fluence determination and hence the actual excitation strength is often lacking. Instead of relating different τ_M values to the corresponding fluences, the demagnetization time is therefore often related to the laser induced maximum degree of demagnetization, $-\Delta M_z^{max}/M_{z,0}$, as shown in Fig. 2.12.

In literature, also fluence independent demagnetization times are reported for the 3*d* ferromagnets, e. g., $\tau_M \approx 180$ fs in a Ni thin film [176], or $\tau_M \approx 160$ fs in a $[Co/Pd]_{30}$ multilayer [37]. As shown in Fig. 2.12, τ_M only weakly increases with $-\Delta M_z^{max}/M_{z,0}$, so that from investigations over a limited fluence regime in combination with relatively large experimental errors, a fluence independent τ_M might be deduced. For example in Ref. [15] a potentially slightly

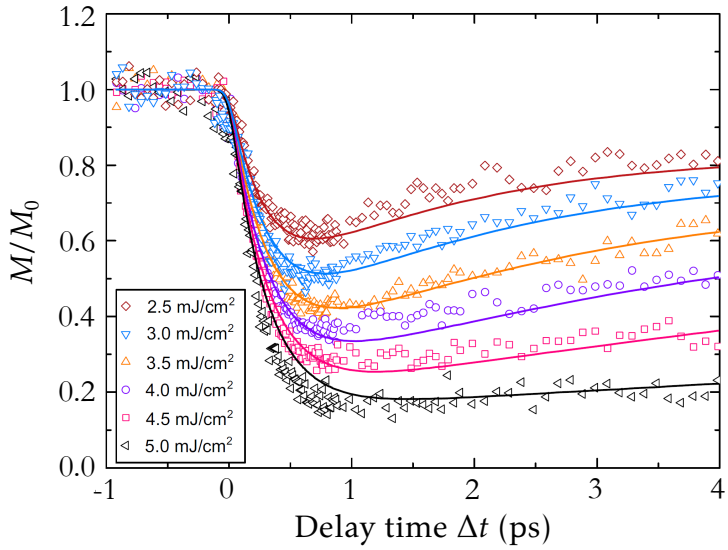

Figure 2.13.: Fluence dependence of ultrafast magnetization dynamics in a 15 nm Ni thin film measured by TR-MOKE at room temperature (taken from Ref. [160]). The magnetization is normalized to its value at negative delay times, M_0. Lines are calculations via the M3TM.

increasing demagnetization time from $\tau_M \approx 75\,\text{fs}$ for $-\Delta M_z^{\max}/M_{z,0} \approx 15\%$ to $\tau_M \approx 100\,\text{fs}$ for $-\Delta M_z^{\max}/M_{z,0} \approx 45\%$ was within the error of $\approx 25\,\text{fs}$. In such magnetic multi-domain systems, a fluence independent τ_M was proposed to stem from a direct transfer of spin angular momentum between neighboring domains via superdiffusive spin currents. It was furthermore proposed that the speed of angular momentum transfer should primarily depend on the specific properties of the domain system such as the domain boundaries, from which one could infer a demagnetization time that is largely independent from fluence [15]. However, the overall contribution from superdiffusive spin transport to ultrafast demagnetization is expected to be small in the here investigated Co/Pt multilayers, as Pt is a strong spin-scatterer and the samples possess multi-domain states with average domain periodicities of a few 100 nm (section 2.5.1.4).

Note that according to the M3TM (section 2.5.1.3), a transition from a one-step (type-I) to a two-step (type-II) demagnetization can be expected in 3*d* transition metal ferromagnets at high fluences or elevated temperatures close to T_C. The transition from type-I to type-II demagnetization in Ni, heated to a temperature of $T = 550\,\text{K}$, is shown in Fig. 2.12 as a red dotted line. To the author's knowledge, experimental evidence for this transition was only found for high temperatures, e. g., in Refs. [133, 160]. For high fluences still a one-step demagnetization, accompanied by a drastic slowing down of the magnetization recovery dynamics, is observed, which was described as type-II remagnetization in Ref. [146]. The fluence dependence of the remagnetization or energy equilibration time, τ_E, is outlined in the following.

Typically observed magnetization transients for various laser fluences (degrees of demagnetization) in 3*d* ferromagnets are shown in Fig. 2.13 together with calculations via the M3TM [160]. Aside from the fluence-dependent shift of the maximum degree of demagnetization towards

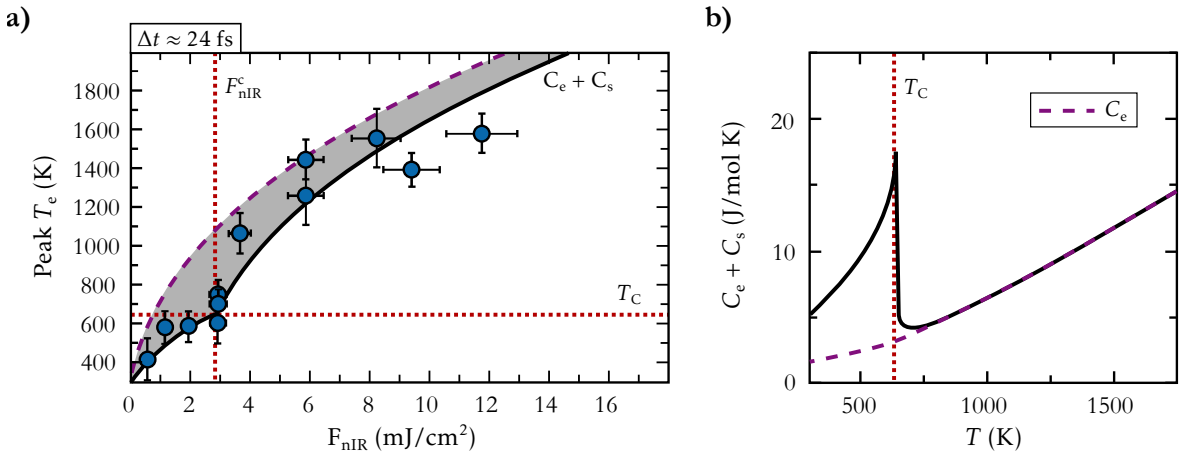

Figure 2.14.: a) Peak electron temperature ≈ 24 fs after nIR-laser excitation, obtained by fluence-dependent TR-ARPES measurements on a Ni(111) single-crystalline film (reproduced from Ref. [176]). The increase of T_e was found to be strongly suppressed at a critical fluence of F^c_{nIR}. The non-equilibrium T_e could be well-fitted by taking into account the transient specific heat of the combined electron and spin system, $C_e + C_s$ (solid black line), rather than the specific heat of the electron system alone, C_e (dashed purple line). The gray shaded area corresponds to the energy that is stored in the spin system. b) Critical behavior of the specific heat of the combined electron–spin system, $C_e + C_s$, close to T_C (reproduced from Ref. [176]).

later times (fluence-dependent increase of τ_M), qualitative differences in the remagnetization dynamics (fluence-dependent increase of τ_E) are observed. On the one hand, for low laser fluences, a pronounced fast-recovery of magnetization on the characteristic time scale for energy equilibration, $\tau_E \approx (0.5\text{–}1)$ ps, is observed, followed by a slow-recovery of magnetization on a much longer time scale (heat diffusion). According to eq. (2.48), the energy equilibration time at low fluences scales linearly with the electron temperature, $\tau_E \approx C_e/G_{e\ell} = \gamma T_e/G_{e\ell}$. This approximation, however, might fail at high fluences, as $G_{e\ell}$ in general is temperature dependent and especially the assumption of $C_s = 0$ is highly questionable for laser-induced temperature excursions close to T_C. In particular, at high fluences that induce almost full demagnetization, τ_E is significantly increased, i. e., a drastic *slowing down* of the magnetization recovery dynamics is observed close to the ferro-to-paramagnetic phase transition, e. g., in Refs. [131, 146, 177, 178].

Considering equilibrium conditions, the ferro-to-paramagnetic phase transition is known to be connected to *critical phenomena* such as the divergence of the magnetic heat capacity, as shown in Fig. 2.14 b). By employing TR-ARPES with increasing laser fluences to measure the peak electron temperature above E_F in a Ni(111) single-crystalline film, P. Tengdin *et al.* found strong indications that such critical phenomena also govern the *non-equilibrium* ferro-to-paramagnetic phase transition [176]. At a critical fluence (F^c_{nIR}), that corresponds to a peak electron temperature $T_e \approx T_C$, the temperature rise in the electron system was found to

be strongly suppressed (Fig. 2.14 a)). It was concluded that a significant amount of energy is stored in the spin system already ≈ 20 fs after nIR-laser excitation. Furthermore, the transient T_e from TR-ARPES could be well-fitted by considering the divergence of the specific heat of the strongly coupled electron and spin system ($C_e + C_s$) rather than the specific heat of the electron system alone. The divergence of $C_e + C_s$ around T_C was determined from equilibrium measurements [179], individually for $T_e < T_C$ and $T_e > T_C$, as shown in Fig. 2.14 b). At high temperatures ($T_e \gg T_C$), the electron system was approximated as a free-electron gas ($C_e \approx \gamma T_e$) and the specific heat was evaluated from the TR-ARPES measurements.

Furthermore, the interaction between the electron and spin system is predicted to reduce to zero close to the critical point, $T_s \approx T_C$, according to the theory on laser-induced magnetization dynamics at high temperatures provided by A. Manchon *et al.*, meaning that the demagnetization process comes to a rest [180]. More precisely, an energy relaxation rate that is proportional to the cube of the magnetization, $G_{es} \propto M(T_s)^3$, was derived. It was argued that due to a vanishingly small G_{es}, the spin temperature stays constant for a extended period of time (several picoseconds), i. e., τ_E diverges close to the critical point T_C [180]

$$\tau_E \propto \tau_d \propto \left(1 - \frac{T_s}{T_C}\right)^{-\delta}, \tag{2.55}$$

where τ_d is called the *slowdown time* and the exponent $\delta = 0.34$ for the $3d$ ferromagnets.

By combining experiments with micromagnetic and atomistic simulations, the slowing down of the magnetization recovery upon high-fluence nIR-laser excitation was connected to the existence of a strongly disordered magnetic state, i. e., a loss of *memory* of the initial state [177, 178, 181]. According to these simulations, the recovery of magnetization from a highly disordered state (large degree of demagnetization) involves the formation of magnetically ordered regions with sizes on the order of a few nanometers. The orientation of these locally ordered regions is, however, random which leads to considerable frustration and a slowing down of the remagnetization dynamics that may extend over several 10 ps. According to this interpretation, the slowing down of the fast-recovery of magnetization crucially depends on the initially absorbed energy in the electron-system and its ability of transferring the energy to the spin-system, i. e., to induce a high degree of disorder in the magnetic state.

2.5.1.6. Thickness Dependence of Ultrafast Magnetization Dynamics

The thickness dependence of ultrafast demagnetization in few monolayer (ML) Ni and Co thin films was studied in Ref. [125]. Using the same fluence of $F_{nIR} = 10\,mJ/cm^2$, a decreasing maximum degree of demagnetization of 22%, 15% and 3% was obtained for increasing Co-layer thicknesses of 2 ML, 3 ML and 4 ML, respectively, which was attributed to a rapid increase of T_C with thickness. In that publication, a $\tau_M = (260–280)$ fs was found, independent from

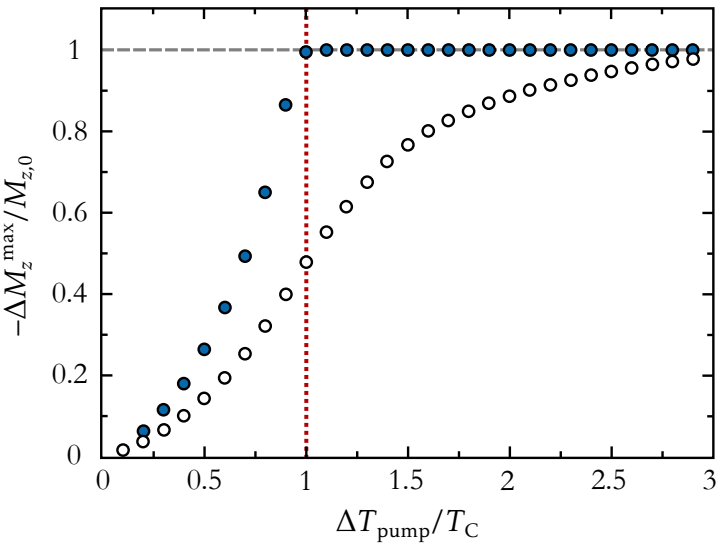

Figure 2.15.: Fluence (or temperature) dependence of $-\Delta M_z^{\max}/M_{z,0}$ for isolated Ni thin films of thicknesses $d = 5\,\mathrm{nm}$ (filled symbols) and $d = 30\,\mathrm{nm}$ (open symbols) modeled via the M3TM (reproduced from Ref. [182]). The model explicitly takes into account the finite attenuation length of nIR light in Ni, which yields a z-dependent electron-temperature profile, $\Delta T_{\mathrm{e}}(z) = \Delta T_{\mathrm{pump}} \exp(-z/\delta_{\mathrm{Ni}})$.

Co and Ni ML coverages, in agreement with the understanding of ultrafast demagnetization via the 3TM (section 2.5.1.1). In contrast, the electron–phonon relaxation time was found to initially increase from $\tau_{\mathrm{E}} \approx 0.7\,\mathrm{ps}$ for a single-ML Ni film to $\tau_{\mathrm{E}} \approx 3\,\mathrm{ps}$ for a 6 ML Ni film. It was proposed that the phonon spectrum of few-ML thin films has not reached its full 3D character and cannot accommodate electronic energy at the same rate as in bulk Ni. Indications for a fully developed 3D character, accompanied by a speed-up of τ_{E} with increasing thickness, were found to start at about 8 ML of Ni.

The thickness dependence of ultrafast demagnetization in thicker films was modeled by K. C. Kuiper *et al.* in Ref. [182], as shown in Fig. 2.15, where non-homogeneous heating and heat dissipation along the direction of the sample's surface normal (z-direction) were included in the M3TM. The ultrafast magnetization dynamics were simulated for two different Ni film thicknesses of $d = 5\,\mathrm{nm}$ (filled symbols) and $d = 30\,\mathrm{nm}$ (open symbols). For the simulations, an exponentially decaying electron-temperature rise along the sample z-direction, $\Delta T_{\mathrm{e}}(z) = \Delta T_{\mathrm{pump}} \exp(-z/\delta_{\mathrm{Ni}})$, was used, where $\delta_{\mathrm{Ni}} \approx 15\,\mathrm{nm}$ is the attenuation length of nIR light in Ni and ΔT_{pump} is the laser induced electron-temperature rise at the surface. Hence, a larger maximum degree of demagnetization can be expected in the 5 nm compared to the 30 nm-thin Ni film for all different fluences. In the former case, the maximum degree of demagnetization strongly increases with laser fluence, reaching full demagnetization for $\Delta T_{\mathrm{pump}} \approx T_{\mathrm{C}}$ (red dotted line). In the latter case, a contrasting behavior is predicted, i. e., the maximum degree of demagnetization increases on a more shallow slope for low fluences and shows a saturating behavior at high fluences, reaching full demagnetization for $\Delta T_{\mathrm{pump}} \approx 3T_{\mathrm{C}}$. The saturation of the maximum degree of demagnetization at high fluences was experimentally observed, e. g., in a 30 nm thin Ni film in Ref. [183], and can intuitively be explained by a z-dependent electronic heating. While only a limited fluence is needed to heat up the top part

of the film to T_C, it requires a much higher fluence to drive also the rear side of the film above T_C, for cases where the film thickness exceeds the attenuation length of nIR light. Within this thesis, the z-dependent laser heating in Co/Pt multilayers, with total film thicknesses between $d = (8.6–15.2)\,\mathrm{nm}$, is taken into account in order to evaluate the laser-induced temperature rise after electron–phonon equilibration (section 5.4.2.3).

An increased demagnetization time, τ_M, in the thinner sample was found by the calculations in Ref. [182], which was proposed to stem from the non-homogeneous temperature and heat diffusion in thin (isolated) films. An faster demagnetization in samples that are in contact to conducting substrates is in agreement with experimental observations, e. g., $\tau_M \lesssim 100\,\mathrm{fs}$ in a $[Co/Pd]_{30}$ multilayer fabricated on a 30 nm-thick Al buffer layer [15], that increases to $\tau_M \approx 160\,\mathrm{fs}$ in a comparable but isolated $[Co/Pd]_{30}$ multilayer [37].

2.5.2. All-Optical Magnetization Reversal

After a decade of intense research on ultrafast demagnetization, another fascinating magneto-optical phenomenon called *all-optical switching* (AOS) has been discovered in ferrimagnets (section 2.5.2.1) and a few years later also in ferromagnets (section 2.5.2.2). The phenomenon of switching a magnetic state all-optically is of great interest not only from a pure scientific perspective, by fully understanding the transfer of angular momentum during the switching process, but also from a technological point of view, as it promises to write magnetic information, in principle, on ultrafast time scales and at a low energy cost. The differences between AOS in ferrimagnets and ferromagnets are outlined in the following.

2.5.2.1. Single-Pulse AOS in Ferrimagnets

The phenomenon of switching a magnetic state all-optically (AOS) was first discovered by C. D. Stanciu *et al.* in 2007 in ferrimagnetic GdFeCo [22] and later confirmed, e. g., in ferrimagnetic TbCo [184] and TbFe [185] alloy thin films as well as artificial ferrimagnetic structures like Fe/FePt multilayers [186].

The deterministic AOS by a single 40 fs-short circularly polarized nIR-laser pulse, as reported by C. D. Stanciu *et al.*, is depicted in Fig. 2.16 which was originally explained by two cooperating effects. Firstly, the laser pulse heats the ferrimagnetic thin film close to T_C, creating a non-equilibrium state, i. e., an ultrafast demagnetization on a femtosecond timescale (section 2.5.1). And secondly, the circularly polarized laser pulse acts as an effective opto-magnetic field on this excited state via the inverse Faraday effect (IFE) [138–140], which, in thermal equilibrium and for transparent media can be expressed as [8, 187, 188]

$$\mathbf{H}_{OM}(t,r) = \varepsilon_0 \alpha \left(\mathbf{E}(t,r) \times \mathbf{E}^*(t,r)\right), \tag{2.56}$$

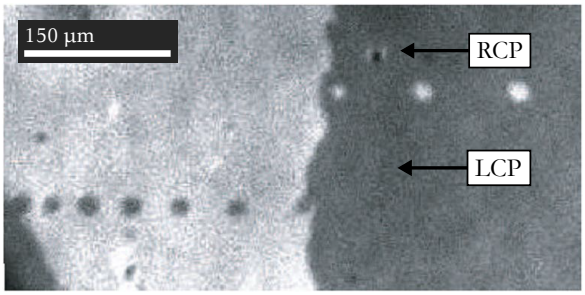

Figure 2.16.: Demonstration of single-pulse AOS in a $Gd_{22}Fe_{74.6}Co_{3.4}$ alloy thin film (taken from Ref. [22] with minor modifications). Bright and dark regions show magnetic contrast with respect to the surface normal. The pulsed laser beam ($F_{\mathrm{nIR}} \approx 2.9\,\mathrm{mJ/cm^2}$) was swept at high speed ($\approx 50\,\mathrm{mm/s}$) across the surface of the thin film so that every 40 fs-short laser pulse impinged on a different spot.

with α being the magneto-optical susceptibility. In isotropic media, the $\mathbf{H}_{\mathrm{OM}}$-field is directed along the wave vector of light and changes its sign when the helicity of the laser pulse is reversed. For an estimation of H_{OM}, the amplitude of the electric field can be expressed via the fluence, F, and the pulse duration, τ, of the laser pulse, $F/\tau \approx c\varepsilon_0 |E_0|^2/2$. Assuming a Gaussian spatial laser profile, the IFE induced opto-magnetic field is given by [187]

$$\mathbf{H}_{\mathrm{OM}}(t,r) = \sigma \frac{2\alpha F}{c\tau} f(t) \exp\left(-\frac{r^2}{2r_0^2}\right)\mathbf{n}, \tag{2.57}$$

where σ is the degree of polarization (± 1 for LCP/RCP and 0 for LP), $\mathbf{n}$ is the unit vector in the direction of the wave vector of light and $f(t)$ describes the temporal profile of the electric field. Taking realistic values for α in GdFeCo, effective field strengths on the order of $\mu_0 H_{\mathrm{OM}} \approx 1\,\mathrm{T\,mJ^{-1}\,cm^{-2}}$ were estimated [22, 187]. In a recent publication, taking into account the non-negligible absorption of laser light in metals, it was shown that the induced magnetization is strongly materials and frequency dependent [189]. According to these calculations, both spin and orbital induced magnetizations exist and the imparted magnetization in ferromagnets is only asymmetric (different strengths) and not antisymmetric (different signs) in the helicity of the laser light. To conform with previous approaches, the effective opto-magnetic field, that would be needed to induce the same magnetization as imparted by the IFE, was calculated, yielding $\mu_0 H_{\mathrm{OM}} = (40\text{–}65)\,\mathrm{T}$ in Fe and $\mu_0 H_{\mathrm{OM}} = (100\text{–}200)\,\mathrm{T}$ in Co [189].

Today, AOS in ferrimagnetic GdFeCo is understood to be largely independent on the light's helicity, but to originate from the different demagnetization times $\tau_{\mathrm{Fe}} = (100 \pm 25)\,\mathrm{fs}$ and $\tau_{\mathrm{Gd}} = (430 \pm 100)\,\mathrm{fs}$ of the two antiferromagnetically coupled Fe (Co) and Gd sublattices [23].[17] In that publication, the different demagnetization times of Fe and Gd were obtained by element selectively measuring ultrafast demagnetization upon LP laser excitation in resonance with the Fe L_3 and the Gd M_5 absorption edges. The results show that the switching evolves via a transient ferromagnetic-like state owing to the different dynamics of the Fe and Gd sublattices in non-equilibrium ($\tau_{\mathrm{Gd}}/\tau_{\mathrm{Fe}} \approx 4$), supported by atomistic simulations. A magnetic state that has switched Fe and Gd sublattice magnetizations was argued to be due to the different

[17] Note that there might exist a narrow fluence regime for a helicity-dependent AOS in GdFeCo [187].

dynamics of the two sublattices in non-equilibrium and their antiferromagnetic exchange interaction [190].

Further time-resolved experiments at LCLS [191], and FERMI [192], as well as at table-top setups [188, 193], reproduced a helicity *independent*, purely heat-driven AOS in GdFeCo which is also called *toggle switching* and can be tuned via the laser pulse parameters [194]. It was furthermore reported that inhomogeneities in the sample's microstructure can influence the magnetization switching behavior, suggesting a non-local transfer of angular momentum via superdiffusive spin currents to contribute to AOS [34]. The toggle switching in ferrimagnetic materials can occur upon a single laser-pulse excitation [22] and proceeds on a femto to picosecond time scale [190]. A comparably slow, multi-pulse mechanism is observed in ferromagnetic materials, which is introduced in the following.

2.5.2.2. Single vs. Multi-Pulse HD-AOS in Ferromagnets

The possibility to reverse a magnetic state all-optically by sub-100 fs short laser pulses is a phenomenon that is not unique to ferrimagnetic materials. A *helicity dependent* AOS (HD-AOS) of the magnetization in ferromagnets was first demonstrated by C-H. Lambert *et al.* in 2014 in single Co films, Co/Pt and Co/Ni multilayers as well as FePt(Ag)C thin films [24]. Importantly, these ferromagnetic thin films do not possess two magnetic sublattices as GdFeCo, so that a different underlying switching mechanism has to be at work.

In particular, the HD-AOS in ferromagnetic Co/Pt multilayers was found to depend on the interplay of electronic heating and heat dissipation within the sample structure [24]. On the one hand, it requires to overcome a particular fluence threshold to induce HD-AOS, i. e., a heating of the sample close to T_C. On the other hand, if the thermal energy was too large, no switching but the formation of a multi-domain state was observed upon sample cooling, i. e., a minimizing of dipolar energy. A permanent HD-AOS is thus observed only in particularly thin Co/Pt multilayers, e. g., the widely studied $[Co(0.4)/Pt(0.7)]_3$ multilayer, that possess a small total Co amount and thus small dipolar energy circumventing a decay into a multi-domain state. Note that the pure thermal demagnetization during sample cooling in thicker Co/Pt multilayers was circumvented by applying small OOP magnetic fields of a few-1 mT in order to stabilize the reversed magnetic state (see supplemental to Ref. [24]).

In analogy to the original interpretation of AOS in *ferrimagnets*, C-H. Lambert *et al.* proposed the IFE (see previous section) as the underlying mechanism to mediate HD-AOS in ferromagnets [24], which was supported by micromagnetic and atomistic simulations [25, 196, 197]. Aside from the distinct interplay between heating close to T_C and subsequent heat dissipation, the duration of the opto-magnetic field, H_{OM}, seems to play a decisive role in an IFE-induced HD-AOS, with a minimum lifetime to induce switching of ≈ 0.1 ps for $\mu_0 H_{OM} \approx 20$ T [196]. The H_{OM} field could, however, be present in the material for 2–6 times longer than the pulse

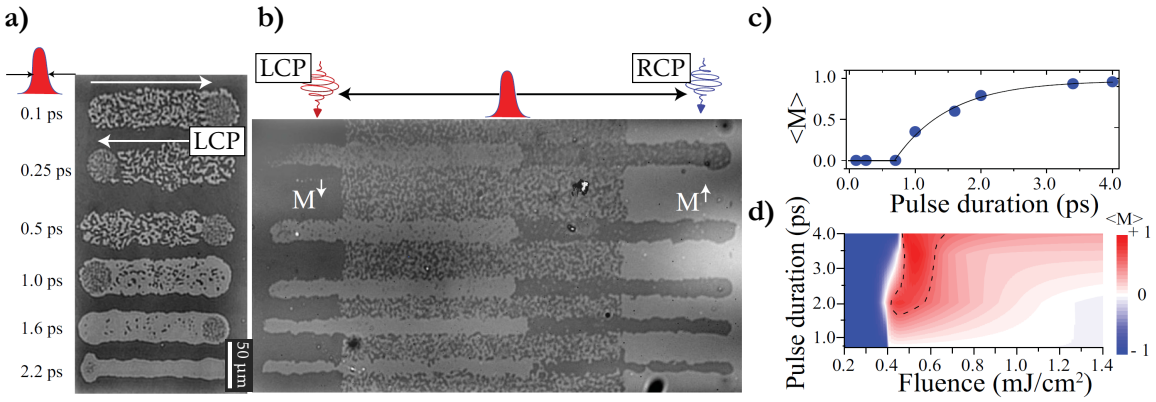

Figure 2.17.: Fluence and pulse-duration dependence of HD-AOS in a ferromagnetic $[Co(0.4)/Pt(0.7)]_3$ multilayer (taken from Ref. [195] with minor modifications): a) Magneto-optical image obtained after sweeping LCP laser pulses with increasing pulse duration from 0.1 ps (top) to 2.2 ps (bottom) and a fluence of 0.5 mJ/cm^2 across the sample surface (repetition rate 500 Hz). Bright and dark regions show up and down-magnetized domains with respect to the sample's surface normal. Arrows indicate the direction of the sweep. b) HD-AOS induced by sweeping LCP and RCP laser pulses with a pulse duration of 4.0 ps across the sample surface (multi-pulse excitation). Irrespective of the initial magnetic state, the final state is determined by the helicity of the laser pulses. The average size of the switched area increases with fluence from 0.45 mJ/cm^2 (bottom) to 0.7 mJ/cm^2 (top). c) Average value of the photo-induced magnetization, $\langle M \rangle$, as a function of the pulse duration. d) Phase diagram of $\langle M \rangle$ as a function of the pulse duration and fluence. The dashed contour shows the region of pump fluences and pulse durations for which efficient AOS was observed.

duration [25], so that the H_{OM} field might effectively couple to the magnetization well after laser excitation on a picosecond time scale. As magnetization recovery is extended to several picoseconds when exciting the magnetic states to temperatures close to T_C (section 2.5.1.5), it is likely an interplay of a highly excited state and a helicity-dependent H_{OM} that results in HD-AOS during the magnetization recovery on a picosecond time scale. Consequently, for the right set of laser parameters in combination with a well-designed sample structure, single-pulse HD-AOS mediated by the IFE is predicted to be possible [196].

In experiments, mostly multi-pulse HD-AOS is observed in ferromagnetic thin films, which was studied by R. Medapalli *et al.* in dependence on several external parameters, i. e., the laser fluence and pulse duration (Fig. 2.17), as well as the number of laser pulses (Fig. 2.18). An efficient multi-pulse switching was found in the $[Co(0.4)/Pt(0.7)]_3$ multilayer for laser pulses above a threshold fluence of $F_{nIR} \approx 0.5$ mJ/cm^2 and a pulse duration in the picosecond regime [195].

An alternative mechanism to an IFE-mediated HD-AOS in granular ferromagnetic thin films is a *stochastic* multi-pulse switching with a probability that depends on the helicity of the laser light [198–200]. In such a scenario, the switching of a magnetic state is initialized via the stochastic nucleation of reversed domains (Fig. 2.18 a)). A final micrometer-sized switched

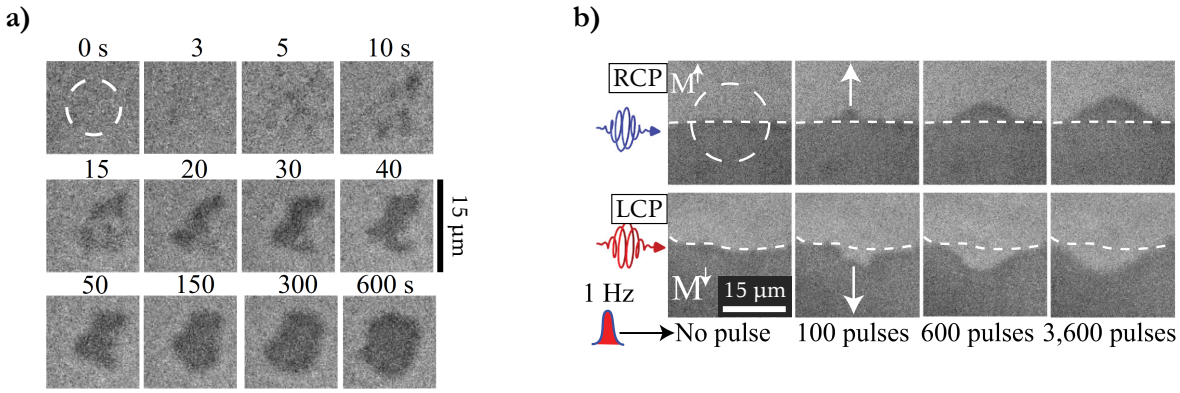

Figure 2.18.: Magneto-optical images from a $[Co(0.4)/Pt(0.7)]_3$ multilayer upon irradiation by optical laser pulses with a repetition rate of 1 Hz (taken from Ref. [195] with minor modifications). a) Nucleation and growth processes upon irradiation of an up-magnetized domain by LCP laser pulses with a fluence of 0.5 mJ/cm^2. Images were taken after different laser-exposure times (1 s = 1 pulse). b) Domain wall displacement upon irradiation of the center (dashed circle) of an up–down domain pair by RCP and LCP laser pulses with a fluence of 0.4 mJ/cm^2 and a pulse duration of 4.0 ps. Dashed lines indicate the original positions of the domain walls. The direction of the displacement is determined by the helicity of the laser pulses.

area would occur either due to consecutive helicity-dependent nucleation processes or due to helicity-independent nucleation followed by a helicity-dependent growth of the reversed domains through laser induced domain-wall motion (Fig. 2.18 b)).

Consecutive Helicity-Dependent Nucleation According to atomistic simulations, a stochastic HD-AOS occurs via a thermal hopping ($k_B T$) of individual magnetic grains over the anisotropy barrier (KV) [25], which is reduced at elevated temperatures due to magnetization fluctuations [201]. On the one hand, in magnetic materials with a large anisotropy energy, like FePt thin films or Co/Pt multilayers, no switching of the magnetic grains is induced at low laser fluences (large value $KV/k_B T$). On the other hand, a finite switching probability up to 50% for a full demagnetization of the magnetic grain can be expected at high fluences (small value $KV/k_B T$) [25]. Importantly, in ferromagnetic materials the absorption of energy from a light pulse is dependent on the relative orientations of the light's helicity and the magnetization, known as the MCD effect (section 2.4.1). Higher temperatures, and thus higher switching probabilities, P_s, are expected in magnetic grains with the magnetization directed parallel to the light's helicity. An external magnetic field can act as a bias to the energy barrier and thus may increase or decrease the switching probability, depending on whether it is oriented parallel (reduced P_s) or antiparallel (increased P_s) to the initial magnetization direction. Importantly, these nucleation processes are *non-deterministic* with a maximum probability to switch a magnetic grain of $P_s = 0.5$ [25]. For describing the stochastic HD-AOS macroscopically, an ensemble of magnetic grains was considered in Ref. [25]. Those grains with a magnetization

oriented in the higher absorption direction with respect to the laser polarization reach a higher temperature and thus a higher switching probability. Any such switched grains reside in the (now) lower absorption direction, with a reduced probability of switching back. As a consequence, a higher probability for a final state with the magnetization oriented along the lower absorption direction, i. e., antiparallel to the light's helicity, is predicted, which further builds up under repetitive, multi-pulse laser irradiation.

Nucleation and Consecutive Domain-Wall Motion Helicity dependent domain-wall motion was studied in Ref. [195] by subjecting the center of an up–down domain pair to multiple CP laser pulses (Fig. 2.17 b)). The helicity dependence is clearly evidenced in the magneto-optical images, showing a domain-wall displacement that gradually decreases with the number of laser pulses. A strong displacement/pulse of 45 nm was found within the first 100 s (= 100 pulses at a repetition rate of 1 Hz). The displacement gets weaker for the subsequent laser excitations with a displacement/pulse of 11 nm within (100–600) s and reaching almost saturation within (600–3600) s with a displacement/pulse of only 2 nm, which is due to the reduced temperature gradient across the domain wall upon its displacement away from the position of the laser focal spot. The helicity dependence of such an *all-thermal* magnetization switching is believed to arise from the MCD as well [25]. The helicity dependent domain-wall displacement in Ref. [195] could be explained by a differential absorption of the circularly polarized laser pulses. This creates a temperature gradient across the domain wall (approximately 0.2 K/nm, assuming a 1 K temperature difference and a 5 nm-broad domain wall), that drives a magnonic spin current from the hotter to the colder region. Due to angular momentum conservation, the domain wall at the same time is dragged towards the hotter region, with a velocity that depends on the temperature gradient and the damping constant. For a constant temperature gradient, a velocity of the domain-wall displacement on the order of 10 nm/ns can be expected [195, 202].

Up to now the role of the IFE and the MCD in HD-AOS is still under debate. Both IFE and MCD could explain the frequently observed (stochastic) multi-pulse HD-AOS in experiments [203], whereas only an IFE-based mechanism could explain a (deterministic) single-pulse HD-AOS [26, 200]. The two might be distinguished from each other, utilizing time-resolved experiments, as an IFE-induced (single-pulse) switching is expected to occur within 2–6 times the laser pulse duration (picosecond regime), but a stochastic (multi-pulse) switching depends on the time for nucleation and growth of domains (nanoseconds and longer). Note that a few experiments report a single-pulse switching in ferromagnets, e. g., by applying small magnetic fields [204] or by exchange coupling the ferromagnetic Co/Pt multilayer with ferrimagnetic GdFeCo [205]. Single-pulse AOS might furthermore be achieved by controlling the sample thickness and thus the equilibrium size of the magnetic domains [206]. Indeed, by

matching the laser spot size with the intrinsic domain size, single-pulse AOS was recently reported in a thin Co/Pt multilayer [207].

3 Co/Pt-Multilayer Samples

Among the most frequently used samples for studying ultrafast magnetization dynamics in nanoscopic multi-domain states are Co/Pt multilayers (see, e. g., Refs. [135–137, 146, 208]). In particular, they are promising candidates for future all-optical magnetic data-storage devices, as outlined in the previous sections. This is, not at last, because their magnetic properties such as the Curie temperature, the domain size, or the magnetic anisotropy, can be tailored by changing the individual layer thicknesses and/or multilayer repeats (see, e. g., Refs. [68, 70, 209–214]). The Co/Pt-multilayer samples in this work were fabricated using ion-beam and DC-magnetron sputtering techniques (section 3.1), following a well-established recipe that was developed at the University of Hamburg. Co/Pt, as well as the similar Co/Pd-multilayer samples, that were fabricated by this recipe, have been successfully used in various campaigns at synchrotron and FEL facilities, e. g., in Refs. [30, 32, 215]. Within this thesis, a series of Co/Pt-multilayer samples with different individual Co and Pt-layer thicknesses as well as different Co/Pt-bilayer repeats were prepared and the magnetic properties of the samples were characterized by Kerr microscopy and MOKE (section 3.2). For the TR-mSAXS experiments, three particularly thin Co/Pt multilayers were selected that possess perpendicular magnetic anisotropy (PMA), multi-domain ground states with average domain sizes in the range of a few 100 nm as well as full remanence.

3.1. Sample Fabrication

For synchrotron and FEL experiments in transmission geometry, the thin magnetic films have to be deposited on substrates that are sufficiently transparent for the used XUV and soft X-ray radiation. Past experiments showed that 50 nm-thin Si_3N_4 membranes, that possess a transmission of $\approx 38\%$ for XUV ($E_{ph} = 59.8\,eV$) and $\approx 93\%$ for soft X-ray radiation ($E_{ph} = 778.2\,eV$)[1], are well-suited for that. The Si_3N_4 membranes are part of commercially available Si/Si_3N_4 multi-membrane chips from *Silson Ltd*[2] with a frame size of $(10 \times 10)\,mm^2$. The multi-membrane chips contain an 8×8 array of Si_3N_4-membrane windows with a size of $(50 \times 50)\,\mu m^2$ and a pitch of 1 mm in both x and y-directions, that are etched from the backside

[1] CXRO database: http://henke.lbl.gov
[2] Silson Ltd, Warwickshire, Englang: https://www.silson.com/

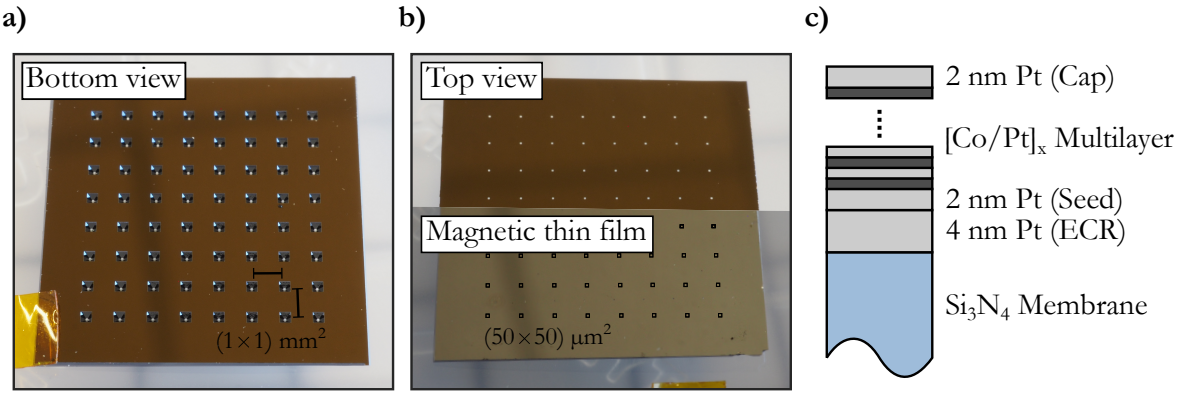

Figure 3.1.: a) Bottom and b) top view of the Si/Si_3N_4 multi-membrane chip. The magnetic thin films are deposited on the top side of the substrate via sputtering techniques. c) Multilayer structure of the magnetic thin films.

into the Si/Si_3N_4 frame. The bottom and the top-view of the Si/Si_3N_4 multi-membrane chip are pictured in Fig. 3.1 a) and b), respectively.

The multilayer structure of the magnetic thin films is illustrated in Fig. 3.1 c). For manufacturing the Co/Pt-multilayer samples, a recipe that was developed at the University of Hamburg was employed, optimized to achieve smooth interfaces as well as a pronounced texture of the polycrystalline thin films in order to maximize the PMA. For details on the fabrication process and the typical structural properties of the Co/Pt multilayers it is referred to Refs. [71, 82, 118].

Prior to sputtering the magnetic thin films, the Si/Si_3N_4 multi-membrane chips were exposed to an O_2 plasma in order to reduce surface-roughness variations of the Si_3N_4 membranes. The Co/Pt multilayers were grown at room temperature at a base pressure of $< 1 \cdot 10^{-8}$ mbar. At first, a 4 nm Pt layer was deposited on the multi-membrane chip by ion-beam sputtering, using an electron cyclotron resonance (ECR), which was found to result in a pronounced (111) texture and a grain size of ≈ 10 nm [118, 216]. Thin films that are grown on top retain both texture and grain size [71]. Next, a 2 nm Pt seed-layer followed by the Co/Pt-multilayer stack were grown by DC-magnetron sputtering, exhibiting smooth interfaces with an interface roughness of about one monolayer and an interdiffusion zone of about two to three monolayers [82, 118]. The multilayer structure was sputtered from 2 inch Co and 1 inch Pt targets at an argon pressure of $\approx 3.5 \cdot 10^{-4}$ mbar with sputter rates of ≈ 0.025 nm/s and ≈ 0.05 nm/s, respectively. A series of $[\mathrm{Co}(d_{\mathrm{Co}})/\mathrm{Pt}(d_{\mathrm{Pt}})]_x$ multilayers was fabricated with individual Co-layer thicknesses in the range of $0.4\,\mathrm{nm} \leq d_{\mathrm{Co}} \leq 1.4\,\mathrm{nm}$, individual Pt-layer thicknesses in the range of $0.4\,\mathrm{nm} \leq d_{\mathrm{Pt}} \leq 2.0\,\mathrm{nm}$ and number of bilayer repetitions of $2 \leq x \leq 8$. To prevent the samples from oxidation, the Co/Pt-multilayer stacks were capped by a 2 nm Pt cap-layer independent from their individual layer compositions (the cap layer is the final layer of the Co/Pt-multilayer stack). Note that

the Co/Pt multilayers were simultaneously sputtered on Si/SiO_2 substrates. These reference samples were used for the pre-studies via Kerr microscopy and MOKE, presented in the following sections.

3.2. Sample Properties

From the series of Co/Pt multilayers, three samples were selected for investigating the nIR-laser induced ultrafast magnetization dynamics, namely $[Co(1.0)/Pt(1.2)]_3$, $[Co(0.8)/Pt(1.4)]_6$ and $[Co(0.6)/Pt(0.8)]_8$-multilayer samples[3] with total film thicknesses in the range of the penetration depth of nIR light in Co ($\delta_{Co} \approx 13\,nm$ [217]) and Pt ($\delta_{Pt} \approx 8\,nm$ [218]). In such optically thin samples that possess the same 2 nm-thin cap layer, any indirectly induced demagnetization, e. g., by hot-electron transport [37], can be expected to be negligibly small. The selection of the three samples was furthermore based on systematic pre-studies of their magnetic properties, i. e., their domain size in the multi-domain ground state determined by Kerr microscopy (section 3.2.1) and their magnetic hysteresis measured by MOKE (section 3.2.2). The focus of this work was on ultrafast magnetization dynamics, i. e., on ultrafast demagnetization in the three $[Co/Pt]_x$ multilayers (chapter 5) and on AOS-like dynamics in nanoscopic multi-domain states of the $[Co/Pt]_6$ multilayer in the presence of external magnetic fields (chapter 6). To obtain the maze-like multi-domain ground state, the $[Co/Pt]_x$ multilayers were subjected to out-of-plane (OOP) demagnetization cycles prior to the TR-mSAXS experiments (section 3.2.3).

3.2.1. Domain-Size Investigations

Aside from a total film thickness in the range of the attenuation length of nIR light in Co, another criterion for the selection of the $[Co/Pt]_x$-multilayer samples was a domain size in the multi-domain ground state of a few 100 nm. Especially because TR-mSAXS experiments have to be set-up for detecting the scattering from magnetic inhomogeneities on a certain length scale, an estimation of the average domain size prior to the experiments is essential. Therefore the multi-domain ground states of the Co/Pt multilayers were systematically imaged via Kerr microscopy. The working principle of a Kerr microscope is based on the rotation of the polarization plane of light when reflected from the surface of a magnetic material (MOKE), as outlined in section 2.4, which is visualized in the polarizing microscope. In multi-domain states, the analyzer can be set to exactly extinguish the light coming from one type of domains. As a result, this type of domains appears dark whereas the other type of domains appears bright. For details on the working principle of a Kerr microscope as well as on how to improve the magnetic contrast, it is referred to Ref. [90].

[3] The numbers in parentheses are the individual layer thicknesses in nanometers.

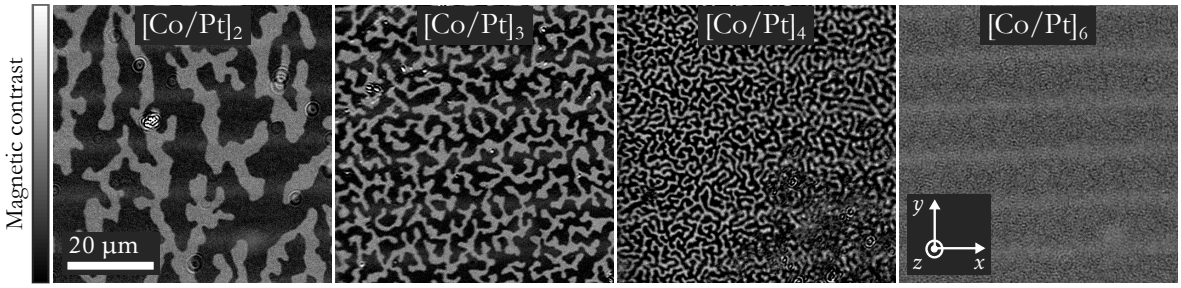

Figure 3.2.: Kerr-microscopy images of the multi-domain ground state in the series of $[\mathrm{Co}(0.8)/\mathrm{Pt}(1.4)]_x$ multilayers with increasing number of Co/Pt-bilayer repetitions from $x = 2$–6. Dark and bright areas show domains with magnetization pointing up or down with respect to surface normal (z-direction). In d) the maximum resolution of the Kerr microscope of $\approx 500\,\mathrm{nm}$ is exceeded, which is used as a criteria for selecting $[\mathrm{Co/Pt}]_x$ multilayers with few-100 nm-sized domains. Circularly shaped contrast variations and blurred areas are optical artifacts.

To fulfill the criterion of few-100 nm-sized domains, samples with a multi-domain ground state just below the resolution limit of the Kerr microscope of $\approx 500\,\mathrm{nm}$ were selected. The evolution of the multi-domain ground state with the number of Co/Pt-bilayer repetitions in the series of $[\mathrm{Co}(0.8)/\mathrm{Pt}(1.4)]_x$-multilayers, with $x = 2$, 3, 4 and 6, is depicted in Fig. 3.2. All of the multi-domain ground states show a large magnetic contrast, i. e., a large magnetization component along the OOP direction ($\pm z$-direction). The domain structures develop from an island-like configuration with few-micrometer sized domains to a maze-like configuration with few 100 nm sized domains when increasing the number of Co/Pt-bilayer repetitions from $x = 2$ to $x = 6$. Smaller domains are formed as a consequence of the increasing magnetostatic energy with increasing amount of Co material, i. e., with increasing sample thickness, as outlined in section 2.3. Similar is observed for the other series of $[\mathrm{Co}(d_{\mathrm{Co}}/\mathrm{Pt}(d_{\mathrm{Pt}})]_x$ multilayers, however, they show the transition to a nanoscopic multi-domain state at smaller or larger x, depending on the individual Co-layer thicknesses. In general, few 100 nm sized multi-domain states were obtained for $d_{\mathrm{Co}}^{\mathrm{tot}} \gtrsim 3.0\,\mathrm{nm}$, as it is the case for the selected $[\mathrm{Co}(1.0)/\mathrm{Pt}(1.2)]_3$, $[\mathrm{Co}(0.8)/\mathrm{Pt}(1.4)]_6$ and $[\mathrm{Co}(0.6)/\mathrm{Pt}(0.8)]_8$ multilayers.

3.2.2. Magnetic Hysteresis

As TR-mSAXS experiments in transmission geometry (z-axis is quantization axis) are sensitive to the z-component of magnetization only (section 2.4.3), Co/Pt multilayers with a PMA are required.[4] The energetically preferred orientation of magnetization in the $[\mathrm{Co/Pt}]_x$ multilayers was systematically investigated by means of MOKE (see section 2.4) using the MOKE setup described in Ref. [71].

[4] Note that in principle also samples with a canted easy-axis of magnetization (small M_z component) and even samples with an in-plane magnetization (by tilting the sample) can be used in resonant magnetic scattering or

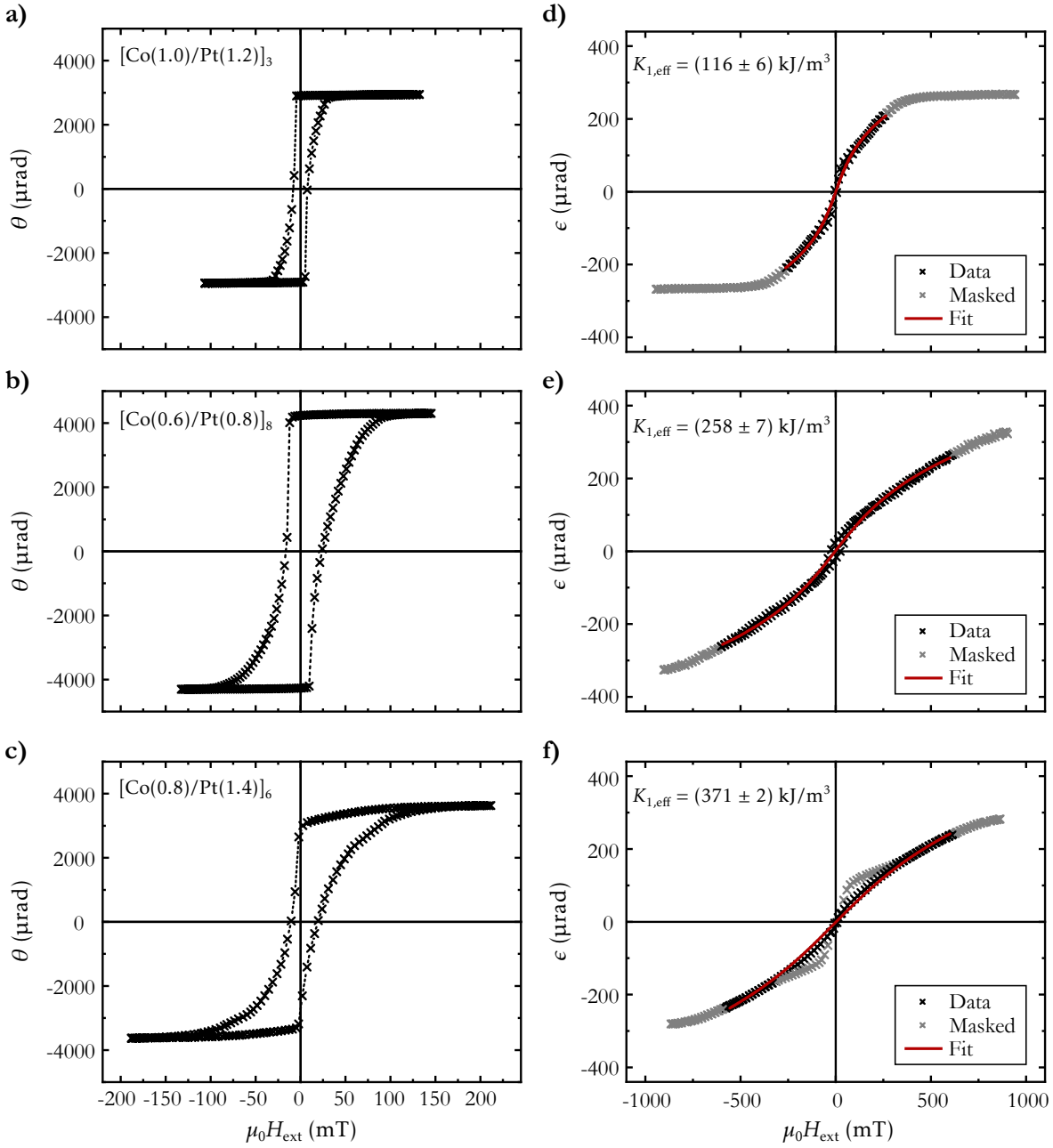

Figure 3.3.: a)–c) Out-of-Plane ($H_{ext} = H_{OOP}$) and d)–f) in-plane ($H_{ext} = H_{IP}$) hysteresis loops of the $[Co(1.0)/Pt(1.2)]_3$, $[Co(0.6)/Pt(0.8)]_8$ and $[Co(0.8)/Pt(1.4)]_6$ multilayers measured via polar and longitudinal MOKE, respectively. Results are arranged from the thinnest to the thickest sample (top to bottom). All samples show easy-axis behavior along the OOP direction, i. e., perpendicular magnetic anisotropy (PMA), evidenced by positive values for $K_{1,eff}$ obtained by fitting eq. (2.15) to the (inverse) hard-axis loops. Residual polar signals in the longitudinal MOKE measurements (see f)), as well as the regime close to saturation were masked for fitting.

In this setup, an electromagnet that provides magnetic fields up to $\mu_0 H_{\text{ext}} \approx \pm 1\,\text{T}$ can be rotated around the sample position, allowing for both polar ($H_{\text{ext}} = H_{\text{OOP}}$) and longitudinal ($H_{\text{ext}} = H_{\text{IP}}$) MOKE under an incident angle of the laser of 45°. Details on the MOKE technique can be found in Ref. [98]. The combination of an analyzer and a photo diode was used to measure the rotation, Θ, of the polarization plane of linearly polarized incident laser light ($\lambda = 635\,\text{nm}$) upon reflection from the surface of the magnetic thin films. Additionally inserting a $\lambda/4$ waveplate in front of the photo diode allowed to measure the ellipticity, ϵ, of the reflected laser light. Parasitic signals of the about ten times stronger polar MOKE, superimposed on the longitudinal one, can be extinguished by inverting the laser-beam path. In first-order approximation, Θ and ϵ depend linearly on the magnetization, hence, they give direct access to $m(H_{\text{OOP}})$ and $m(H_{\text{IP}})$ dependencies. For the TR-mSAXS experiments, samples that show an easy-axis behavior along the OOP direction and a hard-axis behavior along the IP direction were selected. The measured $\Theta(H_{\text{OOP}})$ and $\epsilon(H_{\text{IP}})$ for the three selected $[\text{Co/Pt}]_x$-multilayer samples are shown in Figs. 3.3 a)–c) and Figs. 3.3 d)–f), respectively.

The OOP hysteresis loops (left side) reveal some fundamental magnetic properties of the three samples, i. e., a coercivity of $\mu_0 H_{\text{c}} \lesssim 30\,\text{mT}$, an increasing saturation field from $\mu_0 H_{\text{s}} \approx 50\,\text{mT}$ to $\mu_0 H_{\text{s}} \approx 150\,\text{mT}$ (top to bottom) and an almost fully remanent magnetization ($M_{\text{r}} \approx M_{\text{S}}$). The latter shows that the single-domain configuration (investigated area $\approx (1 \times 1)\,\text{mm}^2$) is an energetic minimum in all of the samples. The overall shape of the easy-axis loops, however, is slightly changing from a square-like shape in the thinnest, $[\text{Co/Pt}]_3$ multilayer, to a more s-like shape in the thickest, $[\text{Co/Pt}]_6$ multilayer. Note that a further increase of the Co content, and thus a further increase of the stray-field energy, eventually results in $M_{\text{r}} = 0$, i. e., the single-domain state is no longer an energetic minimum at $\mu_0 H_{\text{ext}} = 0\,\text{mT}$, but breaks up into (self-organized) multi-domains. By fitting eq. (2.15) to the (inverse) hard-axis loops, the (first-order) effective anisotropy constant is determined to $K_{1,\text{eff}} = (116 \pm 6)\,\text{kJ/m}^3$ in the $[\text{Co/Pt}]_3$, $K_{1,\text{eff}} = (258 \pm 7)\,\text{kJ/m}^3$ in the $[\text{Co/Pt}]_8$ and $K_{1,\text{eff}} = (371 \pm 2)\,\text{kJ/m}^3$ in the $[\text{Co/Pt}]_6$ multilayer under the assumption of a constant $K_2 = 70\,\text{kJ/m}^3$.

3.2.3. Field Treatment Prior to FEL Experiments

It was shown in the previous sections that the selected $[\text{Co/Pt}]_x$ multilayers possess PMA and a stable single-domain state at zero external field. For investigating ultrafast magnetization dynamics on nanoscopic length scales, however, few 100 nm-sized multi-domain state were prepared by OOP demagnetization cycles. The final domain configuration thereby depends on the demagnetization procedure, i. e., the direction and maximum value of the applied field as well as the speed at which the field is swapped in the demagnetization cycles.

In order to ensure a proper demagnetization, i. e., the generation of the maze-like multi-

imaging experiments in transmission geometry [215, 219].

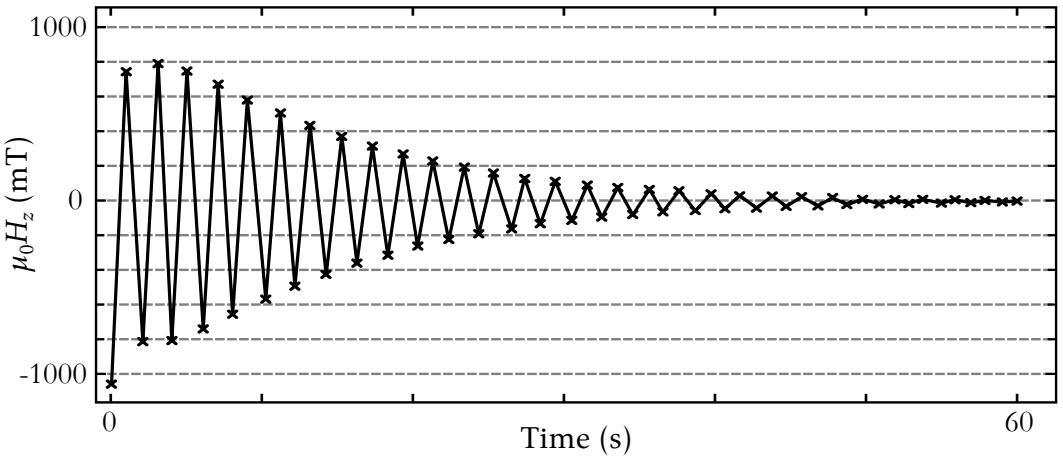

Figure 3.4.: Measurement of the magnetic field during an OOP demagnetization cycle (maximum field: $\mu_0 H_{\mathrm{OOP}} \approx \pm 1\,\mathrm{T}$, termination criterion: $\mu_0 H_{\mathrm{OOP}} < \pm 2\,\mathrm{mT}$), used to generate the maze-domain ground state of the Co/Pt multilayers.

domain ground state, OOP magnetic fields with a maximum strength of $\mu_0 H_{\mathrm{max}} \approx \pm 1\,\mathrm{T}$ ($H_{\mathrm{max}} \gg H_{\mathrm{s}}$) with exponentially decreasing amplitude were applied to the samples (Fig. 3.4). The OOP demagnetization cycles were terminated for a magnetic field amplitude $\mu_0 H_{\mathrm{min}} \leq 2\,\mathrm{mT}$, which was reached after $\approx 60\,\mathrm{s}$. Following that procedure, magnetic multi-domain states close to the global energetic minimum are generated, named the *maze-domain ground state* in the following. Characteristics of this maze-domain ground state, aside from a domain size of a few-100 nm, is a disordered domain configuration with an equal area filling of up and down-magnetized domains.

4 Experimental Methods and FEL Setups

The ultrafast magnetization dynamics of the three $[Co/Pt]_x$ multilayers with $x = 3$, 6 and 8 upon nIR-laser excitation was investigated by means of time-resolved mSAXS (TR-mSAXS) utilizing high-intensity and sub-100 fs-short XUV pulses from the free-electron laser (FEL) sources FLASH in Hamburg and FERMI@Elettra in Trieste. One of the exceptional properties of FEL radiation is described by its *brilliance*, also known as spectral brightness, which is a measure for the number of photons at a given energy that are emitted per second, area and angle within a small energy interval [112, 220]

$$[\text{brilliance}] = \frac{\text{photons}}{\text{s} \cdot \text{mrad}^2 \cdot \text{mm}^2 \cdot 0.1\%\text{BW}}. \tag{4.1}$$

A high brilliance plays the decisive role for TR-mSAXS experiments, as not only a large number of photons but also a small energy spread is important to overcome the small resonant magnetic scattering efficiency of thin magnetic films (section 2.4.5). FELs are today's most brilliant light sources reaching peak values of 10^{29}–10^{30} at FLASH [221], $6 \cdot 10^{32}$ at FERMI [222] and even $5 \cdot 10^{33}$ at EuXFEL [223]. Remarkably, this is about a factor of 10^{25} higher than a conventional X-ray tube and still a factor of 10^{10} higher than the most brilliant synchrotron sources with a peak value of, e. g., 10^{21} at PETRA III [224].

Apart from their high brilliance, today, FELs cover a wide spectral range including the M edges (XUV regime) and often also the L edges (soft X-ray regime) of the $3d$ elements Fe, Co and Ni, which allows to probe laser-induced magnetization dynamics in compound materials, such as Co/Pt multilayers, with elemental sensitivity. The working principle of TR-mSAXS at FEL facilities is outlined in section 4.1 and the experimental setups at the BL3 beamline at FLASH and the DiProI beamline at FERMI are presented in section 4.2. As a pre-study for the time-resolved experiment at FERMI, the nanoscopic multi-domain states of $[Co/Pt]_6$ multilayers were imaged via Fourier-transform holography (FTH) at the synchrotron PETRA III. A short introduction to FTH is given in the last section of this chapter (section 4.3).

4.1. Time-Resolved mSAXS at FEL Facilities

In contrast to a synchrotron, FELs provide XUV (or X-ray) pulses with a pulse duration typically below 100 fs and therefore are ideally suited for studying highly non-equilibrium

physics on femtosecond timescales, such as ultrafast demagnetization (section 2.5.1).[1] In this work, the magnetization dynamics were studied at two different FEL facilities, i. e., at FLASH, which is based on the self-amplified spontaneous emission (SASE) scheme [221, 226], and at FERMI, which is a seeded FEL based on the high-gain harmonic generation (HGHG) scheme [227–229]. Even though the working principles of the two FELs are different, both can be seen as single-pass electron lasers providing sub-100 fs-short XUV pulses of high brilliance and coherence [230, 231].

4.1.1. Laser-Like XUV-Pulse Properties

The exceptional properties of FEL-generated XUV pulses originate from high-quality electron bunches that are accelerated in a linear accelerator to relativistic energies of ≈ 1 GeV (see Fig. 4.1 a)) and guided through a periodic arrangement of many short dipole magnets of alternating polarity, called undulator. Due to this forced oscillatory motion at relativistic velocities, the electron bunches emit XUV (or X-ray) radiation that is collimated in a narrow cone around the undulator axis. The laser-like and ultrashort XUV-pulse properties in a FEL are achieved by modulating the electron bunches, so-called microbunching, either by the emitted EM field in the undulator itself (SASE), or by an external optical laser (HGHG). The schematics of the SASE FEL FLASH is shown in Fig. 4.1 a), the XUV-pulse generation in a HGHG FEL like FERMI is illustrated in Fig. 4.1 b). More details on the working principle of an FEL can be found in Refs. [233–235].

The FEL-generated XUV pulses possess an inherent bandwidth of ≈ 1% at FLASH [221] and even ≈ 0.05% at FERMI [236], which allows for a stable operation at the resonance energy, $E_{\mathrm{ph}} = 59.8$ eV (Co $M_{2,3}$ edge), in TR-mSAXS experiments without the need for further monochromatization. However, the significantly narrower bandwidth at FERMI is believed to be the main reason for a strongly enhanced magnetic scattering signal in the respective multi-pulse TR-mSAXS experiment (section 6.3.1). Further differences between SASE and HGHG generated FEL pulses are the achievable wavelength, longitudinal coherence length and spectral composition. SASE FELs, in principle, are capable of generating FEL pulses with wavelengths of $\lambda < 0.1$ nm (hard X-ray regime)[2], however, possessing a comparably short longitudinal coherence length as well as strong variations in their spectral composition from one pulse to another (see, e. g., Refs. [237, 238]). In HGHG FELs like FERMI, the output wavelength is currently limited to the soft X-ray regime, providing FEL pulses with a minimum

[1] Note that in principle, the comparably long pulse duration of ≈ (30–100) ps provided by synchrotron sources can be reduced by slicing the electron bunches, as it is realized, e. g., at BESSY II in Berlin [225]. The slicing, however, comes at the expense of photon flux and thus often requires to accumulate data over a longer time.

[2] Hard X-ray FELs are, e. g., SACLA in Japan, LCLS in USA or EuXFEL in Germany. The advent of hard X-ray FELs opens new possibilities to disentangle different atomic spin-dynamics contributions to ultrafast demagnetization, by probing compound materials such as Co/Pt multilayers or $L1_0$ ordered FePt in resonance with, e. g., the Pt L_3 edge at $E_{\mathrm{ph}} \approx 11.5$ keV, as demonstrated in Ref. [41].

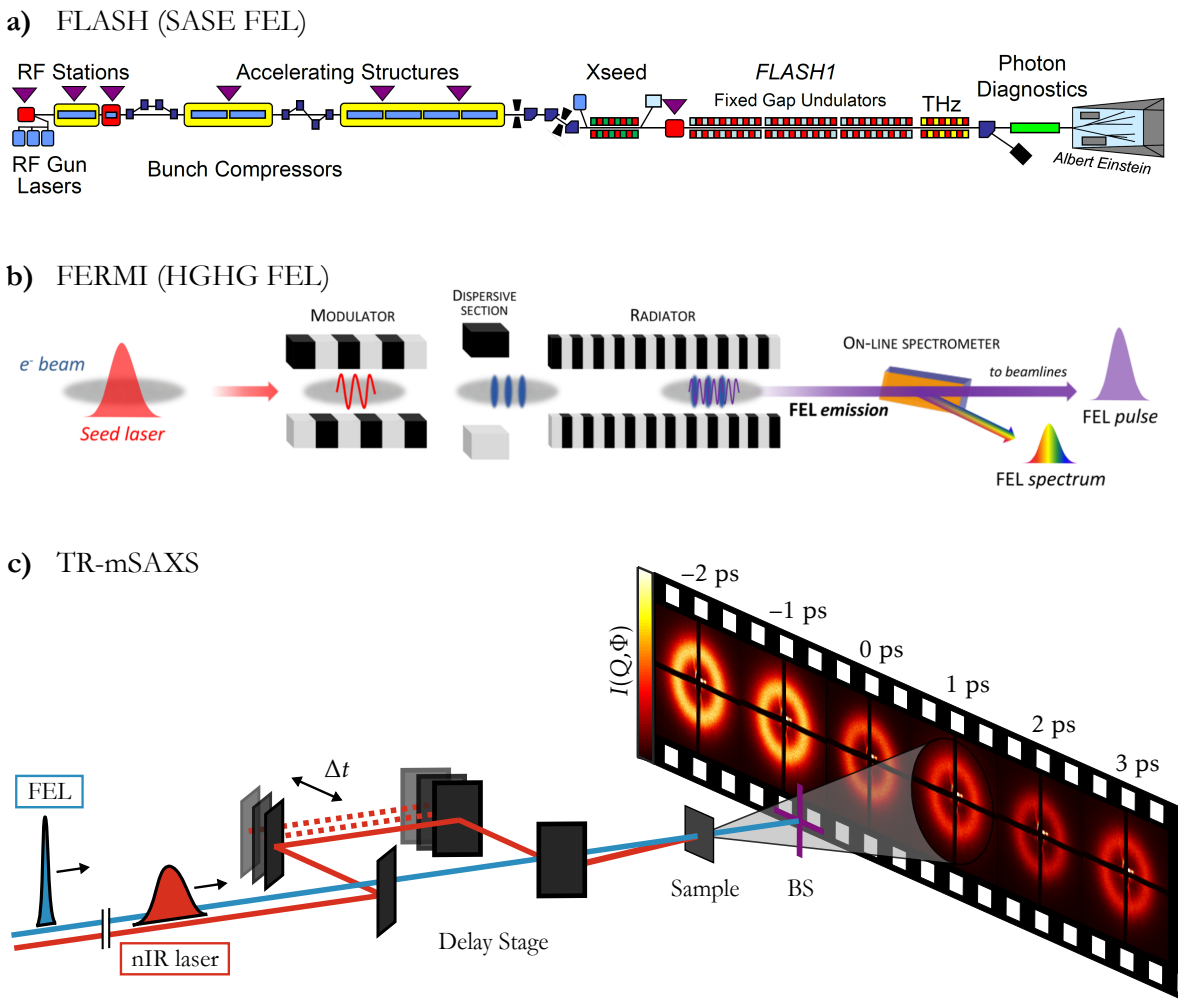

Figure 4.1.: a) Schematics of the SASE FEL FLASH1 (taken from Ref. [232]). In a SASE FEL, the EM field in the undulator becomes strong enough to modulate the electron bunches. Almost all electrons in a so-called microbunch begin to coherently emit EM radiation. Through constructive interference the pulse intensity is exponentially increased along the undulator. b) Layout of a HGHG FEL (taken from Ref. [230]): the modulation is achieved by superimposing the electron bunches with the EM field of a UV seed laser in a first modulator. The UV laser pulse imprints its temporal properties on the electron energy distribution, a dispersive section converts the energy modulation into a density modulation at the seed wavelength, λ_0, and at its higher harmonics. The radiator is set to amplify a specific harmonic, thereby reaching XUV wavelengths. c) Illustration of time-resolved magnetic small-angle X-ray scattering (TR-mSAXS) in transmission geometry. By temporally delaying nIR-laser pulses with respect to the FEL pulses in an optical delay stage allows to follow the time evolution of magnetization on femto to picosecond time scales.

fundamental wavelength of $\lambda \approx 4\,\mathrm{nm}$ [236]. A HGHG generated FEL pulse, however, has a temporal coherence length that is comparable to the pulse duration as well as a single-mode spectrum [229, 230]. Both at FLASH and FERMI, the FEL-pulse parameters are controlled online in a non-invasive way via a series of monitoring devices like intensity and beam-position monitors and spectrometers [221, 222].

4.1.2. Pump-Probe Experiments

The sub-100 fs-short XUV pulses, generated by the FEL, were used to probe the magnetic multi-domain states by means of mSAXS (section 2.4.3). In order to investigate magnetization dynamics in these multi-domain states, the nIR-pump–XUV-probe mode was employed, where a ultrashort nIR-laser pulses excite the magnetic state before resonant XUV probing. The two pulses can be delayed in time with respect to each other by changing the path-length of the nIR-laser pulses in an optical delay stage, as illustrated in Fig. 4.1 c). By that, both negative and positive delay times, Δt, with step sizes down to a few femtoseconds are possible, allowing to record a "movie" of the nIR-laser induced magnetization dynamics in reciprocal space. Each frame of the movie, i. e., each mSAXS image, is thereby recorded at a fixed delay time, Δt.

The HGHG scheme at FERMI shows an improved temporal stability between nIR-pump and XUV-probe pulses compared to the SASE scheme at FLASH. At FERMI, the electron bunches are seeded by the same optical laser that also provides the pulses exciting the magnetic thin film. Consequently, the nIR-laser and XUV pulses are intrinsically synchronized in time, providing an exceptional temporal stability in nIR-pump–XUV-probe experiments with a timing jitter of $\approx 6\,\mathrm{fs}$ [239, 240]. At SASE FELs like FLASH, the nIR-laser has to be extrinsically synchronized to the radio frequency source that drives the electron accelerator [221]. The synchronization is continuously adapted via control electronics during the measurements, providing still an excellent timing jitter of $\approx 33\,\mathrm{fs}$ [241].

In the beginning of each beamtime, the temporal overlap of the two pulses, i. e., $\Delta t = 0$, has to be evaluated which is described for the experiment at FLASH and at FERMI in section 4.2.1 and section 4.2.2, respectively.

4.1.3. Coherent Scattering in Multi-Pulse Mode

Ideally, the whole information on a magnetic multi-domain state is collected by exposing the sample to a single FEL pulse. In principle, the high brilliance of FEL-generated XUV pulses is more than sufficient to overcome the small resonant magnetic scattering efficiency with a calculated (maximum) value of $\rho_{\mathrm{RMS}} \approx 10^{-5}$ in the here investigated samples (section 2.4.5). Indeed, it has been demonstrated that mSAXS [30], but also holographic imaging [31] and even time-resolved X-ray absorption [40] experiments on magnetic thin films are possible, using a single FEL-pulse exposure.

To maintain a large magnetic scattering signal, single-pulse measurements typically require high FEL-pulse fluences. When using a single FEL pulse with a fluence of about 8 mJ/cm^2, permanent changes in the magnetic domain structure were detected, i. e., an increased size of the scattering ring, Q_{peak}, which was explained by FEL-induced structural changes [30]. Both a growth of the grain size and atomic diffusion at the interfaces affect the magnetic properties of the sample, such as the magnetocrystalline surface anisotropy, and thus the multi-domain configuration. These structural changes, however, do not proceed on ultrafast time scales, shown by the fact that a magnetic scattering image could still be recorded within the 100 fs-short FEL snapshot when using a destructive fluence of $\approx 5\,\text{J/cm}^2$ [33]. In that case, the magnetic scattering intensity was reduced by a factor of 20 compared to a reference measurement at a three orders of magnitude lower fluence, which shows that the FEL pulse itself acts as a pump at high fluences, thus, acting as an invasive probe.[3] To avoid alterations or even a destruction of the magnetic thin film by a single high-intensity FEL pulse, the pulse intensity was attenuated by a gas attenuator and/or a set of thin solid-state filters in the here conducted TR-mSAXS experiments. A large magnetic scattering intensity was maintained, by accumulating the scattering intensity from 100 low-intensity FEL-pulse exposures. Note that the acquisition of a delay-time scan in this multi-pulse or stroboscopic way requires the reversibility of the nIR-laser induced changes, i. e., the magnetic state has to recover its initial configuration prior to the consecutive nIR-pump–XUV-probe event.

In mSAXS, using highly coherent XUV radiation, the scattered intensity is not uniformly distributed in the ring but shows spikes and valleys on top of an average intensity distribution (Fig. 4.2 a)), which originates from constructive and destructive interference between the coherently scattered photons. The grainy scattering pattern, accumulated over 100 FEL-pulse exposures, could be interpreted as the so-called *speckle pattern*, which is a unique fingerprint of the exact spatial arrangement of the magnetic domains. The existence of such a non-uniform intensity distribution shows that the domain pattern does not significantly change during the 100 repetitive XUV-pulse exposures.

One main characteristic of a speckle pattern is the speckle size, s, which is directly related to the size of the illuminated area, i. e., the FEL beam size, A, on the sample [242, 243]

$$A_{x,y} = \frac{\lambda L}{\langle s_{x,y} \rangle}. \tag{4.2}$$

As before, L is the sample-detector distance, $\lambda = 20.8\,\text{nm}$ is the XUV wavelength and the subscripts x and y denote the size in x and y-directions. For determining the average speckle

[3] Note that aside from this intra-pulse demagnetization at high fluences, a main finding of this work is that the FEL pulses, in conjunction with the nIR-laser pulses, can influence the lateral domain configuration already at much lower fluences, which is discussed in section 6.4.3. The lateral modifications, however, evolve slowly and independently from the ultrafast magnetization dynamics.

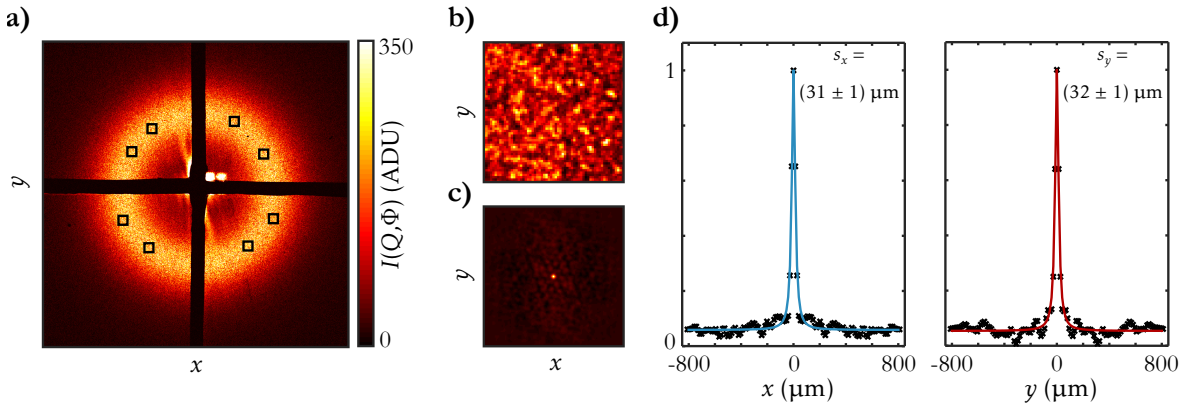

Figure 4.2.: a) Scattering pattern of the maze-domain ground state in a $[Co/Pt]_6$ multilayer using TR-mSAXS at $\Delta t = -1$ ps, obtained by accumulating the scattered intensity from 100 FEL-pulse exposures. b) Selected high-intensity region of the scattering pattern and c) corresponding spatial intensity correlation, $g(\mathbf{r})$. d) Determination of the speckle size, $s_{x,y}$ (FWHM), obtained from fitting $g(x,y)$ via a Lorentzian function.

size, regions of high intensity were selected from the scattering images for which the spatial intensity correlation function, $g(\mathbf{r}) = \langle I(\mathbf{r}+\mathbf{R})I(\mathbf{r})\rangle/\langle I\rangle^2$, was calculated [244]. The speckle size was determined as the width (FWHM) of a Lorentzian function that was fitted to line-cuts through $g(\mathbf{r})$ in x and y-directions, taking into account the pixel size of 13.5 µm (Fig. 4.2 b)–d)). Finally, the sizes from the different regions were averaged, resulting in an average speckle size of $\langle s_{x,y}\rangle = (31 \times 32)\,\mu m^2$ in the TR-mSAXS experiment at FERMI.

Significant differences are observed, when comparing the evaluated FEL beam size from speckle analysis with the value that was measured via online diagnostics, i. e., via fluorescent-screen measurements or scanning a diode across the FEL beam (Fig. 5.1 on p. 79 and Fig. 6.3 on p. 127). Utilizing the latter two approaches, FEL beam sizes of $A \approx (38 \times 61)\,\mu m^2$ and $A \approx (180 \times 240)\,\mu m^2$ were measured in the experiments at FLASH and at FERMI, respectively, in good agreement with the requested values. The speckle analysis, however, gives the same $A \approx (100 \times 100)\,\mu m^2$ in both cases. Even when taking into account a correction factor, α, that depends on the properties of the sample as well as the exact shape of the beam [245], the large differences can not be explained. Possible reasons for this discrepancy are an overall large FEL beam, which yields small speckles with a size in the range of the pixel size, but also FEL pointing instabilities, i. e., the probing of a slightly different area of the multi-domain pattern by each of the 100 FEL pulses, which leads to larger but blurred speckles.

4.2. Beamline End Stations

The laser-like XUV pulses and the time-delayed nIR-laser pulses are guided to the experimental end stations via dedicated beam paths. The TR-mSAXS experiments had to be conducted in

vacuum ($p \approx 5 \cdot 10^{-6}$ mbar), as XUV radiation with a photon energy of $E_{\mathrm{ph}} = 59.8$ eV has an absorption length of only a few-10 µm in air. Currently, the BL3 beamline at FLASH has no permanent end station. Hence, for the TR-mSAXS experiment, a custom-made end station that was developed in the FS-CXS group at DESY was connected to the beamline. It was equipped with a series of diagnostic tools that allowed for measuring the arrival time as well as the beam profiles of both FEL and nIR-laser pulses close to the sample position (section 4.2.1). The DiProI beamline at FERMI is equipped with a permanent end station, where similar diagnostic tools close to the sample position are provided by the facility (section 4.2.2).

4.2.1. Setup at the BL3 Beamline at FLASH

The custom-made end station, that was used in the nIR-pump–XUV-probe experiment at the BL3 beamline at FLASH, was originally designed to conduct THz-pump–XUV-probe experiments. For the present experiment, the end station was upgraded for using nIR-laser pulses to excite the magnetic states. Modifications included a change of optics as well as a change in position for incoupling nIR-laser instead of THz pulses. The modified setup is shown in Fig. 4.3.

The end station has an additional 2 m-long beam path for the XUV pulses, originally designed to account for the path-length difference of the THz with respect to the XUV pulses. At the end of this beam path, a parabolic multilayer mirror with a focal length of 3.5 m focuses the XUV pulses to the sample. The mirror is optimized to reflect XUV radiation of (21 ± 1.35) nm, consisting of 15 repeats of Mo/Si bilayers that reflect $\approx 34\%$ of the incoming XUV intensity [246, 247] (see Fig. 4.3–**3**).

For pumping the magnetic thin films, the Ti:sapphire laser available at FLASH was used, which provides 60 fs short and up to 20 mJ intense nIR-laser pulses of 800 nm central wavelength synchronized to the 10 Hz repetition rate of FLASH [248]. The nIR-laser pulses are guided along a dedicated beamline to a position close to the FEL-beamline exit flange. The nIR-laser pulse parameters were set via a pulse compressor, located close to experimental end station (Fig. 4.3–**1**), which provides pulse durations between $\tau_{\mathrm{nIR}} = (60\text{–}3000)$ fs (FWHM), as well as a series of optical elements (Fig. 4.3–**2**). Those were lenses with a focal length of 4 m to focus the laser pulses to the sample position, a $\lambda/4$ wave plate to set the state of polarization to linear or circular, a set of neutral density (ND) filters to attenuate the pulse energy down to $E_{\mathrm{ph}} \geq 5$ µJ and high-reflectivity mirrors to guide the laser pulses quasi co-linearly with the XUV pulses to the sample position. As safety measure, the whole experimental end station as well as the optical elements outside the vacuum chamber were enclosed by the laser tent provided by FLASH. The nIR-pump and XUV-probe pulses could be delayed in time via an optical delay stage with a minimum step size of 30 fs and sub-femtosecond precision.

A custom-made sample holder provided space for up to eight samples with a frame size of

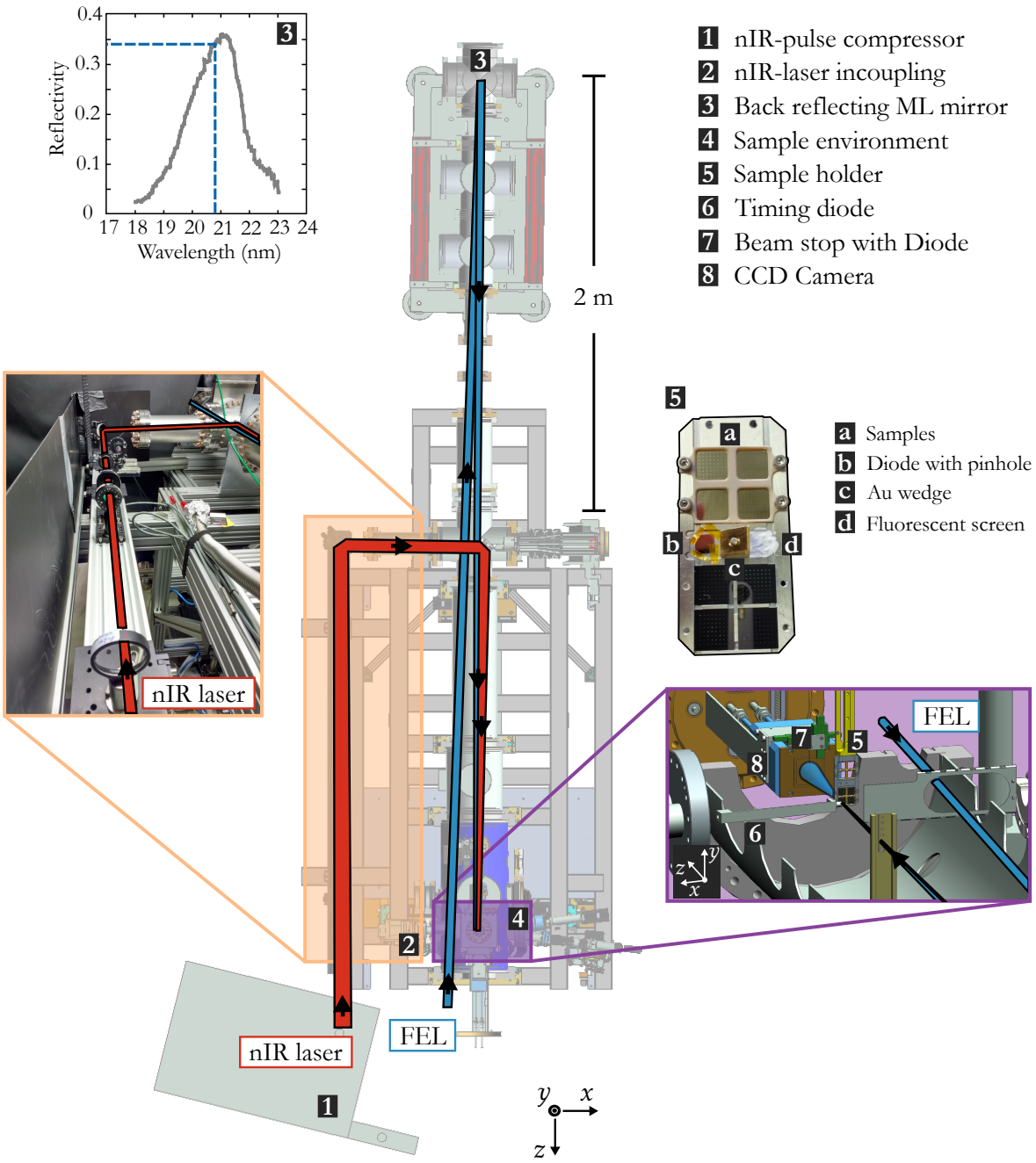

Figure 4.3.: Schematics of the custom-made end station for TR-mSAXS experiments at the BL3 beamline at FLASH. The nIR-laser pulse duration is set by a pulse compressor (**1**), the fluence and polarization are controlled by focusing optics, a series of neutral density filters and a $\lambda/4$-waveplate (**2**). The FEL pulses are back-reflected from the end of a 2 m long extra beam path by a Laue multilayer mirror (**3**) and focused to the sample environment (**4**). The sample environment contains a movable sample holder with diagnostic tools (**5**), a timing diode (**6**), a beam stop (**7**) and a CCD camera (**8**).

$(10 \times 10)\,\mathrm{mm}^2$ (Fig. 4.3–**5**). The individual $(50 \times 50)\,\mu\mathrm{m}^2$ sized membrane windows could be positioned along with the FEL beam via step motors with a precision of $\approx 1\,\mu\mathrm{m}$ in all three translational degrees of freedom. Additionally, three different diagnostic tools were mounted on the sample holder to monitor both nIR-laser and XUV-pulse characteristics at the sample position.

As a first tool, a diode was shielded by an opaque Au/Pt multilayer on a Si_3N_4/Si waver with a pinhole of $2\,\mu\mathrm{m}$ in diameter in the center to measure the FEL and nIR-laser pulse profiles (Fig. 4.3–**5 b**). For that, the diode was scanned across the beams in horizontal (x) and vertical (y) directions. The respective beam sizes and corresponding fluences were determined as described in section 5.1.1.

The second tool was used for measuring the temporal overlap of the FEL and nIR-laser pulses. A gold-plated aluminum wedge (Fig. 4.3–**5 c**) reflects/scatters both nIR-laser and FEL pulses towards a fast-responsive diode with a rise time of 700 ps, that measures their arrival time (Fig. 4.3–**6**). To determine the temporal overlap of the two pulses with a precision of $\lesssim 20\,\mathrm{ps}$, their diode signals are recorded using a high-frequency oscilloscope. The delay between the arrival times could be varied by delaying the nIR-laser pulses with respect to the FEL pulses in the optical delay-stage. During the experiment, $\Delta t = 0$ is refined by determining the temporal position of the onset of ultrafast demagnetization. By this procedure, $\Delta t = 0$ can be determined within $\approx \pm 50\,\mathrm{fs}$ during the experiment. The remaining uncertainty in $\Delta t = 0$ is taken into account as a fit parameter in the further analysis of the demagnetization data (section 5.4.2.1).

As a last tool, part of the sample holder is covered by a fluorescent screen (Fig. 4.3–**5 d**) to monitor the spatial overlap of the two beams. Spatial overlap can be controlled via a camera that is installed under an angle of $\approx 45°$ on top of the end station.

The scattering intensity is detected by a charge coupled device (CCD) camera with (2048×2048) pixels and a pixel size of $13.5\,\mu\mathrm{m}$ (Fig. 4.3–**8**). A 100 nm-thin aluminum filter, blocking any nIR or visible light, is mounted directly in front of the camera chip. The camera chip is cooled by Peltier elements and held at a constant temperature of $-40\,°\mathrm{C}$ to reduce the electronic-readout background. The detector is mounted at a distance of $L = 177\,\mathrm{mm}$ from the sample position, which results in an observable Q-range of $Q = (0.004\text{–}0.038)\,\mathrm{nm}^{-1}$, covering the scattered intensity from magnetic multi-domain states with an average domain periodicity in the range of $T_{\mathrm{av}} \approx (160\text{–}1600)\,\mathrm{nm}$. The signal-to-noise ratio (SNR) is improved through 2-by-2 binning of the (2048×2048) pixels, resulting effectively in (1024×1024) pixels with a pixel size of $(27 \times 27)\,\mu\mathrm{m}^2$.

Damage through the direct FEL beam is prevented by a beam stop (Fig. 4.3–**7**) that is installed on the CCD camera only millimeters away from the aluminum filter. Importantly, the beam stop is also used as a diagnostic tool. It is a custom-made circuit board with a photo diode acting as both, beam stop and intensity monitor. The diode signal serves as a measure for

pulse-to-pulse fluctuations of the FEL intensity and therefore can be used for normalization of the scattering data (section 5.1). Note that for attenuated FEL pulse intensities of $< 1\,\mu J$ no non-linearities in the measured signal are expected.

4.2.2. Setup at the DiProI Beamline at FERMI

The nIR-pump–XUV-probe experiment at FERMI@Elettra in Trieste was conducted at the diffraction and projection imaging (DiProI) beamline [249, 250]. Compared to the BL3 beamline, the DiProI beamline possesses a permanent end station that is specifically designed for scattering and imaging experiments.

At FERMI the so-called photon analysis, delivery and reduction system (PADReS) provides a series of photon diagnostic tools, including an online spectrometer that gives shot-by-shot information on the FEL-pulse's spectral components and intensity. The FEL-pulse intensity, that can be attenuated by a gas cell and a number of solid-state absorbers [222], is measured most accurately by the four-quadrant photo diode (FQPD), positioned right before the sample environment. A pair of Kirkpatrick-Baez (KB) focusing mirrors focuses the FEL pulses to the sample position. The nIR-laser and FEL-beam profiles are measured close to the sample position via a fluorescent screen, as shown in section 6.2.1, their temporal overlap ($\Delta t = 0$) is determined in two steps. In a first step, a coarse timing with sub-50 ps precision is achieved via the generated signal from a copper antenna (wire) that is connected to a fast oscilloscope. For fine timing with a precision of ≈ 300 fs, the change of the reflected nIR-laser intensity from a Si_3N_4 sample is measured when scanning the nIR-laser with respect to the FEL-pulses via the delay stage (see Ref. [240]). For more details on the capabilities of the end station at the DiProI beamline, it is referred to Ref. [251].

For the TR-mSAXS experiment at FERMI, in situ Helmholtz coils were designed and manufactured in-house, to provide magnetic field pulses with a strength of up to $\mu_0 H_z = \pm 50$ mT at the sample position. An image and a CAD drawing of the setup at the end station of the DiProI beamline, including the custom-made Helmholtz coils, is shown in Fig. 4.4 a) and b), respectively. The Helmholtz coils were operated in pulsed mode, synchronized to the 50 Hz repetition rate of FERMI. The magnetic field pulses reach the target field strength well within 200 µs, stay constant for 250 µs and decrease in strength with a decay time of ≈ 1 ms. By triggering the **H**-field pulses 250 µs prior to the FEL pulses, a constant magnetic field at the time of the nIR-pump–XUV-probe events is ensured. Pulsed operation of the magnetic field moreover reduces the duty cycle, showing no measurable increase in temperature throughout the duration of the whole beamtime.

The end station at the DiProI beamline uses the same type of CCD camera, with 2048×2048 pixels and a pixel size of 13.5 µm, as the one at FLASH. The detector was positioned at a distance $L = 150$ mm from the sample, covering a Q-range of $Q = (0.003\text{–}0.037)\,\mathrm{nm}^{-1}$. The

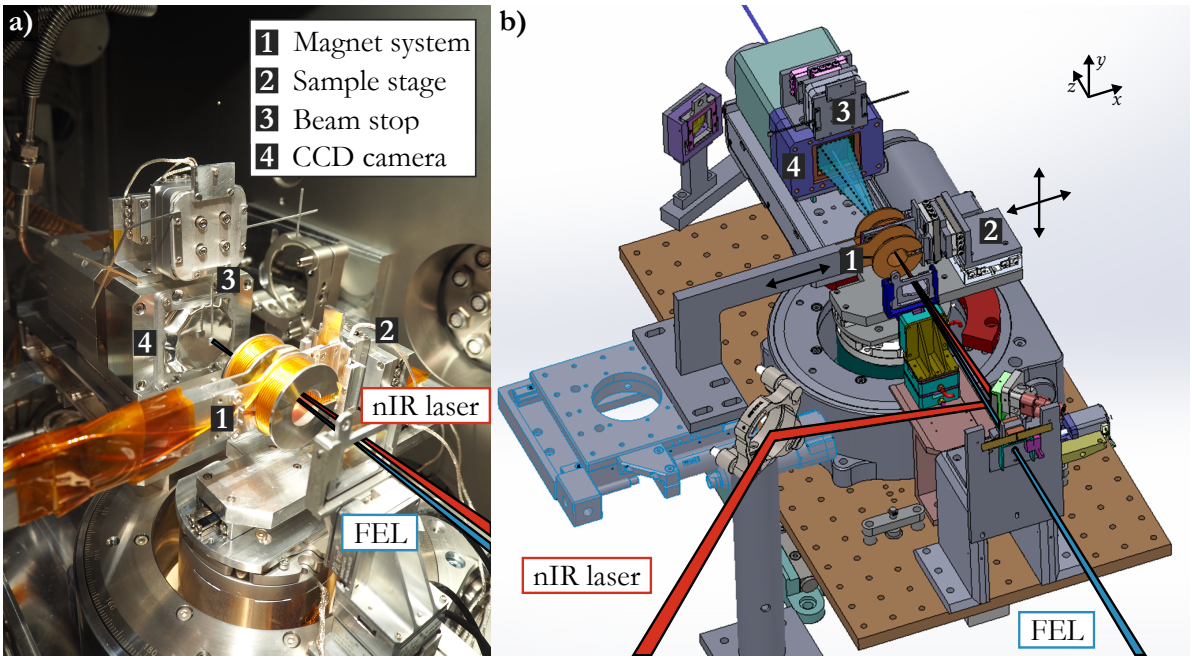

Figure 4.4.: a) Image and b) CAD-drawing of the end station at the DiProI beamline at FERMI@Elettra (with permission from F. Capotondi). The nIR-laser and FEL pulses are guided co-linearly to the sample position, where custom-made Helmholtz coils provide magnetic field pulses of $\mu_0 H_z \leq \pm 50\,\mathrm{mT}$ that are synchronized to the 50 Hz repetition rate of FERMI (**1**). A sample stage, with translational degrees of freedom in x and y-directions, gives access to two different samples (**2**). The scattering intensity is recorded by the same type of CCD camera, that is used in the TR-mSAXS experiment at FLASH (**4**). A cross-shaped beam stop protects the camera from the direct FEL beam (**3**).

experimental geometry was designed such, that the scattering intensity from the $[\mathrm{Co/Pt}]_6$ multilayer with an average domain size of $D_{\mathrm{av}} \approx 220\,\mathrm{nm}$ ($Q_{\mathrm{peak}} = 0.0136\,\mathrm{nm}^{-1}$) is well located on the detector. Note that due to the large magnetic scattering efficiency in this experiment (section 6.3.1), 2-by-2 binning of the pixels was not necessary.

4.3. Imaging of Nanoscopic Multi-Domain States by Fourier-Transform Holography

A new method to image nanoscopic magnetic multi-domain patterns, that could only be realized due to the exceptional coherence properties of synchrotron and FEL radiation, is Fourier-transform holography (FTH). FTH is a far-field lensless microscopy technique with a maximum resolution that is only limited by the wavelength of the used radiation, $d_{\mathrm{res}} = \lambda/2$, known as the Abbe diffraction limit [252]. Conventional Kerr microscopy, using polarized optical laser light, allows to image magnetic multi-domain structures with a spatial resolution down to $\approx 500\,\mathrm{nm}$, as shown in Fig. 3.2 on p. 58. An already improved spatial resolution of (20–

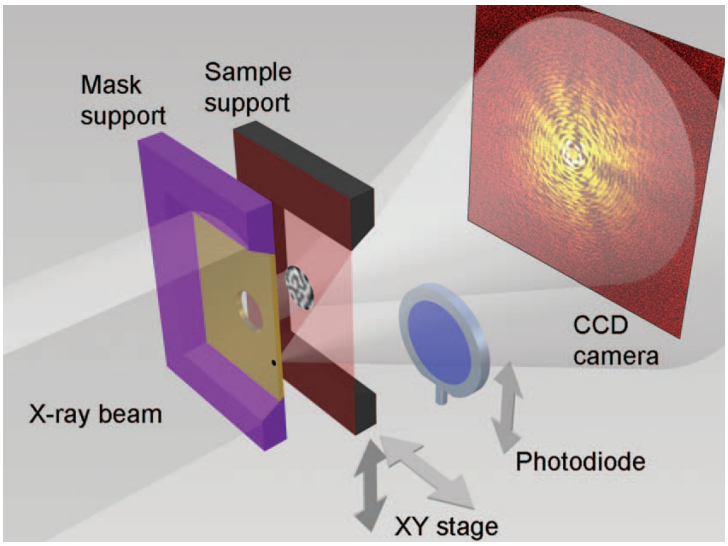

Figure 4.5.: Schematic of the X-ray holographic microscopy (XHM) setup (taken from Ref. [264]). In the XHM setup, sample and holography mask are separated from each other. While the mask is fixed, the sample can be moved perpendicular to the beam direction with high resolution to image different parts of the sample. The holograms are recorded by a CCD camera, similar to the ones used for the TR-mSAXS experiments.

100) nm is achieved by magnetic force microscopy (MFM) and the highest resolution of < 10 nm for imaging magnetic domains currently is reached by, e. g., scanning electron microscopy with polarization analysis (SEMPA), spin-polarized scanning tunneling microscopy (SP-STM), or magnetic transmission electron microscopy (Lorentz-microscopy) [253]. An excellent spatial resolution of sub-50 nm can also be reached by lensless X-ray imaging techniques, such as coherent diffractive imaging (CDI) [254–256], X-ray ptychography [257, 258] or FTH [259–262].

Real-space holographic imaging of a nanoscopic magnetic multi-domain structure was demonstrated in 2004 by S. Eisebitt *et al.* using a $[Co(0.4)/Pt(0.7)]_{50}$ multilayer on Si_3N_4 with an integrated 600 nm-thick Au holography mask on the back side of the membrane [263]. Since then the method has been further explored taking real-space imaging to the ultrafast regime at FEL sources [31, 35] and even use two FEL pulses, that are shifted in energy (*two-color mode* at FERMI), to image the magnetic domain-state in a $[Co(0.6)/Pt(0.8)]_{20}$ multilayer in resonance with both the Co $M_{2,3}$ and the Pt N_7 edge in a single image [38].

Here, an FTH experiment was conducted at the P04 beamline at the synchrotron PETRA III to image nanoscopic multi-domain states of Co/Pt multilayers under the influence of external magnetic fields (section 6.1). For that, the X-ray holographic microscope (XHM) end station, developed at the University of Hamburg [264], was installed at the P04 beamline. The setup was further modified to allow for both FTH and mSAXS experiments during the same beamtime by adjusting the sample–detector distance (see, e. g., Ref. [215]).

The magnetic scattering intensity is given by the squared modulus of the transmitted **E** field. As a consequence, the information on the imaginary part of $\mathbf{E}_T^{\pm}$ in eq. (2.27), i. e., the information on the phase $\exp(-i\delta k_z d)$, is lost, which is known as the phase problem in X-ray crystallography. In FTH, the phase problem is overcome by a special sample design, or a

combination of the magnetic sample with a so-called holography mask, as it is realized in the XHM setup shown in Fig. 4.5. The holography mask is typically an opaque Au film of $\approx 1\,\mu m$ thickness on a Si_3N_4 membrane which is aligned coplanar and in close vicinity to the magnetic sample (transmission geometry). It contains a circular hole of $d_{OH} \approx 2\,\mu m$ in diameter, called the object hole (OH), which defines the field of view in FTH. In addition a point-like reference hole (RH), with a diameter of $d_{RH} \approx 20\,nm \ll d_{OH}$, is milled through both the mask and the magnetic thin film. Even though theoretically a spatial resolution of a few nanometers is possible when using soft or hard X-ray radiation, it is practically limited by the size of the reference hole, d_{RH}. The here used holography masks have been shown to yield a spatial resolution down to $\approx 10\,nm$ [71]. The scattered **E** field from the magnetic object, which experienced a phase shift due to the magneto-optical effects, interferes with the reference **E** field, thereby encoding the phase information. Interference, first, requires the same state of polarization for the transmitted object and reference waves, a prerequisite which is met only by CP X-rays (section 2.4.1).[4] Second, interference requires a coherent illumination of both object and reference hole. The X-ray pulses from a synchrotron source are partially coherent, e. g., at the P04 beamline at PETRA III, partially coherent X-ray pulses with coherent fractions of 90% in vertical and between 4% and 20% in horizontal direction are provided. However, the transverse coherence properties of the X-ray beam can be improved by cutting the beam via an optical aperture, which increases the coherent fraction in horizontal direction above 90% [267].

The resulting interference pattern from the magnetic object and the reference contains both a polarization dependent magnetic, but also a polarization independent charge contribution, described by the total scattering amplitude in eq. (2.35). Upon switching the polarization from RCP to LCP, the charge contribution remains unchanged while the magnetic contribution, based on the XMCD effect, changes its sign. Examples for the different interference patterns using RCP and LCP X-rays, obtained by FTH on a $DyCo_3$ alloy thin film, are shown in Fig. 4.6 a). By subtracting the two (Fig. 4.6 b)), the charge contribution gets canceled out, while the magnetic contribution is enhanced by a factor of two. The so-called difference hologram contains the full information on the magnetic multi-domain pattern in reciprocal space. The magnetic multi-domain state in real space can then be reconstructed by an inverse Fourier transformation. A great advantage of the possibility to spatially separate the sample from the holography mask is the extended accessible area for imaging. By that, larger areas than the $\approx 2\,\mu m$ field of view can be imaged (see Fig. 4.6 c) and d)), which allows to, e. g., investigate magnetic multi-domain states along a direction of varying sample thickness [215, 264].

[4] RCP and LCP X-rays are provided at the P04 beamline at PETRA III [265] or also at the DiProI beamline at FERMI [251], by an advanced planar polarized light emitter or short APPLE II-type undulator. As an undulator with variable polarization is not the standard, alternatively, an X-ray polarizer can be used at facilities that only provide linear polarized X-rays (see Ref. [266]).

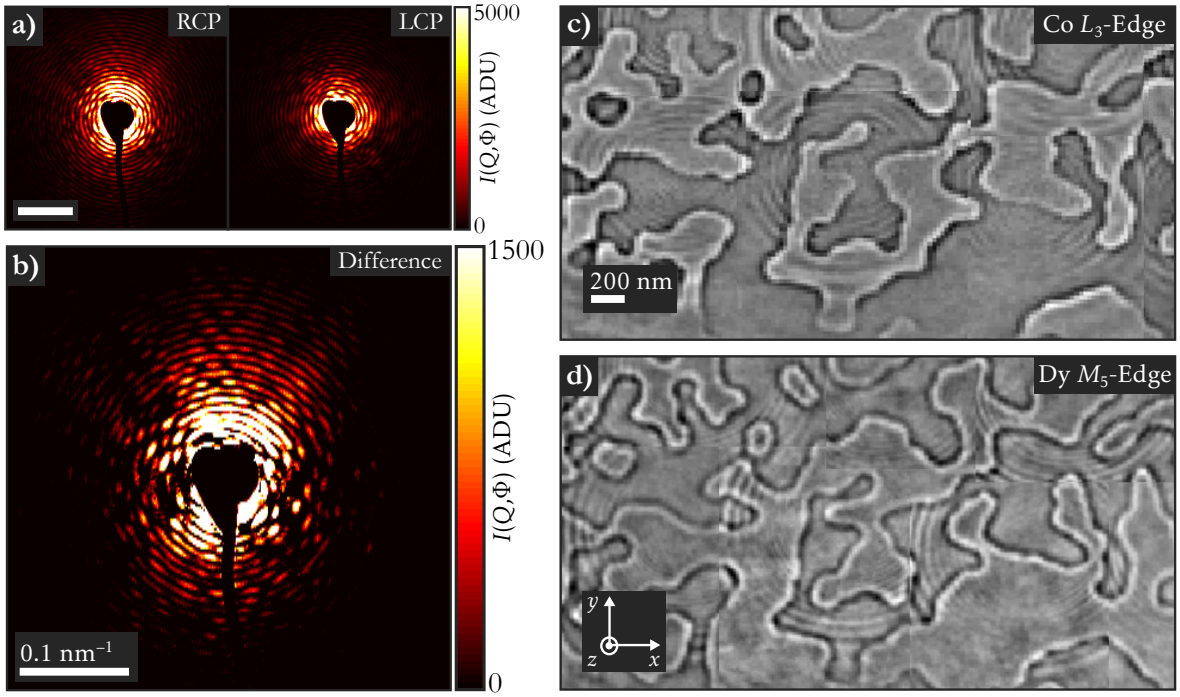

Figure 4.6.: a) Interference patterns obtained by FTH on a 50 nm $DyCo_3$ alloy thin film using RCP and LCP soft X-rays with a photon energy of $E_{ph} = 778.6$ eV (Co L_3 edge). The experiment was conducted at the P04 beamline at PETRA III using the XHM setup. b) Corresponding difference hologram. c) Reconstructed (real-space) magnetic domain structure in $DyCo_3$ obtained via Fourier transformation of the difference hologram. The image shows an extended region, obtained by combining a number of individual reconstructed holograms with a field of view of $\approx 2\,\mu$m. d) The same multi-domain pattern is obtained by FTH in resonance with the Dy M_5 edge at a photon energy of $E_{ph} = 1295$ eV, which shows the strong coupling between the two magnetic sublattices.

Such a $[Co/Pt]_6$-multilayer wedge-sample was used in the pre-study at PETRA III for studying the influence of external magnetic fields on the multi-domain states at different Co/Pt compositions via FTH in tandem with static mSAXS (section 6.1). First, this allowed to identify **H**-field induced modifications in the nanoscopic multi-domain states in the TR-mSAXS experiment at FERMI (section 6.4.2 and section 6.4.3). And second, it allowed for an interpretation of the nIR-laser induced changes of the average domain periodicity, T_{av} and the lateral correlation length, ξ, in real space (section 6.4.3.2). For more details on FTH the reader is referred to Refs. [71, 268–270].

5 Multi-Parameter Study of Ultrafast Demagnetization in Thin Co/Pt Multilayers

In the TR-mSAXS experiment at the BL3 beamline at FLASH in Hamburg, ultrafast demagnetization was investigated in the three particularly thin $[Co/Pt]_x$ multilayers, with $x = 3$, 8 and 6, possessing total film thicknesses of $d = 8.6\,\text{nm}$, $d = 13.2\,\text{nm}$ and $d = 15.2\,\text{nm}$, respectively (see chapter 3). For the first time, ultrafast demagnetization in nanoscopic multi-domain states of such optically thin Co/Pt multilayers was studied by resonant magnetic scattering using highly brilliant FEL pulses.[1]

In ferromagnets, so far, mostly comparably thick films with $d \gtrsim 30\,\text{nm}$ were studied in resonant scattering experiments at FEL sources, e. g., in Refs. [29, 30, 32, 37]. On the one hand, thicker samples are preferable from an experimental point of view, as they typically contain a larger amount of magnetic material and thus provide a large magnetic scattering signal (section 2.4.5). On the other hand, from a physics' and an application point of view, particularly thin films are of interest as, e. g., AOS was found only in few-repetition $[Co/Pt]_x$ multilayers with $x \leq 3$ and a total film thickness of $d < 20\,\text{nm}$ [24]. Using such optically thin samples, i. e., Co/Pt multilayers with a total film thicknesses comparable to the attenuation length of nIR radiation ($\lambda = 800\,\text{nm}$) in Co ($\delta_{Co} \approx 13\,\text{nm}$) and Pt ($\delta_{Pt} \approx 8\,\text{nm}$), ensures a quasi-homogeneous excitation throughout the multilayer structure, allowing for a simple modeling and interpretation of the data.

The ultrafast response of magnetization upon nIR-laser excitation was studied by TR-mSAXS in resonance with the Co $M_{2,3}$ edge ($E_{ph} = 59.8\,\text{eV}$), using various nIR-laser pulse parameters: three fluences of $F^1_{nIR} = 3.8\,\text{mJ/cm}^2$, $F^2_{nIR} = 9.6\,\text{mJ/cm}^2$ and $F^3_{nIR} = 18.9\,\text{mJ/cm}^2$, two pulse durations of $\tau^1_{nIR} = 70\,\text{fs}$ and $\tau^2_{nIR} = 300\,\text{fs}$ as well as linear (LP) and circular (CP) polarization. Through that, important aspects of ultrafast demagnetization, like the possibility of a full demagnetization at non-destructive nIR-laser fluences [131, 146, 182, 183], or its dependence on nIR-laser polarization and pulse duration [12, 187, 204, 272], are addressed.

The chapter starts with an overview of the experimental parameters and a description of the used pulse scheme (section 5.1). Details on how the scattering patterns from TR-mSAXS have to be processed in order to extract the magnetic-scattering contribution (charge-

[1] Note that a few FEL experiments report on ultrafast magnetization dynamics in sub-20 nm GdFeCo thin films, e. g., in Refs. [39, 271].

background subtraction) and to allow for the comparison of scattering patterns at different delay times (normalization), are given in section 5.2. The magnetic scattering patterns are characterized and converted to the magnetization as described in section 5.3 and the results on nIR-laser induced ultrafast magnetization dynamics are presented in section 5.4. As it could be expected, all the three samples show ultrafast demagnetization within a $\approx 100\,\mathrm{fs}$ time scale, followed by a magnetization recovery on a (sub-)picosecond time scale. Distinct differences in the ultrafast magnetization dynamics are observed between the three $[\mathrm{Co/Pt}]_x$ multilayers as well as nIR-laser fluences. When taking the thickness-dependent absorption of nIR light in Co and Pt into account, in a good approximation, the three samples can be treated as different realizations of an optically thin Co/Pt-multilayer system. Important aspects of ultrafast magnetization dynamics at high fluences, i. e., a suppression of the thickness-dependence of the maximum degree of demagnetization and a significantly extended magnetization recovery, are discussed. Following recent theoretical predictions, an analytical expression for the energy equilibration time, τ_E, including the non-linear behavior at high temperatures, is proposed. Aside from the sample thickness and nIR-laser fluence, no dependencies of the ultrafast magnetization dynamics on the nIR-laser polarization and pulse duration are found, in agreement with findings in literature.

5.1. Experimental Parameters and Measurement Procedure

At first, the experimental parameters of the TR-mSAXS experiment at the BL3 beamline at FLASH are presented, starting with the XUV and nIR-laser pulse characteristics in section 5.1.1, followed by an introduction to the measurement procedure, i. e., the multi-pulse nIR-pump–XUV-probe mode, in section 5.1.2.

5.1.1. XUV and nIR-Laser Pulse Characteristics

The ultrafast response of magnetization upon nIR-laser excitation in the three $[\mathrm{Co/Pt}]_x$ multilayers was studied by TR-mSAXS using 60 fs-long linearly polarized XUV pulses tuned to resonance with the Co $M_{2,3}$ edge at a photon energy of $E_\mathrm{ph} = 59.8\,\mathrm{eV}$. The experiment was conducted at the BL3 beamline at FLASH using the costum-made end station described in section 4.2.1.

The FEL-intensity profile was measured by scanning the sample holder, containing a diode with a pinhole, across the FEL beam. The FEL beam size was determined to $d_{x,y} \approx (38 \times 61)\,\mu\mathrm{m}^2$ (FWHM) by fitting a Gaussian function to linecuts through its intensity profile in x and y-directions (Fig. 5.1 a)). Throughout the experiment, the FEL-pulse energy was fluctuating between (35–40) µJ. Up to the end station, the FEL-pulse energy is reduced to 60% [221] due to the beamline optics and is further reduced by two 420 nm thick solid-state

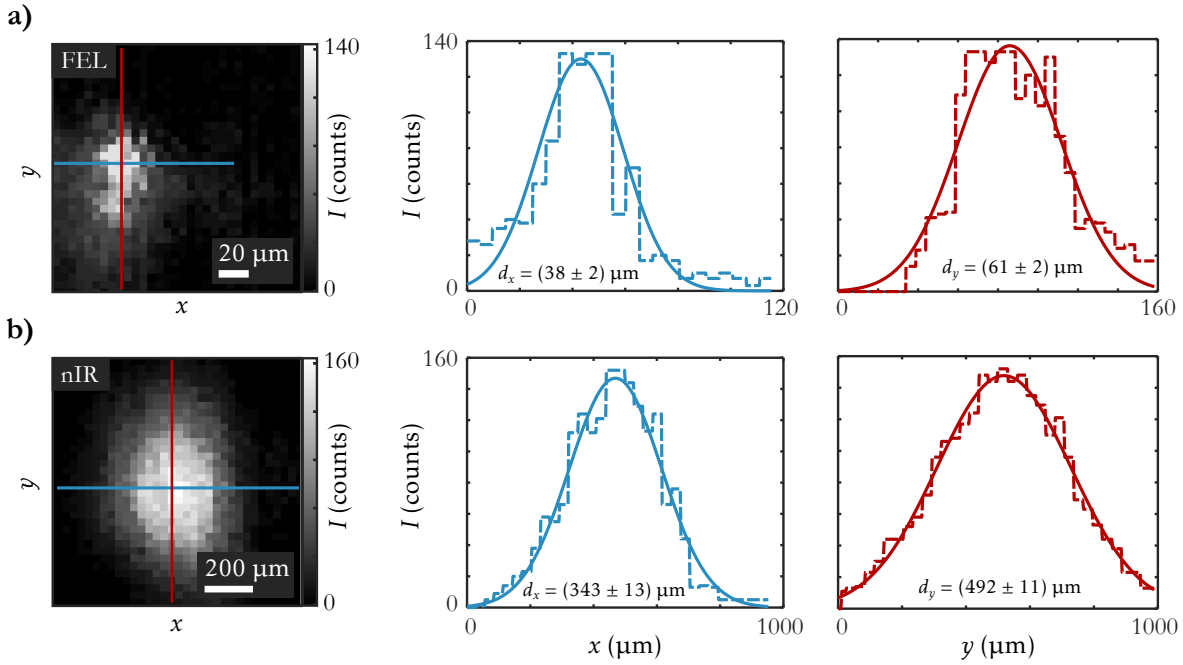

Figure 5.1.: a) FEL and b) nIR-laser pulse profiles measured by scanning the diode (+pinhole) on the sample holder across the respective beams (Fig. 4.3). Beam sizes, $d_{x,y}$, at FWHM are determined by fitting a Gaussian function to linecuts through high-intensity regions along the x (blue) and y-directions (red).

silicon absorbers with a transmission of 30% each. Finally, taking into account the reflectivity of the back-reflecting Laue multilayer mirror of 34% (section 4.2.1), the FEL fluence on the sample has a calculated value of $F_{\mathrm{FEL}} \approx (30\text{–}35)\,\mathrm{mJ/cm^2}$, assuming an elliptically shaped pulse profile. As it can be seen in Fig. 5.1 a), the FEL beam profile shows extended tails in both x and y-directions, leading to a slight overestimation of the FEL fluence.

A homogeneous excitation of the probed area was ensured by using a large nIR-laser beam with respect to the FEL beam. The nIR-laser-intensity profile was obtained analogue to the FEL-intensity profile, i. e., by scanning the diode on the sample holder across the nIR-laser beam (Fig. 5.1 b)). A nIR-laser beam size of $d_{x,y} \approx (343 \times 492)\,\mu\mathrm{m}^2$ (FWHM) was determined by fitting a Gaussian function to linecuts through its intensity profile along the x and y-direction.

The nIR-laser pulses were attenuated by a series of neutral density (ND) filters to 5.0 µJ, 12.7 µJ and 25.0 µJ, resulting in nIR-laser fluences of $F^1_{\mathrm{nIR}} = 3.8\,\mathrm{mJ/cm^2}$, $F^2_{\mathrm{nIR}} = 9.6\,\mathrm{mJ/cm^2}$ and $F^3_{\mathrm{nIR}} = 18.9\,\mathrm{mJ/cm^2}$, respectively, assuming an elliptically shaped pulse profile. The latter was sufficient to fully quench the magnetic scattering intensity in the $[\mathrm{Co/Pt}]_3$-multilayer sample, which was utilized to determine the charge-scattering background (section 5.2.3). For excitation of the magnetic thin films, both circularly (CP) and linearly (LP) polarized nIR-laser pulses with pulse durations of $\tau^1_{\mathrm{nIR}} = 70\,\mathrm{fs}$ and $\tau^2_{\mathrm{nIR}} = 300\,\mathrm{fs}$ were used.

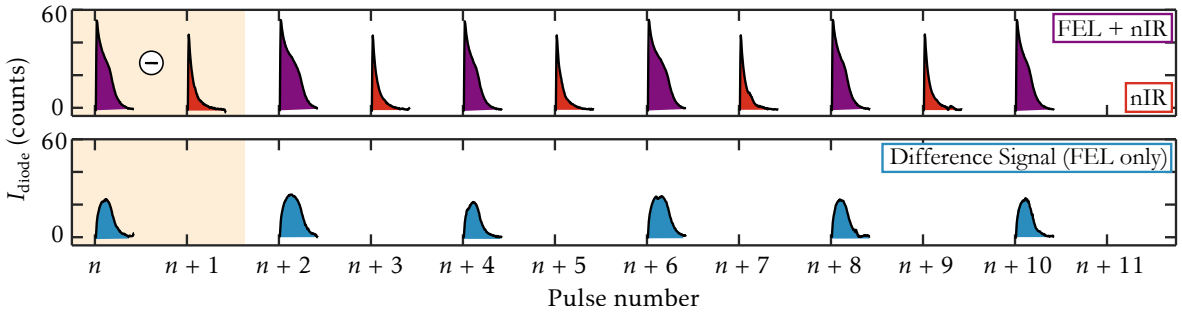

Figure 5.2.: Pulse structure as measured by the photo diode on the beam stop. The FEL probes the magnetic states at a repetition rate of 5 Hz, whereas the nIR laser pumps the samples at a repetition rate of 10 Hz (top panel). Subtracting consecutive nIR-laser (at $n+1$, $n+3$, …) from combined nIR-laser and FEL signals (at n, $n+2$, …) provides a measure for relative intensity fluctuations of the FEL pulses, which can be used for normalization of the scattering data (bottom panel).

5.1.2. Pulse Scheme of the nIR-Pump–XUV-Probe Experiments

For the nIR-pump–XUV-probe experiments, FLASH was operated in the single-bunch mode, providing single FEL pulses at a repetition rate of 10 Hz. The pulse pattern of the experiment, as recorded by the photo diode on the beam stop, is shown in the top panel of Fig. 5.2. Due to technical constraints of the FLASH fast shutter, every second FEL pulse was blocked, limiting the repetition rate of the FEL pulses to 5 Hz. The nIR laser was operated at 10 Hz, so that the photo diode detects the combined FEL+nIR signal and the nIR-only signal in an alternating way. The relative fluctuations of the nIR-only intensity throughout the acquisition of a scattering image (100 pulses) are in the range of only (2–4)%. Therefore, assuming a perfectly stable nIR laser, the upper bound for the error of the photo-diode measurements is $\delta I_{\mathrm{nIR}} \approx 2\%$. A highly stable nIR-laser signal throughout the measurements enables the accurate determination of the FEL-only intensity by subtracting the intermittent nIR-only from the combined FEL+nIR signals, as illustrated in Fig. 5.2. The resulting 100 FEL-only signals of each scattering image are summed-up, providing a high-quality normalization value for the scattering data (section 5.2.2).

The irradiation of the magnetic samples by 100 repetitive nIR-laser (FEL) pulses with a low repetition rate of 10 Hz (5 Hz) is particularly favorable, because it reduces the accumulation of heat in the sample during image acquisition. As TR-mSAXS experiments using FEL pulses with photon energies in the XUV regime have to be conducted in vacuum, the induced heat from the nIR-laser and FEL pulses is mainly dissipated via the sample substrate to the sample holder. As the substrate is a 50 nm-thin isolating Si_3N_4 membrane, only weak heat transport away from the interaction area in the magnetic thin film occurs. Note that an impact of nIR-laser heating on the magnetic scattering distribution, and thus the multi-domain configuration, was only observed for the highest nIR-laser fluence of $F^3_{\mathrm{nIR}} = 18.9\,\mathrm{mJ/cm^2}$ (appendix A.1).

For each sample and set of nIR-laser pulse characteristics (fluence, polarization and pulse duration), high-resolution delay-time scans in the range of $-1.5\,\mathrm{ps} \leq \Delta t \leq 2.5\,\mathrm{ps}$ with a step size of 50 fs, as well as low-resolution delay-time scans in the range of $-5\,\mathrm{ps} \leq \Delta t \leq 50\,\mathrm{ps}$ with a step size of 800 fs were recorded. At each delay point, the nIR-pump–XUV-probe event was repeated 100 times, to ensure statistically significant photon counts on the CCD detector. The resulting image therefore is composed of the accumulated intensity from 100 scattered FEL pulses.

5.2. Data Processing

The scattering intensity in TR-mSAXS experiments is composed of both charge and magnetic-scattering contributions (section 2.4.3) and the scattered intensity furthermore differs for each image, due to the fluctuating FEL-pulse intensity. The raw-data therefore has to be further processed, as outlined in the following sections. In a first step, the scattering images are corrected by dark images and a mask is applied excluding areas of parasitic charge scattering, e. g., high-intensity streaks close to the position of the beam (section 5.2.1). In order to provide comparability within a series of scattering images in the time-resolved measurements, the scattering intensity has to be normalized to the respective FEL intensity, which is shown in section 5.2.2. Finally, the magnetic-scattering contribution is extracted by identifying the charge-scattering background in section 5.2.3.

5.2.1. Masking and Dark Subtraction

The scattering images, $I(Q,\Phi)$, obtained by TR-mSAXS on the maze-domain pattern of the $[Co/Pt]_6$, $[Co/Pt]_8$ and $[Co/Pt]_3$-multilayer samples at a negative delay time of $\Delta t = -1\,\mathrm{ps}$, are shown in Fig. 5.3 a), b) and c), respectively. As expected, the scattering patterns from the disordered maze-domain patterns have the shape of a ring (section 2.4.3). Note that the small radius of the scattering ring of the $[Co/Pt]_3$ multilayer results in a disk-shaped scattering intensity so that a potential fall-off of the magnetic scattering intensity close to $Q = 0$ is shadowed by the beam stop (Fig. 5.3 c)).

Besides the ring-shaped magnetic scattering intensity, the images contain horizontal and vertical high-intensity streaks intersecting at $Q = 0$ (Fig. 5.3 a)–c): Raw). These originate from the charge difference between the membrane window and the thick silicon frame and can be used to determine the position of the direct beam (BC), i. e., $Q = 0$. The streaks, as well as other parasitic charge-scattering contributions, e. g., from neighboring membrane windows, are masked prior to further analysis (Fig. 5.3 a)–c): Masked). The noise level and inhomogeneity of the detector is accounted for by subtracting dark images of the same exposure time as was

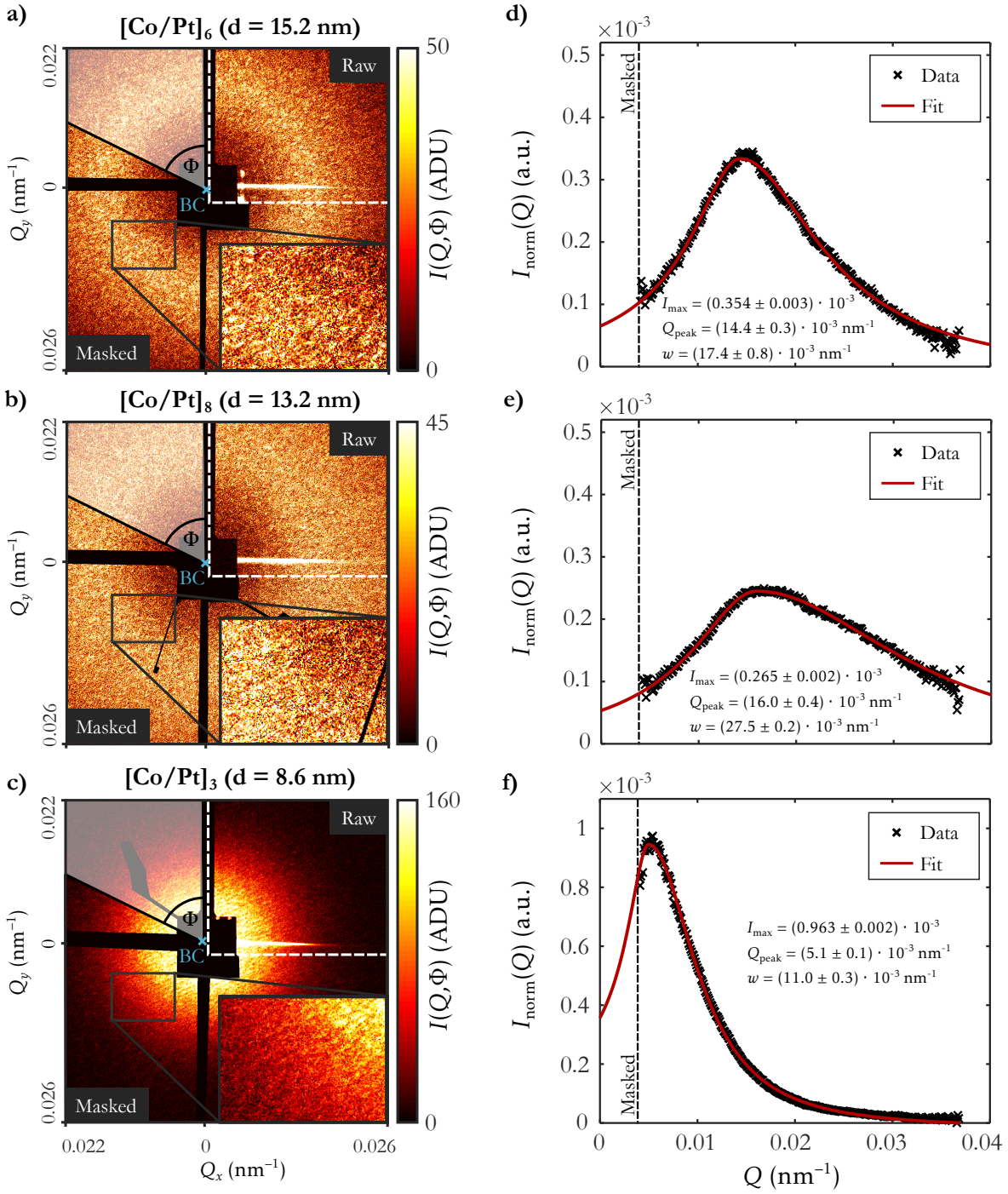

Figure 5.3.: Dark-corrected scattering images of a) the $[Co/Pt]_6$, b) the $[Co/Pt]_8$ and c) the $[Co/Pt]_3$ multilayer obtained at $\Delta t = -1$ ps. Images show the accumulated scattering intensity from 100 FEL-pulse exposures. Parasitic charge scattering, e. g., from membrane edges (Raw) is masked prior to further analysis (Masked). The insets show zoom-ins to the grainy structure of the scattering patterns.
d)–f) Corresponding magnetic-scattering distributions, $I_{norm}(Q)$, after processing the images as described in this section (section 5.2). The $I_{norm}(Q)$ are characterized through fitting with a split Pearson type-VII function (see section 5.3.1).

used for the scattering images, i. e., 21 s (the time needed for 100 pulses at a repetition rate of 5 Hz and a 1 s overhead time).

The $I(Q,\Phi)$ in Fig. 5.3 a)–c) differ in maximum intensity and shape, reflecting magnetic domain configurations with different domain sizes and domain-size distributions, a consequence of the samples' different intrinsic magnetic properties (section 3). The $I(Q,\Phi)$ are azimuthally averaged around the position of the direct beam, $I(Q) = \langle I(Q,\Phi)\rangle_\Phi$, normalized (section 5.2.2) and charge-background corrected (see section 5.2.3). The resulting magnetic scattering distributions, $I_{\mathrm{norm}}(Q)$, are shown in Fig. 5.3 d)–f). The differences in amplitude, I_{max}, peak position, Q_{peak} and width, w, between the three $I_{\mathrm{norm}}(Q)$ are quantified through fitting with a split Pearson type-VII function, as described in section 5.3.1).

5.2.2. Normalization

As outlined in section 4.1.1, the FEL intensity fluctuates from pulse to pulse. These fluctuations were determined from the signal of the photo diode mounted on the beam stop, by subtracting the intermittent nIR-laser signal from the combined FEL+nIR-laser signal, as shown in section 5.1.2. Summing up the FEL-only photo-diode signal from the 100 pulses that contribute to a certain CCD image, yields the respective normalization value. Alternatively, the FEL-pulse energy, I_{pulse}, measured non-invasively by a gas monitor detector (GMD) up-stream in the beamline, can be used for normalization. The relative FEL-pulse fluctuations, measured by the diode ($\Delta I_{\mathrm{diode}}$) and the GMD ($\Delta\langle I_{\mathrm{pulse}}\rangle$) are shown exemplary for three delay-time scans in the top panels of Fig. 5.4 a)–c).

The relative fluctuations of the FEL-pulse intensity throughout the selected delay-time scan of approximately ±25% are presented in the top panel of Fig. 6.7 a). The FEL intensity (average over 100 shots) is relatively stable throughout the delay-time scans, fluctuating by $\approx \pm 10\%$ from its average value of $\approx 37\,\mu$J/pulse. In addition, instabilities in the FEL intensity on second to minute time scales are observed, i. e., drifts of the FEL intensity on the order of $\approx \pm 20\%$, that are counteracted by the FLASH feedback system ($\Delta I_{\mathrm{diode}}$ drifts in the top panels of Fig. 5.4 b) and c)). Overall, the FEL intensity measured by the photo diode at the sample position is well correlated to the FEL intensity measured by the GMD up-stream in the beamline. During the stronger intensity drifts, however, $\Delta I_{\mathrm{diode}}$ shows noticeable stronger fluctuations than $\Delta\langle I_{\mathrm{pulse}}\rangle$, indicating that pointing instabilities lead to additional intensity fluctuations at the sample position presumably, e. g., through clipping of the FEL beam by beamline apertures. For data analysis, the dark-corrected and masked scattering images are azimuthally averaged around the position of the beam, $I(Q) = \langle I(Q,\Phi)\rangle_\Phi$ and normalized to the sum of the corresponding 100 FEL-pulse intensities, as measured by the diode on the beam stop, $I'_{\mathrm{norm}}(Q) = I(Q)/I_{\mathrm{diode}}$ (or by the GMD, $I'_{\mathrm{norm}}(Q) = I(Q)/\langle I_{\mathrm{pulse}}\rangle$). Scattering images for selected delay times, Δt, are shown in Fig. 5.4 d)–f). The integrated normalized scattering

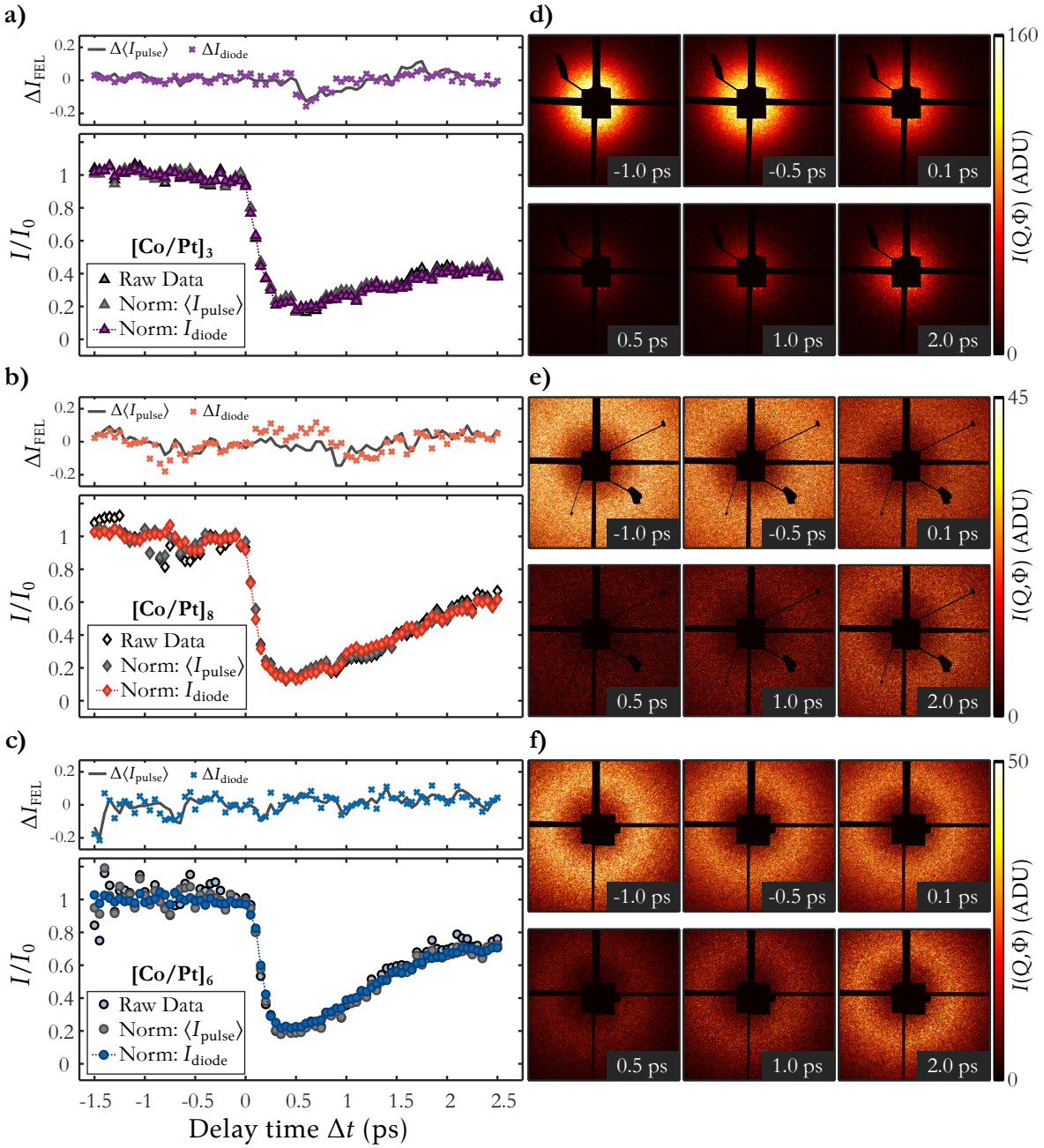

Figure 5.4.: Different ways of normalizing the scattering data obtained by TR-mSAXS at FLASH, exemplary shown for three delay-time scans on a) the $[Co/Pt]_6$, b) the $[Co/Pt]_8$ and c) the $[Co/Pt]_3$ multilayer. a)–c) Relative FEL-intensity fluctuations $\Delta\langle I_{pulse}\rangle$ and ΔI_{diode}, measured by the GMD upstream and the photo diode on the beam stop, respectively (top panel), and their effect on normalizing the raw data, $I_{norm}(\Delta t) = I(\Delta t)/\langle I_{pulse}\rangle$ and $I_{norm}(\Delta t) = I(\Delta t)/I_{diode}$ (main panel). For a direct comparison, both raw and normalized data are related to the corresponding average intensity at negative delay times, $I_0 = \langle I(\Delta t < 0\,\text{ps})\rangle$. d)–f) Corresponding dark-corrected and masked scattering images for selected delay times, Δt.

intensities, $I'_{\mathrm{norm}} = \int I'_{\mathrm{norm}}(Q)\,\mathrm{d}Q$, for all different delay times, Δt, are shown in the main panels of Fig. 5.4 a)–c), together with the corresponding un-normalized data (Raw). For a direct comparison, relative changes in the scattering intensity are shown, i. e., both raw and normalized data are related to the corresponding average intensity at negative delay times, $I_0 = \langle I(\Delta t < 0\,\mathrm{ps})\rangle$. In principle, the GMD as well as the diode at the sample position are valid tools to normalize the scattering data, as both result in improved SNRs in the delay-time scans. The diode signal, however, yields a normalization superior to the GMD signal (see Fig. 5.4 a) and b)), best seen in the delay-time scans for $\Delta t < 0$, hence, is exclusively used for further analysis. The final $I_{\mathrm{norm}}(\Delta t)$ is obtained by subtracting the charge-scattering contribution from the $I'_{\mathrm{norm}}(\Delta t)$ as described in the following section.

5.2.3. Correction for Charge-Scattering Background

In resonant mSAXS experiments, the scattering images are composed of both scattering from charge and magnetic inhomogeneities. To a large extent, the two contributions are spatially separated on the detector in the here presented case, due to the sample properties and the experimental geometry. The Co/Pt-multilayer samples, fabricated by sputtering techniques as described in section 3.1, are polycrystalline with an average grain size of $\approx 10\,\mathrm{nm}$ [82]. The maximum scattering intensity from these periodic charge inhomogeneities lies at a Q-position of $Q_{\mathrm{peak}} \approx 0.6\,\mathrm{nm}^{-1}$. This is well separated from the maximum scattering intensity from the magnetic domain structures, with average domain periodicities of $T_{\mathrm{av}} \approx 400\,\mathrm{nm}$, that lies at $Q_{\mathrm{peak}} \approx 0.016\,\mathrm{nm}^{-1}$.

Further contributions to the scattering intensity might originate from inhomogeneities on larger lengths scales, e. g., a waviness of the membrane. These charge-scattering contributions are thus expected to be largest close to the position of the direct beam ($Q = 0$) and are often modeled by scattering from spheres which have a Q^{-4} + const. scattering dependency (see, e. g., Ref. [270]). This approach, however, is feasible only if the magnetic-scattering contribution is well separated from $Q = 0$. The few-repetition $[\mathrm{Co/Pt}]_x$ multilayers, that were investigated in this thesis, have an $I(Q,\Phi)$ that extends over a large Q-range with substantial contributions at low Q, as shown in Fig. 5.3. A reliable determination of only the charge-scattering contribution through the spherical model is therefore not feasible here. At last, the scattering intensity might contain residual scattering from beamline apertures which not necessarily has a distinct Q-dependence (diffuse nature) and is likely to be different in every experiment, depending on the setup.

Here, an alternative approach is employed to separate the magnetic from the charge-scattering contribution, which does not rely on any modeling. The objective is to directly measure the above mentioned charge-scattering contributions by subjecting the sample to a high nIR-laser fluence that leads to a full quenching of the magnetic scattering signal.

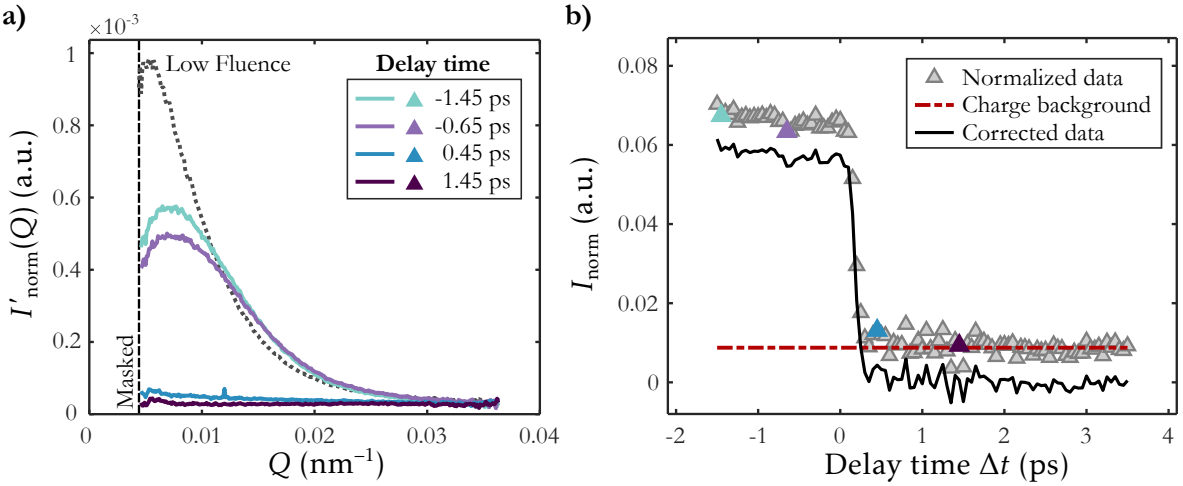

Figure 5.5.: Evaluation of the charge-scattering background by fully quenching the magnetic scattering signal in the thinnest, $[Co/Pt]_3$ multilayer using a nIR-laser fluence of $F^3_{nIR} = 18.9\,mJ/cm^2$. a) Normalized, azimuthally averaged scattering intensity, $I'_{norm}(Q) = \langle I(Q,\Phi)\rangle_\Phi / I_{diode}$, for selected delay times, Δt. The charge-scattering background is identified as the residual scattering intensity at positive delay times. Note that $I'_{norm}(Q)$ has permanently changed as compared to the case of a low-fluence excitation (see appendix A). b) Time evolution of the Q-integrated intensity, $I'_{norm} = \int I'_{norm}(Q)\,dQ$. The normalized data are corrected for the charge-scattering background, which has an integrated value of 0.0088 ($\approx 10\%$ of the scattering signal at negative delay times), yielding the magnetic scattering intensity, $I_{norm}(\Delta t)$.

Consequently, the residual scattering intensity has to be attributed to the charge-scattering background, i. e., to charge and diffuse scattering of various origin. The difficulty of this approach lies on the experimental side. Especially in comparably thick samples with total film thicknesses of $d \approx 30\,nm$, that have widely been used in other FEL experiments (e. g., in Refs. [15, 32, 37]), a complete quenching of the magnetic scattering intensity often cannot be achieved, due to the finite absorption length of nIR-light in Co of $\delta_{Co} \approx 13\,nm$. A full quenching of the magnetic scattering intensity, i. e., also at the rear side of the sample, therefore often requires nIR-laser fluences that exceed the damage threshold of the sample.

Here, the magnetic scattering intensity could be fully quenched in the thinnest, $[Co/Pt]_3$-multilayer sample ($d = 8.6\,nm$), using a high nIR-laser fluence of $F^3_{nIR} = 18.9\,mJ/cm^2$ that was, however, still below the damage threshold. The full quenching of the magnetic scattering intensity is identified, first, by a complete vanishing of the magnetic scattering peak, $I'_{norm}(Q)$, at positive delay times, as it is exemplarily shown for $\Delta t = 0.45\,ps$ and $\Delta t = 1.45\,ps$ in Fig. 5.5 a). And second, the magnetic scattering intensity remains quenched for an extended period of time, showing no signs of a recovery within $\Delta t \lesssim 4\,ps$. Note that TR-mSAXS is sensitive to magnetic inhomogeneities on a particular length scale, covering the maximum scattering intensity from domain structures with $T_{av} \approx (160\text{–}1600)\,nm$ in this experiment. Thus, the here defined full demagnetization does not exclude that either very small ($< 160\,nm$) or very

large (> 1600 nm) magnetic inhomogeneities persist upon strong nIR-laser excitation. While the latter seems rather unlikely in highly disordered magnetic states, the former is subject to current investigations [39, 178, 273].

The residual scattering intensity at $\Delta t \gtrsim 0.5$ ps is attributed to scattering from non-magnetic charge inhomogeneities. As this charge-scattering background has no Q-dependence, it is likely to originate from diffuse scattering from beamline apertures rather than from sample-dependent charge inhomogeneities. As no signs for a Q-dependent charge-scattering background could be detected in the $I'_{\mathrm{norm}}(Q)$ of the other samples, the same Q-independent charge-scattering background was assumed for all measurements.

The delay-time scan shown in Fig. 5.5 b) is obtained by integrating the normalized magnetic scattering distribution over the measured Q range, $I'_{\mathrm{norm}} = \int I'_{\mathrm{norm}}(Q)\,\mathrm{d}Q$, for each delay time, Δt. The resulting $I'_{\mathrm{norm}}(\Delta t)$ (gray triangles) are corrected for the residual charge-scattering background, which has an integrated value of ≈ 0.0088 (red dashed line), yielding the magnetic scattering intensity, $I_{\mathrm{norm}}(\Delta t)$ (black solid line). The relation between the integrated scattering intensity at negative delay times and the charge-scattering background is evaluated to 10.3, 11.8 and 11.8 in the $[\mathrm{Co/Pt}]_6$, $[\mathrm{Co/Pt}]_8$ and $[\mathrm{Co/Pt}]_3$ multilayer, respectively. The charge-scattering background thus accounts for $\approx 10\%$ of the total measured scattering intensity. Note that the remaining slope in $I_{\mathrm{norm}}(\Delta t)$ at negative delay times is presumably due to ongoing structural changes in the maze-domain pattern, resulting in a change of the shape of $I_{\mathrm{norm}}(Q)$ (see appendix A.2). However, these steadily evolving modifications can be well-distinguished from the ultrafast dynamics at $\Delta t \geq 0$. When investigating laser-induced changes in $I_{\mathrm{norm}}(Q)$, i. e., in Q_{peak} and w, on ultrafast time scales, however, the magnetic state should be probed in-between two pump-probe images, in order to be able to identify transient and permanent modifications. The impact of laser heating on the lateral domain configuration in Co/Pt multilayers was studied in the TR-mSAXS experiment at FERMI, where such an alternative reference–pump-probe scheme was employed (chapter 6).

5.3. Characterization of Scattering Patterns

For further analysis, the radial symmetry of the scattering images is taken into account, i. e., the scattering images are azimuthally averaged around the position of the direct beam, reducing the 2D scattering patterns to 1D intensity distributions. In the following section (section 5.3.1), it is shown how these $I_{\mathrm{norm}}(Q)$ are fitted with a phenomenological fit function in order to obtain ensemble averaged information on the domain patterns, i. e., the average domain periodicity, T_{av}, and the lateral correlation length, ξ. In order to check for the comparability of the results from the three samples, the total magnetic scattering intensity, $I_{\mathrm{tot}} = \iint I(Q,\Phi)\,\mathrm{d}Q\,\mathrm{d}\Phi$, is related to the incoming intensity, I_{in}, and compared to the expected scattering efficiency (section 5.3.2).

The integrated values of the magnetic scattering intensities, $I_{\mathrm{norm}} = \int I_{\mathrm{norm}}(Q)\,\mathrm{d}Q$, are finally converted to relative changes in the magnetization, as shown in section 5.3.3.

5.3.1. Fitting of the Magnetic Scattering Distributions

For characterization of the scattering patterns, $I(Q,\Phi)$, the TR-mSAXS data are processed according to the descriptions in the previous sections, i. e., dark-corrected, masked, azimuthally averaged around the position of the direct beam, normalized to the FEL intensity at the sample position and corrected for the charge-scattering contribution. Differences in the processed magnetic scattering distributions, $I_{\mathrm{norm}}(Q)$, of the three $[\mathrm{Co/Pt}]_x$-multilayer samples are quantified by fitting the data with a split Pearson type-VII function, which has been used before to describe magnetic scattering distributions, obtained from mSAXS experiments [32]. The fit function is given by [274]

$$I_{\mathrm{norm}}(Q) = I_{\mathrm{max}}\left(1 + \frac{(Q - Q_{\mathrm{peak}})^2}{m_{1,2}a_{1,2}}\right)^{-m_{1,2}}, \tag{5.1}$$

where I_{max} and Q_{peak} are the amplitude and the peak position of $I_{\mathrm{norm}}(Q)$, respectively. The function is fitted individually to the left (a_1, m_1) and the right (a_2, m_2) tail of $I_{\mathrm{norm}}(Q)$, accounting for its asymmetric shape. The shape of each scattering distribution is reflected by its kurtosis, $m_{1,2}$, and its width, $w_{1,2} = 2a_{1,2}\sqrt{m_{1,2}(2^{1/m_{1,2}} - 1)}$. The resulting fits by eq. (5.1) to the $I_{\mathrm{norm}}(Q)$ of the $[\mathrm{Co/Pt}]_6$, $[\mathrm{Co/Pt}]_8$ and $[\mathrm{Co/Pt}]_3$ multilayers are shown in Fig. 5.3 d)–f) on p. 82.

The corresponding fit parameters are summarized in table 5.1, together with the calculated average domain periodicity, $T_{\mathrm{av}} = 2\pi/Q_{\mathrm{peak}}$, the lateral correlation length, $\xi = 2\pi/w$, as well as the fraction ξ/T_{av}, which is a measure for the degree of order in the domain patterns. With the same total Co amount of $d_{\mathrm{Co}}^{\mathrm{tot}} = 4.8\,\mathrm{nm}$, the $[\mathrm{Co}(0.8)/\mathrm{Pt}(1.4)]_6$ and the $[\mathrm{Co}(0.6)/\mathrm{Pt}(0.8)]_8$ multilayer possess a comparable $I_{\mathrm{norm}}(Q)$ with a relative difference in I_{max} of $< 30\%$ and a relative difference in Q_{peak} of $\approx 10\%$. Hence, both multi-domain patterns possess a comparable average domain periodicity of $T_{\mathrm{av}} = (436 \pm 9)\,\mathrm{nm}$ and $T_{\mathrm{av}} = (390 \pm 10)\,\mathrm{nm}$, respectively. The peak width increases from the $[\mathrm{Co/Pt}]_6$ to the $[\mathrm{Co/Pt}]_8$ multilayer, which is related to a decrease in the lateral correlation length and thus a decrease in the degree of short-range order from $\xi/T_{\mathrm{av}} = 0.83 \pm 0.04$ to $\xi/T_{\mathrm{av}} = 0.58 \pm 0.01$. Note that values of $\xi/T_{\mathrm{av}} < 1$ resemble highly uncorrelated domain patterns, i. e., a short-range order that extends not even over a distance of 1 times the average domain periodicity. These small values for ξ/T_{av} are a consequence of the repetitive FEL-pulse irradiation with a high fluence of $F_{\mathrm{FEL}} = (30\text{–}35)\,\mathrm{mJ/cm^2}$, that presumably causes alterations of the sample structure and thus of $I_{\mathrm{norm}}(Q)$ (appendix A.2). Note that these alterations do not affect the ultrafast magnetization dynamics, as they are completed after a series of FEL-pulse excitations (on the order of 10^3 pulses) and each membrane has been

Table 5.1.: Fit parameters from fitting a split Pearson type-VII function to the scattering distributions, $I_{\mathrm{norm}}(Q)$, from the three $[\mathrm{Co/Pt}]_x$ multilayers. The widths are determined as $w = (w_1 + w_2)/2$ (see text). Additionally included are the calculated average domain periodicities, $T_{\mathrm{av}} = 2\pi/Q_{\mathrm{peak}}$ (eq. (2.37)), the lateral correlation lengths, $\xi = 2\pi/w$ (eq. (2.38)) and the relation ξ/T_{av}, which is a measure for the degree of order in the domain patterns. The width of the $I_{\mathrm{norm}}(Q)$ of the $[\mathrm{Co/Pt}]_3$ multilayer was evaluated by only taking into account the right tail of the distribution, $w = w_2$

	$[\mathrm{Co/Pt}]_6$	$[\mathrm{Co/Pt}]_8$	$[\mathrm{Co/Pt}]_3$
$I_{\mathrm{max}}\,(\times 10^{-3}\,\mathrm{a.u.})$	0.354±0.003	0.265±0.002	0.963±0.002
$Q_{\mathrm{peak}}\,(\times 10^{-3}\,\mathrm{nm}^{-1})$	14.4±0.3	16.0±0.4	5.1±0.1
$a_1\,(\times 10^{-3}\,\mathrm{nm}^{-2})$	6.5±0.7	8.4±0.9	—
$a_2\,(\times 10^{-3}\,\mathrm{nm}^{-2})$	10.0±0.6	18.2±1.4	5.0±0.1
m_1	0.67±0.16	0.71±0.19	—
m_2	0.86±0.12	0.94±0.42	0.98±0.12
$w\,(\times 10^{-3}\,\mathrm{nm}^{-1})$	17.4±0.8	27.5±0.2	11.0±0.3
$T_{\mathrm{av}}\,(\mathrm{nm})$	436±9	393±10	1232±24
$\xi\,(\mathrm{nm})$	361±17	228±2	571±15
ξ/T_{av}	0.83±0.04	0.58±0.01	0.46±0.01

irradiated by a much larger number of FEL pulses before recording a delay-time scan. Note that, in fact, the ultrafast magnetization dynamics is found to be independent on the domain configuration, i. e., the demagnetization time, τ_{M}, is the same for the three multi-domain states (or samples), as discussed in section 5.4.3.

The formation of larger magnetic domains in the $[\mathrm{Co}(1.0)/\mathrm{Pt}(1.2)]_3$ multilayer, with an average periodicity of $T_{\mathrm{av}} = (1230 \pm 24)\,\mathrm{nm}$, can be understood by the reduced amount of Co material of $d_{\mathrm{Co}}^{\mathrm{tot}} = 3.0\,\mathrm{nm}$ (section 2.3). In that case, the Q_{peak} position is located at small radii, so that the $I_{\mathrm{norm}}(Q)$ is not well separated from the beam stop (Fig. 5.3 f) on p. 82). Hence, the scattered intensity from various length scales is accumulated in a comparably small number of pixels, resulting in a relative increase in I_{max} by $\approx 270\%$ as compared to the $[\mathrm{Co/Pt}]_6$ multilayer. As the $I_{\mathrm{norm}}(Q)$ is only partially contained on the detector, only the fit results from the right tail of the intensity distribution are used for further analysis. As it could be expected from imaging micrometer-sized magnetic domain patterns in thin Co/Pt multilayers via Kerr microscopy (Fig. 3.2 on p. 58), the degree of order is further reduced to $\xi/T_{\mathrm{av}} = 0.46 \pm 0.01$ in the $[\mathrm{Co/Pt}]_3$ multilayer, presumably forming a more island-like instead of a maze-like domain pattern.

5.3.2. Comparison of Magnetic Scattering Intensity from the Three Samples

A question that arises is whether the information on the magnetization, i. e., the total magnetic scattering intensity, is still contained in the scattering image of the $[\mathrm{Co/Pt}]_3$ multilayer, even though the shape of $I_{\mathrm{norm}}(Q)$ is skewed. To answer this question, the total magnetic scattering

intensity, $I_{\mathrm{tot}} = \iint I(Q,\Phi)\,\mathrm{d}Q\,\mathrm{d}\Phi$ is related to the incoming FEL intensity and compared to the expected scattering efficiency of the three samples at the Co $M_{2,3}$ edge (section 2.4.5). The summed-up magnetic scattering intensity (in ADU) is divided by 100, the number of FEL pulses per image, and divided by 7, taking into account the ADU-to-photon conversion of the detector at $E_{\mathrm{ph}} = 59.8\,\mathrm{eV}$.[2] The magnetically scattered number of photons from the $[\mathrm{Co/Pt}]_6$, $[\mathrm{Co/Pt}]_8$ and $[\mathrm{Co/Pt}]_3$-multilayer samples are evaluated to $I_{\mathrm{tot}} = 3.4 \cdot 10^4$ photons/pulse, $I_{\mathrm{tot}} = 3.6 \cdot 10^4$ photons/pulse and $I_{\mathrm{tot}} = 4.4 \cdot 10^4$ photons/pulse, respectively. This is to be compared to the incoming number of photons per FEL pulse. A measured FEL-pulse energy of $\approx 40\,\mu\mathrm{J}$ at 59.8 eV corresponds to a total number of incoming photons of $I_{\mathrm{in}} = 4 \cdot 10^{12}$ photons/pulse, which, considering the beamline transmission and absorbers as described in section 5.1.1, relates to an incoming intensity of $I_{\mathrm{in}} \approx 6.7 \cdot 10^{10}$ photons/pulse at the sample position. Taking the ratio $I_{\mathrm{tot}}/I_{\mathrm{in}}$, a comparable magnetic scattering efficiency of $\rho_{\mathrm{RMS}} = (5.1\text{–}6.6) \cdot 10^{-7}$ is found for the three $[\mathrm{Co/Pt}]_x$-multilayer samples which is reduced by a factor of 30–50 as compared to the calculated (maximum) values (see section 2.4.5). However, variations in ρ_{RMS} of $\lesssim 23\%$ are within the calculated variations of $\approx 40\%$. This strongly indicates that the magnetic scattering intensity is largely contained on the detector, i. e., also for the $[\mathrm{Co/Pt}]_3$ multilayer with a skewed $I_{\mathrm{norm}}(Q)$, which allows to compare relative changes in the integrated values I_{norm} between the three samples. How these relative changes in I_{norm} for different delay times, Δt, are translated into relative changes of the magnetization, M_z, is shown in the following.

5.3.3. Conversion of Magnetic Scattering Intensity to the Magnetization

The normalized magnetic scattering intensity, obtained by the procedure described in the previous section 5.2, is translated to a relative change of the z-component of magnetization according to eq. (2.36) via

$$\frac{\Delta M_z}{M_{z,0}} = \sqrt{\frac{I_{\mathrm{norm}}}{I_0}} - 1, \tag{5.2}$$

where I_0 is the average scattering intensity at negative delay times, i. e., $I_0 = \langle I_{\mathrm{norm}}(\Delta t < 0)\rangle$.

The non-linear relation between magnetic scattering intensity, I_{norm}, and magnetization, M_z, has important consequences for the demagnetization data. For a weakly quenched magnetic scattering intensity, i. e., $I_{\mathrm{norm}}/I_0 \approx 1$, small fluctuations in I_{norm} translate to small fluctuations in $\Delta M_z/M_{z,0}$, so that significant changes in $\Delta M_z/M_{z,0}$ can be trusted. In contrast, for a strongly quenched I_{norm}/I_0 also significant changes in $\Delta M_z/M_{z,0}$ could originate from small fluctuations in I_{norm}, i. e., the sensitivity to changes in $\Delta M_z/M_{z,0}$ is reduced. The situation is illustrated for the cases of $I_{\mathrm{norm}}/I_0 = 0.70$ and $I_{\mathrm{norm}}/I_0 = 0.15$ in Fig. 5.6 a).

The experimental error of the degree of demagnetization, $\delta(\Delta M_z/M_{z,0})$, is determined by

[2] The ADU-to-photon conversion factor of the detector at a photon energy of 59.8 eV has been linearly extrapolated from experiments at a higher photon energy.

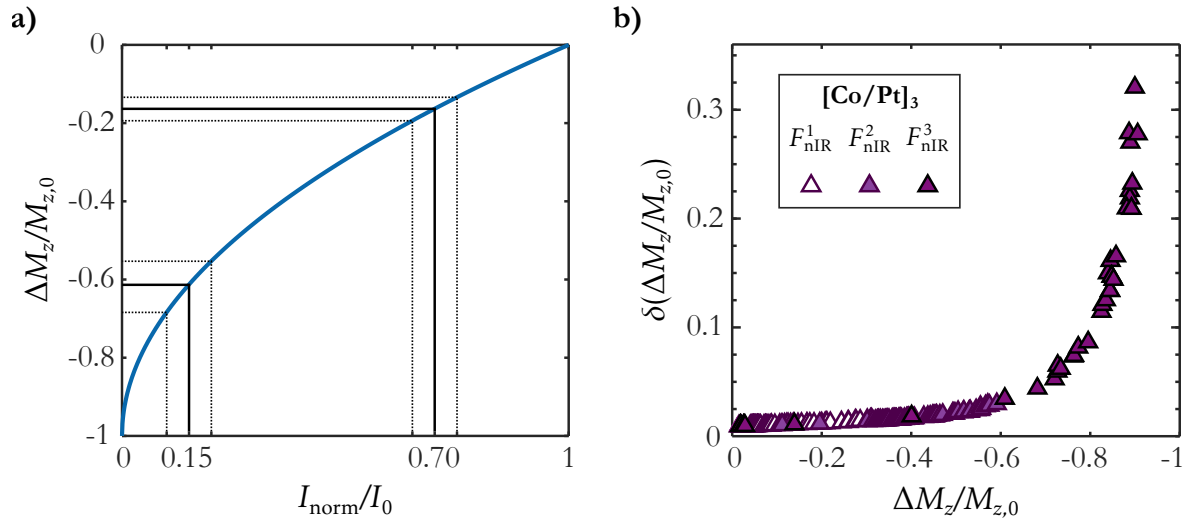

Figure 5.6.: a) Conversion of the magnetic scattering intensity, I_{norm}/I_0, to the relative change of magnetization, $\Delta M_z/M_{z,0}$. Indicated by the black solid lines are two cases of a weakly and a strongly quenched magnetic scattering intensity of $I_{norm}/I_0 \approx 70\%$ and $I_{norm}/I_0 \approx 15\%$, respectively. In the former case, small fluctuations in I_{norm} remain small in $\Delta M_z/M_{z,0}$, while in the latter case the same small fluctuations translate to stronger changes in $\Delta M_z/M_{z,0}$ (dotted lines). Due to this non-linearity, the sensitivity to differences in $\Delta M_z/M_{z,0}$ is significantly reduced for strongly quenched magnetic scattering signals. b) Relative error of the magnetization, $\delta(\Delta M_z/M_{z,0})$, versus the degree of demagnetization, calculated from the three magnetization transients of the $[Co/Pt]_3$ multilayer.

taking into account the individual errors that affect the magnetic scattering intensity, I_{norm}. These are, the error of the total magnetic scattering intensity, δI, with $I = \int \langle I(Q,\Phi)\rangle_\Phi \, dQ$ in number of photons and the error of the normalization value, i. e., the error of the measured FEL-intensity, $\delta I_{FEL} \equiv \delta I_{diode}$. The error of the total magnetic scattering intensity, $\delta I = \delta I_{stat} + \delta I_{scatt}$, stems from the statistical error, evaluated via Poisson statistics, $\delta I_{stat} = \sqrt{I}/I$, and the error of the scattering intensity due to variations in the nIR-laser intensity, $\delta I_{scatt} = \delta I_{diode}$, measured by the same diode as the FEL. From that, the error of the normalized magnetic scattering intensity is evaluated as

$$\delta I_{norm} = \sqrt{\left(\frac{1}{I_{FEL}}\right)^2 \delta I^2 + \left(\frac{I}{I_{FEL}^2}\right)^2 \delta I_{FEL}^2}. \tag{5.3}$$

The statistical error takes small values of $\approx \pm 1\%$ for the unpumped images (large values of I) and increases non-linearly for quenched magnetic scattering intensities (small values of I). While it remains small for quenched magnetic scattering intensities in the delay-time scans using nIR-laser fluences of F^1_{nIR} ($\delta I_{stat} \leq \pm 1.5\%$) and F^2_{nIR} ($\delta I_{stat} \leq \pm 2.5\%$), it diverges for the delay-time scan with a fully quenched magnetic scattering intensity (F^3_{nIR}), taking values of $\delta I_{stat} \approx \pm 30\%$.

The relative error of the FEL and nIR-laser signals, that were measured by the diode on the beam stop, is approximated to $\delta I_{\mathrm{scatt}} = \delta I_{\mathrm{FEL}} \approx 2\%$ (section 5.1.2). Thereafter, the relative error of the normalized magnetic scattering intensity is ±(3–4.5)% and reaches up to ±32% in the delay-time scan with a fully quenched magnetic scattering signal.

The error of the magnetization, $\delta(\Delta M_z/M_{z,0})$, is evaluated by error propagation according to

$$\delta\left(\frac{\Delta M_z}{M_{z,0}}\right) = \frac{1}{2\sqrt{I_{\mathrm{norm}}/I_0}}\delta I_{\mathrm{norm}}. \tag{5.4}$$

The non-linear relation between the error of the magnetization and the degree of demagnetization is shown in Fig. 5.6 b). The error is calculated for the $[\mathrm{Co/Pt}]_3$ multilayer according to the above descriptions, where the whole range of degrees of demagnetization between 0 and −1 are reached by nIR-laser excitations with fluences of F^1_{nIR}, F^2_{nIR} and F^3_{nIR}. The error of the magnetization only slightly increases with the degree of demagnetization up to a $-\Delta M_z/M_{z,0} \approx 60\%$ and then rapidly diverges when approaching full demagnetization. In the following, for the sake of clarity, error bars are shown exemplarily and only if their size exceeds the data-point size.

5.4. Experimental Results

The scattering data from the TR-mSAXS experiment at FLASH are processed according to the descriptions in section 5.2 and converted to transient changes in the magnetization, as described in section 5.3.3. The resulting magnetization transients, obtained by exciting the multi-domain states of the three Co/Pt multilayers by 70 fs-short LP nIR-laser pulses with fluences of $F^1_{\mathrm{nIR}} = 3.8\,\mathrm{mJ/cm^2}$, $F^2_{\mathrm{nIR}} = 9.6\,\mathrm{mJ/cm^2}$ and $F^3_{\mathrm{nIR}} = 18.9\,\mathrm{mJ/cm^2}$, are presented in Fig. 5.7.[3]

As a first observation, all three samples undergo type-I ultrafast demagnetization, i. e., a one-step demagnetization that reaches its maximum well within the first ≈ 500 fs (section 2.5.1.3). For the lowest fluence (open symbols), a pronounced fast-recovery of magnetization within a comparable time scale of $\tau_{\mathrm{E}} \lesssim 1$ ps is observed in the three samples, that starts slowing down for the higher fluence (filled symbols) and completely vanishes for the highest fluence (dark filled triangles). Hence, the data in principle show the expected fluence dependence of ultrafast demagnetization, as described in detail in section 2.5.1.5.

For the highest fluence, F^3_{nIR}, full demagnetization, i. e., the complete loss of magnetic order in the multi-domain states on the observable length scale of $T_{\mathrm{av}} \approx (160\text{–}1600)\,\mathrm{nm}$, is reached (see Fig. 5.5 a)). Note that the SNR is strongly reduced and the experimental error is

[3] The same set of data was obtained for CP nIR-laser pulses. No noticeable differences are observed in the ultrafast magnetization dynamics using LP and CP. Thus, the following discussions are mainly focused on the data using LP nIR-laser excitation. A comparison to the data using CP pump pulses is given in section 5.4.5.

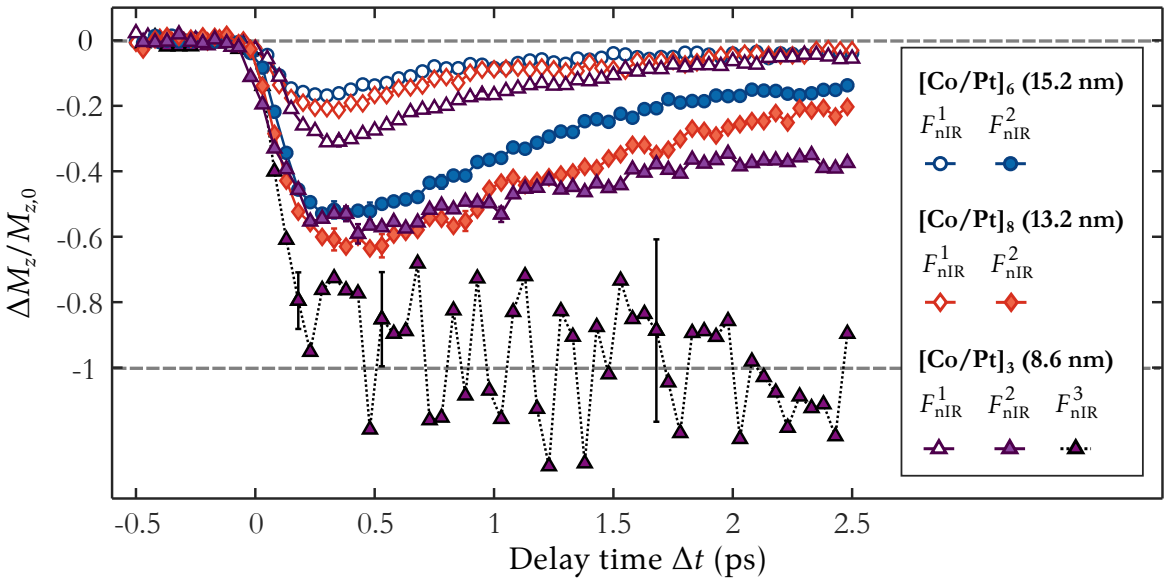

Figure 5.7.: Magnetization transients, $\Delta M_z(\Delta t)/M_{z,0}$, of the $[Co/Pt]_6$ (blue circles), $[Co/Pt]_8$ (red diamonds) and $[Co/Pt]_3$ multilayer (purple triangles), obtained by using LP nIR-laser pulses with a pulse duration of $\tau^1_{\mathrm{nIR}} = 70\,\mathrm{fs}$ and fluences of $F^1_{\mathrm{nIR}} = 3.8\,\mathrm{mJ/cm^2}$ (open symbols), $F^2_{\mathrm{nIR}} = 9.6\,\mathrm{mJ/cm^2}$ (filled symbols) and $F^3_{\mathrm{nIR}} = 18.9\,\mathrm{mJ/cm^2}$ (dark purple triangles). The experimental error is exemplarily shown for those data where it exceeds the size of the data points.

significantly increased in that case ($I_{\mathrm{norm}} \approx 0$), due to the square root relation between the magnetic scattering intensity and the magnetization (section 5.3.3).

Prominent differences in the magnetization transients in Fig. 5.7 are the different maximum degrees of demagnetization, $-\Delta M_z^{\mathrm{max}}/M_{z,0}$, that increase with nIR-laser fluence. For the lowest fluence, $F^1_{\mathrm{nIR}} = 3.8\,\mathrm{mJ/cm^2}$, an increasing $-\Delta M_z^{\mathrm{max}}/M_{z,0}$ is furthermore observed from the thickest, $[Co/Pt]_6$ (open blue circles), to the thinnest, $[Co/Pt]_3$ multilayer (open purple triangles). These sample-dependent differences, however, are not persisting for the higher fluence of $F^2_{\mathrm{nIR}} = 9.6\,\mathrm{mJ/cm^2}$. As this TR-mSAXS study is the first to address ultrafast demagnetization in optically thin Co/Pt multilayers by highly brilliant FEL pulses, the fluence dependence of the maximum degree of demagnetization, $-\Delta M_z^{\mathrm{max}}/M_{z,0}$, is compared to reported literature values, where conventional TR-MOKE was used to measure the magnetization dynamics (section 5.4.1).

For a quantitative analysis of the ultrafast magnetization dynamics, described via the demagnetization time, τ_{M}, and the remagnetization or energy equilibration time, τ_{E}, the magnetization transients are fitted by a phenomenological fit function that is based on the three temperature model (3TM) (section 5.4.2). From the fits, the corresponding amplitudes A_1 and A_2 are obtained, which can be interpreted as effective spin-temperature rises on the femto and picosecond time scale, respectively. The temperature dependence of the demagnetization time, τ_{M}, is discussed in section 5.4.3.

Further prominent differences between the magnetization transients in Fig. 5.7 are observed in the remagnetization dynamics, τ_E. Within the first ≈ 2 ps the magnetization has almost fully recovered in all the three samples for the lowest fluence (open symbols). For the higher fluence (filled symbols), the samples remain demagnetized by a few 10% while the initial magnetization recovery on a picosecond time scale completely vanishes in the fully demagnetized $[Co/Pt]_3$ multilayer (dark purple triangles). After the first few picoseconds after laser excitation, the electron, spin and phonon system reach thermal equilibrium and thus can be described by a single equilibrium temperature, T. The equilibrium temperature rise, ΔT, is calculated from the absorbed laser intensity, considering the total heat capacity ($C_\ell + C_s + C_e$) and taking into account the finite attenuation length of nIR light of $\delta_{Co} \approx 13$ nm in Co and $\delta_{Pt} \approx 8$ nm in Pt. It is shown in section 5.4.2 that T scales linearly with A_2. Hence, in a good approximation, the three samples can be treated as one Co/Pt-multilayer system when taking into account the different individual layer compositions allowing to describe the temperature dependence of the remagnetization dynamics, $\tau_E(T)$, by an analytical expression (section 5.4.4).

Aside from the different nIR-laser fluences, the three samples were subjected to nIR-laser pulses with linear (LP) and circular polarization (CP) as well as a pulse durations of $\tau^1_{nIR} = 70$ fs and $\tau^2_{nIR} = 300$ fs. The polarization and pulse-duration dependence of ultrafast magnetization dynamics are discussed in section 5.4.5.

5.4.1. Fluence Dependence of Demagnetization

Up to three different nIR-laser fluences, $F^1_{nIR} = 3.8\,mJ/cm^2$, $F^2_{nIR} = 9.6\,mJ/cm^2$ and $F^3_{nIR} = 18.9\,mJ/cm^2$, were used to excite the magnetic multi-domain states of the three Co/Pt multilayers with total film thicknesses of $d = (8.6–15.2)$ nm. The maximum degrees of demagnetization, $-\Delta M_z^{max}/M_{z,0}$, extracted from the above shown magnetization transients (Fig. 5.7), are presented in Fig. 5.8, alongside reported literature values. First, the fluence dependence of $-\Delta M_z^{max}/M_{z,0}$ in the thinnest of the three samples is discussed, as only for the $[Co/Pt]_3$ multilayer delay-time scans could be recorded for all the three fluences during the beamtime. Its fluence dependence relative to the thicker $[Co/Pt]_8$ and $[Co/Pt]_6$ multilayers is addressed thereafter.

5.4.1.1. Thin-Film Behavior

The $[Co/Pt]_3$ multilayer shows an already substantial $-\Delta M_z^{max}/M_{z,0} = (31 \pm 1)\%$ for F^1_{nIR} that increases almost linearly with fluence to $(59 \pm 3)\%$ for F^2_{nIR} and $100^{+0}_{-32}\%$ (full demagnetization) for F^3_{nIR}. A strongly increasing $-\Delta M_z^{max}/M_{z,0}$ with laser fluence can be expected in optically thin magnetic films with a total film thickness below the attenuation length of nIR light of $\delta_{Co} \approx 13$ nm in Co (section 2.5.1.6). Such thin films are *quasi*-homogeneously excited along

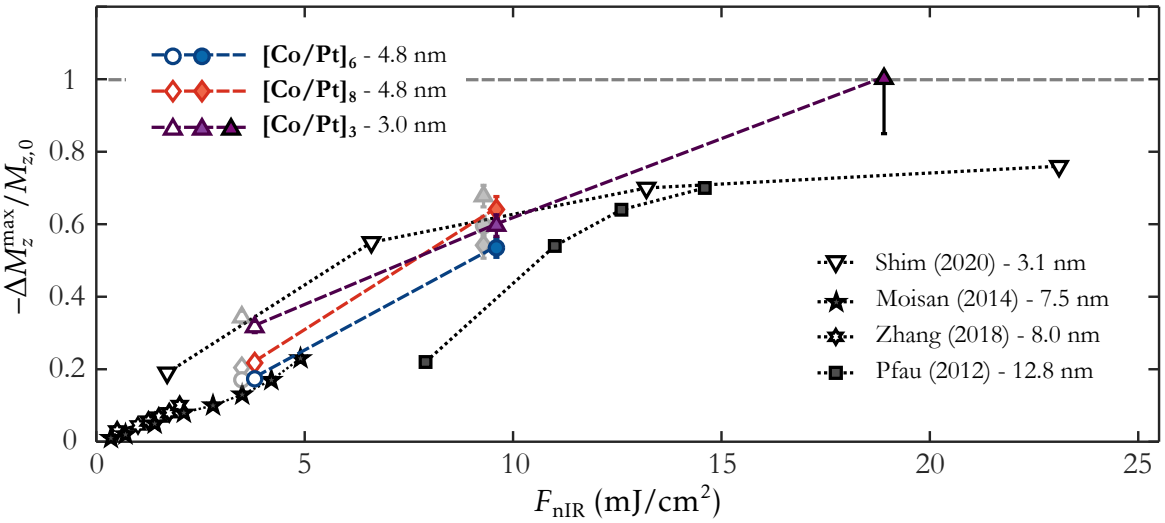

Figure 5.8.: Fluence dependence of the maximum degree of demagnetization, $-\Delta M_z^{\max}/M_{z,0}$, in the $[Co/Pt]_6$ (blue), $[Co/Pt]_8$ (red) and $[Co/Pt]_3$ multilayer (purple). Data obtained by CP nIR-laser excitation are shown as blurred gray data points, slightly shifted in fluence for clarity. Selected literature values on various Co/Pt multilayers are included for comparison, namely the results from J. H. Shim (2020) on a $[Co(0.62)/Pt(0.77)]_5$ [146], N. Moisan (2014) on a $[Co(0.5)/Pt(1.0)]_{15}$ [135], W. Zhang (2018) on a $[Co(0.4)/Pt(0.7)]_{20}$ [137] and B. Pfau (2012) on a $[Co(0.8)/Pt(1.4)]_{16}$ multilayer [32]. Numbers in nanometer are the samples' total Co-layer thicknesses.

the multilayer structure and full demagnetization can be expected at a fluence that induces a temperature rise at the surface of $\Delta T_{\text{pump}}/T_C \approx 1$ [182].

The here-obtained data on $-\Delta M_z^{\max}/M_{z,0}$ are set in context to the results from J. H. Shim *et al.*, who studied ultrafast demagnetization in a very similar $[Co(0.62)/Pt(0.77)]_5$ multilayer with the same total Co-layer thickness and for fluences of $F_{\text{nIR}} = (1.7\text{–}23.1)\,\text{mJ/cm}^2$, using TR-MOKE [146]. Their results, shown in Fig. 5.8 as open black triangles, follow a comparable trend for the two lower fluences, i. e., they find a $-\Delta M_z^{\max}/M_{z,0} = 19\%$ for $F_{\text{nIR}} = 1.7\,\text{mJ/cm}^2$ that increases to 55% for $F_{\text{nIR}} = 6.6\,\text{mJ/cm}^2$.

For high fluences, differences are observed between TR-MOKE and TR-mSAXS data. A saturated $-\Delta M_z^{\max}/M_{z,0} \approx 76\%$ is reported in Ref. [146] for fluences of $F_{\text{nIR}} \gtrsim 10\,\text{mJ/cm}^2$, whereas here, full demagnetization is reached for $F_{\text{nIR}} \leq 18.9\,\text{mJ/cm}^2$. A non-linear relation between $-\Delta M_z^{\max}/M_{z,0}$ and laser fluence in the high-fluence regime is a phenomenon that is typically observed in thicker samples (see section 2.5.1.6), e. g., in a $CoPt_3$ alloy thin film with $d = 48.4\,\text{nm}$ [131] or a Ni thin film with $d = 30\,\text{nm}$ [183]. For comparison, the results from a previous collaborative TR-mSAXS experiment on a relatively thick Co/Pt multilayer ($d = 40.8\,\text{nm}$) are included in Fig. 5.8 as filled squares [32]. In that case, only a relatively small $-\Delta M_z^{\max}/M_{z,0} \approx 20\%$ was obtained for $F_{\text{nIR}} = 7.9\,\text{mJ/cm}^2$ and signs for a starting saturation were observed around $F_{\text{nIR}} \approx (12.6\text{–}14.6)\,\text{mJ/cm}^2$.

Differences in the maximum degrees of demagnetization between the $[Co/Pt]_3$ and $[Co/Pt]_5$ multilayer at high fluences cannot be explained by this thickness dependence, as their total film thicknesses are almost identical. A first possible explanation refers to their different sample structures. According to the simulations in Ref. [182], where heat dissipation along the sample z-direction was included in the M3TM, a $-\Delta M_z^{\max}/M_{z,0} < 100\%$ is predicted also for thin films with $d < 10\,\text{nm}$, if they are fabricated on thermally conducting substrates. The larger maximum degree of demagnetization in this experiment might thus be due to the fact that the $[Co/Pt]_3$ multilayer was fabricated on a 50 nm-thin isolating Si_3N_4 membrane, whereas the $[Co/Pt]_5$ multilayer in Ref. [146] was fabricated on a thick Si substrate.

A second possible explanation lies in the two different methods, i. e., TR-MOKE and TR-mSAXS. While TR-MOKE measures the macroscopic magnetization, typically in an external field stronger than the saturation field, TR-mSAXS provides access to the nanoscopic magnetization distribution, here, to the scattered intensity from magnetic structures with average domain periodicities in the range of $T_{\text{av}} \approx (160\text{–}1600)\,\text{nm}$. Hence, differences might exist in the obtained results from the two techniques. Those could originate from the presence of the external field in TR-MOKE measurements, that might suppress large degrees of disorder in the magnetic state, or the existence of very small (few-10 nm) or very large (few micrometer) magnetic structures in the disordered state, that are detected by the one but not by the other technique. While the formation of large magnetically ordered structures is unlikely in highly disordered magnetic states, the formation of few-nanometer sized magnetic structures upon high-fluence nIR-laser excitation are subject of current investigations [39, 177, 178, 273]. They might play an important role for the observed slowing down of the magnetization recovery which is discussed in section 5.4.4. By choosing a different experimental geometry, TR-mSAXS experiments can be set up to specifically address ultrafast dynamics in this interesting regime of sub-100 nm magnetic length scales (see, e. g., Ref. [39]). In a collaborative TR-mSAXS experiment at the SCS beamline at EuXFEL, signatures for such nanometer-scale magnetic fluctuations on ultrafast time scales have been observed in a comparable Co/Pt multilayer [273].

5.4.1.2. Sample-Dependent Differences

In general, the thicker $[Co/Pt]_8$ and $[Co/Pt]_6$ multilayers show a comparably steep increase of $-\Delta M_z^{\max}/M_{z,0}$ with fluence as the thinner $[Co/Pt]_3$ multilayer (Fig. 5.8). Sample or thickness-dependent differences can be observed for both low and high-fluence excitation, as detailed in the following.

For the lowest fluence, the maximum degree of demagnetization decreases with increasing total layer thickness from $(31 \pm 1)\%$ in the $[Co/Pt]_3$, $(21 \pm 1)\%$ in the $[Co/Pt]_8$ to $(16 \pm 1)\%$ in the $[Co/Pt]_6$ multilayer (see open symbols in Fig. 5.8). Note that the same results are obtained within the experimental error when using CP nIR-laser excitation (open gray data points). As

discussed in the previous section, the results from the $[Co/Pt]_3$ multilayer with $d = 8.6\,nm$ are in good agreement with the results from a $[Co/Pt]_5$ multilayer with $d = 7.0\,nm$ in Ref. [146]. The reduced $-\Delta M_z^{max}/M_{z,0}$ in the thicker samples is in qualitative agreement with the thickness dependence of ultrafast demagnetization (see section 2.5.1.6), which can be understood from the exponentially decaying nIR-laser intensity with a finite attenuation length of $\delta_{Co} \approx 13\,nm$ and $\delta_{Pt} \approx 8\,nm$. In thicker samples, the laser heats the multilayer *non-homogeneously*, i. e., the front sides are excited much stronger than the rear sides, which results in a temperature and thus a magnetization profile along the multilayer stack. A comparison to reported literature values in Fig. 5.8 shows that the fluence dependence of $-\Delta M_z^{max}/M_{z,0}$ in the $[Co/Pt]_8$ and $[Co/Pt]_6$ multilayers is in better agreement with the data from N. Moisan *et al.* on a $[Co/Pt]_{15}$ mulitlayer with a total film thickness of $d = 22\,nm$ [135].

For the higher nIR-laser fluence, F^2_{nIR}, the maximum degree of demagnetization increases by a factor of 3.3 to $(53 \pm 2)\%$ in the $[Co/Pt]_6$, by a factor of 3.0 to $(64 \pm 4)\%$ in the $[Co/Pt]_8$ but only by a factor of 1.9 to $(59 \pm 3)\%$ in the $[Co/Pt]_3$ multilayer, i. e., the fluence-dependent increase of $-\Delta M_z^{max}/M_{z,0}$ seems to be suppressed in the thinnest sample. Note that the larger the maximum degree of demagnetization, the less sensitive is TR-mSAXS to differences in $-\Delta M_z^{max}/M_{z,0}$ (eq. (5.2)) and the larger is the experimental error ($\approx \pm(2\text{–}4)\%$). When repeating the experiments with CP nIR-laser pulses (filled gray data points), the reduced sensitivity is evidenced by differences in the maximum degree of demagnetization of $\lesssim 8\%$. However, the comparably large difference in $-\Delta M_z^{max}/M_{z,0} \approx (15 \pm 1)\%$ between the thickest and the thinnest sample observed for F^1_{nIR}, suggests a physical origin for the suppression at F^2_{nIR} which is discussed in the following.

As it will be shown in section 5.4.2.3, the three samples that were excited by up to three different fluences can be treated, in a good approximation, as one Co/Pt-multilayer system that reaches different temperatures. When considering the temperature dependence of spontaneous magnetization, $M \propto T_s^{3/2}$ and even $M \propto T_s^{5/2}$ at high temperatures [65, 275], a spin temperature close to the Curie temperature, i. e., $T_s/T_C \gtrsim 0.95$, can be expected for a $-\Delta M_z^{max}/M_{z,0} \approx 0.6$, i. e., the system is already within $\approx 50\,K$ to T_C. Close to the ferro-to-paramagnetic phase transition, the ultrafast magnetization dynamics were found to be governed by critical phenomena, such as the divergence of the spin specific heat (see section 2.5.1.5). Note that theoretically, $C_s(T)$ should be divergent only for $T_s/T_C > 0.9995$, a criterion which could be weakened in experiments due to residual external magnetic fields [180]. From that, a saturation of the maximum degree of demagnetization at the higher fluence could be understood from a divergent $C_s(T)$, which would allow to store an increasing amount of energy in the spin system without inducing a significant further increase in $-\Delta M_z^{max}/M_{z,0}$. Moreover, A. Manchon *et al.* derived an electron–spin relaxation rate that scales with the cube of the magnetic order parameter, $G_{es} \propto M(T_s)^3$, becoming vanishingly small close to the critical point T_C [180]. Thus, not only an increased thermal reservoir in the spin system (divergent $C_s(T)$), but also a reduced

energy transfer from the laser excited electrons to the spin system ($G_{es} \approx 0$) might contribute to a suppression of the increase in $-\Delta M_z^{max}/M_{z,0}$ at high fluences (or temperatures).

Further indications for the presence of critical phenomena in the $[Co/Pt]_3$ multilayer using F_{nIR}^2, are found in a slowing down of the remagnetization dynamics. This *critical slowing down* can be modeled by including a divergent spin specific heat, $C_s(T)$, in the description of the temperature dependence of the energy equilibration time, $\tau_E(T)$, as shown in section 5.4.4.

5.4.2. Modeling of Ultrafast Magnetization Dynamics

For a quantification of the involved time scales in the ultrafast magnetization dynamics, τ_M and τ_E, the magnetization transients of the three Co/Pt multilayers are fitted by a phenomenological fit function (section 5.4.2.1). The fit results show that the maximum degrees of demagnetization can be interpreted as non-equilibrium temperature rises in the electron–spin system, given by the fit parameter $A_1 \propto -\Delta M_z^{max}/M_{z,0}$ (section 5.4.2.2). An absolute (equilibrium) temperature, T, is evaluated in section 5.4.2.3, by calculating the layer-dependent absorption of the nIR-laser intensity for the three Co/Pt multilayers, which is found to be well-correlated to the fitted equilibrium temperature rise in the electron–spin system, A_2. Through that, the three different samples, that were excited by up to three different fluences, can be treated as one Co/Pt-multilayer system that reaches different equilibrium temperatures. The dependence of the demagnetization time, τ_M, on the maximum degree of demagnetization, $-\Delta M_z^{max}/M_{z,0} \propto A_1$, and the dependence of the energy equilibration time, τ_E, on the equilibrium temperature, $T \propto A_2$, are discussed in section 5.4.3 and section 5.4.4, respectively. The influence of the nIR-laser pulse polarization (CP and LP) and pulse duration ($\tau_{nIR}^1 = 70\,fs$ and $\tau_{nIR}^2 = 300\,fs$) on the magnetization dynamics is discussed in section 5.4.5.

5.4.2.1. Fitting of Magnetization Transients

Differences in the magnetization transients of the three Co/Pt multilayers (Fig. 5.7 on p. 93) are quantified by fitting the data with the analytical solution of the 3TM (section 2.5.1.1). The fit function is obtained from eq. (2.52), by assuming a linear relation between the magnetization and the spin temperature, i. e., by linearization of the M vs. T curve (see Fig. 2.11 c) on p. 35). The effective spin-temperature rise after equilibration of the electron and spin system on a 100 fs time scale, $\Delta T_1'$, and the effective spin-temperature rise after equilibration of the electron, spin and phonon system on a picosecond timescale, ΔT_2, are expressed by the fit parameters A_1 and A_2 in arbitrary units, respectively. The final fit function is obtained by including a

phenomenological heat diffusion term to account for the slow recovery of magnetization

$$\frac{\Delta M_z(\Delta t-\delta t)}{M_{z,0}} = \Bigg\{\Theta(\Delta t-\delta t)\Bigg[\underbrace{\frac{A_1\tau_\mathrm{E}-A_2\tau_\mathrm{M}}{\tau_\mathrm{E}-\tau_\mathrm{M}}\exp\left(-\frac{\Delta t-\delta t}{\tau_\mathrm{M}}\right)}_{\text{Ultrafast demagnetization}} \\ \underbrace{-\frac{\tau_\mathrm{E}(A_1-A_2)}{\tau_\mathrm{E}-\tau_\mathrm{M}}\exp\left(-\frac{\Delta t-\delta t}{\tau_\mathrm{E}}\right)}_{\text{Fast recovery}}\underbrace{-A_2\exp\left(-\frac{\Delta t-\delta t}{\tau_0}\right)}_{\text{Slow recovery}}\Bigg]\Bigg\}\otimes\Gamma(\Delta t-\delta t). \tag{5.5}$$

The magnetization transients are characterized by the sum of three exponential functions with individual characteristic decay times. The first term describes *ultrafast demagnetization* within the demagnetization time, τ_M. As outlined in section 2.5.1.2, τ_M includes both spin–electron and spin–phonon contributions to demagnetization, which makes eq. (5.5) well-suited to extract a characteristic timescale without any presumptions about the underlying mechanism. The second and the third term account for the *fast* and the *slow recovery* of magnetization, proceeding on characteristic timescales for energy equilibration, τ_E, and heat diffusion, τ_0, respectively. The heaviside function, $\Theta(\Delta t-\delta t)$, represents the start of the demagnetization process at $\Delta t = 0$, which takes into account the uncertainty in determining $\Delta t = 0$ via a small variation of $\delta t = \pm 50\,\mathrm{fs}$. The experimental time resolution is introduced via a convolution with a Gaussian function $\Gamma(\Delta t-\delta t)$. For the width of $\Gamma(\Delta t-\delta t)$, the sum of the timing jitter (40 fs) and the convolution of the nIR-laser and FEL pulse temporal profiles, which are assumed to be Gaussian, is taken. With pulse durations of $\tau_\mathrm{FEL} = 60\,\mathrm{fs}$ and $\tau^1_\mathrm{nIR} = 70\,\mathrm{fs}$ ($\tau^2_\mathrm{nIR} = 300\,\mathrm{fs}$), peak widths for $\Gamma(\Delta t-\delta t)$ of 132 fs (346 fs) at FWHM are obtained. An example of the fitted $\Delta M_z(\Delta t-\delta t)/M_{z,0}$ is given in Fig. 5.9, showing the individual contributions to the overall fit function, i. e., ultrafast demagnetization, fast and slow recovery of magnetization, as well as the Gaussian that accounts for the experimental time resolution.

For each sample and nIR-laser pulse parameter, the magnetization transients are recorded for $-1\,\mathrm{ps} \le \Delta t \le 2.5\,\mathrm{ps}$ with high resolution, i. e., a step size of 50 fs, as well as for $-5\,\mathrm{ps} \le \Delta t \le 50\,\mathrm{ps}$ with a lower resolution, i. e., a step size of 800 fs. The fit parameters that describe the femtosecond demagnetization, i. e., A_1 and τ_M, are extracted from the high-resolution delay-time scans. For the lowest nIR-laser fluence ($F^1_\mathrm{nIR} = 3.8\,\mathrm{mJ/cm^2}$) also the fit parameters that describe the fast-recovery of magnetization, i. e., A_2 and τ_E, are obtained from the high-resolution delay-time scans, as the magnetization transients show a *completed* fast-recovery of magnetization within $\Delta t \le 2.5\,\mathrm{ps}$. For the higher fluence ($F^2_\mathrm{nIR} = 9.6\,\mathrm{mJ/cm^2}$), i. e., for the cases of an extended fast-recovery of magnetization, the fit parameters A_2 and τ_E are iteratively fitted to the high and low-resolution delay-time scans until the fit converges. The fitting by eq. (5.5) fails for the magnetization transient of the $[\mathrm{Co/Pt}]_3$ that was excited by

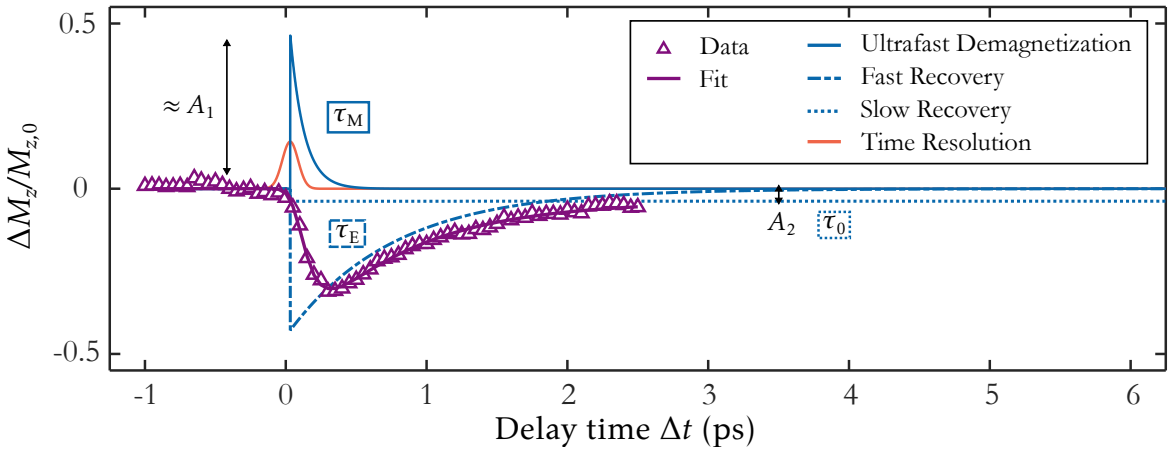

Figure 5.9.: Example of modeling the magnetization transients. Shown are the best fit of eq. (5.5) to the magnetization transient of the $[Co/Pt]_3$ multilayer, using LP 70 fs-short nIR-laser pulses with a fluence of $F^1_{nIR} = 3.8\,mJ/cm^2$ (purple), the model's three individual contributions (blue) as well as the Gaussian that accounts for the experimental time resolution (red).

$F^3_{nIR} = 18.9\,mJ/cm^2$, due to the completely vanished fast-recovery of magnetization. In that case, only the demagnetization time, τ_M, was fitted by neglecting the fast-recovery term in eq. (5.5), setting $\tau_E = 0$ and strongly restricting the fit parameter A_2.

In all cases the slow-recovery of magnetization, τ_0, cannot be reliably obtained from fitting, due to the limited maximum time range of 50 ps and therefore is set constant to a reasonable value for heat diffusion of $\tau_0 = 1000\,ps$. Note that alternatively, often an inverse square root function is used to model the slow-recovery of magnetization [12, 14]. For the here investigated timescale of $\Delta t \leq 50\,ps$, no significant differences have been observed between the two approaches.

5.4.2.2. Fit Results

The results from fitting eq. (5.5) to the magnetization transients of the three samples are presented in Fig. 5.10 a) and b) for a nIR-laser excitation by F^1_{nIR} and F^2_{nIR}, respectively. The insets show the time evolution of the magnetization up to a delay time of $\Delta t = 50\,ps$, obtained in separate measurements with a reduced time resolution.[4] The obtained fits, shown as solid lines in Fig. 5.10 a) and b), reproduce the data with excellent precision. The corresponding fit parameters are presented in Fig. 5.10 c)–f), showing low-fluence (F^1_{nIR}) and high-fluence (F^2_{nIR}) results as open and closed symbols, respectively. The fit parameters describing ultrafast demagnetization, i. e., the effective non-equilibrium temperature rise, A_1, and the demagnetization time, τ_M, are presented in Fig. 5.10 c) and d), respectively. For the lower fluence, F^1_{nIR},

[4] Note that due to the step size of 800 fs, the maximum degree of demagnetization is not accurately represented in the low-resolution delay-time scans.

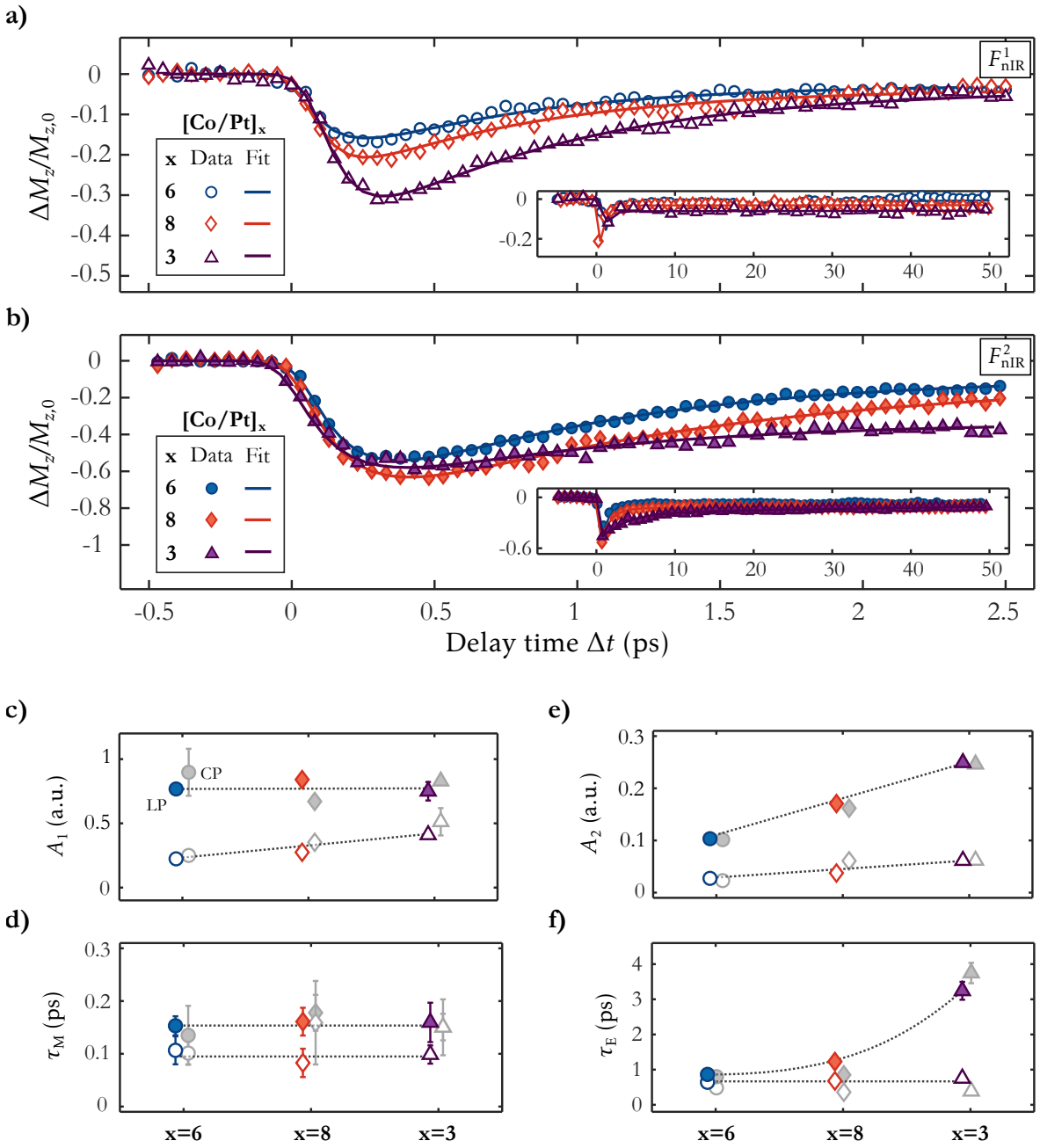

Figure 5.10.: a) and b) Fits of eq. (5.5) to the magnetization transients of the $[\mathrm{Co/Pt}]_x$ multilayers with $x = 6$ (blue), $x = 8$ (red) and $x = 3$ (purple), using LP 70 fs-short nIR-laser pulses with fluences $F^1_{\mathrm{nIR}} = 3.8\,\mathrm{mJ/cm^2}$ and $F^2_{\mathrm{nIR}} = 9.6\,\mathrm{mJ/cm^2}$, respectively. The insets show $\Delta M_z(\Delta t)/M_{z,0}$ up to a delay time of $\Delta t = 50\,\mathrm{ps}$, obtained in separate measurements. c)–f) Corresponding fit parameters, A_1, τ_M, A_2 and τ_E. The fit parameters from fitting the magnetization transients using CP nIR-laser excitation (transients not shown) are included for comparison (blurred gray). Dotted lines indicate the trends for decreasing total layer thicknesses.

the increasing maximum degree of demagnetization from ≈ 16% in the thicker to ≈ 31% in the thinner sample is represented by an increasing non-equilibrium temperature rise from $A_1 = (0.22 \pm 0.02)$ a.u. to $A_1 = (0.41 \pm 0.02)$ a.u. For the higher fluence, F^2_{nIR}, the maximum degree of demagnetization reaches values of around 60% in all three samples leading to fit parameters A_1 in the range of (0.75–0.84) a.u. (Fig. 5.10 c)). Note that the fit parameter A_1 is proportional to the maximum degree of demagnetization, $-\Delta M_z^{\mathrm{max}}/M_{z,0}$ (section 5.4.2.3). Hence, the values for $-\Delta M_z^{\mathrm{max}}/M_{z,0}$, discussed in dependence on the laser fluence in section 5.4.1, can also be interpreted as non-equilibrium temperature rises in the (electron and) spin system. At a given fluence, the demagnetization time is the same for the three samples within the error margin of about ±25 fs, taking values of $\tau_{\mathrm{M}} \approx 100$ fs for F^1_{nIR} and $\tau_{\mathrm{M}} \approx 150$ fs for F^2_{nIR} (Fig. 5.10 d)). The temperature dependence of τ_{M}, i. e., the dependence of τ_{M} on the maximum degree of demagnetization, $-\Delta M_z^{\mathrm{max}}/M_{z,0} \propto A_1$, is discussed in section 5.4.3.

The fit parameters that describe the picosecond recovery of magnetization, i. e., the effective equilibrium temperature rise after thermal equilibration of the (electron and) spin and phonon system, A_2, and the energy relaxation time, τ_{E}, are presented in Fig. 5.10 e) and f), respectively. For both fluences, increasing equilibrium temperature rises, A_2, are obtained from the thicker to the thinner sample (Fig. 5.10 e)). As it will be shown in the following section, the fit parameter A_2 is proportional to the calculated equilibrium temperature rise, ΔT, which allows to convert the A_2 values to absolute temperatures. The energy equilibration time, τ_{E}, shows a rather non-intuitive behavior. While it only slightly increases from the thicker to the thinner sample for F^1_{nIR}, i. e., $\tau_{\mathrm{E}} \approx (0.64\text{–}0.75)$ ps, it shows a drastic increase for F^2_{nIR} from $\tau_{\mathrm{E}} = (0.86 \pm 0.09)$ ps in the thickest to $\tau_{\mathrm{E}} = (3.24 \pm 0.25)$ ps in the thinnest sample (Fig. 5.10 f)). The dependence of τ_{E} on the equilibrium temperature $T \propto A_2$ is discussed in section 5.4.4.

For comparison, the results from fitting the magnetization transients using CP nIR-laser excitation are included in Fig. 5.10 c)–f) as blurred gray symbols. The effect of the nIR-laser polarization on the ultrafast magnetization dynamics is discussed in section 5.4.5. Fit parameters obtained from modeling magnetization transients using LP and CP nIR-laser excitation are summarized in table B.1 and table B.2, respectively.

5.4.2.3. Evaluation of the Temperature Scale

From fitting the magnetization transients the fit parameters A_1 and A_2 are obtained, which are measures for an effective *non-equilibrium* and *equilibrium* temperature rise, respectively. Within the 3TM, the electron, spin and phonon system are considered out-of-equilibrium within the first 100 fs, reaching the maximum degree of demagnetization within $\tau_{\mathrm{M}} = (100\text{–}150)$ fs. As shown in Fig. 5.11 a), the fit parameter A_1 scales linearly with the maximum degree of demagnetization, i. e., the $-\Delta M_z^{\mathrm{max}}/M_{z,0}$ is a good measure for the non-equilibrium temperature rise A_1. It furthermore indicates that the three $[\mathrm{Co/Pt}]_x$ multilayers can be treated

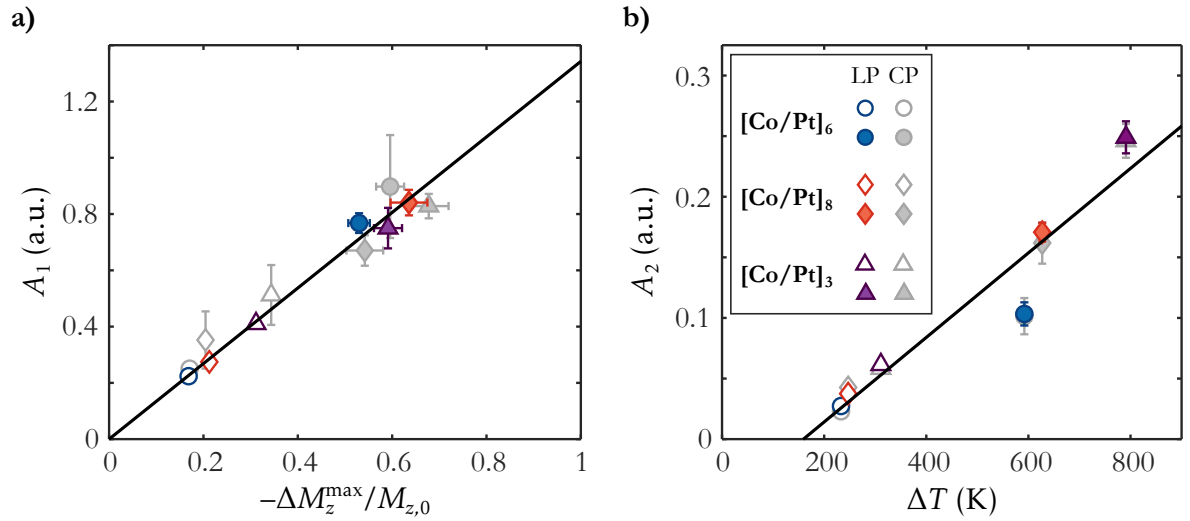

Figure 5.11.: a) Correlation between the fit parameter A_1 and the maximum degree of demagnetization, $-\Delta M_z^{max}/M_{z,0}$. The black line shows a linear fit through the origin to the data. b) Correlation between the fit parameter A_2 and the calculated equilibrium temperature rise, ΔT. For the evaluation of A_2 in absolute temperatures, the values are divided by a scaling factor of $3.5 \cdot 10^{-4}$ K^{-1}, obtained from a linear fit to the data (black line): $A_2(\Delta T) = (3.5 \pm 0.35) \cdot 10^{-4} \Delta T - (0.055 \pm 0.02)$.

as realizations of a single Co/Pt-multilayer system reaching different $-\Delta M_z^{max}/M_{z,0} \propto A_1$ at a given fluence.

The electron, spin and phonon system thermalize within the characteristic time for energy equilibration, τ_E, until they reach a common temperature A_2. For an evaluation of the absolute temperature scale of A_2, the absorbed nIR-laser pulse energy in the individual Co (and Pt) layers, ΔI_x, is calculated, considering a total equilibrium specific heat, C_{tot}. The equilibrium temperature rise in the x-th Co layer, ΔT_x, is determined according to, e. g., Ref. [276], as

$$\Delta T_x = \frac{\Delta I_x}{V C_{tot}}, \tag{5.6}$$

where $V = A_{nIR} \cdot d_{Co}$ is the heated layer volume, given by the elliptically shaped nIR-laser beam profile at the sample position, A_{nIR}, with $d_{x,y} = (343 \times 492)\,\mu m^2$ (FWHM), and the different individual Co-layer thicknesses, d_{Co}, in the three Co/Pt multilayers. For calculating the laser-induced temperature rise, the total specific heat, $C_{tot} = C_\ell + C_e + C_s$, is employed with $C_{tot}^{Co} = 3.74 \cdot 10^6\,Jm^{-3}K^{-1}$ [157]. Note that C_{tot} is dominated by the lattice contribution, whereas C_s and C_e are at least one order of magnitude smaller at low temperatures (see, e. g., Ref. [133]). The equilibrium temperature rise in the Pt layers is calculated accordingly, using the different individual Pt-layer thicknesses, d_{Pt}, as well as the total specific heat of Pt, $C_{tot}^{Pt} = 2.81 \cdot 10^6 Jm^{-3}K^{-1}$ [277].

The absorbed nIR-laser pulse energy in the x-th Co layer is calculated as the difference of the

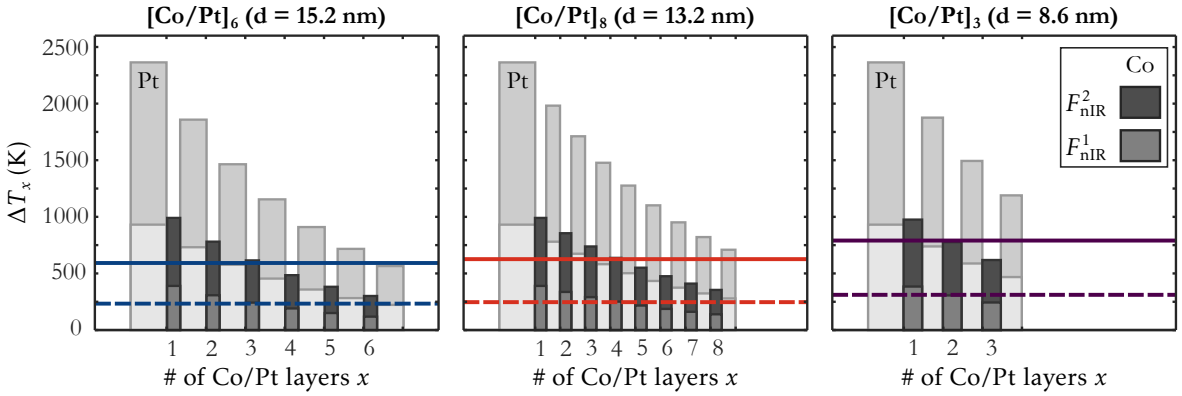

Figure 5.12.: Calculated layer-dependent equilibrium temperature rise, ΔT_x, in the three $[Co/Pt]_x$ multilayers, with $x = 6$, 8, and 3, for the two nIR-laser fluences $F^1_{nIR} = 3.8\,mJ/cm^2$ and $F^2_{nIR} = 9.6\,mJ/cm^2$ (bright and dark fillings, respectively). The average equilibrium temperature rises, $\Delta T = \langle \Delta T_x \rangle_x$, in the Co layers are shown as dashed and solid lines, respectively. The temperature profiles in the Pt layers are shown as light gray columns.

incoming and transmitted nIR-laser pulse energies, $\Delta I_x = I_x^{in} - I_x^{out}$, employing Beer-Lambert's law [1]

$$\begin{aligned} I_x^{in} &= I_{nIR} \exp\left(-\frac{d_{cap}}{\delta_{Pt}}\right) \exp\left(-(x-1)\left[\frac{d_{Co}}{\delta_{Co}} + \frac{d_{Pt}}{\delta_{Pt}}\right]\right) \\ I_x^{out} &= I_x^{in} \exp\left(-\frac{d_{Co}}{\delta_{Co}}\right), \end{aligned} \tag{5.7}$$

where $I^1_{nIR} = 5.0\,\mu J$ and $I^2_{nIR} = 12.5\,\mu J$ are the nIR-laser pulse energies that correspond to the fluences $F^1_{nIR} = 3.8\,mJ/cm^2$ and $F^2_{nIR} = 9.6\,mJ/cm^2$, respectively. The nIR-laser's attenuation length in Co and Pt is given by $\delta_{Co} = 13\,nm$ [217] and $\delta_{Pt} = 8\,nm$ [218], respectively. Furthermore, the nIR-laser attenuation in the Pt cap layer with a thickness of $d_{Cap} = 2\,nm$ is taken into account. The calculated layer-dependent temperature profiles, ΔT_x, for the three $[Co/Pt]_x$ multilayers are presented in Fig. 5.12.

As it can be expected from thickness-dependent absorption, an increasing average temperature rise, ΔT, with decreasing total film thickness is obtained for both F^1_{nIR} and F^2_{nIR}. In particular, the calculated ΔT are well-correlated to the fitted A_2, as shown in Fig. 5.11 b). The fairly linear relation between the two shows that A_2 represents the laser-induced temperature rise, solely given by the material-specific nIR-laser absorption. It shows that no losses through heat dissipation have to be considered within the first few picoseconds but the Co/Pt multilayers, fabricated on 50 nm-thin isolating Si_3N_4 membranes, can be considered thermally isolated from the environment. It further shows that the three $[Co/Pt]_x$ multilayers can be treated as realizations of one Co/Pt-multilayer system that reaches different temperatures

depending on sample thickness and pump fluence. A linear fit to the data in Fig. 5.11 b) gives a factor of $(3.5 \pm 0.4) \cdot 10^{-4}\,\mathrm{K}^{-1}$ for converting the fitted A_2 values to absolute temperatures, ΔT. Note that fitting of eq. (5.5) to experimental data produces a temperature offset in A_2 of $\Delta T_0 \approx 160\,\mathrm{K}$, which has to be attributed to the simplicity of the model. Note that, e. g., the nIR reflectivity of the system, that acts as a sub-wavelength optical element [278], has not been considered here. The linear relation between A_2 and T, however, shows that the fitting of eq. (5.5) is not only valid in the low-fluence regime, but produces reliable values for A_2 also at higher fluences. Hence, while the absolute values of T are of limited validity, they still serve as a good measure for *relative* differences in the laser-induced temperature rise and therefore are used as a temperature scale for the discussion on the temperature dependence of the energy equilibration time, τ_E, in section 5.4.4.

5.4.3. Temperature Dependence of the Demagnetization Time

This section deals with the temperature dependence of the demagnetization time, τ_M. A measure for the non-equilibrium temperature rise, A_1, is provided by the maximum degree of demagnetization, $-\Delta M_z^\mathrm{max}/M_{z,0}$ (section 5.4.2.3). The dependence of τ_M on $-\Delta M_z^\mathrm{max}/M_{z,0}$ is shown in Fig. 5.13 together with reported literature values on elemental Co and a $[\mathrm{Co/Pt}]_{11}$ multilayer from Ref. [136]. For maximum degrees of demagnetization of $-\Delta M_z^\mathrm{max}/M_{z,0} \lesssim 30\%$, a demagnetization time of $\tau_\mathrm{M} \approx (100 \pm 20)\,\mathrm{fs}$ is found in all three samples. The demagnetization time slightly increases to $\tau_\mathrm{M} \approx (150 \pm 25)\,\mathrm{ps}$ for maximum degrees of demagnetization of $-\Delta M_z^\mathrm{max}/M_{z,0} \approx 60\%$, and remains about the same for $-\Delta M_z^\mathrm{max}/M_{z,0} \approx 100\%$. The same behavior is observed for the results using CP nIR-laser excitation (blurred gray data), however, possessing larger errors for individual τ_M values. This can be attributed to individual lower-quality delay-time scans, i. e. a less-defined demagnetization onset or maximum degree of demagnetization (see Fig. 5.15 on p. 111), presumably due to larger FEL instabilities.

The τ_M versus $-\Delta M_z^\mathrm{max}/M_{z,0}$ behavior of the optically thin Co/Pt-multilayer system follows the same trend as what was observed for elemental Co and a $[\mathrm{Co/Pt}]_{11}$ multilayer in Ref. [136], as indicated by the gray dashed line in Fig. 5.13. In that publication, an increase in τ_M by about a factor of two was observed between elemental Co and a $[\mathrm{Co/Pt}]_{11}$ multilayer. The τ_M versus $-\Delta M_z^\mathrm{max}/M_{z,0}$ behavior of the two samples was simulated via the M3TM (see section 2.5.1.3 for details), yielding an increase in the spin-flip probability by about a factor of four, from $a_\mathrm{sf} = 0.025 \pm 0.005$ in Co to $a_\mathrm{sf} = 0.105 \pm 0.005$ in the $[\mathrm{Co/Pt}]_{11}$ multilayer. The simulations via the M3TM are included as black dashed lines in Fig. 5.13. The main difference between elemental Co and Co/Pt multilayers are the additional Pt interlayers that increase the SOC through an increase of the effective atomic number, Z. It was conjectured that the increase of a_sf is a result of the increased SOC, in line with the descriptions in Ref. [157]. In the M3TM, the demagnetization rate, i. e., the initial slope of the magnetization transients and thus τ_M,

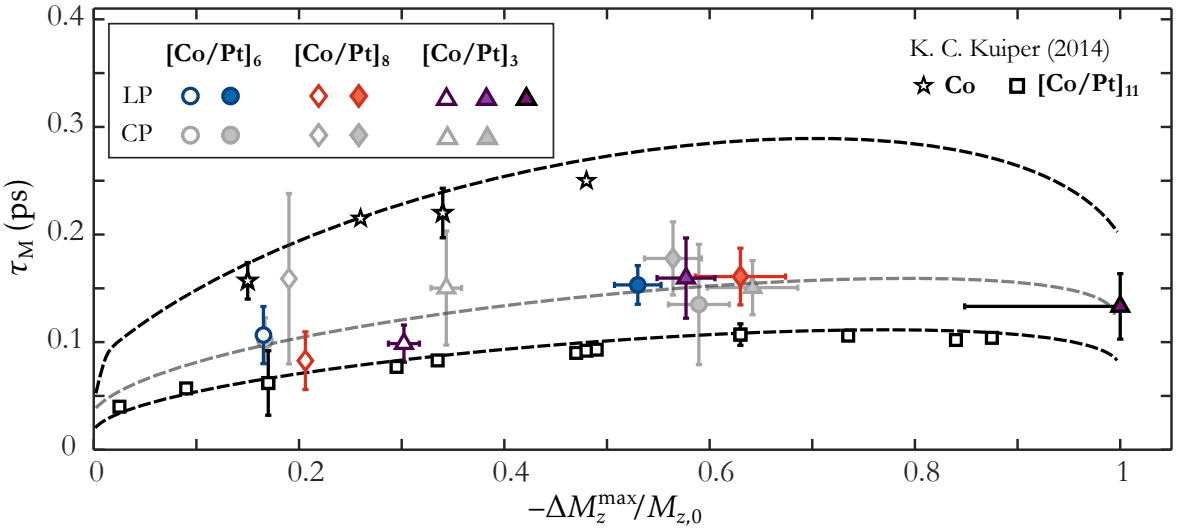

Figure 5.13.: Dependence of the demagnetization time, τ_M on the maximum degree of demagnetization, $-\Delta M_z^{max}/M_{z,0}$, obtained from fitting eq. (5.5) to the magnetization transients of the three Co/Pt multilayers using F_{nIR}^{1} (open symbols) and $F_{nIR}^{2,3}$ (filled symbols). For comparison, the data from K. C. Kuiper *et al.*, obtained by fluence-dependent ultrafast demagnetization in an elemental Co thin film (open stars) and a $[Co/Pt]_{11}$ multilayer (open squares) are included, together with fits to the data via the M3TM (black dashed lines) [136]. The gray dashed line is a guide to the eye.

scales inversely with a material-specific parameter $R \propto a_{sf} T_C^2/\mu_{at}$ [157]. Smaller values of τ_M in Co/Pt multilayers compared to elemental Co can thus be directly related to larger values of $R \propto a_{sf}$ (assuming constant T_C). Moreover, as R is reasonably temperature independent in that temperature regime ($G_{e\ell} \approx$ const. in eq. (2.54)), larger values τ_M are obtained for larger degrees of demagnetization (for higher temperatures).

As compared to the $[Co/Pt]_{11}$ multilayer in Ref. [136], the here obtained data show a general trend towards larger τ_M values. According to the M3TM, the effective a_{sf} in the here investigated samples should thus be smaller than in the $[Co/Pt]_{11}$ multilayer. This appears reasonable as the individual Co and Pt layers are slightly thicker here, which reduces the effective number of Co and Pt next-nearest neighbors and thus the effect of SOC.

Due to the good agreement of the τ_M versus $-\Delta M_z^{max}/M_{z,0}$ behavior with the one in Ref. [136], it is natural to interpret the results according to the M3TM as well, i. e., as ultrafast demagnetization that is mainly driven by (local) electron–phonon momentum scattering events with a spin-flip probability of $a_{sf} \approx 0.1$ (section 2.5.1.3). This interpretation is supported by the fact that there exist no significant differences between the τ_M values of the three Co/Pt multilayers, possessing multi-domain states with average domain sizes between $D_{av} = (615–196)$ nm, for both low and high-fluence excitation. Hence there appears to be no significant contribution of (non-local) superdiffusive spin transport across domain boundaries to τ_M on these length scales, in agreement with recent experimental findings [135, 137].

5.4.4. Temperature Dependence of the Energy Equilibration Time

The temperature dependence of the energy equilibration time is discussed in the following. For that, the τ_E values are related to the temperature, T, calculated from the total absorbed laser-pulse energy under consideration of the individual Co/Pt-multilayer compositions (section 5.4.2.3). In the 3TM, the absorbed laser-pulse energy is assumed to initially lead to a temperature rise in the electron system only (T_e) which subsequently thermalizes with the spin ($T_e = T_s$) and the lattice system ($T_e = T_s = T_\ell$). Note that the energy equilibration time, τ_E, in 3*d* ferromagnets shows the same behavior both for increasing fluences (at room temperature) [146, 160] and increasing ambient temperatures (at a constant low fluence) [133, 160]. It thus appears reasonable to discuss the τ_E values with respect to the laser-induced temperature rise, T, even though the subsystems might not yet be fully thermalized within the first picosecond.

The τ_E versus T behavior in the optically thin Co/Pt-multilayer system is shown in Fig. 5.14 a). The energy equilibration time shows the expected temperature (or fluence) dependence of ultrafast magnetization dynamics (section 2.5.1.5), i. e., it slowly increases with temperature in the low-temperature regime ($T \lesssim 800\,\mathrm{K}$) and drastically increases in the high-temperature regime ($T \approx 1000\,\mathrm{K}$). This drastic slowing down of the remagnetization dynamics at high temperatures is a frequently observed phenomenon in the elemental ferromagnets Fe, Co and Ni [125, 169, 175–177], as well as compound materials that contain the elemental ferromagnets like $CoPt_3$ alloy thin films [131] or chemically ordered $Fe_{46}Cu_6Pt_{48}$ thin films [133], but also Co/Pd [37] and Co/Pt multilayers [35, 146, 178]. The reason for this slowing down at high temperatures is believed to be connected to the complete loss of electronic correlations [181], accompanied by the formation of randomly oriented, magnetically ordered structures on nanometer length scales that lead to considerable frustration of the magnetization [178]. In such a frustrated magnetic state, it takes much longer for the magnetization to recover its initial value (energy remains stored in the spin system).

In the following the data are modeled, starting with a description of the low-temperature data via the 3TM. An analytical expression to describe both the low and the high-temperature regime of $\tau_E(T)$ is proposed thereafter. The model includes a spin contribution in the description of the remagnetization dynamics following theoretical predictions by A. Manchon *et al.* in Ref. [180].

An energy equilibration time of $\tau_E = (0.64 \pm 0.09)\,\mathrm{ps}$ at low temperatures ($T = 380\,\mathrm{K}$) is in good agreement with reported literature values for Co/Pt multilayers [137]. Its linear increase to $\tau_E = (1.23 \pm 0.21)\,\mathrm{ps}$ at $T = 790\,\mathrm{K}$ can be understood by the low-temperature dependence of τ_E, derived within the 3TM (section 2.5.1.2)

$$\tau_E(T) \approx \frac{C_e(T)}{G_{e\ell}} = \frac{\gamma T}{G_{e\ell}}, \tag{5.8}$$

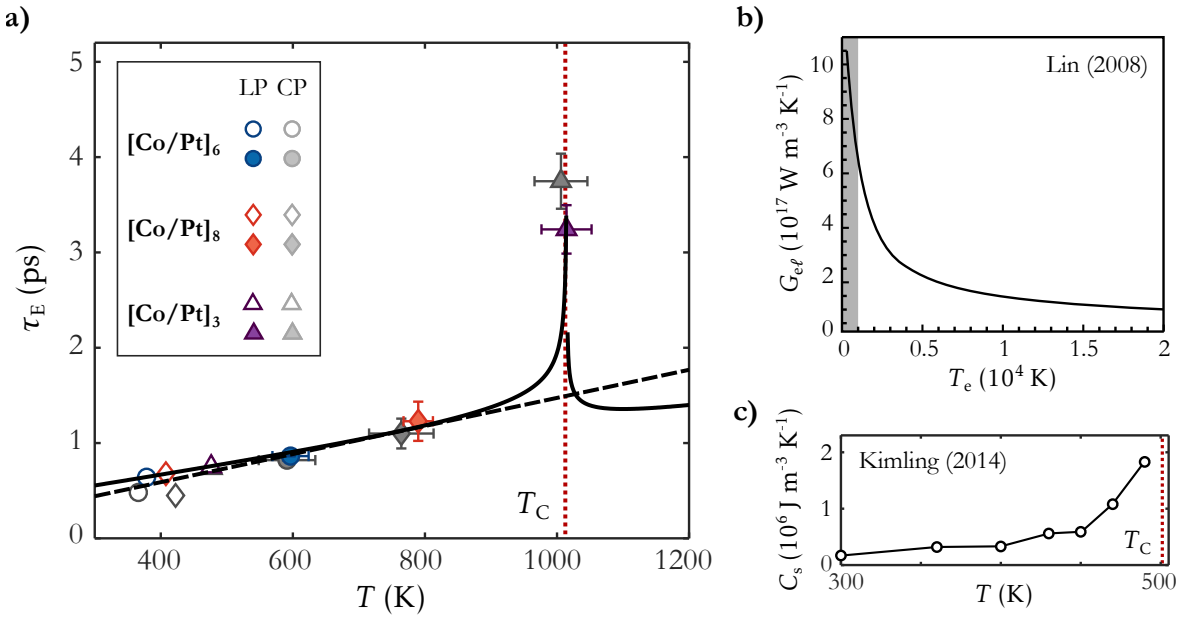

Figure 5.14.: a) Temperature dependence of the energy equilibration time, $\tau_E(T)$. Data were obtained from fitting eq. (5.5) to the magnetization transients of the three Co/Pt multilayers using F^1_{nIR} (open symbols) and $F^{2,3}_{nIR}$ (filled symbols). The black dashed line shows the best fit of eq. (5.8) to the low-temperature data ($T \leq 800\,K$). The black solid line shows the best fit of eq. (5.10) to all data. Both model functions are introduced in the text. b) Dependence of the electron–phonon coupling factor, $G_{e\ell}$, on the electron temperature, T_e (reproduced with modifications from Ref. [279]). c) Temperature dependence of the spin specific heat, C_s, in a ferromagnetic thin film with $T_C \approx 500\,K$ (reproduced with modifications from Ref. [133]).

assuming $T = T_e$. A fit of eq. (5.8) to the low-temperature data ($T < 800\,K$) yields a value of $\gamma = (1474 \pm 104)\,Jm^{-3}K^{-2}$, which is in the range of reported low-temperature values in the $3d$ ferromagnets [136, 137, 279]. For the fit, shown in Fig. 5.14 a) as a black dashed line, a low-temperature value for the electron–phonon coupling parameter of $G_{e\ell} = 1 \cdot 10^{18}\,Js^{-1}m^{-3}K^{-1}$ is used (Fig. 5.14 b)).[5] Clearly, the low-temperature behavior of $\tau_E(T)$ up to $T = 800\,K$ is well-described by eq. (5.8), i. e., by a linear increase in T with a slope that is determined by the material-specific parameter, γ, and the electron–phonon coupling parameter, $G_{e\ell}$.

The linear increase, however, cannot explain the drastic slowing down of the energy equilibration with $\tau_E = (3.24 \pm 0.25)\,ps$ at $T \approx 1000\,K$, reached by exciting the thinnest $[Co/Pt]_3$ multilayer with a nIR-laser fluence of $F^2_{nIR} = 9.6\,mJ/cm^2$. Upon further increasing the nIR-laser fluence to $F^3_{nIR} = 18.9\,mJ/cm^2$, no signs of a recovery of the magnetization could be observed up to $\Delta t \approx 4\,ps$ (see Fig. 5.5 on p. 86), indicating that the sample reaches temperatures above T_C. As no value for τ_E could be determined in this case, the data point is omitted in Fig. 5.14 a).

[5] In general, both $G_{e\ell}$ and γ are temperature dependent quantities. Thus, quite different values are reported in literature for the modeling of experimental data, i. e., $\gamma \approx 0.6 \cdot 10^3\,Jm^{-3}K^{-2}$ at low temperatures to $\gamma \approx 6 \cdot 10^3\,Jm^{-3}K^{-2}$ at high temperatures [5, 136, 137, 182, 279] and $G_{e\ell} \approx (0.5\text{–}4) \cdot 10^{18}\,Js^{-1}m^{-3}K^{-1}$ [5, 157, 182, 279].

A model to describe $\tau_E(T)$ in both the low and the high-temperature regime is proposed in the following. Consider that, when deriving eq. (5.8) the spin specific heat is neglected, $C_s = 0$. In the low-temperature regime, the energy equilibration time can be well-approximated by the electron specific heat, C_e, and the electron–phonon coupling parameter $G_{e\ell}$, i. e., the ability of the system to transfer energy between the electron and the lattice system, as shown above. Even though reasonable results are obtained when using eq. (5.8) to describe low-temperature data, the assumption of $C_s = 0$ seems questionable, as it is already on the same order as C_e at low temperatures [133] and strongly increases at high temperatures, as shown in Fig. 5.14 c). In fact, assuming a non-zero C_s with a divergence at T_C was necessary to describe the experimentally observed suppression of the electron-temperature rise close to T_C [176] (Fig. 2.14 on p. 44). It was concluded in that publication that a substantial amount of energy is stored in the spin system already $\approx 20\,\mathrm{fs}$ after laser excitation, i. e., the spin-system seems to react similarly fast to ultrashort laser excitation as the electron system, with a heat capacity that is at least of the same size. Following these findings, it is proposed here to include also a spin contribution in the description of the remagnetization dynamics, i. e., to treat the remagnetization dynamics via a strongly coupled electron–spin system

$$\tau_E(T) \approx \frac{C_{es}(T)}{G_{e\ell}} = \frac{C_e(T) + C_s(T)}{G_{e\ell}}, \tag{5.9}$$

using $T = T_e = T_s$. For the electron contribution, eq. (5.8) is employed as for the description of the low-temperature data. For the spin contribution, i. e., in order to account for the high-temperature behavior of $\tau_E(T)$, the theoretically predicted temperature dependence of the *slowdown time*, $\tau_d \propto \tau_E$ (eq. (2.55), is used, yielding

$$\begin{aligned} \tau_E(T) &= \frac{C_e(T) + C_s(T)}{G_{e\ell}} \\ &= \frac{1}{G_{e\ell}} \left[\gamma T + C_{s,\mathrm{low}} \left(1 - \frac{T}{T_C} \right)^{-\delta} \right]. \end{aligned} \tag{5.10}$$

For the $3d$ ferromagnets, an exponent of $\delta = 0.34$ was predicted [180]. The proposed model treats the drastic slowing down of τ_E at $T \approx 1000\,\mathrm{K}$ as a divergence when approaching the critical point, i. e., the Curie temperature T_C. Explicitly, the high-temperature behavior of $\tau_E(T)$ is included by a diverging $C_s(T)$, which shows the same temperature dependence as proposed in eq. (5.10) [179].[6] A fit of eq. (5.10) to the data, taking the low-temperature value for $G_{e\ell} = 1 \cdot 10^{18}\,\mathrm{W/m^3K}$ as before and assuming a $T_C = 1015\,\mathrm{K}$, yields the $\tau_E(T)$ behavior shown by the black solid line in Fig. 5.14 a), with fit parameters $\gamma = (1005 \pm 392)\,\mathrm{Jm^{-3}K^{-2}}$

[6] The temperature dependence of the specific heat close to T_C is governed by the critical exponent α, which can be expected to have a value of $\alpha \approx 0.1$ [179]. The here-used exponent of $\delta = 0.34$ from Ref. [180] was found to agree better with the obtained results.

and $C_{s,low} = (0.225 \pm 0.082) \cdot 10^6\,\mathrm{Jm^{-3}K^{-1}}$. For the fit, the material-specific parameter $\gamma = 1474\,\mathrm{Jm^{-3}K^{-2}}$ was used as starting value, obtained from the low-temperature behavior of $\tau_E(T)$.The proposed model given by eq. (5.10) resembles both the low and the high-temperature regime of $\tau_E(T)$. The fitted γ and $C_{s,low}$ thereby agree well with reported low-temperature values in the 3*d* ferromagnets (see Fig. 5.14 c) or Refs. [133, 179] for $C_{s,low}$). It is noted that the chosen $T_C = 1015\,\mathrm{K}$ is within the expected range of the Curie temperature in the here investigated samples (section 2.1). The good agreement between the phenomenological model and the data suggests that, instead of describing the ultrafast magnetization dynamics by the energy exchange within three individual thermal baths, it might be more appropriate to treat the electron and spin system as a single, strongly coupled electron–spin system (or an electron system with spin-degrees of freedom) that equilibrates with the phonon system on a time scale of $\tau_E(T)$. While the linear increase of $\tau_E(T)$ at low temperatures is mainly governed by the linearly increasing electron specific heat, $C_e(T)$, its drastic increase close to T_C is only well-accounted for when considering a diverging spin specific heat, $C_s(T)$.

The model suggests that an equilibrium temperature close to the Curie temperature is reached in the thinnest, $[Co/Pt]_3$ multilayer upon nIR-laser excitation by $F^2_{nIR} = 9.6\,\mathrm{mJ/cm^2}$. Interestingly, in that case no full demagnetization but a maximum degree of demagnetization of only $\approx 60\%$ was obtained (see Fig. 5.8 on p. 95). This non-intuitive result could be connected to a divergent $C_s(T)$ (and probably other critical phenomena close to T_C such as a divergent χ) as well. A highly susceptible spin system with a large specific heat at high temperatures enables fluctuations of spontaneous magnetization on nanometer length scales as well as to store an increasing amount of energy without a significant further increase in the degree of demagnetization (or further temperature rise). In fact, just very recently, it was reported that the spin system could be the dominating heat sink in the initial few hundreds of femtoseconds, implying a transient nonthermal state of the spins [280]. Using the same approach of a strongly coupled electron–spin system that equilibrates with the phonon system as here, an accurate description of the lattice dynamics in Ni upon ultrashort laser excitation was achieved. In particular, it was found that the spin temperature may exceed the electron temperature already $\approx 150\,\mathrm{fs}$ after laser excitation, initializing the remagnetization dynamics by an energy flow within the electron–spin system, i. e., from spin back to electronic degrees of freedom. Such a back-flow of energy could hold as an explanation for the here-observed suppression of the temperature-dependent increase of the maximum degree of demagnetization at high temperatures.

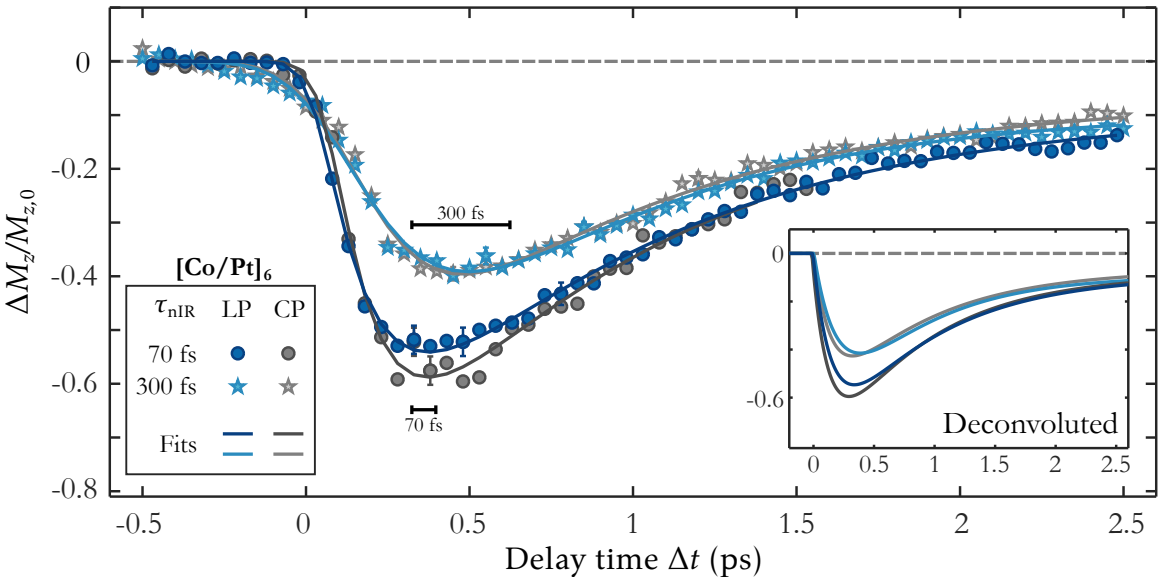

Figure 5.15.: Magnetization transients, $\Delta M_z(\Delta t)/M_{z,0}$, of the $[Co/Pt]_6$ multilayer upon excitation by LP and CP nIR-laser pulses with a pulse duration of $\tau^1_{nIR} = 70\,fs$ and $\tau^2_{nIR} = 300\,fs$. The fluence is $F^2_{nIR} = 9.6\,mJ/cm^2$. Fits to the data by eq. (5.5) are shown as solid lines. The inset shows the deconvoluted fit curves taking into account the different time resolutions using τ^1_{nIR} and τ^2_{nIR}.

5.4.5. Polarization and Pulse-Duration Dependence of Ultrafast Magnetization Dynamics

Aside from the temperature dependence discussed in the previous sections, the ultrafast magnetization dynamics in the optically thin Co/Pt multilayers was studied in dependence on the polarization as well as the duration of the nIR-laser pulses. The magnetization transients, obtained from the $[Co/Pt]_6$ multilayer upon excitation by linear (LP, blue) and circular polarized (CP, gray) nIR-laser pulses as well as pulse durations of $\tau^1_{nIR} = 70\,fs$ (circles) and $\tau^2_{nIR} = 300\,fs$ (stars) are shown in Fig. 5.15. For all presented magnetization transients a nIR-laser fluence of $F^2_{nIR} = 9.6\,mJ/cm^2$ was used.[7] As before, type-I demagnetization dynamics are observed for all of the data, characterized by a one-step demagnetization within the first $\approx 500\,fs$ and a two-step magnetization recovery on a pico and nanosecond time scale.

5.4.5.1. Polarization Dependence

Due to the polarization-dependent absorption in magnetic materials, i .e., the magnetic circular dichroism effect (MCD) (section 2.4.1), possible differences could arise in the maximum degree of demagnetization, $-\Delta M_z^{max}/M_{z,0}$, for linearly polarized (LP) and circularly polarized (CP)

[7] Due to the limited beamtime, the magnetization transients using nIR-laser pulses with a pulse duration of 300 fs could only be recorded for the $[Co/Pt]_6$ multilayer.

nIR-laser pulses. Such differences, however, are expected to be small in magnetic multi-domain systems with equal area filling of up and down-magnetized domains. In particular, the differences are expected to be much smaller than in a *homogeneously* magnetized sample, i. e., the magnetic single-domain state, where they were found to be of the size of only ≈ 5% [204]. In agreement with these considerations, no differences are observed in $-\Delta M_z^{\max}/M_{z,0}$ in the magnetization transients in Fig. 5.15 between LP (blue) and CP (gray) nIR-laser excitation within the error of the fit for both pulse durations.

The magnetization transients in Fig. 5.15 furthermore show the same ultrafast demagnetization as well as fast-recovery of magnetization for LP and CP nIR-laser excitation. This observation is quantified by fitting the magnetization transients with the phenomenological fit function, introduced in section 5.4.2.1. The resulting fits are shown as solid lines in Fig. 5.15. The $[Co/Pt]_6$ multilayer undergoes ultrafast demagnetization on the same characteristic demagnetization time within the error of the fit of $\tau_M = (153 \pm 18)$ fs for LP and $\tau_M = (135 \pm 56)$ fs for CP nIR-laser excitation. Similar is observed when using a longer pulse duration of $\tau_{nIR} = 300$ fs, giving a $\tau_M = (198 \pm 47)$ fs for LP and $\tau_M = (141 \pm 40)$ fs for CP excitation. Also, the same fast-recovery of magnetization is obtained by the fit, giving the same polarization independent energy equilibration time of $\tau_E \approx (0.72\text{–}0.86)$ ps within the fit error of approximately ±0.1 ps for both pulse durations.

Polarization-independent ultrafast magnetization dynamics have been reported before in a homogeneously magnetized thin film using various pump-pulse polarizations [12]. It was concluded that, a coherent transfer of angular momentum between the photons and the excited electrons only plays a minor role in the ultrafast magnetization dynamics with a contribution of approximately ±0.01%. The here obtained results support this conclusion and complement the findings in Ref. [12] for inhomogeneously magnetized, i. e., magnetic multi-domain systems.

As it could be shown that no significant exist in the ultrafast magnetization dynamics when using CP nIR-laser pulses, the discussion in the previous sections was focused on the more complete data set using LP nIR-laser pulses.

5.4.5.2. Pulse-Duration Dependence

While no polarization dependence is found in the magnetization transients in Fig. 5.15, two prominent differences can be observed between the two nIR-laser pulse durations of $\tau_{nIR}^1 = 70$ fs and $\tau_{nIR}^2 = 300$ fs. First, for a nIR-laser excitation with the longer pulse duration of 300 fs, the $[Co/Pt]_6$ multilayer seems to demagnetize on a more shallow slope compared to a pulse duration of 70 fs. It has to be considered, however, that the obtained demagnetization data is convoluted with the temporal profiles of the nIR-pump and the FEL-probe pulses. A *smearing out* of the demagnetization onset thus occurs naturally, when using pump pulses with longer pulse durations. Through fitting of the magnetization transients by eq. (5.5), the

same demagnetization time, $\tau_M \approx 150\,\text{fs}$, and energy equilibration time, $\tau_E \approx 0.80\,\text{ps}$, are found within the error margin (the fit parameters are summarized in table B.3). A second observation is the reduction of the maximum degree of demagnetization from $\approx 56\%$ for the shorter to $\approx 40\%$ for the longer pulse duration. As mentioned above, the measured magnetization transients are the ultrafast demagnetization convoluted with the temporal resolution of the experiment, defined by the nIR-laser and FEL pulse duration. Aside from a more shallow slope, this results in a reduction of the observed $-\Delta M_z^{\max}/M_{z,0}$ for longer pulse durations. However, when deconvoluting the magnetization transients, as shown in the inset of Fig. 5.15, the effect of the reduced time resolution on $-\Delta M_z^{\max}/M_{z,0}$ is found to be $\lesssim 3\%$, which can not explain the observed reduction by $\approx 13\%$.

The reduction could be understood when considering the theoretical predictions in Refs. [281, 282]. In that publication, a variety of data from ultrafast demagnetization experiments using sub-100 fs laser pulses of different fluences could be accurately described by taking into account the amplitude rather than the fluence of the nIR-laser pulses. The nIR-laser fluence at the surface of the sample is given by $F_{\text{nIR}} = 2nc\varepsilon_0 A^2 \tau_{\text{nIR}} \sqrt{\pi/2}$, where n is the refractive index, c is the speed of light, ε_0 is the vacuum permittivity, A is the amplitude of the laser field and τ_{nIR} is the pulse duration [281]. At a constant fluence, a relation of $(\tau^2_{\text{nIR}}/\tau^1_{\text{nIR}})^{1/2} \approx A_1/A_2 \approx \Delta M_z^{\max,1}/\Delta M_z^{\max,2}$ can be expected, while here a ratio of $(\tau^2_{\text{nIR}}/\tau^1_{\text{nIR}})^{1/2} \approx 2.1$ and $\Delta M_z^{\max,2}/\Delta M_z^{\max,1} \approx 1.4$ is obtained.

Note that the theory in Refs. [281, 282] only considers sub-100 fs long nIR-laser pulses. Deviations from the theoretical predictions might thus already be explained by possible limitations of the theory for the here used pulse duration of $\tau^2_{\text{nIR}} = 300\,\text{fs}$. It is furthermore pointed out in Ref. [281] that it is not only the amplitude that determines $-\Delta M_z^{\max}/M_{z,0}$, but other aspects, like the efficiency of the optically induced electronic transitions, have to be considered too. Taking into account these uncertainties, the reduction of $-\Delta M_z^{\max}/M_{z,0}$ for the longer pulse duration is in reasonable agreement with a reduction of the nIR-laser amplitude, $A \propto -\Delta M_z^{\max}/M_{z,0}$. Note that strong deviations from this simple analogy are found in the TR-mSAXS experiment at FERMI, where a large degree of demagnetization of $-\Delta M_z^{\max}/M_{z,0} \approx 80\%$ was obtained by 3500 fs-long nIR-laser pulses with a fluence of $F_{\text{nIR}} = 13.4\,\text{mJ/cm}^2$ (chapter 6). Further systematic investigations on the influence of the nIR-laser pulse duration on $-\Delta M_z^{\max}/M_{z,0}$ would be an interesting task, e. g., in the context of AOS, where the interplay between the two seems to play a decisive role for whether or not a switching of the magnetic state can be achieved (section 2.5.2.2).

5.5. Summary

The results from the TR-mSAXS experiment at FLASH, where three optically thin Co/Pt multilayers with total film thicknesses between $d = (8.6\text{–}15.2)\,\text{nm}$ were excited by nIR-laser

pulses of different fluence, polarization and pulse duration, are summarized as follows.

Maximum Degree of Demagnetization: The three Co/Pt multilayers show a strongly increasing maximum degree of demagnetization, $-\Delta M_z^{\max}/M_{z,0}$, with laser fluence (Fig. 5.8), as it could be expected for ultrafast demagnetization in optically thin films (section 2.5.1.6).

A thickness-dependent increase of the maximum degree of demagnetization from $(16 \pm 1)\%$ in the thickest, to $(31 \pm 1)\%$ in the thinnest Co/Pt multilayer is observed for the lowest fluence $F^1_{\mathrm{nIR}} = 3.8\,\mathrm{mJ/cm^2}$. Differences between the three Co/Pt multilayers can be understood from thickness-dependent absorption of nIR light along the Co and Pt layers, which leads to higher (average) temperatures the thinner the sample (Fig. 5.12). However, more comparable maximum degrees of demagnetization are observed in the three samples upon excitation by $F^2_{\mathrm{nIR}} = 9.6\,\mathrm{mJ/cm^2}$, i. e., the increase of $-\Delta M_z^{\max}/M_{z,0}$ appears to be suppressed in the thinnest, $[\mathrm{Co/Pt}]_3$ multilayer. Calculations of the laser induced temperature rise hint at a temperature rise close to T_C, where critical phenomena, such as a diverging susceptibility and heat capacity, may influence a further increase of $-\Delta M_z^{\max}/M_{z,0}$ (section 5.4.1.2). According to recent findings, an energy flow from the spin system back to the electron system on ultrafast time scales could further contribute to this suppression of $-\Delta M_z^{\max}/M_{z,0}$ at high fluences [280]. Full demagnetization was finally achieved in the thinnest, $[\mathrm{Co/Pt}]_3$ multilayer using a fluence of $F^3_{\mathrm{nIR}} = 18.9\,\mathrm{mJ/cm^2}$, which was close to the destruction threshold of the sample.

The maximum degree of demagnetization was found to be independent from the nIR-laser polarization, i. e., polarization dependent absorption (MCD) has a minor influence on $-\Delta M_z^{\max}/M_{z,0}$ in magnetic multi-domain states (section 5.4.5.1). When increasing the pulse duration from $\tau^1_{\mathrm{nIR}} = 70\,\mathrm{fs}$ to $\tau^2_{\mathrm{nIR}} = 300\,\mathrm{fs}$, the maximum degree of demagnetization was found to be reduced from $\approx 60\%$ to $\approx 40\%$, using F^2_{nIR}. This reduction, to a certain extent, agrees with theoretical descriptions, where a dependence of $-\Delta M_z^{\max}/M_{z,0}$ on the amplitude of the nIR-laser pulse is predicted.

Ultrafast Demagnetization: Modeling of the magnetization transients (section 5.4.2) reveals that the three different $[\mathrm{Co/Pt}]_x$ multilayers can be treated as a single, optically thin Co/Pt-multilayer system that undergoes laser-induced temperature rises $A_1 \propto -\Delta M_z^{\max}/M_{z,0}$ and $A_2 \propto T$.

The Co/Pt-multilayer system shows the expected type-I ultrafast demagnetization within a demagnetization time of $\tau_{\mathrm{M}} \approx 100\,\mathrm{fs}$ at low temperatures ($-\Delta M_z^{\max}/M_{z,0} \lesssim 30\%$), that increases to $\tau_{\mathrm{M}} \approx 150\,\mathrm{fs}$ for higher temperatures ($-\Delta M_z^{\max}/M_{z,0} \approx 60\%$) and remains almost constant for the highest reached temperature ($-\Delta M_z^{\max}/M_{z,0} \approx 100\%$) (Fig. 5.13). Except the temperature dependent increase, no differences within the fit errors are observed in τ_{M}, neither between the three magnetic multi-domain states nor when changing the nIR-laser polarization from linear to circular. The results can thus be understood by mere nIR-laser heating (polarization

independent absorption), i. e., by an initial non-equilibrium heating of the electron system that reaches thermal equilibrium with the spin system (the maximum degree of demagnetization) on a time scale of $\approx 100\,\mathrm{fs}$. As the data follow the same trend that is described within the M3TM, they support the picture of ultrafast demagnetization being induced by electron–phonon spin-flip scattering, with a spin-flip probability of $a_{\mathrm{sf}} \approx 0.1$ (section 2.5.1.3).

Energy Equilibration: The fast-recovery of magnetization is governed by energy equilibration between the electron, spin and lattice systems proceeding on a characteristic time scale of $\tau_{\mathrm{E}} = (0.64 \pm 0.09)\,\mathrm{ps}$ at low temperatures ($T = 380\,\mathrm{K}$), which is in agreement with reported low-temperature values in Co/Pt multilayers (section 5.4.4). The linear increase with temperature to $\tau_{\mathrm{E}} = (1.23 \pm 0.21)\,\mathrm{ps}$ at $T = 790\,\mathrm{K}$ is moreover in agreement with the low-fluence solution of the 3TM, where the energy equilibration time is approximated by the electron specific heat and the electron–phonon coupling parameter, $\tau_{\mathrm{E}}(T) \approx C_{\mathrm{e}}(T)/G_{\mathrm{e}\ell}$, with $C_{\mathrm{e}}(T) = \gamma T$ (section 2.5.1.2). At even higher temperatures, however, a drastic slowing down of the remagnetization dynamics is observed, i. e., the energy equilibration time strongly deviates from its linear behavior at low temperatures, reaching $\tau_{\mathrm{E}} = (3.24 \pm 0.25)\,\mathrm{ps}$ at $T \approx 1000\,\mathrm{K}$ (Fig. 5.14). Both the low and the high-temperature data can be modeled by including a spin contribution to $\tau_{\mathrm{E}}(T)$, taking into account recent theoretical predictions for the so-called slowdown time at high temperatures [180]. The spin contribution is given by the spin specific heat, $C_{\mathrm{s}}(T)$, which shows critical behavior at elevated temperatures, i. e., a divergence at T_{C}. The good agreement between model and data suggests that it is more accurate to describe the electron and spin system as a strongly coupled electron–spin system determining the energy equilibration time via $\tau_{\mathrm{E}}(T) = (C_{\mathrm{e}}(T) + C_{\mathrm{s}}(T))/G_{\mathrm{e}\ell}$.

6 Double-Pulse Induced Permanent Modifications in Nanoscopic Multi-Domain States of a Thin Co/Pt Multilayer

A further TR-mSAXS experiment at the DiProI beamline at FERMI@Elettra in Trieste was focused on studying ultrafast lateral modifications in nanoscopic magnetic multi-domain states of the $[Co/Pt]_6$ multilayer, which can be detected through changes in the peak position, Q_{peak}, and the width, w, of the magnetic scattering ring. On the one hand, it was reported that above a certain threshold fluence, laser-induced ultrafast demagnetization of nanoscopic multi-domain states (100 fs time scale) is accompanied by *transient* lateral modifications due to non-local superdiffusive spin transport [32, 34, 39]. On the other hand, the repetitive laser-pulse irradiation of a magnetic state may induce *permanent* lateral modifications, i. e., the nucleation and possible helicity-dependent growth of reversed domains, known as HD-AOS in ferromagnets (section 2.5.2). In that case, the initial nucleation processes mediated by thermal activation are stochastic in nature and thus do not proceed on ultrafast time scales. However, a consecutive helicity-dependent growth, e. g., due to an IFE-induced opto-magnetic field, would likely proceed during (the extended) magnetization recovery on a picosecond time scale [196].

Here, nanoscopic multi-domain states, ranging from the maze-domain ground state up to a close-to single-domain state, were investigated, with the idea to overcome the "problem" of initial domain nucleation and directly address a possible helicity-dependent growth of one type of domains over the other on a picosecond time scale. Emphasis was thereby laid on distinguishing between *transient* and *permanent* domain modifications. For that an FEL-reference image was recorded in-between two consecutive nIR-pump–XUV-probe images, which yields the information on the multi-domain configuration seconds after laser excitation (quasi-static).

According to recent micromagnetic and atomistic simulations based on the IFE, a high probability for HD-AOS in ferromagnets requires a high-enough laser fluence (threshold fluence) as well as a pulse duration in the picosecond regime (section 2.5.2). A large degree of demagnetization in the very same $[Co/Pt]_6$ multilayer was observed for a nIR-laser fluence of $F_{nIR} \gtrsim 10\,mJ/cm^2$ in the TR-mSAXS experiment at FLASH (Fig. 5.8 on p. 95). In such highly excited magnetic states the remagnetization dynamics significantly slow down, with an energy

equilibration time that extends over several picoseconds (Fig. 5.14 on p. 108). In order to ensure a high probability of AOS-like processes in the multi-domain states, nIR-laser pulses with a fluence of $F_{\mathrm{nIR}} = 13.4\,\mathrm{mJ/cm^2}$ and a pulse duration of $\tau_{\mathrm{nIR}} = 3500\,\mathrm{fs}$ were used.

A possible helicity dependence of the all-optically induced domain modifications was addressed by using left-circular (LCP) and right-circular polarized (RCP) nIR-laser pulses. In the maze-domain ground state, helicity-dependent differences in the degree of demagnetization due to the IFE (or MCD) are expected to be small due to an equal area filling of up and down-magnetized domains. In fact, in the maze-domain ground state no polarization dependence of the ultrafast magnetization dynamics was observed (section 5.4.5.1). Furthermore, no changes in the shape and position of $I_{\mathrm{norm}}(Q)$, that could be related to a helicity-dependent growth of one type of domains, were detected during ultrafast demagnetization of the maze-domain ground state. An imbalance in the area filling of up and down-magnetized domains was induced by OOP magnetic fields from the custom-made Helmholtz coils. Apart from changing the area filling of up and down-magnetized domains, the H_z field may support or counteract the IFE, depending on the helicity of the nIR-laser polarization.[1] The influence of magnetic fields on the maze-domain ground state was investigated in a dedicated pre-study at PETRA III, combining mSAXS with imaging of the multi-domain states using Fourier-transform holography (FTH) (section 6.1). By that, mere H_z-field induced changes in Q_{peak} and w could be identified in the TR-mSAXS experiment at FERMI and a link of the nIR-laser induced changes in Q_{peak} and w to lateral changes in the domain configuration could be made.

The multi-domain states, excited by the 3500 fs-long nIR-laser pulses, were probed by 70 fs-short XUV pulses from FERMI's FEL-1, tuned to resonance with the Co $M_{2,3}$ edge at a photon energy of $E_{\mathrm{ph}} = 59.8\,\mathrm{eV}$. Details on the nIR-laser and FEL pulse parameters as well as the FEL-reference–nIR-pump–XUV-probe mode are given in section 6.2, followed by a description on data processing in section 6.3. The outcome of the TR-mSAXS experiment is presented in section 6.4. While transient changes on ultrafast time scales could not be observed, permanent domain modifications that evolve independently from the ultrafast magnetization dynamics were detected. The modifications only occurred, however, if an OOP magnetic field was applied and both nIR and XUV-laser pulses irradiated the sample at the same time. The outcome shows that the FEL pulses do not probe the magnetic states non-invasively but they also interact with the sample. The distinct interplay between nIR and XUV radiation thereby suggests that the permanent modifications might be controlled by the temporal overlap and the photon energy of the light pulses. The results are summarized in section 6.5.

[1] Note that according to theoretical predictions, the IFE in ferromagnetic metals is not simply an antisymmetric effect in the light's helicity as commonly argued for absorption-free materials [189]. A helicity dependence, however, could stem from nomagnetic Pt in Co/Pt multilayers where the IFE-induced magnetization is predicted to be antisymmetric in the light's helicity.

6.1. Pre-Study at PETRA III: Impact of Magnetic Fields on the Maze-Domain Ground State

Prior to the TR-mSAXS experiment at FERMI the influence of external magnetic fields on the magnetic maze-domain ground state of $[Co/Pt]_6$ multilayers was studied by mSAXS in tandem with FTH at the P04 beamline at PETRA III in collaboration with the group of H. P. Oepen from the University of Hamburg. For that, the custom-made X-ray holographic microscope (XHM) end station (section 4.3) was installed at the P04 beamline. The end station was equipped with a magnet system to provide external **H** fields at the sample position with a strength of up to 145 mT in both IP and OOP directions. The magnetic multi-domain patterns were investigated by circularly polarized soft X-rays with a photon energy tuned to resonance with the Co L_3 edge ($E_{ph} = 778.2$ eV). Details on the XHM setup and the typically used experimental parameters at the P04 beamline can be found in Ref. [71].

In this pre-study, first, the influence of external **H** fields on the lateral configuration of the magnetic maze-domain ground state was studied in reciprocal space by mSAXS, via analysis of the maximum intensity, I_{max}, position, Q_{peak}, and width, w, of the (first-order) scattering ring. These quantities directly relate to ensemble-averaged information of the maze-domain patterns, i. e., the average domain periodicity, $T_{av} = 2\pi/Q_{peak}$, and the lateral correlation length, $\xi = 2\pi/w$ (section 2.4.4). Second, the effect of external **H** fields on the maze-domain ground state was imaged via FTH with a spatial resolution of ≈ 10 nm which allows to directly connect changes in Q_{peak} and w to lateral modifications in the multi-domain patterns. The aim of this pre-study was to evaluate mere **H**-field induced effects on I_{max}, T_{av} and ξ, in order to be able to distinguish between **H**-field and laser induced effects in the time-resolved measurements at FERMI.

The sample in this pre-study was a $[Co/Pt]_6$-multilayer wedge measured at a composition of $[Co(1.3)/Pt(2.0)]_6$ for OOP magnetic fields and a composition of $[Co(1.6)/Pt(2.0)]_6$ for IP magnetic fields. Hence, the magnetic maze-domain patterns in this pre-study exhibit slightly different characteristics through T_{av} and ξ as well as a different susceptibility to external magnetic fields, compared to the much thinner $[Co(0.8)/Pt(1.4)]_6$ multilayer that was investigated in the main time-resolved mSAXS study at FERMI, as shown in section 6.4.1.

6.1.1. In-Plane Magnetic Fields

The impact of increasing in-plane (IP) magnetic fields, $\mathbf{H} = (H_x,0,0)$, on the maze-domain ground state of the $[Co(1.6)/Pt(2.0)]_6$ multilayer is presented in Fig. 6.1. The reconstructed images from FTH show the impact of increasing H_x fields on the multi-domain pattern in real space (Fig. 6.1 a)), the scattering images, $I(Q,\Phi)$, obtained after resetting the maze-domain ground-state by OOP demagnetization cycles and applying the same H_x fields, show the

Table 6.1.: Fit parameters obtained by fitting a split Pearson type-VII function to the first-order magnetic scattering peak from the $[Co(1.6)/Pt(2.0)]_6$ multilayer for increasing IP magnetic fields. Also included are the calculated average domain period, $T_{av} = 2\pi/Q_{peak}$, the lateral correlation length, $\xi = 2\pi/w$, and the ratio ξ/T_{av}, which is a measure for the degree of order in the magnetic multi-domain patterns

IP	0 mT	50 mT	140 mT
I_{max} (ADU)	1984±11	2800±18	3507±30
Q_{peak} (10^{-3} nm^{-1})	43.7±0.1	49.0±0.1	52.0±0.1
w (10^{-3} nm^{-1})	10.9±0.3	11.4±0.4	9.8±0.4
T_{av} (nm)	144±1	128±1	121±1
ξ (nm)	576±16	551±19	641±26
ξ/T_{av}	4.00±0.11	4.30±0.15	5.30±0.21

corresponding situation in reciprocal space (Fig. 6.1 b)).[2] In order to extract ensemble-averaged information on the multi-domain states, i. e., the average domain periodicity, T_{av}, and the lateral correlation length, ξ, the scattering images were azimuthally averaged around the beam center in a restricted angular range, i. e., along the direction of the high-intensity lobs (see 140 mT case). The resulting $\langle I(Q)\rangle_\Phi$ are shown in Fig. 6.1 c), together with fits to the first-order magnetic scattering peak by a split Pearson type-VII function (section 5.3.1).

The maze-domain ground state ($\mu_0 H_x = 0$ mT) shows the expected equal area filling of up and down-magnetized domains, which is referred to as the *symmetric* domain configuration in the following (filling ratio of 1:1). Due to the disordered nature of the maze-domain pattern, the corresponding scattering intensity, $I(Q,\Phi)$, is equally distributed in all lateral directions in the shape of a ring, with intensity maxima at positions $Q_n = n \cdot 2\pi/T_{av}$. Note that, even at $\mu_0 H_x = 0$ mT a small anisotropy is present in the scattering ring, with a preferred alignment along the x-direction. This is presumably due to insufficient OOP demagnetization cycles with a maximum field of $\mu_0 H_z = 140$ mT after aligning the domains in stripes. From fitting the first-order scattering peak, an average domain periodicity of $T_{av} = (144 \pm 1)$ nm is found in the maze-domain ground state of the $[Co(1.6)/Pt(2.0)]_6$ multilayer corresponding to an average domain size of $D_{av} = T_{av}/2 = 72$ nm. The comparably narrow width of the scattering ring, corresponding to a lateral correlation length of $\xi = (576 \pm 16)$ nm, reveals a short-range order over a distance of 4.00 ± 0.11 times the domain periodicity in the disordered maze-domain ground state. Due to this substantial short-range order, a non-vanishing 3rd-order magnetic scattering intensity is observed, while due to the equal area filling of up and down-magnetized domains (symmetric domain configuration), the 2nd-order magnetic scattering intensity is strongly suppressed (section 2.4.4). The fit parameters from fitting a split Pearson type-VII function to the first-order magnetic scattering peak, $\langle I(Q)\rangle_\Phi$, are summarized in table 6.1.

[2] Note that in FTH the field-of-view is defined by the object hole, which is about 2 µm in diameter, whereas in mSAXS, the field-of-view is defined by the X-ray beam size of $\lesssim (100 \times 100)\,\mu m^2$.

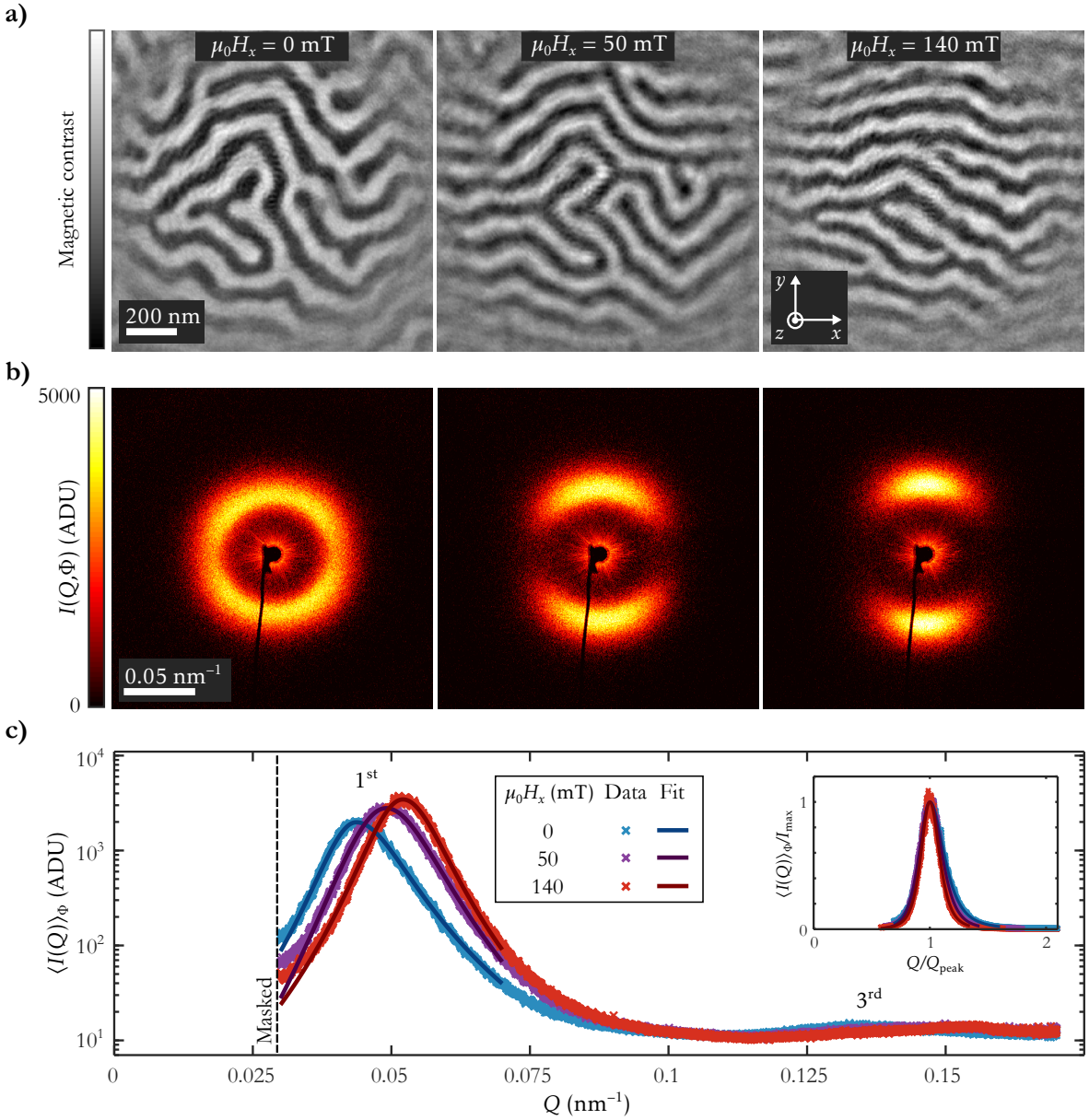

Figure 6.1.: Impact of increasing IP magnetic fields, $\mu_0 H_x = 0$, 50 and 140 mT, on the maze-domain ground state of the $[Co(1.6)/Pt(2.0)]_6$ multilayer. a) Magnetic holograms obtained via FTH. Bright and dark contrast show the up and down-magnetized domains (magnetization oriented parallel or antiparallel to the z-direction). Increasing IP magnetic fields couple to the IP component of the magnetic domain-walls, resulting in an alignment of the magnetic domains along the external field direction. b) Corresponding scattering images, $I(Q,\Phi)$, obtained by mSAXS. c) Azimuthally averaged scattering intensity, $\langle I(Q)\rangle_\Phi$, for the three H_x-field conditions. Note that only regions along the high-intensity lobs were considered for the averaging procedure. The inset shows the $\langle I(Q)\rangle_\Phi$ normalized to both the maximum intensity, I_{max}, and the position of the maximum intensity, Q_{peak}.

For increasing H_x fields (hard-axis direction), the disordered maze-domain pattern is subsequently transformed into a stripe-domain pattern (Fig. 6.1 a)). A high magnetic contrast in all the three holograms is evidence for a still large magnetization component along the z-direction, i. e, the H_x-field induced tilt of the magnetization towards the IP direction is small as H_x is far below the saturation field. At an applied H_x field, the IP components in the domain walls align parallel to H_x, thereby minimizing the total free energy via minimizing the Zeeman energy contribution (section 2.2). As the stripe domains and the domain walls reorient parallel to the x-direction (Fig. 6.1 a), right panel), the magnetization within the domain walls rotates within the wall plane (x-z-plane), i. e., the domain walls exhibit Bloch-wall character (section 2.3).

The transition from maze to stripe-domain pattern from $\mu_0 H_x = 0\,\mathrm{mT}$ to $\mu_0 H_x = 140\,\mathrm{mT}$ is seen in reciprocal space by a change of the scattering distribution, $I(Q,\Phi)$, from a uniform ring to two confined lobs, oriented perpendicular to the direction of the stripe domains. Due to this alignment, firstly, a larger magnetic scattering intensity is measured along the direction of the two lobs, increasing by $\approx 76\%$. Secondly, the width of the scattering peak, w, is reduced which relates to an increase in the lateral correlation length by $\approx 11\%$. Thirdly, the reorientation of the magnetic domains into stripes is found to be accompanied by an increasing radius of the scattering distribution, i. e., a reduction of the average domain periodicity by $\approx 16\%$. For all H_x-field strenghts, the multi-domain systems have a symmetric domain configuration, resulting in a suppression of the 2^{nd}-order magnetic scattering intensity, and a substantial short-range order, resulting in a detectable 3^{rd}-order magnetic scattering intensity. From the evolutions of T_{av} and ξ with H_x field, an increasing short-range order from $\xi/T_{\mathrm{av}} = 4.00 \pm 0.11$ in the maze-domain pattern ($\mu_0 H_x = 0\,\mathrm{mT}$) to $\xi/T_{\mathrm{av}} = 5.30 \pm 0.21$ in the stripe-domain pattern ($\mu_0 H_x = 140\,\mathrm{mT}$) is found. Normalizing all curves with respect to their maximum intensities and Q_{peak} positions (inset in Fig. 6.1 c)), consequently, shows a decreasing peak width for increasing H_x field. As all curves exhibit a comparable shape (the curves do not intersect at the flanks), it can further be assumed that no significant change in the distribution of length scales occurs.

6.1.2. Out-of-Plane Magnetic Fields

The impact of out-of-plane (OOP) magnetic fields, $\mathbf{H} = (0,0,H_z)$, on the maze-domain ground state was studied on a position of the sample that corresponds to a multilayer composition of $[\mathrm{Co}(1.3)/\mathrm{Pt}(2.0)]_6$. The reconstructed holograms from FTH for $\mu_0 H_z = 0\,\mathrm{mT}$, $\mu_0 H_z = 50\,\mathrm{mT}$ and $\mu_0 H_z = 100\,\mathrm{mT}$, the corresponding scattering images from mSAXS, and the fits to the first-order magnetic scattering peaks of the azimuthally averaged scattering distributions, $\langle I(Q)\rangle_\Phi$, are shown in Fig. 6.2 a)–c), respectively.

After OOP demagnetization cycles and in the absence of a magnetic field ($\mu_0 H_z = 0\,\mathrm{mT}$),

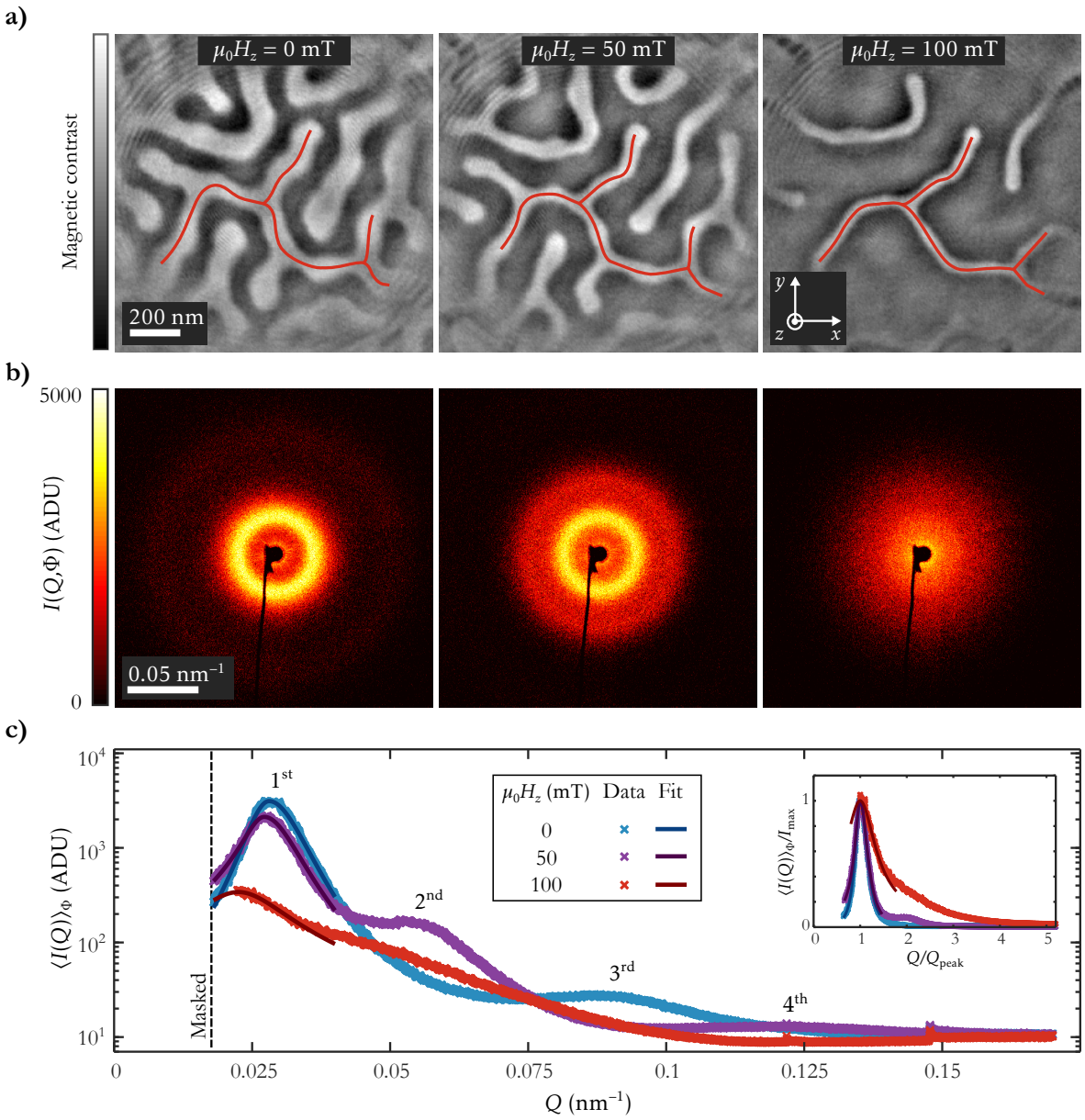

Figure 6.2.: Impact of increasing OOP magnetic fields, $\mu_0 H_z$ = 0, 50 and 100 mT, on the maze-domain pattern of the $[Co(1.3)/Pt(2.0)]_6$ multilayer. a) Magnetic holograms obtained via FTH. Bright and dark contrast show the up and down-magnetized domains (magnetization oriented parallel or antiparallel to the z-direction). Increasing OOP magnetic fields promote the growth of magnetic domains that are oriented parallel to the field direction, inducing an increasing asymmetry in the area filling between up and down-magnetized domains. b) Corresponding scattering images, $I(Q,\Phi)$, obtained by mSAXS. c) Azimuthally averaged scattering intensity, $\langle I(Q)\rangle_\Phi$, for the three H_z-field conditions. The inset shows $\langle I(Q)\rangle_\Phi$ normalized to the maximum intensity, I_{max}, and the position of the maximum intensity, Q_{peak}.

Table 6.2.: Fit parameters obtained by fitting a split Pearson type-VII function to the first-order magnetic scattering peak from the $[Co(1.3)/Pt(2.0)]_6$ multilayer for increasing OOP magnetic fields. Also included are the calculated average domain period, $T_{av} = 2\pi/Q_{peak}$, the lateral correlation length, $\xi = 2\pi/w$, and the fraction ξ/T_{av}, which is a measure for the degree of order in the magnetic multi-domain patterns

OOP	0 mT	50 mT	100 mT
I_{max} (ADU)	3144±19	2149±16	343±5
Q_{peak} (10^{-3}nm^{-1})	28.0±0.1	27.1±0.1	22.5±0.4
w (10^{-3}nm^{-1})	8.7±0.3	9.5±0.4	20.3±1.0
T_{av} (nm)	224±1	232±1	279±3
ξ (nm)	722±25	661±28	310±15
ξ/T_{av}	3.22±0.11	2.85±0.12	1.11±0.05

the expected maze-like domain pattern with a symmetric domain configuration is obtained (Fig. 6.2 a)). Due to the lower total Co content and thus a lower stray-field energy for a multilayer composition of $[Co(1.3)/Pt(2.0)]_6$, as compared to a composition of $[Co(1.6)/Pt(2.0)]_6$ in the previous section 6.1.1, the maze-domain pattern develops larger domains. As before, the ensemble-averaged information is extracted from the corresponding scattering images obtained by mSAXS (Fig. 6.2 b)), by fitting the azimuthally averaged first-order magnetic scattering peak with a split Pearson type-VII function (Fig.6.2 c)). From that, an average domain periodicity of $T_{av} = (224 \pm 1)$ nm, that corresponds to an average domain size of $D_{av} = 112$ nm, is obtained for the maze-domain ground state. A narrow scattering peak, which corresponds to a lateral correlation length of $\xi = (722 \pm 25)$ nm, reveals a short-range order over a distance of 3.22 ± 0.11 times the average domain periodicity, which is slightly reduced as compared to the thicker multilayer composition on the wedge. However, the scattering distribution for $\mu_0 H_z = 0$ mT also shows a substantial 3rd-order magnetic scattering intensity, as well as a strongly suppressed 2nd-order magnetic scattering intensity, reflecting the symmetric domain configuration. The fit parameters from fitting the first-order scattering peak of $\langle I(Q)\rangle_\Phi$ are summarized in table 6.2.

For increasing OOP magnetic fields (easy-axis direction) of $\mu_0 H_z = 50$ mT and $\mu_0 H_z = 100$ mT an increasing imbalance in the area filling of up and down-magnetized domains is induced, which is referred to as the *asymmetric* domain configuration in the following. The domains with a magnetization directed along the external field direction (dark color in the magnetic holograms) are referred to as *majority* domains, the domains with a magnetization opposite to the external field direction (bright color in the magnetic holograms) are referred to as *minority* domains. At an applied H_z field, OOP components in the magnetic domains align in parallel with H_z, minimizing the total free energy via minimizing the Zeeman energy contribution (section 2.2). As a consequence, for increasing H_z fields, the imbalance of majority to minority domains increases, eventually reaching the single-domain configuration. While

the overall configuration of the maze-domain pattern is largely preserved for $\mu_0 H_z = 50\,\mathrm{mT}$, only few minority domains remain magnetized opposite to the external field for $\mu_0 H_z = 100\,\mathrm{mT}$ (close-to single-domain state). These remaining minority domains may be energetically stabilized most likely due to pinning at structural defects and thus, to a certain extent, withstand the increasing H_z field. The red lines in Fig. 6.2 a) indicate one domain that retains its original shape upon increasing the H_z field.

The increasing asymmetry in the multi-domain pattern for increasing H_z fields is identified by mSAXS via obvious changes in the magnetic scattering distribution, as shown in Fig. 6.2 b). In the slightly asymmetric domain configuration ($\mu_0 H_z = 50\,\mathrm{mT}$) only minor changes in the first-order magnetic scattering ring are observed, i. e., its shape remains largely unchanged, as shown by the $\langle I(Q/Q_{\mathrm{peak}})\rangle_\Phi / I_{\mathrm{max}}$ in the inset of Fig. 6.2 c). Firstly, the growth of majority over minority domains is seen by a reduction of the maximum scattering intensity by $\approx 32\%$ which can be understood by the reduced number of minority domains, i. e., a reduced number of magnetic scatterers. Secondly, slight changes in the shape of the first-order magnetic scattering peak are observed, i. e., an increase of the average domain periodicity by $\approx 4\%$ and a reduction of the lateral correlation length by $\approx 8\%$, which yield a slightly reduced short-range order over a distance of 2.85 ± 0.12 times the average domain periodicity. Thirdly, the condition for a strongly suppressed 2^{nd}-order magnetic scattering intensity in the symmetric domain configuration ($\mu_0 H_z = 0\,\mathrm{mT}$) is uplifted in the asymmetric domain configurations. Instead, the intensity in the 3^{rd}-order magnetic scattering peak is suppressed for $\mu_0 H_z = 50\,\mathrm{mT}$ which is indicative for a filling ratio of up to down-magnetized domains of approximately 2:1, as seen in the simulations in section 2.4.4 and reported in Ref. [119].

Further increasing the magnetic field to $\mu_0 H_z = 100\,\mathrm{mT}$ results in a further growth of the majority domains and a complete break-up of the maze-domain pattern. As only a few isolated minority domains remain pinned to structural defects for $\mu_0 H_z = 100\,\mathrm{mT}$, i. e., as the domain configuration is close to the single-domain state, the maximum scattering intensity in the first-order scattering peak is strongly reduced by $\approx 90\%$ as compared to the $\mu_0 H_z = 0\,\mathrm{mT}$ case. Such a strong reduction of I_{max} at high H_z fields can be expected from the H_z-field dependence of the magnetic scattering intensity in Co/Pt-based multilayers (Fig. 2.8 on p. 29). Moreover, the shape of the first-order magnetic scattering peak has drastically changed, as shown by the $\langle I(Q/Q_{\mathrm{peak}})\rangle_\Phi / I_{\mathrm{max}}$ in the inset of Fig. 6.2 c). An increase of the average domain periodicity by $\approx 25\%$ and a reduction of the lateral correlation length by $\approx 57\%$ leads to a strongly reduced short-range order over a distance of only 1.11 ± 0.05 times the average domain periodicity. The magnetic domain structure can thus no longer be seen as a (correlated) multi-domain pattern, but rather has to be seen as a composition of uncorrelated minority domains in an extended majority domain (island-like domain structure).

The results from the pre-study at PETRA III, utilizing mSAXS in tandem with FTH to study the impact of magnetic fields on the maze-domain ground state of $[\mathrm{Co/Pt}]_6$ multilayers, are

summarized as follows. Upon increasing IP magnetic fields, the maze-domain pattern is transformed to a stripe-domain pattern with significantly increased short-range order. The shape of $\langle I(Q/Q_{\mathrm{peak}})\rangle_{\Phi}/I_{\mathrm{max}}$, however, remains largely unchanged showing that no significant changes in the distribution of length scales occurs for increasing IP magnetic fields. Upon increasing OOP magnetic fields, an increasing imbalance in the area filling of up and down-magnetized domains is induced. The shape of (the first-order) $\langle I(Q/Q_{\mathrm{peak}})\rangle_{\Phi}/I_{\mathrm{max}}$ remains largely unchanged for $\mu_0 H_z = 50\,\mathrm{mT}$. The vanishing of the 3$^{\mathrm{rd}}$ order and the appearance of the 2$^{\mathrm{nd}}$ order scattering peak indicate that in this slightly asymmetric maze-domain pattern, an asymmetry in the area filling of majority and minority domains of approximately 2:1 is present. When increasing the magnetic field to $\mu_0 H_z = 100\,\mathrm{mT}$ the domain pattern is transformed to the close-to single-domain state, which is seen in reciprocal space by a drastic change in the shape of $\langle I(Q/Q_{\mathrm{peak}})\rangle_{\Phi}/I_{\mathrm{max}}$ and a reduction of the short-range order to $\xi/T_{\mathrm{av}} \approx 1$.

Symmetric maze-domain, slightly asymmetric multi-domain and close-to single-domain patterns were also investigated in the time-resolved mSAXS experiment at FERMI, which is presented in the following sections. First, the nIR-laser and FEL pulse parameters, that were used to excite the different multi-domain states are presented, followed by a description of the FEL-reference–nIR-pump–XUV-probe mode (section 6.2). A short description on data processing is given in section 6.3 and the experimental results are discussed in section 6.4. In the thinner, $[\mathrm{Co}(0.8)/\mathrm{Pt}(1.4)]_6$ multilayer, a slight asymmetry is induced already at $\mu_0 H_z = 5\,\mathrm{mT}$ and $\mu_0 H_z = 15\,\mathrm{mT}$, and the close-to single-domain state is generated by $\mu_0 H_z = 25\,\mathrm{mT}$, which is identified by comparing the evolution of I_{max}, Q_{peak} and w with H_z field to the results obtained in this pre-study.

6.2. Experimental Parameters and Measurement Procedure

In the TR-mSAXS experiment at the DiProI beamline at FERMI, the dynamics in nanoscopic multi-domain states of a $[\mathrm{Co}(0.8)/\mathrm{Pt}(1.4)]_6$ multilayer was studied, where an asymmetry in the maze-domain ground state was induced by pulsed H_z fields from the custom-made Helmholtz coils (section 4.2.2). Picosecond-long and high-intensity nIR-laser pulses were furthermore used to excite the magnetic multi-domain states in a FEL-reference–nIR-pump–XUV-probe mode. The used XUV and nIR-laser pulse parameters are given in the following section 6.2.1 and details on the FEL-reference–nIR-pump–XUV-probe mode are given in section 6.2.2.

6.2.1. XUV and nIR-Laser Pulse Characteristics

FERMI's FEL-1 was tuned to provide 70 fs-short, circularly polarized XUV pulses with a photon energy tuned to resonance with the Co $M_{2,3}$ edge at $E_{\mathrm{ph}} = 59.8\,\mathrm{eV}$. The FEL beam profile, measured close to the sample position via a fluorescent screen, is shown in Fig. 6.3 a). The

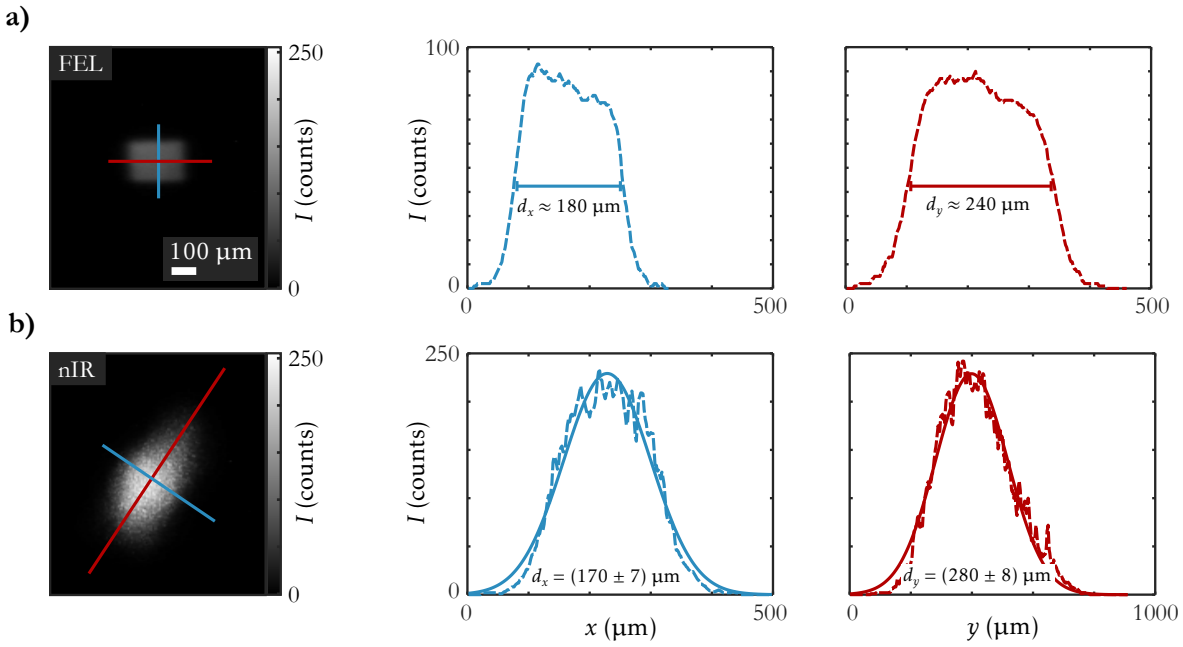

Figure 6.3.: a) FEL and b) nIR-laser pulse profiles measured by a fluorescent screen. The beam sizes in x (blue) and y-direction (red) are evaluated from linecuts through high-intensity regions of the beam profiles: in a) the widths of the flat-top like FEL profiles are extracted manually at half the maximum intensity. In b) the widths of the nIR-laser profiles at FWHM are determined by a Gaussian function.

beam size was determined from linecuts along the x and y-direction through the flat-top like intensity profile, resulting in $d_{x,y} \approx (180 \times 240)\,\mu m^2$ (FWHM).

Throughout the experiment, the FEL-pulse energy was fluctuating between (15–25) µJ. Up to the end station, the FEL-pulse energy was reduced to ≈ 60%[3] due to the beamline optics and was further attenuated by two 100 nm thin solid-state aluminum and zirconium absorbers with a transmission of 87% and 15%, respectively. The combination of the two filters is moreover efficiently blocking higher-harmonic radiation produced by the undulator, alongside with residual UV seed-laser radiation propagating along the XUV beam path. From the attenuated FEL-pulse energy and the FEL beam size, the FEL fluence on the sample has a calculated value of $F_{FEL} = (4.2\text{–}7.0)\,mJ/cm^2$, assuming an elliptically shaped pulse profile.

For the nIR-pump–XUV-probe experiments, left-circularly (LCP) and right-circularly (RCP) polarized nIR-laser pulses with a pulse duration of $\tau_{nIR} = 3500$ fs were used to excite the magnetic multi-domain patterns of the $[Co/Pt]_6$ multilayer. The size of the nIR-laser beam was $d_{x,y} \approx (170 \times 280)\,\mu m^2$ (FWHM), determined by using the same fluorescent screen as for the FEL beam (Fig. 6.3 b)). Note that the nIR-laser beam size was almost the same as the FEL beam size, resulting in a non-homogeneous excitation of the probed area. The experiments were conducted using a nIR-laser pulse energy of 5.0 µJ, corresponding to

[3] FERMI lightsource: https://www.elettra.trieste.it/lightsources/fermi/fel1-2-parameters.html.

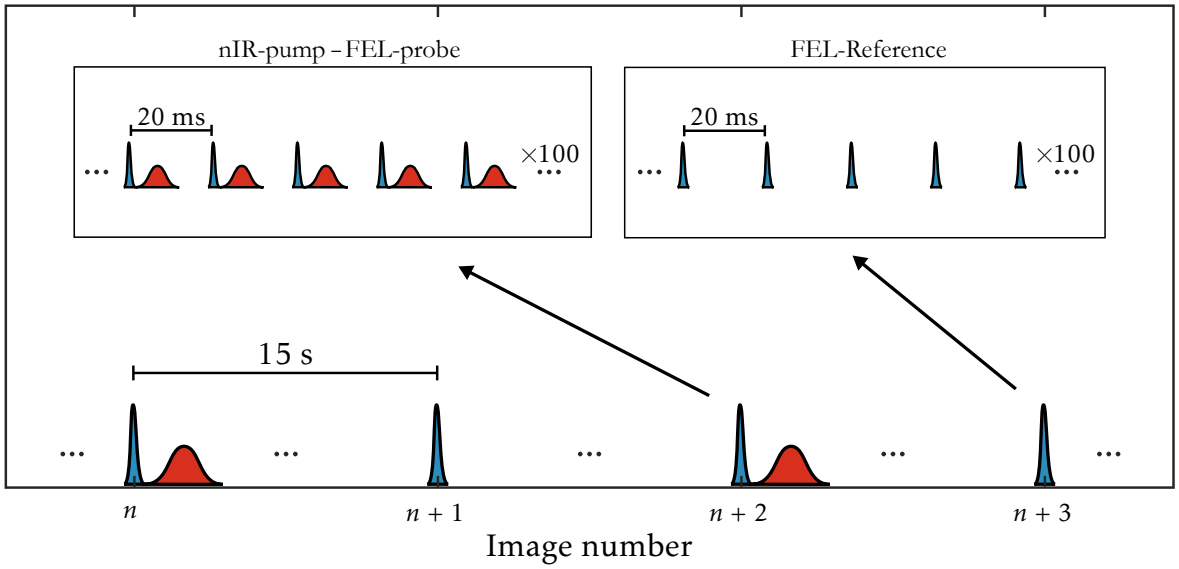

Figure 6.4.: Illustration of the control–pump–probe scheme. Both nIR-pump–FEL-probe and FEL-reference images are composed of the accumulated intensity from 100 FEL-pulse exposures (repetition rate 50 Hz). FEL-reference images were taken in-between nIR-pump–FEL-probe images, with a delay time of ≈ 15 s that is mainly determined by the readout time of the CCD camera. Thus the FEL-reference images act as control measurements, probing whether or not the magnetic multi-domain state has relaxed back to its initial configuration upon repetitive nIR-laser and FEL-pulse irradiation.

a nIR-laser fluence of $F_{\mathrm{nIR}} = 13.4\,\mathrm{mJ/cm^2}$, assuming an elliptically shaped pulse profile. The nIR-laser pulse energy was fluctuating by less than ±2% throughout the duration of the beamtime. Prior to the time-resolved measurements, a nIR-laser pulse energy of 15 µJ, corresponding to a fluence of $F_{\mathrm{nIR}} = 40.2\,\mathrm{mJ/cm^2}$, was used to quench the magnetic scattering signal in the $[\mathrm{Co/Pt}]_6$ multilayer down to ≈ 25% in order to determine the charge-scattering background (section 6.3.3). Note that this fluence is about a factor of two higher as compared to the fluence of $F_{\mathrm{nIR}} = 18.9\,\mathrm{mJ/cm^2}$ for which full demagnetization was obtained in the $[\mathrm{Co/Pt}]_3$ multilayer (section 5.2.3). The main reason for achieving only a partial demagnetization by such high fluences is the almost twice as thick sample, so that the buried layers are exposed to a significantly smaller effective fluence (see section 2.5.1.6).

6.2.2. FEL-Reference–nIR-Pump–XUV-Probe Mode

The TR-mSAXS experiment was conducted in multi-pulse mode, exposing the $[\mathrm{Co/Pt}]_6$ multilayer to 100 consecutive nIR-pump–XUV-probe pulses at a repetition rate of 50 Hz (20 ms between two pump-probe events) to obtain a scattering image, i. e., the exposure time was 2 s. The pulse scheme of the experiment is illustrated in Fig. 6.4. Using a higher nIR-laser fluence of $F_{\mathrm{nIR}} = 13.4\,\mathrm{mJ/cm^2}$ and a higher repetition rate, as compared to the TR-mSAXS experiment at FLASH (10 Hz), might result in a warming-up of the sample during the acquisition of a

scattering image (appendix A.1). A warming-up could result in gradual rearrangements in the multi-domain pattern affecting the maximum intensity, I_{max}, position, Q_{peak}, and width, w, of the (first-order) magnetic scattering ring. In order to identify whether such slow and permanent domain rearrangements occurred, an additional scattering image was acquired in-between two consecutive nIR-pump–XUV-probe images, where the nIR-laser was blocked by a shutter. Taking into account the time to change the delay time as well as the camera read-out time, the time difference between a *FEL-reference* and a nIR-pump–XUV-probe image was $\approx 15\,s$. The FEL-reference image thus shows the multi-domain configuration $\approx 15\,s$ after (before) the last (next) nIR-pump–XUV-probe event. A sequence of the FEL-reference–nIR-pump–XUV-probe measurements on the magnetic multi-domain state of the $[Co/Pt]_6$ multilayer at a magnetic field of $\mu_0 H_z = 15\,mT$ is shown for selected delay times, Δt, in Fig. 6.5.

At negative delay times, both FEL-reference and nIR-pump–XUV-probe images show a scattering ring of the same size and intensity. Noticeable domain rearrangements or a reduction of the magnetization were thus not observed for a nIR-laser fluence of $13.4\,mJ/cm^2$ (20 ms between nIR-pump and XUV-probe at negative delay times). At positive delay times, $\Delta t \gtrsim 0$, the nIR-pump–XUV-probe images show a reduced magnetic scattering intensity due to ultrafast demagnetization followed by the recovery of magnetization on a pico to nanosecond time scale (Fig. 6.5 b)). At the same time, the magnetic scattering intensity in the FEL-reference images remains largely constant, showing that the magnetization has fully recovered to its original value ($\Delta t < 0$) within 15 s after the 100 nIR-pump–XUV-probe exposures.[4] The FEL-reference images are analyzed in the same way as the nIR-pump–XUV-probe images (section 6.3). They are vital in distinguishing between ultrafast transient and slow permanent lateral modifications induced by the combined action of nIR-laser and XUV pulses, as discussed in section 6.4.3.

Using pulsed H_z fields generated by the custom-made Helmholtz coils (Fig. 4.4 on p. 73), synchronized to the 50 Hz repetition rate of FERMI (section 4.2.2), an asymmetry was induced in the magnetic maze-domain ground state of the $[Co/Pt]_6$ multilayer. It is noted that, due to the relatively small maximum applicable field of $\mu_0 H_z \approx 50\,mT$ compared to a saturation field of $\mu_0 H_s \approx 200\,mT$, no complete in-situ demagnetization could be conducted during the experiment. The delay-time scans were first recorded for zero external field, followed by measurements at gradually increasing fields in steps of 5 mT and 10 mT. The delay time, Δt, was changed in the range of $-10\,ps \leq \Delta t \leq 200\,ps$ with a varying step size of 500 fs (demagnetization regime), 2 ps (fast-recovery regime) and 5 ps (slow-recovery regime). Using a larger delay-time range up to $\Delta t = 200\,ps$, this experiment was focused on lateral modifications in the magnetic multi-domain states during the extended magnetization recovery on picosecond time scales.

[4] Note that the images shown in Fig. 6.5 are not normalized to the incoming FEL-pulse intensity.

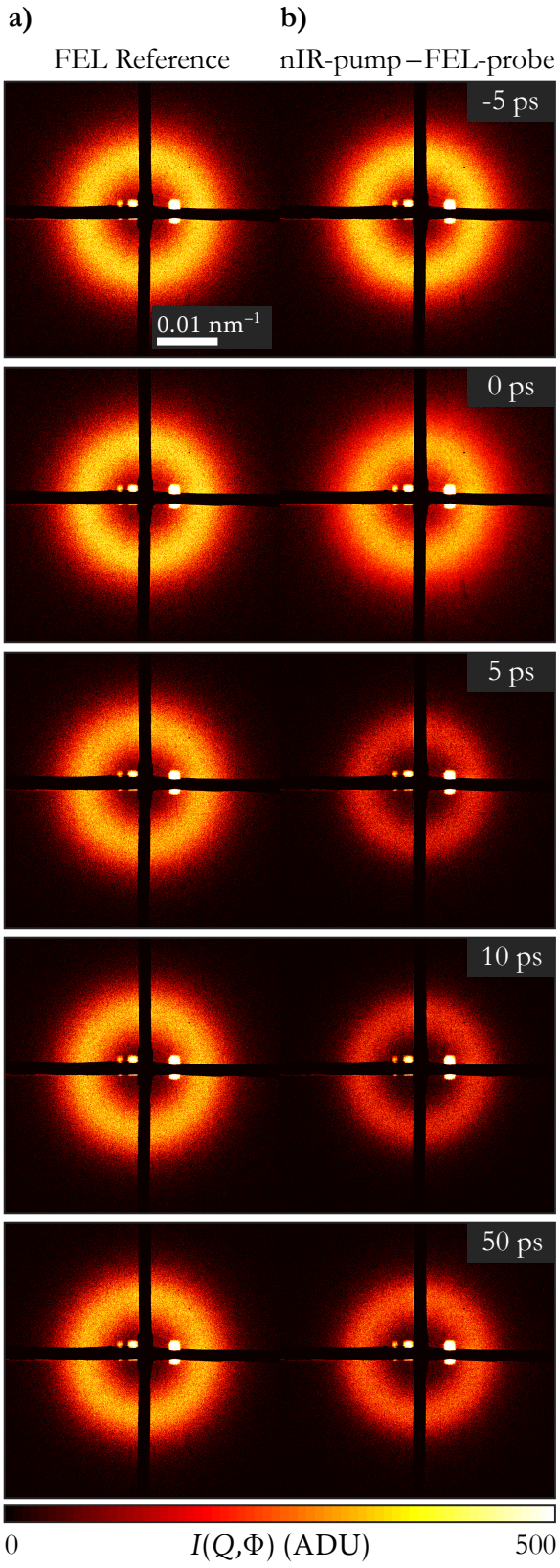

Figure 6.5.: Sequence of a) FEL-reference and b) nIR-pump–FEL-probe measurements on the $[Co/Pt]_6$ multilayer for selected delay times, Δt. Magnetic field pulses, $\mu_0 H_z = 15\,\mathrm{mT}$, synchronized to the FEL pulses at 50 Hz were applied at the sample, inducing an asymmetry in the area filling of up and down-magnetized domains in the maze-domain ground state. The multi-domain state was excited by LCP nIR-laser pulses with a pulse duration of 3500 fs and a fluence of $13.4\,\mathrm{mJ/cm^2}$. Each scattering image contains the accumulated scattering intensity from 100 FEL-pulse exposures. Images are plotted on a logarithmic scale.

6.3. Data Processing

In general, the procedure for treating the data is the same as the one in the TR-mSAXS experiment at FLASH (section 5.2). The charge-scattering background, however, has to be determined independently, as it depends on the experimental setup and a full quenching of the magnetic scattering intensity could not be achieved in the here used thicker sample. Thus, the individual steps of how the scattering data were processed in this TR-mSAXS experiment is briefly outlined in the following sections, starting with masking and dark correction in section 6.3.1, followed by normalization in section 6.3.2 and the evaluation of the charge-scattering background in section 6.3.3.

6.3.1. Masking and Dark Subtraction

The scattering image from the $[Co/Pt]_6$ multilayer, obtained by accumulating the scattered intensity from 100 FEL-pulse exposures at a negative delay time of $\Delta t = -5\,\mathrm{ps}$ and an external magnetic field of $\mu_0 H_z = 0\,\mathrm{mT}$, is exemplarily shown in Fig. 6.6 a). The scattered intensity, $I(Q,\Phi)$, from the magnetic maze-domain ground state, obtained by OOP demagnetization cycles prior to the experiment (section 3.2.3), has the expected shape of a ring. First, the scattering image was corrected by a dark image of the same exposure time, i. e., 2 s (denoted as "Raw" in Fig. 6.6 a)). Second, parasitic scattering features, such as the high-intensity streaks from the membrane edges close to $Q = 0$, are masked prior further analysis (denoted as "Masked" in Fig. 6.6 a)).

It is worth mentioning that a larger magnetic scattering intensity was obtained in this experiment as compared to the TR-mSAXS experiment at FLASH, with a maximum scattering intensity of $I_{max} = (394 \pm 1)\,\mathrm{ADU}$ and a total number of magnetically scattered photons of $I_{tot} \approx (3\text{–}5)\cdot 10^5$ photons/pulse. An incoming FEL-pulse energy at the sample position of $\approx (1.2\text{–}2.0)\,\mu\mathrm{J}$ corresponds to a total number of incoming photons of $I_{in} \approx (1.2\text{–}2.0)\cdot 10^{11}$ photons/pulse at a photon energy of $E_{ph} = 59.8\,\mathrm{eV}$. The magnetic scattering efficiency of the $[Co/Pt]_6$ multilayer of $\rho_{RMS} = I_{tot}/I_{in} \approx (1.5\text{–}4.2)\cdot 10^{-6}$ is about a factor of 10 less than the theoretical value (section 2.4.5), but also about a factor of 2–8 higher than in the TR-mSAXS experiment at FLASH (section 5.3.2).[5] The main reason for this significant increase is believed to be connected to the smaller bandwidth at FERMI of $\approx 0.05\%$ [236] compared to $\approx 1\%$ at FLASH [221] and thus a more stable operation at the resonance energy. Considering that the Co $M_{2,3}$ edge has a resonance width of (1–2) eV (Fig. 2.5 a) on p. 22), fluctuations in the photon energy of $\approx 0.6\,\mathrm{eV}$ at FLASH might lead to substantial pulse-to-pulse variations in the magnetic scattering intensity and thus a reduced total magnetic scattering intensity when accumulating 100 FEL-pulse exposures. In contrast, pulse-to-pulse fluctuations in the photon energy of

[5] Note that the very same $[Co/Pt]_6$-multilayer sample and the same type of CCD camera were used in both experiments, ensuring the comparability of results.

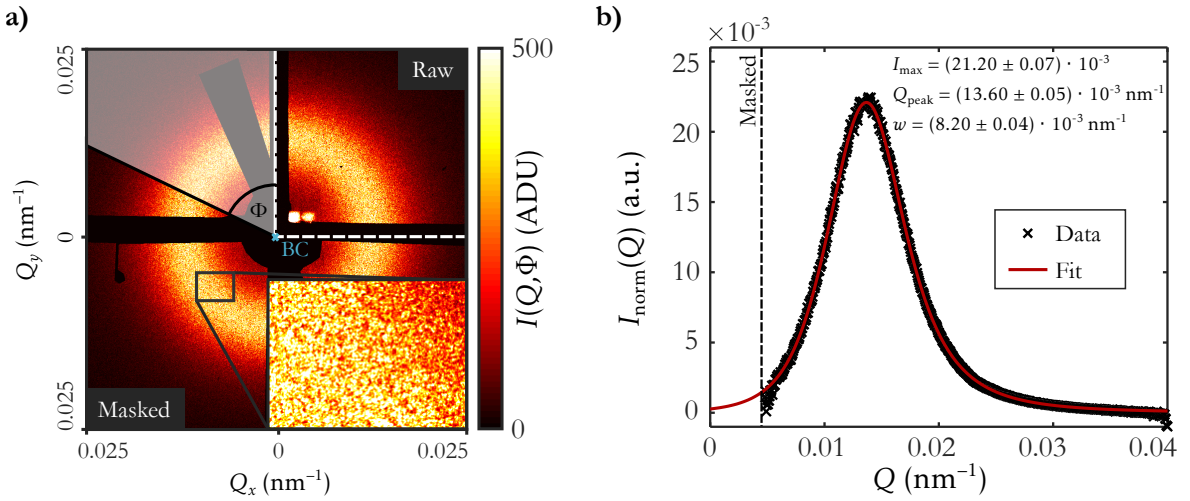

Figure 6.6.: a) Scattering image obtained by mSAXS on the maze-domain ground state of the $[Co/Pt]_6$ multilayer. The image is composed of the accumulated scattering intensity from 100 FEL-pulse exposures and corrected by dark images of the same exposure time. Parasitic scattering, e. g., from adjacent membrane windows, is masked prior further analysis. b) Magnetic scattering distribution, $I_{norm}(Q)$, after processing the scattering image as described in this section. The $I_{norm}(Q)$ and thus the magnetic maze-domain ground state is characterized by fitting the data with a split Pearson type-VII function (see section 5.3.1).

only ≈ 0.03 eV at FERMI ensure the same (large) magnetic scattering intensity for each of the 100 pulses.

Due to the significantly enhanced ρ_{RMS} in the TR-mSAXS experiment at FERMI, it was feasible to conduct single-pulse nIR-pump–XUV-probe measurements on the $[Co/Pt]_6$ multilayer with a maximum magnetic scattering intensity of $I_{max} \approx 20$ ADU at a noise level of ≈ 2 ADU, i. e., a signal-to-noise ratio of ≈ 10 (see Fig. 6.18 a) on p. 156). Remarkably, this is about the same SNR as in the multi-pulse TR-mSAXS experiment at FLASH (see Fig. 5.3 on p. 82).

The dark-corrected and masked scattering images are azimuthally averaged around the position of the beam for further characterization. After applying normalization and charge-scattering background correction as described in the following sections, the magnetic scattering distributions, $I_{norm}(Q)$, are obtained which are fitted by a split Pearson type-VII function (see section 5.3.1). The $I_{norm}(Q)$ of the $[Co/Pt]_6$ multilayer for $\mu_0 H_z = 0$ mT is shown in Fig. 6.6 b), together with the corresponding fit using eq. (5.1). A position of the (first-order) magnetic scattering ring at $Q_{peak} = (13.60 \pm 0.05) \cdot 10^{-3}\,\mathrm{nm}^{-1}$ corresponds to an average domain periodicity of $T_{av} = (462 \pm 2)$ nm ($D_{av} = T_{av}/2 = 231$ nm) in the maze-domain ground state at $\mu_0 H_z = 0$ mT. A similar domain size of $D_{av} = 215$ nm was measured in the TR-mSAXS experiment at FLASH. The difference in D_{av} of $\approx 7\%$, might already be explained by uncertainties in determining the sample detector distance but could also originate from slight differences in the demagnetization procedure prior to the experiment. A width of $w = (8.20 \pm 0.04) \cdot 10^{-3}\,\mathrm{nm}^{-1}$ results in

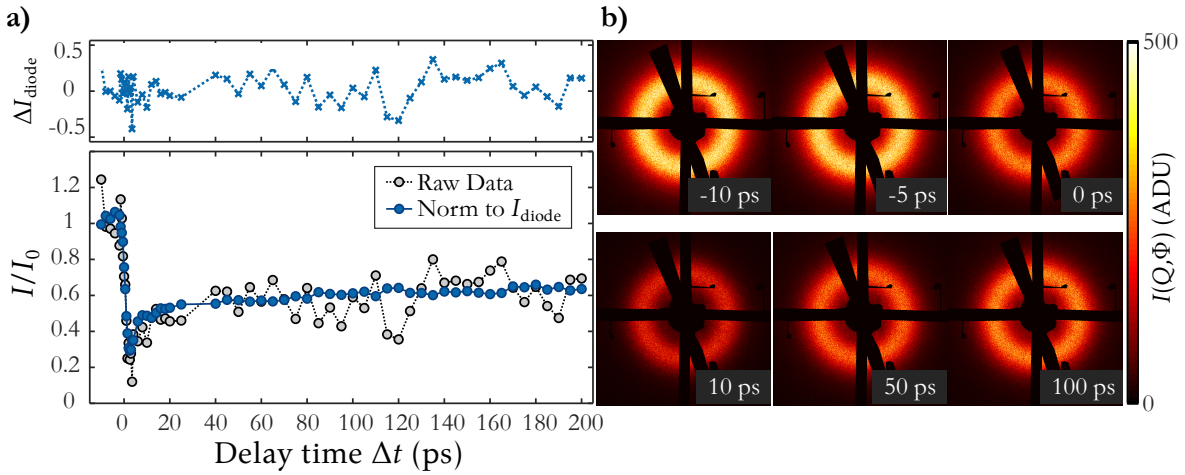

Figure 6.7.: Normalization of the TR-mSAXS data via the four-quadrant photo diode (FQPD). Scattering images, shown for selected delay times in b), are azimuthally averaged around the position of the direct beam, $I(Q) = \langle I(Q,\Phi)\rangle_\Phi$, and integrated over the measured Q-range, $I = \int I(Q)\,\mathrm{d}Q$. a) The raw data, I, are normalized to the incoming FEL intensity, I_{diode}, as measured by the FQPD (top panel of a)). For a direct comparison, both raw and normalized data are related to the corresponding scattering intensity at negative delay times, $I_0 = \langle I(\Delta t < 0)\rangle$ (main panel of a)).

a short-range order of $\xi/T_{\mathrm{av}} = 1.66 \pm 0.01$ which is about the same as the $\xi/T_{\mathrm{av}} = 1.70 \pm 0.03$ measured at FLASH on the non-irradiated (new) membrane of the sample (see appendix A). No alterations in the multi-domain state, or $I_{\mathrm{norm}}(Q)$, are observed here, when irradiating the sample by repetitive FEL pulses with a much lower fluence of $F_{\mathrm{FEL}} = (4.2\text{–}7.0)\,\mathrm{mJ/cm^2}$ as compared to $F_{\mathrm{FEL}} = (30\text{–}35)\,\mathrm{mJ/cm^2}$ in the experiment at FLASH. Details on the characteristics of $I_{\mathrm{norm}}(Q)$ of the $[\mathrm{Co/Pt}]_6$ multilayer when applying external magnetic fields are given in section 6.4.1.

6.3.2. Normalization

At the DiProI beamline, normalization of the TR-mSAXS data is best achieved by the four-quadrant photo-diode (FQPD), which is located at the entrance flange of the sample chamber, i. e., close to the sample position. The fluctuations of the FEL pulse energy, with an absolute value of $\approx (1\text{–}2)\,\mu\mathrm{J}$ at the sample position, were measured via the four individual panels of the FQPD centered around the FEL beam. In that way both intensity and pointing instabilities are recorded. The sum signal of the four panels, I_{diode}, serves as an excellent normalization value that yields a significantly improved SNR, as shown for a selected delay-time scan in Fig. 6.7 a).

The relative fluctuations of the FEL-pulse intensity throughout the selected delay-time scan of approximately ±25% are presented in the top panel of Fig. 6.7 a). The dark-corrected and masked scattering images are azimuthally averaged around the position of the direct beam, $I(Q) = \langle I(Q,\Phi)\rangle_\Phi$. Scattering images for selected delay times are shown in Fig. 6.7 b). The $I(Q)$

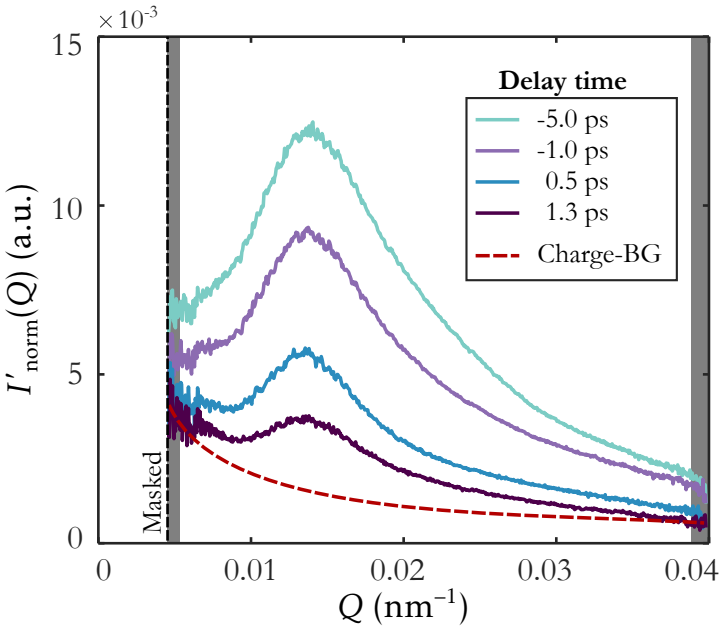

Figure 6.8.: Evaluation of the charge-scattering background by strongly quenching the magnetic scattering intensity, $I'_{\mathrm{norm}}(Q)$, from the $[\mathrm{Co/Pt}]_6$ multilayer using a nIR-laser fluence of $F_{\mathrm{nIR}} = 40.2\,\mathrm{mJ/cm^2}$. The maximum quenched $I'_{\mathrm{norm}}(Q)$ at $\Delta t = 1.3\,\mathrm{ps}$ is fitted at the low and the high-Q ends (gray areas) using a phenomenological fit function of the form $A \cdot Q^B$. The evaluated fit parameters for the charge-scattering contribution are $A = (3.61 \pm 1.13) \cdot 10^{-5}$ and $B = -(1.35 \pm 0.28)$.

are then normalized to the sum of the corresponding 100 incoming FEL-pulse intensities as measured by the FQPD, $I'_{\mathrm{norm}}(Q) = I(Q)/I_{\mathrm{diode}}$. The effect of normalizing the data via the FQPD, is shown by the time evolution of $I'_{\mathrm{norm}} = \int I'_{\mathrm{norm}}(Q)\,\mathrm{d}Q$ in the main panel of Fig. 6.7 a). Note that for the final analysis, first, the charge-scattering background was subtracted from the $I'_{\mathrm{norm}}(Q)$, as described in the following section. For a direct comparison, relative changes in the magnetic scattering intensity are shown, i. e., both raw and normalized data are related to the scattering intensity at negative delay times, $I_0 = \langle I(\Delta t < 0) \rangle$.

6.3.3. Correction for Charge-Scattering Background

The charge-scattering background was determined, following the same approach as in the experiment at FLASH (section 5.2.3), i. e., using a high fluence of $F_{\mathrm{nIR}} = 40.2\,\mathrm{mJ/cm^2}$ to strongly quench the magnetic scattering intensity in the $[\mathrm{Co/Pt}]_6$ multilayer ($d = 15.2\,\mathrm{nm}$) and therewith to identify the charge-scattering background. However, the magnetic scattering intensity could only be quenched to $\approx 25\%$, when using about twice the fluence as compared to the TR-mSAXS experiment at FLASH, where the magnetic scattering intensity could be fully quenched in the thinner $[\mathrm{Co/Pt}]_3$ multilayer ($d = 8.6\,\mathrm{nm}$), as shown in Fig. 6.8. Note that the here used fluence of $F_{\mathrm{nIR}} = 40.2\,\mathrm{mJ/cm^2}$ was close to the destructive limit of the $[\mathrm{Co/Pt}]_6$ multilayer.

In contrast to the TR-mSAXS experiment at FLASH, here, a Q-dependent charge-scattering background is found. While the prominent magnetic scattering peak located at $Q \approx 0.015\,\mathrm{nm^{-1}}$ continuously decreases with delay time, both the low and the high-Q ends start to reach values that do not significantly change with delay time for $\Delta t > 0.5\,\mathrm{ps}$, indicating that these remaining

scattering contributions have a non-magnetic origin.[6] The charge-scattering contribution was phenomenologically described by fitting a function of the form $A \cdot Q^B$ to the low and high-Q ends of the strongly quenched $I'_{\mathrm{norm}}(Q)$ (red dashed line in Fig. 6.8). Note that similar approaches have been used in other experiments to model the charge-scattering background, e. g., using $B = -4$ for spherical charge inhomogeneities, as outlined in section 5.2.3.

The charge-scattering background was fitted individually for measurements on different membrane windows. In any case, comparable fit parameters in the range of $A = (3\text{–}7) \cdot 10^{-5}$ and $B = -(0.6\text{–}1.5)$ were obtained. For further analysis, the individual charge-scattering contributions are subtracted from the $I'_{\mathrm{norm}}(Q)$, yielding the normalized and charge-background corrected magnetic scattering intensity $I_{\mathrm{norm}}(Q)$. [7]

6.4. Experimental Results

The results from the TR-mSAXS experiment at FERMI are presented in the following sections, starting with the impact of H_z fields on the maze-domain ground state of the $[\mathrm{Co}(0.8)/\mathrm{Pt}(1.4)]_6$ multilayer in section 6.4.1, followed by a short discussion on the ultrafast magnetization dynamics in the different multi-domain states in section 6.4.2. The main focus of this experiment was to study laser induced lateral modifications in the nanoscopic multi-domain states (section 6.4.3). Permanent domain modifications were found, when nIR-laser and FEL pulses temporally overlapped on the sample. These double-pulse induced domain modifications, moreover, showed qualitative differences depending on the underlying multi-domain configuration (or external H_z field).

6.4.1. Impact of OOP Fields on the Ground State of the $[\mathrm{Co/Pt}]_6$ Multilayer

The impact of H_z fields on the magnetic scattering intensity from the maze-domain ground state of the $[\mathrm{Co}(0.8)/\mathrm{Pt}(1.4)]_6$ multilayer is presented in Fig. 6.9. The scattering images, $I(Q,\Phi)$, obtained by TR-mSAXS on the multi-domain states at a negative delay time, $\Delta t = -5\,\mathrm{ps}$, show ring-shaped intensity distributions of decreasing radius and maximum intensity with increasing H_z field (Fig. 6.9 a)). The H_z-field induced changes in $I(Q,\Phi)$ are quantified by processing the scattering images as described in the previous section (section 6.3) and fitting the resulting $I_{\mathrm{norm}}(Q)$ with a split Pearson type-VII function, as shown in Fig. 6.9 b). The fit results are summarized in table 6.3.

[6] Analogue to the high-fluence nIR-laser excitation in the TR-mSAXS experiment at FLASH, a continuous reduction of the maximum scattering intensity is observed at $\Delta t < 0$ (appendix A.1).

[7] Note that, by subtracting a Q-dependent charge-scattering contribution from $I'_{\mathrm{norm}}(Q)$, the absolute values of Q_{peak} are changed. As a test for the robustness of this approach, the whole analysis was conducted without subtracting any charge-scattering background. The differences in the absolute values of Q_{peak} between the two approaches are < 0.5%.

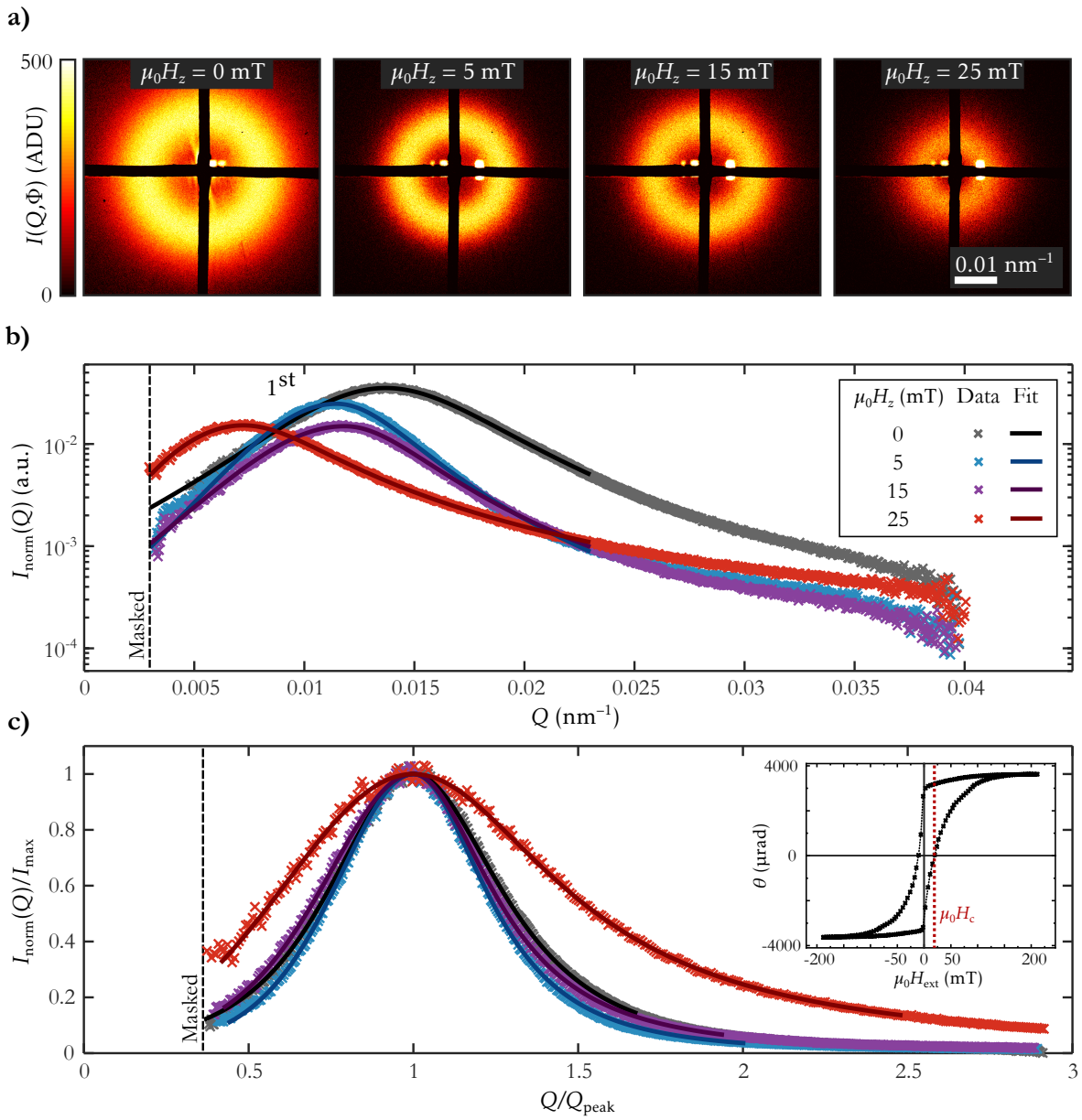

Figure 6.9.: Impact of increasing H_z fields on the maze-domain ground state of the $[Co(0.8)/Pt(1.4)]_6$ multilayer investigated by TR-mSAXS at a negative delay time, $\Delta t = -5$ ps: a) scattering images, $I(Q,\Phi)$, for magnetic fields of $\mu_0 H_z = 0$, 5, 15 and 25 mT. Scattering intensities are shown on a logarithmic scale. b) Corresponding azimuthally averaged intensities, obtained upon processing the scattering images as described in section 6.3. The $I_{norm}(Q)$ are characterized through fitting with a split Pearson type-VII function (section 5.3.1). c) Intensity distributions, $I_{norm}(Q)$, normalized to the respective maximum intensities, I_{max}, and positions of the maximum intensities, Q_{peak}. The inset shows the OOP hysteresis loop of the sample with a coercive field of $\mu_0 H_c \approx 20$ mT.

Table 6.3.: Summarized fit parameters, I_{max} (in units ADU), Q_{peak} and w, obtained by fitting a split Pearson type-VII function to the first-order scattering peak, $I_{norm}(Q)$, obtained by mSAXS on a $[Co(0.8)/Pt(1.4)]_6$ multilayer that was subjected to OOP magnetic fields of $\mu_0 H_z = 0\,mT$, 5 mT, 15 mT, and 25 mT. Also included are the average domain period, $T_{av} = 2\pi/Q_{peak}$, the lateral correlation length, $\xi = 2\pi/w$, and the fraction ξ/T_{av}, which is a measure for the degree of order in the magnetic domain patterns

OOP	0 mT	5 mT	15 mT	25 mT
I_{max} (ADU)	394±1	356±2	289±1	160±1
Q_{peak} (10^{-3}nm^{-1})	13.60±0.05	11.50±0.05	11.80±0.04	7.20±0.09
w (10^{-3}nm^{-1})	8.20±0.04	6.20±0.09	7.20±0.07	7.40±0.07
T_{av} (nm)	462±2	546±2	533±2	873±11
ξ (nm)	766±4	1013±15	872±9	849±8
ξ/T_{av}	1.66±0.01	1.86±0.03	1.64±0.02	0.97±0.01

In absence of an external magnetic field ($\mu_0 H_z = 0\,mT$), the maze-domain pattern possesses an average domain periodicity of $T_{av} = (462 \pm 2)\,nm$ and a lateral correlation length of $\xi = (766 \pm 4)\,nm$ which yields a short-range order of $\xi/T_{av} = 1.66 \pm 0.01$. The short-range order in the maze-domain ground state of the $[Co(0.8)/Pt(1.4)]_6$ multilayer is small compared to $\xi/T_{av} = 3.22 \pm 0.11$ in the $[Co(1.3)/Pt(2.0)]_6$ and $\xi/T_{av} = 4.00 \pm 0.11$ in the $[Co(1.6)/Pt(2.0)]_6$-multilayer composition on the wedge sample that was used in the pre-study at PETRA III (section 6.1). Due to the reduced short-range order in the here-investigated sample, no indications for a 3rd-order magnetic scattering peak are observed for any of the applied fields.[8]

In principle, the maze-domain ground state of the $[Co(0.8)/Pt(1.4)]_6$ multilayer may be visualized similar to the one of the $[Co(1.3)/Pt(2.0)]_6$ and the $[Co(1.6)/Pt(2.0)]_6$-multilayer composition, shown in real space by the magnetic holograms for $\mu_0 H_z = 0\,mT$ in Fig. 6.1 a) and Fig. 6.2 a), respectively. However, the reduced short-range order and the about 2–3 times larger average domain size in the thinner sample, compared to the multilayer compositions in the wedge-shaped sample, hint at a more island-like domain configuration, as observed by imaging Co/Pt multilayers of different sample thicknesses via Kerr microscopy (Fig. 3.2 on p. 58).

When applying a magnetic field of $\mu_0 H_z = 5\,mT$, the maximum scattering intensity, I_{max}, is reduced by about 10%. This agrees with a slightly reduced number of magnetic scatterers, i. e., the growth of majority over minority domains, as observed in the pre-study at PETRA III (section 6.1.2). At the same time, the average domain periodicity, T_{av}, and the lateral correlation length, ξ, increase by approximately 18% and 32%, respectively, yielding a slightly increased short-range order over a distance of 1.86 ± 0.03 times the average domain periodicity. A similar situation is observed for $\mu_0 H_z = 15\,mT$, where a reduction of I_{max} by approximately 26%, with respect to the $\mu_0 H_z = 0\,mT$ case, is accompanied by an

[8] Note that for $\mu_0 H_z = 0\,mT$, the 3rd-order magnetic scattering peak lies outside of the observable Q range.

increase of T_{av} and ξ by approximately 15% and 14%, respectively. The latter changes result in a lateral correlation length of $\xi/T_{av} = 1.64 \pm 0.02$ that is comparable to the one of the maze-domain ground state ($\mu_0 H_z = 0\,\mathrm{mT}$). By normalizing $I_{norm}(Q)$ to both I_{max} and Q_{peak} it is seen that the changes in the shape of $I_{norm}(Q/Q_{peak})/I_{max}$ are small for $\mu_0 H_z = 5\,\mathrm{mT}$ and $\mu_0 H_z = 15\,\mathrm{mT}$ (Fig. 6.9 c)). Similarly small changes in T_{av} and ξ on the order of 10% were observed in the pre-study at PETRA III, when subjecting the maze-domain ground state of the $[Co(1.3)/Pt(2.0)]_6$ multilayer to a magnetic field of $\mu_0 H_z = 50\,\mathrm{mT}$. The multi-domain states of this thinner, $[Co(0.8)/Pt(1.4)]_6$ multilayer for $\mu_0 H_z = 5\,\mathrm{mT}$ and $\mu_0 H_z = 15\,\mathrm{mT}$ may thus also be pictured as slightly asymmetric multi-domain states where the original maze-like domain configuration is largely preserved (see hologram for $\mu_0 H_z = 50\,\mathrm{mT}$ in Fig. 6.2 on p. 123).

The situation considerably changes when applying a magnetic field of $\mu_0 H_z = 25\,\mathrm{mT}$, i. e., a magnetic field that is above the coercive field of $\mu_0 H_c \approx 20\,\mathrm{mT}$ (see easy-axis hysteresis loop in the inset of Fig. 6.9 c)). The reduction of the maximum scattering intensity by $\approx 60\%$, compared to the maze-domain ground state, indicates a large asymmetry in the multi-domain state, i. e., only a small number of minority domains remain magnetized opposite to the H_z field, supported by the drastic increase of the average domain periodicity by $\approx 90\%$. When this is related to the lateral correlation length, that is increased by $\approx 11\%$, a strongly reduced short-range order over a distance of only 0.97 ± 0.01 times the average domain periodicity is obtained. A $\xi/T_{av} \approx 1$ shows that the multi-domain state at $\mu_0 H_z = 25\,\mathrm{mT}$ is completely uncorrelated, seen also, by the significant broadening of $I_{norm}(Q/Q_{peak})/I_{max}$ in Fig. 6.9 c). Similar drastic changes in I_{max} on the order of (50–100)% and a reduction of the short-range order to $\xi/T_{av} \approx 1$ were observed in the pre-study at PETRA III, when subjecting the maze-domain ground state of the $[Co(1.3)/Pt(2.0)]_6$ multilayer to a magnetic field of $\mu_0 H_z = 100\,\mathrm{mT}$. The multi-domain state of the $[Co(0.8)/Pt(1.4)]_6$ multilayer for $\mu_0 H_z = 25\,\mathrm{mT}$ may thus be pictured as a strongly asymmetric multi-domain state, i. e., a domain state that is already close to the single-domain configuration (see hologram for $\mu_0 H_z = 100\,\mathrm{mT}$ in Fig. 6.2 on p. 123).

From that, three H_z-field regimes can be identified for the time-resolved TR-mSAXS study on lateral modifications in the nanoscopic multi-domain states of the $[Co(0.8)/Pt(1.4)]_6$ multilayer:

1. Symmetric domain configuration for $\mu_0 H_z = 0\,\mathrm{mT}$: after OOP demagnetization cycles prior to the experiment as described in section 3.2.3, the maze-domain ground state with an equal area filling of up and down-magnetized domains is generated. The maze-domain ground state may be visualized similar to the one in the pre-study at PETRA III, shown in Fig. 6.2 a) on p. 123, but with larger, presumably more island-like domains with an average domain size of $D_{av} = 231\,\mathrm{nm}$ (pre-study: $D_{av} = 112\,\mathrm{nm}$), and a reduced short-range order of $\xi/T_{av} \approx 1.7$ (pre-study: $\xi/T_{av} \approx 3.2$).

2. Slightly asymmetric domain configurations for $\mu_0 H_z = 5\,\mathrm{mT}$ and $\mu_0 H_z = 15\,\mathrm{mT}$: A small asymmetry is induced in the area filling of up and down-magnetized domains, resulting

in only minor changes in T_{av} and ξ on the order of 10% ($D_{av} \approx 270\,\mathrm{nm}$, $\xi/T_{av} = 1.64$–1.86). This largely preserved domain configuration may be visualized similar to the magnetic hologram for $\mu_0 H_z = 50\,\mathrm{mT}$, shown in Fig. 6.2 a) on p. 123. Again, the domain state consists of larger, presumably more island-like domains.

3. Close-to single-domain state for $\mu_0 H_z = 25\,\mathrm{mT}$: A large asymmetry is induced in the maze-domain ground state, which results in a strong reduction of the maximum scattering intensity by $\approx 60\%$ from $I_{max} = 394\,\mathrm{ADU}$ (for $\mu_0 H_z = 0\,\mathrm{mT}$) to $I_{max} = 160\,\mathrm{ADU}$ as well as a reduction of the short-range order to $\xi/T_{av} \approx 1$. The close-to single-domain state may be visualized similar to the magnetic hologram for $\mu_0 H_z = 100\,\mathrm{mT}$, shown in Fig. 6.2 a) on p. 123.

6.4.2. Ultrafast Magnetization Dynamics in the Presence of OOP Fields

This section deals with ultrafast magnetization dynamics of the $[Co/Pt]_6$ multilayer in the presence of H_z fields. For that, the magnetic scattering intensities, $I_{norm}(Q)$, exemplarily shown for a delay time of $\Delta t = -5\,\mathrm{ps}$ in Fig. 6.9 b), are integrated over the observable Q range for all delay times Δt. The resulting time evolutions of $I_{norm} = \int I_{norm}(Q)\,\mathrm{d}Q$ are shown in Fig. 6.10 a) and b), for LCP and RCP nIR-laser excitation, respectively, for magnetic fields of $\mu_0 H_z = 0\,\mathrm{mT}$ to $\mu_0 H_z = 25\,\mathrm{mT}$.

With increasing H_z field, an asymmetry in the area filling of up and down-magnetized domains is induced in the maze-domain ground state, as discussed in the previous section (section 6.4.1). Due to the reduced number of minority domains (number of magnetic scatterers) when changing the multi-domain state from the symmetric maze-domain ($\mu_0 H_z = 0\,\mathrm{mT}$) to the close-to single-domain configuration ($\mu_0 H_z = 25\,\mathrm{mT}$), the $I_{norm}(\Delta t)$ in Fig. 6.10 have reduced starting values from top to bottom. For all H_z-field cases, an ultrafast quenching of the magnetic scattering intensity within the duration of the 3500 fs-long nIR-laser pulses is observed, followed by a magnetization recovery on pico to nanosecond time scales. The full recovery of magnetization to its initial value at $\Delta t < 0$ is evidenced by FEL-reference measurements that probe the unpumped magnetic multi-domain states in-between nIR-pump–XUV-probe measurements (solid lines in Fig. 6.10).[9]

For the discussion on the ultrafast magnetization dynamics, the $I_{norm}(\Delta t)$ are converted to transient changes in the magnetization, $\Delta M_z(\Delta t)/M_{z,0}$, as described in section 5.3.3. Following the descriptions in that section, the experimental error was determined to $\delta(\Delta M_z/M_{z,0}) \approx \pm(1$–$1.5)\%$ at negative delay times and in the recovery regime ($\Delta t \gtrsim 10\,\mathrm{ps}$), and reaches up to $\delta(\Delta M_z/M_{z,0}) \approx \pm 3\%$ in the demagnetization regime ($\Delta t \approx 0.5\,\mathrm{ps}$). Note that the statistical and

[9] In the beginning of the beamtime, FEL-reference measurements have not been implemented in the experimental procedure. As no proper in-situ OOP demagnetization cycles could be applied to reset the maze-domain ground state, the delay-time scans for $H_z = 0\,\mathrm{mT}$ (including FEL-reference measurements) could not be repeated. However, a constant I_{norm} in the FEL-reference measurements is also expected for $H_z = 0\,\mathrm{mT}$.

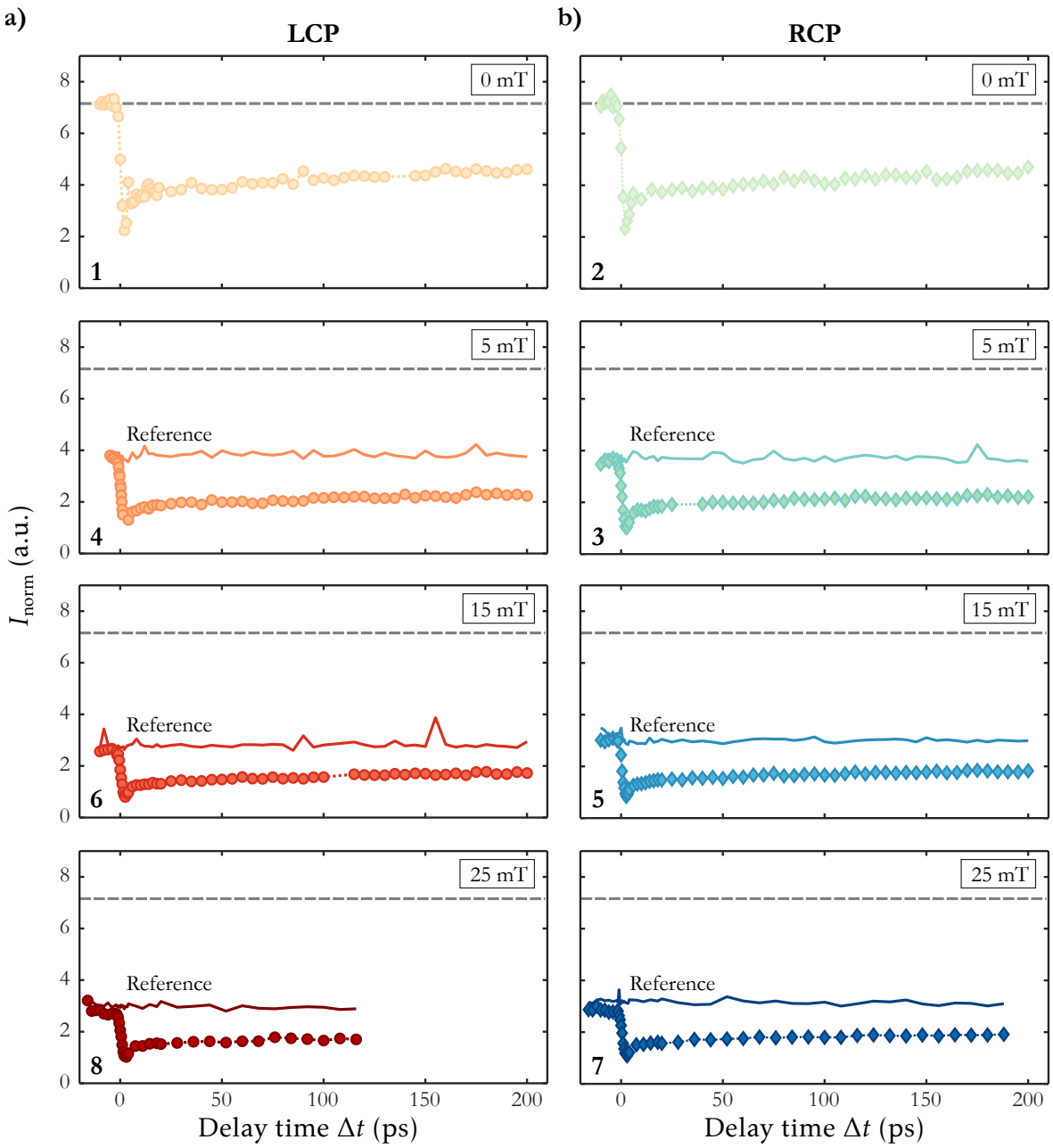

Figure 6.10.: Time evolution of the magnetic scattering intensity, I_{norm}, upon excitation of the $[Co/Pt]_6$ multilayer by a) LCP and b) RCP nIR-laser pulses for increasing magnetic fields of $\mu_0 H_z = 0$, 5, 15 and 25 mT (top to bottom). The pulse duration is $\tau_{nIR} = 3500$ fs, the fluence is $F_{nIR} = 13.4\,mJ/cm^2$. Solid lines show the I_{norm} approximately 15 s after (prior to) the previous (next) nIR-pump–XUV-probe event (FEL-reference). Numbers from **1**–**8** indicate the sequence in which the delay-time scans were recorded.

thus the relative experimental error increases with H_z field, due to the decreasing magnetic scattering intensity. In the following section, the here obtained magnetization transients, using picosecond-long and high-fluence nIR-laser pulses to excite the maze-domain ground state ($\mu_0 H_z = 0\,\mathrm{mT}$), are compared to a selected magnetization transient from the TR-mSAXS experiment at FLASH, where the very same sample was studied (section 6.4.2.1). The H_z-field dependence of the ultrafast magnetization dynamics is discussed in section 6.4.2.2.

6.4.2.1. Ultrafast Magnetization Dynamics in the Absence of Magnetic Fields

First, the ultrafast magnetization dynamics of the $[Co/Pt]_6$ multilayer in the absence of a magnetic field ($\mu_0 H_z = 0\,\mathrm{mT}$) is discussed. The magnetization transients, $\Delta M_z(\Delta t)/M_{z,0}$, obtained by using LCP and RCP nIR-laser pulses to excite the maze-domain ground state, are presented in Fig. 6.11 as filled red circles and blue diamonds, respectively. The same demagnetization and remagnetization behavior is obtained for LCP and RCP nIR-laser pulses, which is in accord with the finding of polarization independent ultrafast magnetization dynamics (section 5.4.5.1).

For a comparison of the results from two different FEL facilities, a selected magnetization transient of the very same $[Co/Pt]_6$ multilayer, recorded in the TR-mSAXS experiment at FLASH, is included in Fig. 6.11, together with the fit to the data using eq. (5.5). Compared to the magnetization transient at FLASH, where an ultrashort ($\tau_{\mathrm{nIR}} = 300\,\mathrm{fs}$) and less intense ($F_{\mathrm{nIR}} = 9.6\,\mathrm{mJ/cm^2}$) nIR-laser excitation was used, here, the $\Delta M_z(\Delta t)/M_{z,0}$ show a less-defined demagnetization onset and a significantly larger persisting degree of demagnetization in the recovery regime. As discussed in section 5.4.5.2, the pump-probe data are the convolution of the time evolution of magnetization and the temporal profiles of nIR-pump and FEL-probe pulses. Hence, a less defined demagnetization onset is obtained here, due to the longer nIR-laser pulse duration.

For a comparison of the magnetization transients the data are modeled by eq. (5.5), starting with the same parameters extracted from fitting the magnetization transient recorded at FLASH, and taking into account the longer pulse duration of $\tau_{\mathrm{nIR}} = 3500\,\mathrm{fs}$. The data can be well-described by using the same demagnetization time of $\tau_{\mathrm{M}} = (198 \pm 47)\,\mathrm{fs}$ and a slightly longer energy equilibration time of $\tau_{\mathrm{E}} = 1.0\,\mathrm{ps}$ ($\tau_{\mathrm{E}} = 0.7\,\mathrm{ps}$ at FLASH). For the modeled curve, shown as a red solid line in Fig. 6.11, moreover, significantly larger amplitudes $A_1 = 1.20$ (FLASH: $A_1 = 0.64$) and $A_2 = 0.29$ (FLASH: $A_2 = 0.09$) were used, which formally correspond to a maximum degree of demagnetization of $-\Delta M_z^{\mathrm{max}}/M_{z,0} \approx 80\%$ and a persisting degree of demagnetization in the recovery regime of $\approx 30\%$, respectively.[10] A deconvolution of the data

[10] Note that fits to the data by eq. (5.5) did not converge, presumably due to the long pump-pulse duration in the range of 15 times τ_{M} or 3 times τ_{E}. The degree of demagnetization is called "formal", as it is of relevance only for the model, where the time structure of the pump and the probe pulse is taken into account by a convolution. Explicitly, the temporally extended excitation by $\tau_{\mathrm{nIR}} = 3500\,\mathrm{fs}$ is not taken into account.

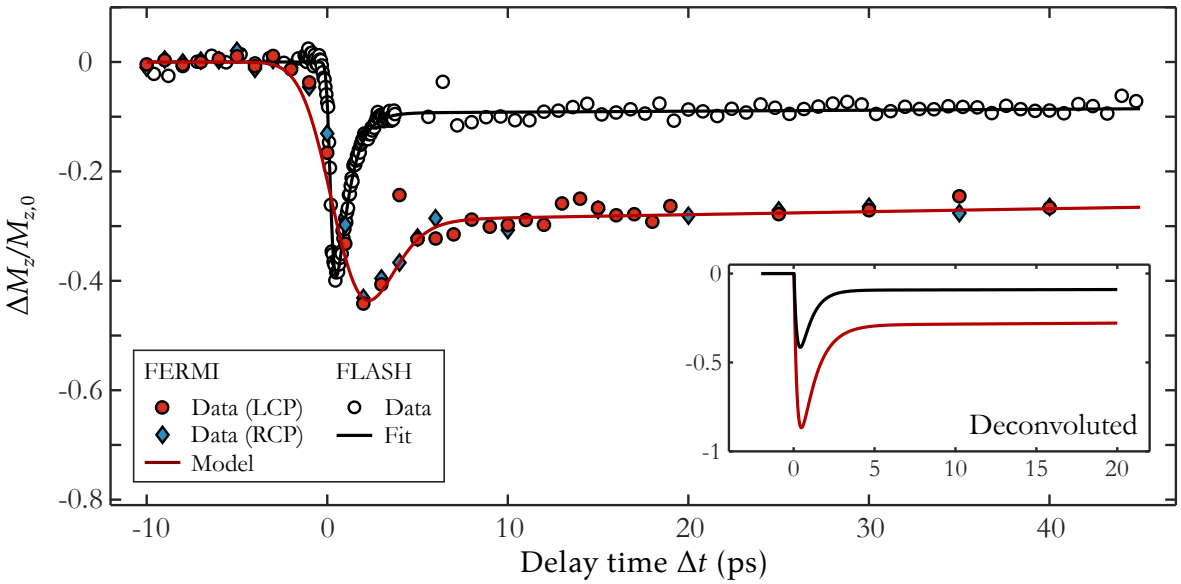

Figure 6.11.: Magnetization transients of the $[Co/Pt]_6$ multilayer using 3500 fs-long LCP and RCP nIR-laser pulses with a fluence of 13.4 mJ/cm^2 ($\mu_0 H_z = 0$ mT). Also shown is the magnetization transient of the very same $[Co/Pt]_6$ multilayer from the TR-mSAXS experiment at FLASH, using 300 fs-long nIR-laser pulses with a fluence of 9.6 mJ/cm^2, together with the fit to the data using eq. (5.5). The data in this experiment are modeled with the same τ_M and adjusted A_1, A_2 and τ_E. The inset shows the deconvoluted magnetization transients, i. e., taking into account the different time resolutions at FLASH and at FERMI.

shows the hypothetical magnetization transient for a delta-like nIR-laser excitation (inset of Fig. 6.11). Note that under the assumption of such an ultrashort nIR-laser excitation (e. g., $\tau_{nIR} = 70$ fs), a $-\Delta M_z^{max}/M_{z,0} \approx 80\%$ for a fluence of $F_{nIR} = 13.4$ mJ/cm^2 is in agreement with the fluence dependence of the maximum degree of demagnetization (Fig. 5.8 on p. 95). Also, the extended τ_E and the larger persisting degree of demagnetization in the recovery regime is in qualitative agreement with the slowing down of the magnetization dynamics at high temperatures (see section 5.4.4).

However, when using a nIR-laser excitation with a pulse duration of $\tau_{nIR} = 3500$ fs an actual reduced maximum degree of demagnetization of $-\Delta M_z^{max}/M_{z,0} \lesssim 50\%$ is obtained, due to intra-pulse relaxation as $\tau_E < \tau_{nIR}$. Considering the pulse-duration dependence of the maximum degree of demagnetization, discussed for ultrashort pulse durations in section 5.4.5.2, a $-\Delta M_z^{max}/M_{z,0} \approx (10\text{–}20)\%$ would have been expected via mere linear extrapolation for $\tau_{nIR} = 3500$ fs and $F_{nIR} = 13.4$ mJ/cm^2. The here obtained data deviate from this prediction by a factor of 2–3, showing that the linear relation between nIR-laser amplitude and maximum degree of demagnetization [281, 282] does not hold for picosecond-long nIR-laser pulses. As mentioned above, this is likely due to the fact that both demagnetization ($\tau_M \approx 200$ fs) and remagnetization processes ($\tau_E \approx 1000$ fs) are present within the duration of the nIR-laser excitation. Nevertheless,

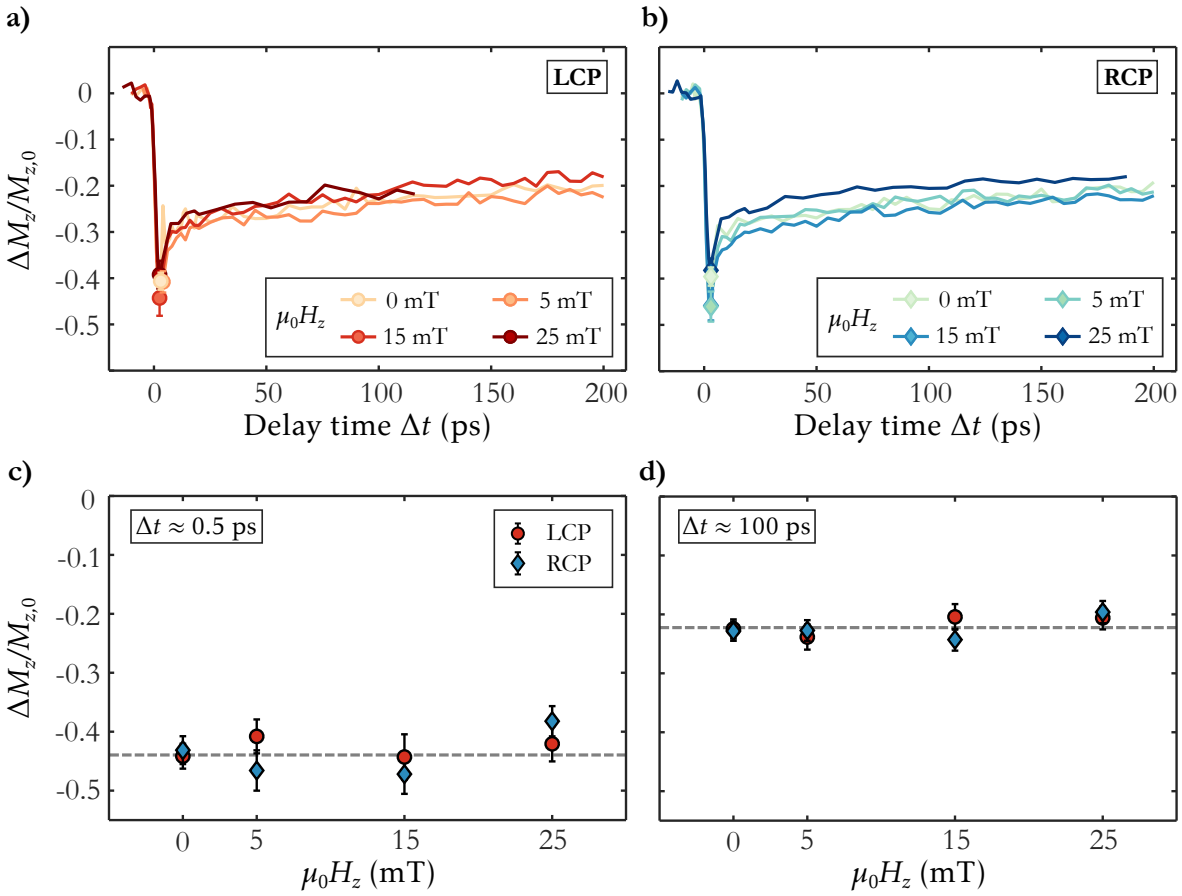

Figure 6.12.: H_z-field dependence of ultrafast magnetization dynamics in the $[Co/Pt]_6$ multilayer. a) and b) show the magnetization transients, $\Delta M_z(\Delta t)/M_{z,0}$, for LCP and RCP nIR-laser pulse excitation with a pulse duration of 3500 fs and a fluence of 13.4 mJ/cm^2, respectively. Data points highlight the maximum degree of demagnetization. c) and d) Degree of demagnetization vs. H_z field at a delay time of $\Delta t \approx 0.5$ ps (maximum degree of demagnetization) and $\Delta t \approx 100$ ps, respectively. In d) the average degree of demagnetization in the delay-time range of 50 ps $< \Delta t <$ 120 ps is shown.

a picosecond-long laser excitation to high temperatures ($-\Delta M_z^{max}/M_{z,0} \approx 50\%$) as well as a slowing down of the remagnetization dynamics ($\tau_E \approx 1.0$ ps) are believed to be preconditions for the observed permanent domain modifications (section 6.4.3).

6.4.2.2. H_z-Field Dependence of Ultrafast Magnetization Dynamics

The dependence of the ultrafast magnetization dynamics on external magnetic field is addressed in the following. The magnetization transients, $\Delta M_z(\Delta t)/M_{z,0}$, obtained by LCP and RCP nIR-laser excitation of the multi-domain states in the presence of OOP magnetic fields of $\mu_0 H_z = (0–25)$ mT, are presented in Fig. 6.12 a) and b), respectively. No differences in $\Delta M_z(\Delta t)/M_{z,0}$ are observed within the experimental error for the different H_z-field cases, neither for LCP

nor for RCP nIR-laser excitation. This gets particularly obvious when comparing their degrees of demagnetization at different delay times, as shown for the maximum degree of demagnetization, $\Delta M_z(\Delta t \approx 0.5\,\mathrm{ps})/M_{z,0}$, in Fig. 6.12 c) and the degree of demagnetization in the recovery regime, $\Delta M_z(\Delta t \approx 100\,\mathrm{ps})/M_{z,0}$, in Fig. 6.12 d). Both are approximately constant within the experimental error for the different H_z fields as well as for LCP and RCP nIR-laser excitation. Note that for the degree of demagnetization in the recovery regime, the average $\Delta M_z(\Delta t)/M_{z,0}$ over a range of delay times of $50\,\mathrm{ps} < \Delta t < 120\,\mathrm{ps}$ was taken. The same ultrafast magnetization dynamics in the symmetric maze-domain, the asymmetric multi-domain as well as the close-to single-domain state, emphasizes that superdiffusive spin transport across domain boundaries plays a minor role in few 100 nm-sized multi-domain states, in agreement with recent experimental findings [135, 137]. No differences between LCP and RCP nIR-laser excitation confirm the previous finding of polarization independent ultrafast magnetization dynamics (see previous section and section 5.4.5.1) for applied OOP magnetic fields.

Note that, a faster realignment of the disordered spins with increasing H_z field, i. e., a faster recovery of $\Delta M_z/M_{z,0}$, was reported in Ref. [208] for the single-domain states of Co/Pt multilayers. This so-called *giant magnetic cooling effect* was, however, found to be strong only in highly excited magnetic states, i. e., in magnetic states where the magnetization recovery is extended over (10–100) ps. In magnetic states where the degree of demagnetization has already recovered by more than 50% within the first few picoseconds, like it is the case here, the magnetic cooling effect was found to be weak.

6.4.3. Double-Pulse Induced Permanent Modifications in Nanoscopic Multi-Domain States

The impact of ultrashort laser excitation on the lateral configuration of the different multi-domain states of the $[Co/Pt]_6$ multilayer is discussed in the following. For that, all scattering images, $I(Q,\Phi)$, obtained at different delay times, Δt, magnetic fields, H_z, and both LCP and RCP nIR-laser excitation, were processed as described in section 6.3. Laser-induced lateral domain modifications are investigated via changes in the positions, Q_{peak}, and widths, w, of the (first-order) magnetic scattering peaks, obtained by fitting a split Pearson type-VII function to $I_{\mathrm{norm}}(Q)$. The resulting $Q_{\mathrm{peak}}(\Delta t)$ and $w(\Delta t)$ are shown in Fig. 6.13 and Fig. 6.14, respectively, for LCP (a)) and RCP (b)) nIR-laser excitation and increasing magnetic fields from $\mu_0 H_z = 0\,\mathrm{mT}$ to $\mu_0 H_z = 25\,\mathrm{mT}$. Note that, due to the increasing asymmetry in the multi-domain states with increasing H_z field, the Q_{peak} and w transients have different starting values (see section 6.4.1). The same scaling of the ordinate, however, enables a direct comparison of changes in Q_{peak} and w for the different H_z-field cases. The FEL-reference data, recorded in order to provide information on the unpumped (or relaxed) magnetic states in-between two consecutive nIR-pump–XUV-probe sequences, are shown as solid lines in Fig. 6.13 and

Fig. 6.14. Note that, no OOP demagnetization cycles were conducted in-between delay-time scans, as the maximum field of $\mu_0 H_z = \pm 50\,\mathrm{mT}$, provided by the in-vacuum Helmholtz coils, is below the saturation field of the sample of $\mu_0 H_s \gtrsim 200\,\mathrm{mT}$ (see inset of Fig. 6.9 on p. 136). For clarity, the sequence in which the delay-time scans were recorded is indicated by bold numbers **1**–**8** in Fig. 6.13 and Fig. 6.14.

The most pronounced features in the Q_{peak} and w transients are peak-like changes at a delay time of $\Delta t = 0$, that show qualitative and quantitative differences for the different helicities and H_z-field cases. In particular for the cases of $\mu_0 H_z \leq 15\,\mathrm{mT}$, the Q_{peak} transients look qualitatively the same as what was observed in a previous collaborative TR-mSAXS experiment at FLASH [32]. At a first sight, the here obtained results could thus be interpreted in an analogue way, i. e., as a transient broadening of the domain-wall profile on femto to picosecond time scales due to superdiffusive spin transport across domain boundaries. The broadening of the domain walls leads to a change in their form factor and thus a change in the shape and position of $I_{norm}(Q)$. However, an important difference compared to the previous experiment is observed in the Q_{peak} transients of the FEL-reference measurements. Unexpectedly, the FEL-reference data, to a large extent, are the same as the nIR-pump–XUV-probe data, including the distinct signature at $\Delta t = 0$.[11] As domain states with the same Q_{peak} and w-values are obtained $\approx 15\,\mathrm{s}$ after laser excitation, the lateral domain modifications can be considered *permanent*. This is in contrast to a transient Q_{peak}-shift due to a temporary domain-wall broadening in Ref. [32]. There, no such pronounced signature at $\Delta t = 0$, but only a drift of the initial Q_{peak} position was observed in the FEL-reference data, as shown for a selected delay-time scan from that experiment, that was re-evaluated within this thesis, in appendix C.

Analogue to the H_z-field induced changes in Q_{peak} and w (section 6.4.1), three H_z-field regimes can be identified for the laser-induced changes.

In the first regime at $\mu_0 H_z = 0\,\mathrm{mT}$ (symmetric maze-domain ground state), no change in the Q_{peak} position and only a step-like reduction of the width by $\Delta w \approx (4\text{–}6)\%$ are observed (scan **1** and scan **2** in Fig. 6.13 and Fig. 6.14) for both LCP and RCP nIR-laser excitation.

A second regime is identified for magnetic fields of $\mu_0 H_z = 5\,\mathrm{mT}$ and $\mu_0 H_z = 15\,\mathrm{mT}$ (slightly asymmetric multi-domain states), shown by scans **3**–**6** in Fig. 6.13 and Fig. 6.14. Utilizing LCP nIR-laser excitation, the Q_{peak} position and width, w, undergo permanent changes of $\approx -5\%$ and $\approx +6\%$ at maximum, respectively, for $\mu_0 H_z = 5\,\mathrm{mT}$, that increase to $\approx -7\%$ and $\approx +11\%$ at maximum for $\mu_0 H_z = 15\,\mathrm{mT}$. Largely the same behavior is observed when using RCP nIR-laser pulses, except for a different starting value in the Q_{peak} transient at $\mu_0 H_z = 15\,\mathrm{mT}$ (see scan **5** in Fig. 6.13). The different starting values are likely due to the fact that no OOP demagnetization

[11] Note that, differences between nIR-pump–XUV-probe and FEL-reference data at $H_z = 15\,\mathrm{mT}$ and $H_z = 25\,\mathrm{mT}$ hint at ongoing domain modifications in the multi-domain states within the first 15 s after laser excitation. This might be due to the transition from reversible to irreversible domain modifications in this H_z-field regime ($H_z \approx H_c$), which is discussed in more detail in the following section (section 6.4.3.1).

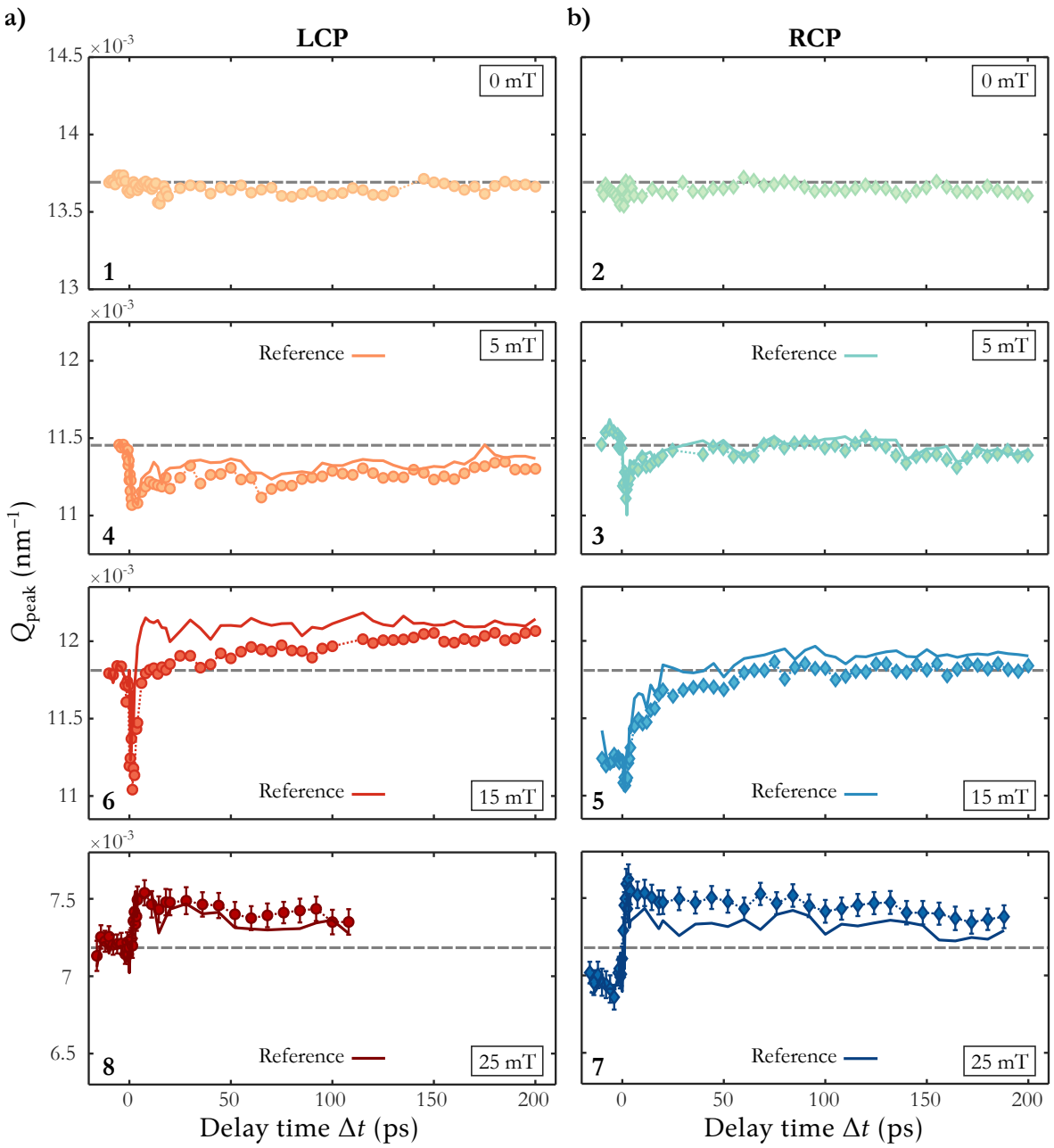

Figure 6.13.: Time evolution of the peak position, Q_{peak}, upon excitation of the $[Co/Pt]_6$ multilayer by a) LCP and b) RCP nIR-laser pulses for increasing magnetic fields of $\mu_0 H_z = 0$, 5, 15 and 25 mT (top to bottom). The pulse duration is $\tau_{nIR} = 3500$ fs, the fluence is $F_{nIR} = 13.4$ mJ/cm^2. Solid lines show the Q_{peak} position obtained from the FEL-reference measurements ≈ 15 s after (before) the previous (next) nIR-pump–XUV-probe events. Numbers from **1**–**8** indicate the sequence in which the delay-time scans were recorded. Fit errors are about the size of the data points for $\mu_0 H_z = (0–15)$ mT.

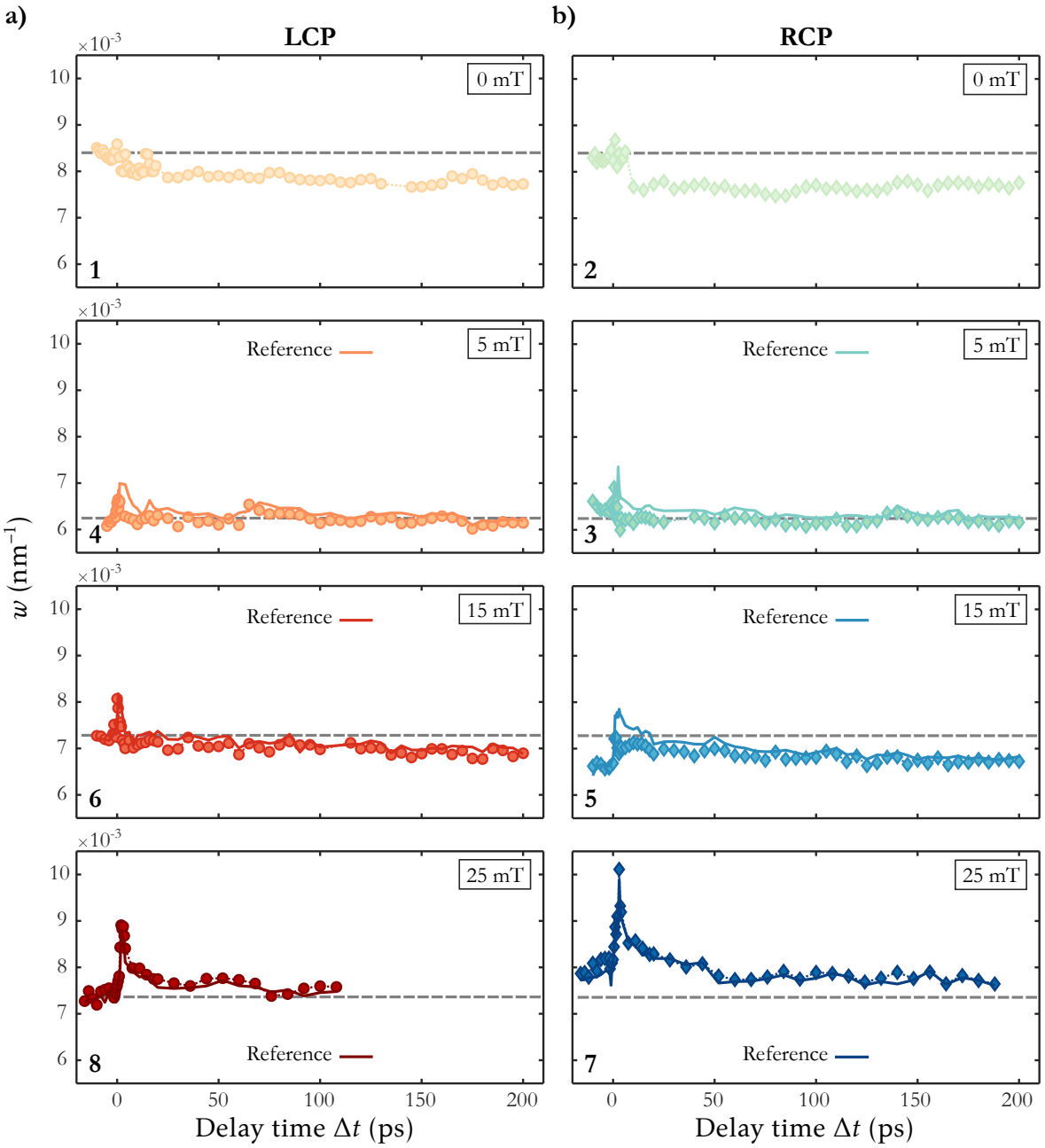

Figure 6.14.: Time evolution of the width, w, upon excitation of the $[Co/Pt]_6$ multilayer by a) LCP and b) RCP nIR-laser pulses for increasing magnetic fields of $\mu_0 H_z = 0$, 5, 15 and 25 mT (top to bottom). The pulse duration is $\tau_{nIR} = 3500$ fs, the fluence is $F_{nIR} = 13.4\,mJ/cm^2$. Solid lines show the Q_{peak} position obtained from the FEL-reference measurements ≈ 15 s after (before) the previous (next) nIR-pump–XUV-probe events. Numbers from **1–8** indicate the sequence in which the delay-time scans were recorded. Fit errors are below the size of the data points.

cycles were conducted in-between delay-time scans as mentioned before. Hence, differences may exist between the multi-domain configuration when setting a new H_z-field value and the multi-domain configuration after excitation by 100 nIR-laser and FEL pulses, i. e., between two delay-time scans using LCP and RCP nIR-laser excitation. A new equilibrium state through thermally activated domain rearrangements gets particularly relevant for magnetic fields close to the coercive field ($\mu_0 H_c \approx 20\,\mathrm{mT}$), where the domain system starts to strive towards the single-domain configuration. This H_z-field regime was found to be connected to irreversible changes in the domain pattern [283], which could hold as an explanation for the different starting values using LCP and RCP nIR-laser excitation. Following the measurement sequence, the final Q_{peak} position in scan **3** resembles the initial Q_{peak} position in scan **4**, and the final Q_{peak} position in scan **5** resembles the initial Q_{peak} position in scan **6**. It thus appears that differences in $Q_{\mathrm{peak}}(\Delta t)$ and $w(\Delta t)$ between LCP and RCP nIR-laser excitation originate from differences in their starting values rather than from a helicity dependence. Note that, when comparing the Q_{peak}-shifts in scans **3**–**6**, almost the same minimum value of $Q_{\mathrm{peak}} \approx 11.0 \cdot 10^{-3}\,\mathrm{nm}^{-1}$ is observed, independent from the different starting values, which is indicative for a particularly stable local energetic minimum of this intermediate state.

In the third regime at $\mu_0 H_z = 25\,\mathrm{mT}$ (close-to single-domain state), the w-shift further increases to $\approx +20\%$ at maximum, while the Q_{peak}-shift, remarkably, changes in sign to $\approx +4\%$ at maximum for LCP nIR-laser excitation. Differences between LCP and RCP nIR-laser excitation, again, seem to originate from differences in the starting values of the respective transients (scan **7** and scan **8** in Fig. 6.13 and Fig. 6.14).

As $Q_{\mathrm{peak}}(\Delta t)$ and $w(\Delta t)$ show distinct signatures only at $\Delta t = 0$ in both the nIR-pump–XUV-probe and the FEL-reference measurements, it has to be concluded that the permanent domain modifications are only induced when nIR-laser and FEL pulses temporally overlap (section 6.4.3.1). An interpretation of the permanent changes of Q_{peak} and w in real space, i. e., a link to possible lateral modifications in the multi-domain patterns, is given in section 6.4.3.2. As each scattering image was recorded by accumulating 100 nIR-pump–XUV-probe pulse exposures, unfortunately, it is not clear whether the permanent modifications are induced by just a single (nIR-laser–FEL) double-pulse or a series of double-pulses, so that no information on the time scale can be obtained. In particular, this means that the "delay time", Δt, in Fig. 6.13 and Fig. 6.14 (and throughout this section) does not show picosecond dynamics, but rather represents the "nIR-laser–FEL pulse overlap". A first insight in the time scale of the underlying processes is given in section 6.4.3.3, where changes in Q_{peak} and w from single-pulse nIR-pump–XUV-probe measurements are analyzed.

6.4.3.1. Combined Action of nIR-laser and FEL Pulses

It is, at first, surprising that there exist distinct changes of $Q_{\mathrm{peak}}(\Delta t)$ and $w(\Delta t)$ at a delay time of $\Delta t = 0$ also in the FEL-reference measurements, as the nIR-laser is blocked by a shutter and Δt is only artificially used to match the FEL-reference data with the corresponding nIR-pump–XUV-probe data. In particular, an irradiation by only the nIR-laser or the FEL pulses has no (permanent) impact on the multi-domain configurations, as there exist no such distinct changes in $Q_{\mathrm{peak}}(\Delta t)$ and $w(\Delta t)$ in the FEL-reference measurements for $\Delta t \ll 0$ and $\Delta t \gg 0$. From that it is concluded that the distinct signature at $\Delta t = 0$ in both nIR-pump–XUV-probe and FEL-reference measurements is a permanent effect that only occurs if nIR-laser and FEL pulses temporally overlap (double-pulse effect). Zoom-ins to the interaction regime ($\Delta t \approx 0$) are shown exemplarily for the Q_{peak} transients at $\mu_0 H_z = 15\,\mathrm{mT}$ and $\mu_0 H_z = 25\,\mathrm{mT}$ in Fig. 6.15 a) and b), respectively.

Even though the changes in Q_{peak} and w are likely to mot proceed on ultrafast time scales, as will be discussed in section 6.4.3.3, the dependence of the size of the changes on the temporal overlap indicates that the quasi-instantaneous heat load from both pulses initiates the process. This sampling of the 70 fs-short XUV-laser (FEL) pulses over the 3500 fs-long nIR-laser pulses is illustrated in Fig. 6.15 c). For an estimation of the relative impacts of the two pulses, the peak intensities (or peak power densities), P, are determined from the respective fluences and pulse durations, $P = F/\tau$, which yields calculated values of $P_{\mathrm{nIR}} = 3.8\,\mathrm{GW/cm^2}$ and $P_{\mathrm{FEL}} = (60.0\text{–}100.0)\,\mathrm{GW/cm^2}$ (variation due to FEL-pulse intensity fluctuations). Note that for both types of pulses, in a first approximation, a comparable (non-equilibrium) heating can be expected as XUV light ($\lambda = 20.8\,\mathrm{nm}$) has almost the same attenuation length of $\delta_{\mathrm{XUV}} \approx 11\,\mathrm{nm}$ in Co as nIR-laser light ($\lambda = 800\,\mathrm{nm}$) with an attenuation length of $\delta_{\mathrm{nIR}} \approx 13\,\mathrm{nm}$. An about 20 times higher FEL-pulse peak intensity, with fluctuations that exceed the nIR-laser peak intensity, however, shows that the absolute value of P alone cannot explain the here-observed distinct Q_{peak} and w-shifts at $\Delta t = 0$. If this was the case, the modifications would be expected to occur randomly throughout the delay-time scan, initiated by the high-intensity XUV-laser pulses alone, and not only at $\Delta t \approx 0$. It thus seems that not only the peak intensity, but also the photon energy, i. e., the type of electronic excitation, plays a role for the here-observed effects. While nIR light with $E_{\mathrm{ph}} \approx 1.6\,\mathrm{eV}$ induces electronic valence-to-conduction band excitations around the Fermi energy, XUV light with $E_{\mathrm{ph}} \approx 60\,\mathrm{eV}$ induces electronic excitations from deep down the electronic band structure ($3p$ core levels) up to the valence band, thereby generating also higher-energetic electrons. From the above given considerations, both effects, i. e., the "warming-up" of the electron-system by the nIR-laser pulses in combination with generating also more high-energetic electrons by the XUV pulses, are required for inducing the permanent changes in Q_{peak} and w.

Qualitative differences of the double-pulse induced Q_{peak} and w-shifts can be connected

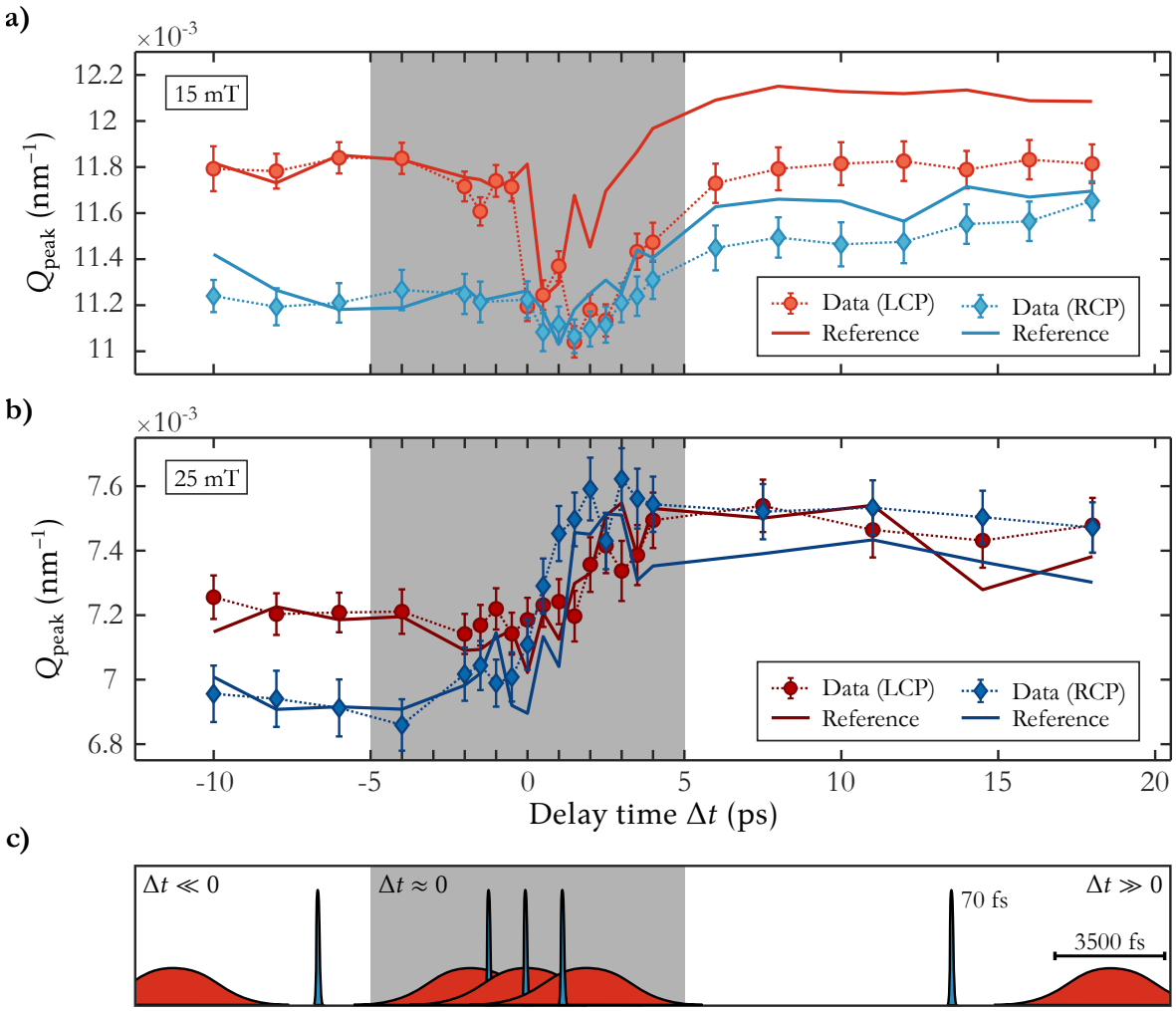

Figure 6.15.: Illustration of the combined action of nIR-laser and FEL pulses on the nanoscopic multi-domain states. a) and b) Zoom-ins to the first few picoseconds of the Q_{peak} transients for $\mu_0 H_z = 15\,\mathrm{mT}$ and $\mu_0 H_z = 25\,\mathrm{mT}$, respectively, for both LCP (red) and RCP (blue) nIR-laser excitation. Solid lines show the corresponding FEL-reference measurements. Permanent lateral modifications are induced only in the regime where nIR-laser and FEL pulses have a temporal overlap (gray shaded area). c) Schematics of sampling the 70 fs-short FEL pulses over the 3500 fs-long nIR-laser pulses. While for $\mu_0 H_z = 15\,\mathrm{mT}$ the lateral modifications are reversed upon passing $\Delta t \approx 0$, they reside in the changed position for $\mu_0 H_z = 25\,\mathrm{mT}$. No changes in Q_{peak} are observed for $\Delta t \ll 0$ and $\Delta t \gg 0$, i. e., no permanent modifications are induced by the nIR-laser or the FEL pulses alone.

to the different H_z-field regimes that were identified in the previous section. While up to $\mu_0 H_z = 15\,\mathrm{mT}$ (see Fig. 6.15 a)), the Q_{peak}-shift is reversed at small positive delay times, $\Delta t \gtrsim 0$ (FEL-pulses overlap with the tail of the nIR-laser pulse's temporal profile), it is not reversed for $\mu_0 H_z = 25\,\mathrm{mT}$ (see Fig. 6.15 b)). A transition from the regime of reversible to the regime of irreversible changes is likely present for a magnetic field of $\mu_0 H_z = 15\,\mathrm{mT}$, i. e., close to the coercive field of $\mu_0 H_c \approx 20\,\mathrm{mT}$. In this case, the reversibility is in principle maintained, but different final domain states are approached after the double-pulse excitations. The same regimes, i. e., reversible domain modifications in slightly asymmetric multi-domain states and irreversible domain modifications in close-to-single domain configurations, were observed in Ref. [283], where the (field-induced) magnetization reversal in a $[\mathrm{Co/Pt}]_{50}$ multilayer was investigated both macroscopically, by the first-order reversal curve (FORC) technique, and microscopically, by transmission X-ray microscopy (TXRM) and mSAXS. In that publication, the regime close to the single-domain state could be associated with irreversible and *avalanche-like* domain modifications. Such ongoing processes, in this work initiated by the double-pulse excitations, could explain small differences between nIR-pump–XUV-probe and FEL-reference data for the $\mu_0 H_z = 15\,\mathrm{mT}$ and $\mu_0 H_z = 25\,\mathrm{mT}$ cases (see Fig. 6.15). An interpretation of the double-pulse induced Q_{peak} and w-shifts in real space, i. e., a link to lateral modifications in the multi-domain patterns, is given in the following section. The interpretation is based on observations in the pre-study at PETRA III using mSAXS in tandem with FTH and a comparison to the observations in Ref. [283].

6.4.3.2. Link between Reciprocal-Space Measurements and Underlying Lateral Domain Modifications

The double-pulse induced permanent changes in Q_{peak} and w are linked to permanent lateral domain modifications, invoking the findings from mSAXS in tandem with FTH in the pre-study at PETRA III (section 6.1). For that, the measured Q_{peak} and w-values are converted the average domain periodicity, $T_{\mathrm{av}} = 2\pi/Q_{\mathrm{peak}}$ and the lateral correlation length, $\xi = 2\pi/w$. The maximum relative changes, obtained by relating the maximum laser-induced changes to the corresponding starting values, $\Delta T_{\mathrm{av}}^{\mathrm{max}}/T_{\mathrm{av},0} = T_{\mathrm{av}}^{\mathrm{max}}/T_{\mathrm{av},0} - 1$, and $\Delta \xi^{\mathrm{max}}/\xi_0 = \xi^{\mathrm{max}}/\xi_0 - 1$, are shown for the different H_z-field cases in Fig. 6.16 b) and c), respectively. Note that for the starting values, the average domain periodicity and lateral correlation length at negative delay times were used, i. e., $T_{\mathrm{av},0} = \langle T_{\mathrm{av}}(\Delta t < 0)\rangle$ and $\xi_0 = \langle \xi(\Delta t < 0)\rangle$.

The three H_z-field cases, i. e., the symmetric maze-domain ground state ($\mu_0 H_z = 0\,\mathrm{mT}$), the slightly asymmetric multi-domain states ($\mu_0 H_z = 5\,\mathrm{mT}$ and $\mu_0 H_z = 15\,\mathrm{mT}$) and the close-to single-domain state ($\mu_0 H_z = 25\,\mathrm{mT}$), represented by the magnetic holograms from FTH at PETRA III in Fig. 6.16 a), are treated individually in the following.[12]

[12] Note that the pre-study at PETRA III was conducted on a thicker $[\mathrm{Co/Pt}]_6$ multilayer and for higher H_z-fields (see

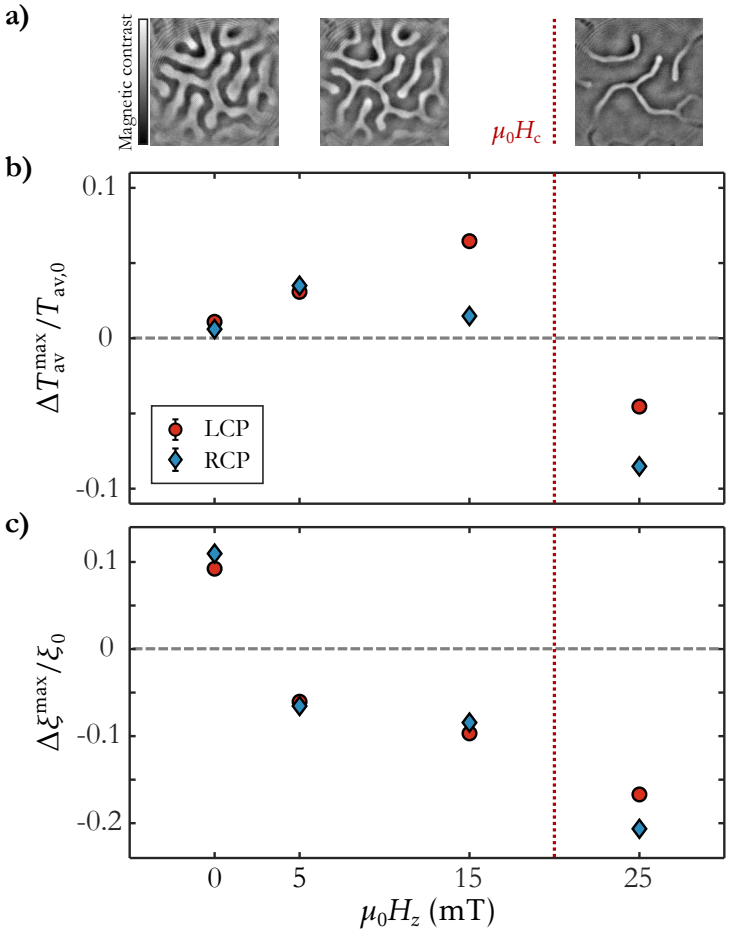

Figure 6.16.: a) Magnetic holograms obtained by FTH in the pre-study at PETRA III (section 6.1.2) from a similar $[Co/Pt]_6$ multilayer. They depict multi-domain states with increasing asymmetry in the area filling of up and down-magnetized domains, analogue to the three H_z-field regimes that were identified in this TR-mSAXS experiment ($\mu_0 H_z = 0\,mT$; $\mu_0 H_z = 5\,mT$ and $\mu_0 H_z = 15\,mT$; $\mu_0 H_z = 25\,mT$). b) Maximum relative change in the average domain periodicity, $\Delta T_{av}^{max}/T_{av,0}$, and c) maximum relative change in the lateral correlation length, $\Delta\xi^{max}/\xi_0$, induced by the combined action of LCP and RCP nIR-laser and FEL pulses. The coercive field of the $[Co/Pt]_6$ multilayer at $\mu_0 H_c \approx 20\,mT$ is indicated by the red dotted line.

Maze-Domain Ground State For an equal area filling of up and down-magnetized domains ($\mu_0 H_z = 0\,mT$), almost no change of the average domain periodicity, with $\Delta T_{av}^{max}/T_{av,0} = +(1.0 \pm 0.3)\%$ (LCP), is observed during the delay-time scan. A maximum relative change in the lateral correlation length of $\Delta\xi^{max}/\xi_0 = +(9.2 \pm 0.6)\%$ (LCP), however, leads to a slight increase of the short-range order, ξ/T_{av}, from 1.66 ± 0.01 to 1.77 ± 0.01. Note that almost the same values are obtained when using RCP nIR-laser pulses. The impact of the combined nIR and XUV-laser pulse irradiation on the domain configuration is weak, i. e., the maze-domain ground state largely resides in its initial (unpumped) configuration. A slight increase in the short-range order is likely due to the fact that not the global but a magnetic state close to the global ground state was obtained by OOP demagnetization cycles prior to the experiment. As mentioned in section 2.3, the exact nanostructure of the multi-domain pattern depends on structural defects such as lattice mismatches or vacancies. Laser heating may cause a depinning of domains from

section 6.1.2). A comparison to the here-observed H_z-field induced changes in section 6.4.1, however, showed that both H_z-field situations are comparable, with larger ($D_{av} \approx 230\,nm$) and more disordered ($\xi/T_{av} \approx 1.7$) magnetic domains in the here-investigated thinner $[Co/Pt]_6$ multilayer. The holograms are used for illustration purposes, the scale bars were removed for this section.

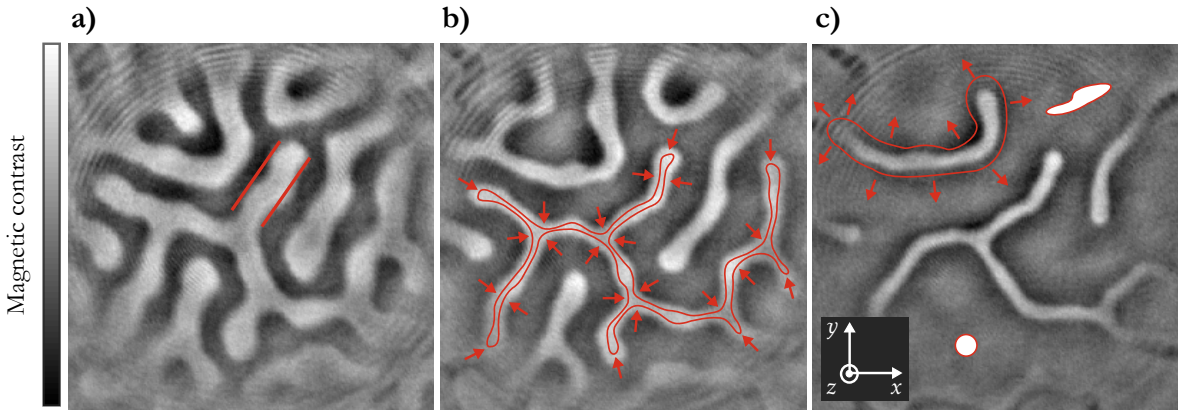

Figure 6.17.: Illustration of the double-pulse induced permanent modifications (red) in nanoscopic multi-domain states with increasing asymmetric domain configuration, based on a comparison of the relative changes in $T_{\mathrm{av}}^{\mathrm{max}}$ and ξ^{max} with the observations by mSAXS in tandem with FTH in the pre-study at PETRA III. a) In the maze-domain ground state ($\mu_0 H_z = 0\,\mathrm{mT}$), no laser induced modifications are observed. Small domain reconfigurations, such as a straightening of wavy domains, could be imagined to account for an initial increase of the short-range order in the maze-domain ground state ($\Delta\xi^{\mathrm{max}}/\xi_0^{\mathrm{max}} \approx +10\%$). b) In the slightly asymmetric multi-domain states ($\mu_0 H_z = 5\,\mathrm{mT}$ and $\mu_0 H_z = 15\,\mathrm{mT}$), the double-pulse induced permanent modifications support the H_z-field induced asymmetry, i. e., a further growth of majority over minority domains. c) In the close-to single-domain state ($\mu_0 H_z = 25\,\mathrm{mT}$), the double-pulse induced modifications oppose the H_z-field induced asymmetry. This could be imagined as a growth of existing minority domains or the nucleation of new minority domains.

such defects, leading only to minor modifications ($\Delta T_{\mathrm{av}}^{\mathrm{max}}/T_{\mathrm{av},0} \approx 0$) and a final domain state that is closer to the global ground state than the one that was set by OOP demagnetization cycles. One possibility for such minor modifications is illustrated in Fig. 6.17 a).

Slightly Asymmetric Multi-Domain State The situation is different for multi-domain states where the symmetry in the area filling of up and down-magnetized domains is broken by external magnetic fields of $\mu_0 H_z = 5\,\mathrm{mT}$ and $\mu_0 H_z = 15\,\mathrm{mT}$. In these cases, an increasing average domain periodicity from $\Delta T_{\mathrm{av}}^{\mathrm{max}}/T_{\mathrm{av},0} = +(3.0 \pm 0.2)\%$ to $\Delta T_{\mathrm{av}}^{\mathrm{max}}/T_{\mathrm{av},0} = +(6.5 \pm 0.3)\%$ and a decreasing lateral correlation length from $\Delta\xi^{\mathrm{max}}/\xi_0 = -(6.1 \pm 0.6)\%$ to $\Delta\xi^{\mathrm{max}}/\xi_0 = -(9.7 \pm 0.6)\%$ is obtained (LCP case).[13] As they both have the same sign as the H_z-field induced changes (section 6.4.1), the double-pulse induced modifications are interpreted in the same way, i. e., as a further growth of majority over minority domains, as illustrated in Fig. 6.17 b). These permanent modifications were found to be (largely) reversed at small positive delay times, $\Delta t \gtrsim 0$ (see Fig. 6.15 a)), and may thus be envisioned as a "breathing" of the multi-domain structure. Interestingly, this *reversibility* of the double-pulse induced modifications in slightly

[13] Differences in $\Delta T_{\mathrm{av}}^{\mathrm{max}}/T_{\mathrm{av},0}$ and $\Delta\xi^{\mathrm{max}}/\xi_0$ between LCP and RCP nIR-laser excitation are likely due to differences in their respective starting values (section 6.4.3).

asymmetric multi-domain states is also seen for H_z-field induced modifications [283]. It thus seems that the sampling of the ultrashort XUV-laser pulses over the picosecond-long nIR-laser pulses has a similar effect as when slightly changing an external H_z field back and forth.

Close-to Single-Domain State In the close-to single-domain state at $\mu_0 H_z = 25\,\mathrm{mT}$ the change of sign to $\Delta T_{\mathrm{av}}^{\mathrm{max}}/T_{\mathrm{av},0} = -(4.5 \pm 0.5)\%$ (LCP case) could be interpreted as a reversal of this effect, i. e., a growth of minority over majority domains.[14] Besides of the growth of already existing minority-domain structures, also the nucleation of new minority-domain structures could explain the smaller average domain periodicity, i. e., a reduction of the asymmetry. The two possible mechanisms are illustrated in Fig. 6.17 c). Note that, the fracturing of string-like domains into smaller magnetic structures, which could be imagined to lead to a magnetic domain state with reduced average domain periodicity as well, in fact, would have the opposite effect, i. e., a further increase in the asymmetry (see previous paragraph). The permanent modifications in the close-to single-domain state were found to remain largely unchanged at small positive delay times, $\Delta t \gtrsim 0$ (see Fig. 6.15 b)). This *irreversibility* of the double-pulse induced modifications is, again, also seen for H_z-field induced changes [283], supporting the interpretation of nucleation and growth processes. The here obtained results could thus be interpreted as the initial stage of AOS in ferromagnetic thin films, i. e., the nucleation of minority domains in an extended majority domain, as described in detail in section 2.5.2.2. It is emphasized that in TR-mSAXS experiments, ensemble-averaged information is recorded, so that a noticeable Q_{peak}-shift of a few percent would have to originate from collective (nucleation and growth) processes. A discussion on the time scale of these processes is given in the following section.

6.4.3.3. Ultrafast vs. Slow Dynamics Investigated by Single-Pulse Measurements

One of the remaining questions is whether the permanent domain modifications can be induced by a single nIR-pump–XUV-probe pulse-pair, possibly on an (sub-)picosecond time scale, or by a series of nIR-pump–XUV-probe pulse-pairs, presumably on a much slower time scale. Obviously this question cannot be answered by multi-pulse but only by single-pulse experiments. Due to the small magnetic scattering cross section of magnetic thin films, however, a single FEL-pulse exposure is often not enough to provide a sufficient signal-to-noise ratio. Presumably due to the narrow bandwidth at FERMI of $\approx 0.05\%$, a large enough magnetic scattering intensity, with a maximum value of $I_{\mathrm{max}} \approx 20\,\mathrm{ADU}$ at a background noise of $\approx 2\,\mathrm{ADU}$, was obtained here by a single FEL-pulse exposure.

To ensure that permanent lateral domain modifications can be induced by the single

[14] Note that a further reduction of $\Delta\xi^{\mathrm{max}}/\xi_0 = -(16.7 \pm 0.7)\%$ results in a further reduction of the short-range order.

pulse-pair, the findings from the previous sections were taken into account, i. e., a close-to single-domain state was generated using a magnetic field of $\mu_0 H_z = 25\,\mathrm{mT}$ and the temporal overlap between nIR-laser and FEL pulses was maximized using a delay time of $\Delta t \approx 0$. Note that prior to the single-pulse measurements, a multi-domain state was generated by manual OOP demagnetization cycles in the maximum field of the in-vacuum Helmholtz coils of $\mu_0 H_z = \pm 50\,\mathrm{mT}$. With a maximum field that is below the saturation field of $\mu_0 H_\mathrm{s} \gtrsim 200\,\mathrm{mT}$ (Fig. 3.3 c) on p. 59), the final multi-domain state using $\mu_0 H_z = 25\,\mathrm{mT}$ must not be imagined the same as the multi-domain state using $\mu_0 H_z = 25\,\mathrm{mT}$ investigated before. As the size and direction of the double-pulse induced domain modifications were found to depend on the underlying domain configuration (or H_z field), the results from the multi and the single-pulse measurements cannot be directly compared. However, as the single-pulse measurements probe the impact on the multi-domain configuration pulse-by-pulse, a first insight in whether an ultrafast (sub-picoseconds) or a comparably slow (picoseconds to seconds) mechanism is at work can be gained. It can furthermore be clarified whether the effect is induced by single or multiple pulse-pairs. Selected scattering images from a series of 25 single-pulse exposures of a close-to single-domain state ($\mu_0 H_z = 25\,\mathrm{mT}$) are shown in Fig. 6.18 a). Prior to a series of 20 pumped single-pulse images, 5 unpumped single-pulse images were recorded as FEL-reference measurements. Note that, the magnetic scattering intensity strongly varies in the different images not only because of ultrafast demagnetization (unpumped and pumped images are shown) but also due to the FEL-pulse-intensity fluctuations. The scattering images were processed according to the descriptions in section 6.3, the resulting pulse-to-pulse evolutions of the integrated intensity, I_norm, the position, Q_peak, and the width, w, of the magnetic scattering peak, $I_\mathrm{norm}(Q)$, are presented in Fig. 6.18 b), c) and d), respectively.

Constant I_norm, Q_peak and w values in the unpumped images (open circles) confirm that the excitation by a single FEL pulse alone has no impact neither on the magnetization nor on the lateral domain configuration. As could be expected for a delay time of $\Delta t = 0$, the magnetic scattering intensity, I_norm, is quenched in all of the pumped images due to ultrafast demagnetization. Contrarily, both the Q_peak position and the width, w, remain the same in the first pumped image, followed by continuous evolutions over the next 2–5 pulses. The single-pulse measurements thus show that the lateral domain modifications do not occur on an ultrafast time scale, but evolve from one pulse to another (independent from ultrafast demagnetization). The actual dependence of this effect on the number of pulses, and not on the time that has passed within acquiring 2–5 scattering images ($\approx (30\text{–}100)\,\mathrm{s}$), is supported by the multi-pulse measurements, where the modified domain state was observed already after an exposure time of 2 s (100 pulses at a repetition rate of 50 Hz).

The results thus point at lateral domain modifications that proceed on a slower time scale, e. g., similar to what was observed in a magnetic stripe-domain pattern of a CoPd alloy thin film in Refs. [36, 284]. Upon almost full demagnetization of the CoPd alloy thin film by a

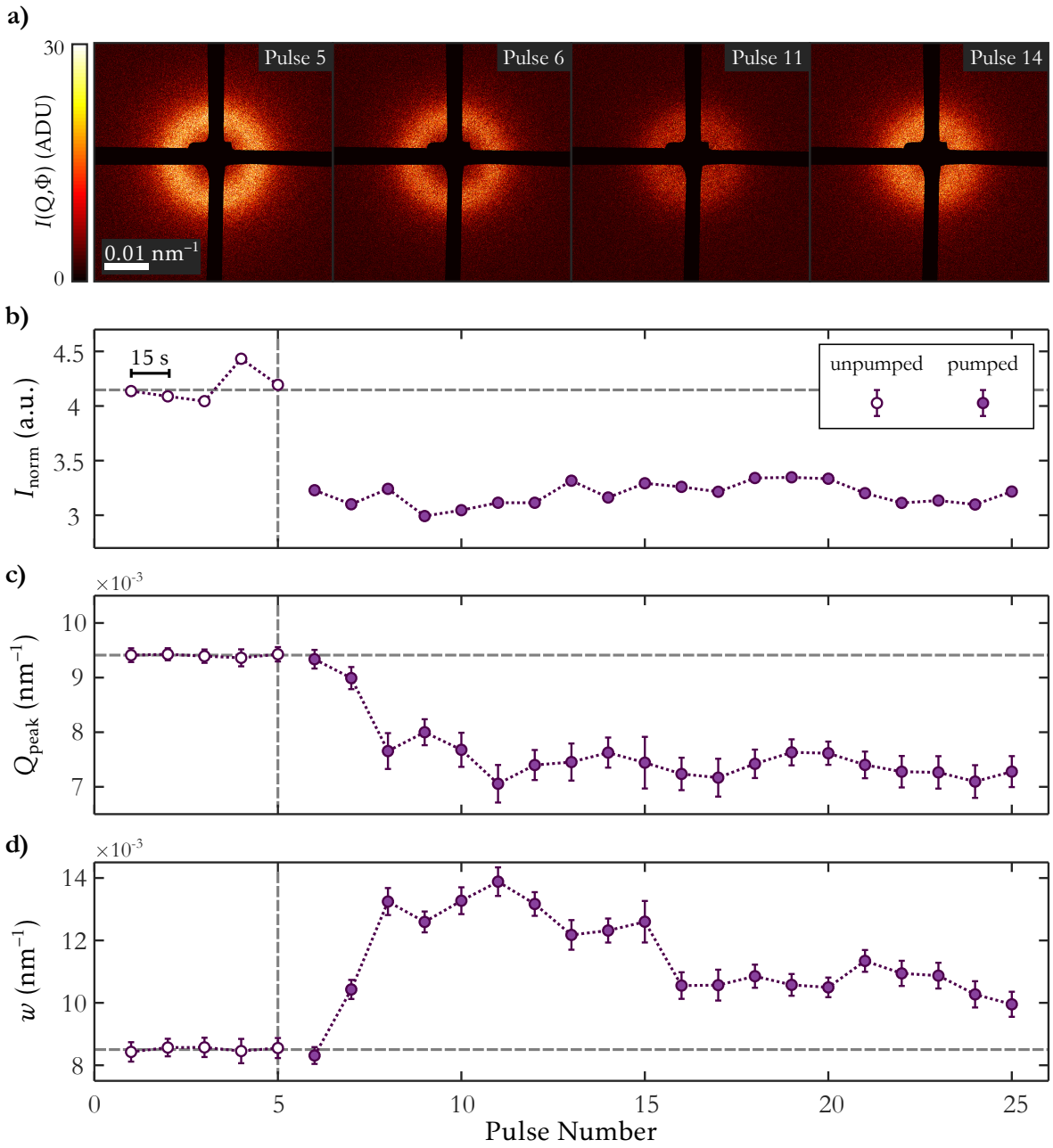

Figure 6.18.: a) Selected scattering images, $I(Q,\Phi)$, from a series of single-pulse measurements on an asymmetric multi-domain state ($\mu_0 H_z = 25\,\mathrm{mT}$) of the $[\mathrm{Co/Pt}]_6$ multilayer using a delay time $\Delta t = 0$. Pulse-to-pulse evolution of b) the normalized magnetic scattering intensity, I_{norm}, c) the peak position, Q_{peak}, and d) the width, w, of the magnetic scattering ring. Prior to a series of pumped images (filled circles), a series of unpumped images (open circles) was recorded (nIR-laser off) as a reference. The nIR-laser pulses were LCP. The time between two consecutive single-pulse measurements is $\approx 15\,\mathrm{s}$.

single-pulse excitation with a high fluence ($F_{\mathrm{nIR}} = 65\,\mathrm{mJ/cm^2}$), a permanent transformation of the stripe-domain pattern was observed with a preferred final domain orientation that depends on the direction of a small IP magnetic field [36].[15] It was proposed that this reconfiguration occurs during the extended magnetization recovery following strong nIR-laser excitation, i. e., on a time scale of $\approx (5\text{–}10)\,\mathrm{ns}$. It was furthermore evidenced by FEL-reference measurements several seconds after nIR-laser excitation that this reorientation is permanent (or frozen). This laser induced permanent reorientation of a stripe-domain pattern recently has been imaged in real space [284]. In this publication, a fluence threshold for the permanent modifications was found ($F_{\mathrm{nIR}} \approx 12\,\mathrm{mJ/cm^2}$) and the time scale on which they occur could be narrowed down to approximately 190 ps.

From a comparison to the reported findings in Refs. [36, 284], permanent lateral domain modifications in the presence of either IP or OOP magnetic fields could be a more general phenomenon. In all cases, a large disorder was induced in the multi-domain states using a high-fluence nIR-laser excitation, accompanied by a extended magnetization recovery on pico to nanoseconds time scales (section 6.4.2.1). While a reorientation of a stripe-domain pattern is observed in the presence of IP magnetic fields, here, an increased or decreased asymmetry is observed in a multi-domain state in the presence of OOP magnetic fields. The similarity of the two observations suggests, that the here observed effect could also take place during the extended magnetization recovery on a few 100 ps time scale. Interestingly, instead of a fluence dependence (fluence-threshold) for the permanent lateral domain modifications in Refs. [36, 284], here, a dependence on the temporal overlap of the picosecond-long nIR-laser pulses ($P_{\mathrm{nIR}} = 3.8\,\mathrm{GW/cm^2}$) with the ultrashort XUV pulses ($P_{\mathrm{FEL}} = (60.0\text{–}100.0)\,\mathrm{GW/cm^2}$) was found (section 6.4.3.1). The single-pulse measurements reveal that these changes evolve over a few double-pulse exposures until the new, energetically more stable configuration is reached.

6.5. Summary

The results of the TR-mSAXS experiment at FERMI, where the same optically thin $[\mathrm{Co/Pt}]_6$-multilayer sample as in the TR-mSAXS experiment at FLASH was investigated, are summarized in the following.

By using pulsed OOP magnetic fields with increasing strengths in the range of $\mu_0 H_z = (0\text{–}25)\,\mathrm{mT}$, an increasing asymmetry in the area filling of up and down-magnetized domains was induced in the maze-domain ground state. The different multi-domain states were excited by LCP and RCP nIR-laser pulses with a pulse duration of $\tau_{\mathrm{nIR}} = 3500\,\mathrm{fs}$ and a fluence of $F_{\mathrm{nIR}} = 13.4\,\mathrm{mJ/cm^2}$, which resulted in a maximum degree of demagnetization of $\approx 50\%$ and an extended magnetization recovery compared to a low-fluence excitation ($\tau_{\mathrm{E}} \approx 1\,\mathrm{ps}$)

[15] Note that no actual IP magnetic field was applied in their experiment, but the small earth magnetic field was put forward to explain the results.

with a substantial persisting degree of demagnetization of $\approx 30\%$ at $\Delta t \approx 100\,\mathrm{ps}$. Ultrafast magnetization dynamics that are independent from the nIR-laser polarization (section 6.4.2.1) as well as the underlying multi-domain configuration (section 6.4.2.2) were found, in agreement with the findings in the experiment at FLASH (chapter 5).

Furthermore, changes in Q_{peak} and w of the (first-order) magnetic scattering peak were observed upon laser excitation independently accompanying the ultrafast magnetization dynamics, but only, if the following two conditions were fulfilled:

1. The symmetry in the area filling of up and down-magnetized domains has to be broken by OOP magnetic fields ($\mu_0 H_z > 0\,\mathrm{mT}$).

2. The 3500 fs-long nIR and the 70 fs-short XUV-laser (FEL) pulses have to temporally overlap. As the peak-intensity fluctuations of the XUV-laser pulses exceed the peak intensity of the nIR-laser pulses, but the changes in Q_{peak} and w only occur at $\Delta t \approx 0$, it is concluded that not only the peak intensity but also the photon energy plays a role for the here-observed effects (section 6.4.3.1).

In contrast to the transient Q_{peak}-shift in a previous collaborative TR-mSAXS experiment at FLASH [32], the here observed changes were found to be permanent, as shown by FEL-reference measurements recorded in-between two consecutive nIR-pump–XUV-probe measurements. The size of these changes was found to scale with the temporal overlap of the two pulses, i. e., the maximum impact on Q_{peak} and w occurs at $\Delta t = 0$.

Qualitative differences of the permanent Q_{peak} and w-shifts are observed for the different H_z-field cases, or multi-domain states. The laser induced permanent changes in Q_{peak} and w were converted to permanent changes in the average domain periodicity and the lateral correlation length via $T_{\mathrm{av}} = 2\pi/Q_{\mathrm{peak}}$ and $\xi = 2\pi/w$. The permanent lateral domain modifications were interpreted based on observations of H_z-field induced modifications in the multi-domain states, investigated in the pre-study at PETRA III, where mSAXS was combined with imaging of the multi-domain states via FTH (section 6.1):

1. In slightly asymmetric multi-domain states ($\mu_0 H_z = 5\,\mathrm{mT}$ and $\mu_0 H_z = 15\,\mathrm{mT}$), the laser pulses induce changes in T_{av} and ξ that have the same sign as the H_z-field induced changes. Hence it is concluded that the laser induced domain modifications support the H_z-field induced asymmetry, i. e., a further growth of majority over minority domains (Fig. 6.17 b)). The effect was found to be reversed at small positive delay times ($\Delta t \gtrsim 0$), so that the full sampling of XUV over nIR-laser pulses could be interpreted as a “breathing” of the multi-domain state.

2. In the close-to single-domain state ($\mu_0 H_z = 25\,\mathrm{mT}$) the sign of the laser induced changes in T_{av} is reversed. Hence it is concluded that the laser induced domain modifications oppose

the H_z-field induced asymmetry. An increasing area filling of minority domains might might be connected to a growth of existing minority domains but also the nucleation of minority domains (Fig. 6.17 c)). In contrast to $\mu_0 H_z \leq 15\,\mathrm{mT}$, these modifications are not reversed at small positive delay times, $\Delta t \gtrsim 0$.

Single-pulse nIR-pump–XUV-probe measurements on a close-to single domain state ($\mu_0 H_z = 25\,\mathrm{mT}$) confirm that the domain modifications do not occur on ultrafast time scales (section 6.4.3.3). The outcome points toward a stochastic nature of the process, since the modifications evolve over as few as 2–5 double-pulse exposures until a new equilibrium domain configuration is reached. The effect can thus be interpreted as the initial stage of stochastic multi-pulse AOS in ferromagnets (section 2.5.2.2), i. e., the nucleation of (an ensemble of) minority domains in an extended majority domain, presumably getting frozen during sample cooling on a few-100 ps–1 ns time scale. A helicity dependence, as it would be expected for AOS in ferromagnets, could, however, not be confirmed. Further investigations where, e. g., the photon energy and the peak intensity of the two laser pulses are systematically varied are required, in order to study the here observed effects in more detail.

7 Conclusions and Outlook

Ultrafast magnetization dynamics in optically thin Co/Pt multilayers was studied in time-resolved magnetic small angle X-ray scattering (TR-mSAXS) experiments using short nIR pump pulses and ultrashort XUV pump/probe pulses from the FLASH (DESY, Hamburg) and FERMI (Elettra, Trieste) Free Electron Lasers (FELs). Thin (few-repetition) Co/Pt multilayers were chosen because of their enhanced sensitivity to all-optical switching effects, their suitability for quasi-homogeneous excitation and probing with nIR ($E_{\mathrm{ph}} \approx 1.6\,\mathrm{eV}$) and XUV radiation ($E_{\mathrm{ph}} \approx 60\,\mathrm{eV}$), and the possibility to influence the area filling of up and down-magnetized domains with help of small OOP magnetic fields. A large magnetic scattering intensity in the experiment at FERMI, presumably due to the small energy bandwidth, allowed also for single-pulse nIR-pump–XUV-probe measurements, which proved to be crucial for the interpretation of part of the results. Complementary Fourier-transform holography (FTH) data were taken at PETRA III enabling a real-space interpretation of the scattering data at FERMI.

Maze-domain ground states of three $[\mathrm{Co/Pt}]_x$ multilayers, with $x = 3$, 6, and 8, with average domain periodicities in the range of $T_{\mathrm{av}} \approx (400\text{–}1200)\,\mathrm{nm}$ were excited by 70 fs and 300 fs-short, linearly and circularly polarized nIR-laser pulses and probed by 60 fs-short XUV-laser pulses from FLASH. The ultrafast magnetization dynamics were found to be independent from the polarization as well as the pulse duration of the nIR-laser pulses. They are moreover independent from the underlying domain configuration.

A strongly increasing maximum degree of demagnetization with nIR-laser fluence was observed in the optically thin samples, reaching full demagnetization in the thinnest, $[\mathrm{Co/Pt}]_3$ multilayer ($d = 8.6\,\mathrm{nm}$) at $F_{\mathrm{nIR}} = 18.9\,\mathrm{mJ/cm^2}$. Thickness-dependent differences existed in the maximum degrees of demagnetization, which can be understood from the absorption of nIR light with finite attenuation length in Co and Pt. However, when taking layer-dependent absorption into account, the three samples can be treated as one optically thin Co/Pt-multilayer system reaching different average temperatures. The temperature dependencies of both the demagnetization time, τ_{M}, and the energy equilibration time, τ_{E}, were modeled within the three-temperature model (3TM) and compared to results from its microscopic extension (M3TM). The results strongly indicate that the ultrafast magnetization dynamics are governed predominantly by electron–phonon spin-flip scattering processes induced by ultrashort nIR-laser heating. Direct transfer of angular momentum from the photons as well as non-local superdiffusive spin transport across domain boundaries, in contrast, play a minor role in the Co/Pt-multilayer

system. For nIR-laser induced temperature rises close to the Curie Temperature, T_C, the maximum degree of demagnetization appeared to be suppressed and the energy equilibration time, τ_E, versus temperature behavior strongly deviated from its linear increase at low temperatures.

Here it is proposed to model both the low and the high-temperature behavior of τ_E, combining the low-temperature dependence of τ_E as described within the analytical solution of the 3TM, with the so-called slowdown time at high temperatures as predicted by theory. This implies that the temperature dependence of τ_E is not only governed by the specific heat of the electron system and the electron–phonon coupling parameter, $C_e(T)/G_{e\ell}$ (low-temperature behavior), but is rather determined by the specific heat of the electron and spin system and the electron–phonon coupling parameter, $(C_e(T) + C_s(T))/G_{e\ell}$. The good agreement of the model with the experimental data suggests that it is more accurate to treat $\tau_E(T)$ by a strongly coupled electron–spin system, rather than the electron system alone. By including a high-temperature contribution to the modeling of $\tau_E(T)$, both the suppression of the maximum degree of demagnetization and the slowing down of the remagnetization dynamics at high temperatures can be understood from the divergence of $C_s(T)$ close to T_C.

The presence of critical phenomena at high temperatures on ultrafast time scales could be further investigated by TR-mSAXS. Direct evidence for magnetization fluctuations with a spatial resolution down to 1 nm could be obtained by adjusting the experimental geometry in combination with using shorter-wavelength radiation, e. g., $\lambda \approx 1.6\,\mathrm{nm}$ for probing the magnetic states in resonance with the Co L_3 edge. Future experiments that aim for finding the ultimate time scale of ultrafast demagnetization, today, still depend upon the development of shorter pump as well as shorter probe pulses, with pulse durations down to the attosecond regime.

Using external magnetic fields in the range of $\mu_0 H_z = (0\text{–}25)\,\mathrm{mT}$, multi-domain states with increasing asymmetry in the area filling of up and down-magnetized domains were produced in a $[Co/Pt]_6$ multilayer. The impact of H_z fields on the maze-domain ground state of a comparable sample was visualized by FTH at PETRA III. The different asymmetric multi-domain states were excited by 3500 fs-long nIR-laser pulses and probed by 70 fs-short XUV-laser (FEL) pulses from FERMI, with focus on investigating changes in the position, Q_{peak}, and width, w, of the first-order magnetic scattering peak.

The analysis of the TR-mSAXS data showed laser induced lateral modifications in the nanoscopic multi-domain states. However, these modifications only occurred if the symmetry in the area filling of up and down-magnetized domains was broken by OOP magnetic fields and the nIR and XUV-laser (FEL) pulses arrived at the sample at the same time ($\Delta t \approx 0$). Their magnitude and sign furthermore depend on the temporal overlap of the two pulses (the extended nIR pump pulse is sampled by the ultrashort XUV probe pulse) and the underlying domain state. The lateral domain modifications were permanent, as shown by FEL-reference

measurements recorded ≈ 15 s after each pump-probe sequence. Since the fluctuations of the FEL pulse peak intensity exceeded the nIR-laser pulse peak intensity, but the lateral domain modifications only occurred at $\Delta t = 0$ (temporal overlap), one is lead to believe that also the photon energy, i. e., the simultaneous generation of both low-energetic electrons ($E_{\mathrm{ph}} \approx 1.6\,\mathrm{eV}$) and high-energetic electrons ($E_{\mathrm{ph}} \approx 60\,\mathrm{eV}$) plays a role for the observed effects. Single-pulse measurements revealed that the domain modifications evolved pulse-by-pulse until a new equilibrium state was reached after the impact of ≈ 2–5 double-pulse exposures.

A detailed analysis shows that in slightly asymmetric multi-domain states ($\mu_0 H_z = 5\,\mathrm{mT}$ and $\mu_0 H_z = 15\,\mathrm{mT}$) the double-pulse induced domain modifications can be interpreted as a growth of majority over minority domains. In the close-to single-domain state ($\mu_0 H_z = 25\,\mathrm{mT}$), the sign of the double-pulse induced Q_{peak}-shift was reversed. This is in agreement with the growth of already existing minority domains or could also be interpreted by the nucleation of minority domains. From these considerations one might speculate that the Q_{peak}-shift in the close-to single domain state shows the initial stage of stochastic multi-pulse all-optical switching (AOS) in ferromagnets, i. e., a collective nucleation (and growth) of minority domains in extended majority domains.

The results show that TR-mSAXS is a powerful tool for investigating ultrafast magnetization dynamics with femtosecond time and nanometer spatial resolution. Further investigations on all-optically induced domain modifications in nanoscopic multi-domain states would certainly benefit from further systematic single-pulse TR-mSAXS experiments. Non-standard delay-time scans, like a reversed sweeping of Δt from positive to negative values, or even in an arbitrary fashion, could be conducted in order to answer the question of whether or not the permanent modifications depend on the history of the temporal overlap between the two pulses, i. e., whether or not the same final domain state is reached for different sequences of the double-pulse exposures. Furthermore, higher repetition rates up to the megahertz regime, as provided, e. g., by Eu-XFEL, in combination with sophisticated FEL-reference–nIR-pump–FEL-probe schemes could be used in the future to narrow down the time scale of the involved processes. A dependence of the permanent modifications on the type of electronic excitation could be investigated by using different photon energies for pumping and/or probing the magnetic states, e. g., a photon energy of $E_{\mathrm{ph}} \approx 778\,\mathrm{eV}$ for probing the magnetic states in resonance with the Co L_3 edge. This higher photon energy ($\lambda \approx 1.6\,\mathrm{nm}$), which is connected with the possibility to investigate magnetic fluctuations down to 1 nm length scales, can help to identify if collective AOS-like nucleation processes are involved. The existence of a threshold for the observed permanent modifications could finally be addressed by systematically changing the pulses' peak intensity via the fluence and/or the pulse duration.

Appendices

A Impact of High-Fluence FEL and nIR-laser Irradiation on Magnetic Scattering Distribution

In the two TR-mSAXS experiments at FLASH and at FERMI, both low-fluence and high-fluence FEL and nIR-laser irradiation were used to pump and probe the magnetic multi-domain states of Co/Pt multilayers. Permanent alterations in the multi-domain patterns, identified via changes in the magnetic scattering distribution, $I_{\mathrm{norm}}(Q)$, are detected from one scattering image to another for both high-fluence FEL and nIR-laser excitation.

A.1. Impact of High-Fluence nIR-Laser Irradiation

In both TR-mSAXS experiments at FLASH and FERMI, high-fluence nIR-laser excitations were used to excite the magnetic multi-domain states. In particular, full demagnetization could be induced in the thinnest, $[\mathrm{Co/Pt}]_3$ multilayer using a fluence of $F^3_{\mathrm{nIR}} = 18.9\,\mathrm{mJ/cm^2}$ in the experiment at FLASH. Similar to the observations at high FEL fluences, the magnetic-scattering distribution, $I_{\mathrm{norm}}(Q)$, permanently changes in intensity and shape upon repetitive (100 pulses) high-fluence nIR-laser excitation at negative delay times, as shown in Fig. A.1 a). Note that no such permanent modifications were observed when using the lower fluences of $F^1_{\mathrm{nIR}} = 3.8\,\mathrm{mJ/cm^2}$ and $F^2_{\mathrm{nIR}} = 9.6\,\mathrm{mJ/cm^2}$. When compared to the low-fluence case of F^1_{nIR}, the maximum intensity of $I_{\mathrm{norm}}(Q)$ is reduced, the Q_{peak}-position is shifted to larger values and the width is increased. Due to the similarity to the FEL-induced alterations, the changes in $I_{\mathrm{norm}}(Q)$ could be interpreted as both thermally activated domain modifications or structural modifications. Aside from the above-mentioned growth of the grain size, also interdiffusion of Co and Pt at the interfaces could affect the magnetic anisotropy in the sample, leading to permanent changes in $I_{\mathrm{norm}}(Q)$.

The increase in the Q_{peak}-position could be interpreted according to the descriptions in Ref. [270]. In that thesis, the as-prepared (demagnetized) maze-domain state (Fig. A.1 b)) was found to segregate into a more grainy, isolated domain structure (Fig. A.1 c)) upon repetitive (≈ 200 pulses) nIR-laser excitation with a fluence of $F_{\mathrm{nIR}} = 14.2\,\mathrm{mJ/cm^2}$. The segregation was explained by a localized magnetization-recovery process during sample cooling. First, due to

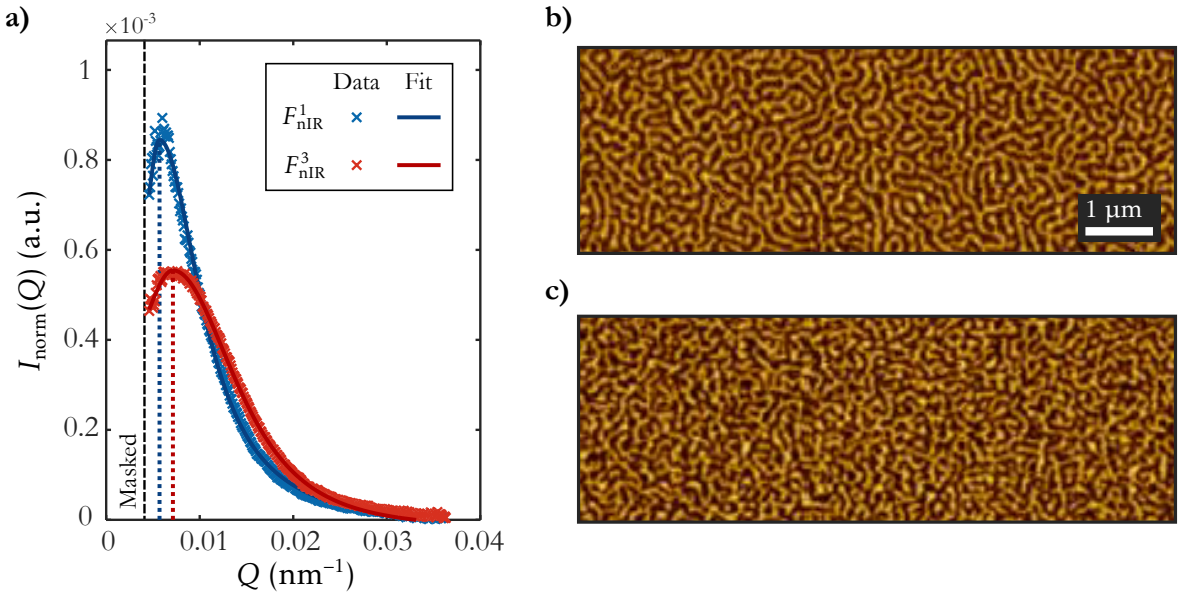

Figure A.1.: a) Magnetic scattering intensities, $I_{norm}(Q,\Delta t = -1\,ps)$, of the $[Co/Pt]_3$ multilayer using $F^1_{nIR} = 3.4\,mJ/cm^2$ and $F^3_{nIR} = 18.9\,mJ/cm^2$, together with fits to the data by a split Pearson type-VII function. The dotted lines show the respective Q_{peak}-positions. b) and c) Magnetic force microscopy (MFM) images of the as-prepared (demagnetized) and altered maze-domain pattern of a $[Co/Pt]_{16}$ multilayer, respectively, upon repetitive high-fluence nIR-laser excitation (taken from Ref. [270]). The alteration of $I_{norm}(Q)$ in a), induced by $F^3_{nIR} = 18.9\,mJ/cm^2$, may be visualized in a similar way, i. e., as a segregation of the maze-domain into a more grainy multi-domain pattern, with smaller average domain size (Q_{peak}-shift to larger values) and reduced in-plane correlation length (broadening of $I_{norm}(Q)$).

the large degree of demagnetization, induced by a high-fluence excitation, the correlation between adjacent domains is largely lost. In the highly excited state, each magnetic region tries to minimize its mean free-energy independently, leading to the formation of smaller domains in the relaxed state. The effect was furthermore found to be of a statistical nature, leading to an asymptotic increase of Q_{peak} with the number of laser-pulse excitations, that is mostly finished after the first few of the ≈ 200 pulses [270].

However, ongoing alterations in the maze-domain pattern of the $[Co/Pt]_3$ multilayer are observed at negative delay times, as shown in Fig. A.2. Throughout the acquisition of the delay-time scan from $\Delta t = -1.5\,ps$ to $\Delta t = 0\,ps$, the maximum intensity decreases by ≈ 17%, the peak width increases by ≈ 10% and the Q_{peak}-position fluctuates by ≈ 13%. Continuing changes in the intensity and shape of $I_{norm}(Q)$ from one image to another hint at structural changes, rather than thermally activated modifications in the maze-domain state like the depinning of domains and domain-wall motion. The latter would be expected to come to a rest, reaching a new equilibrium state after a certain number of nIR-laser pulse excitations. As the magnetic state of the $[Co/Pt]_3$ multilayer is fully demagnetized upon nIR-laser excitation, the fluence F^3_{nIR} was close to the destruction threshold of the sample, which makes ongoing

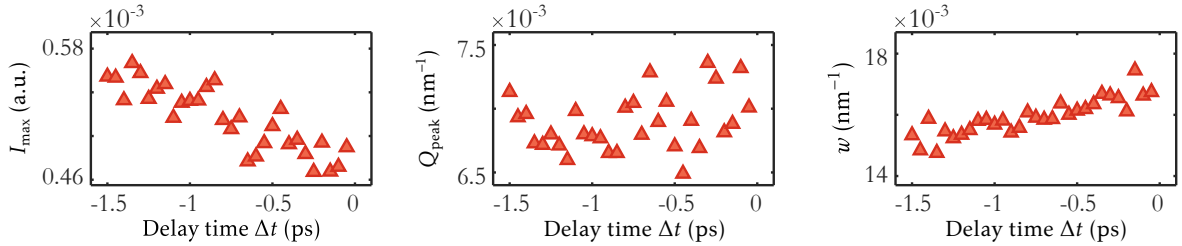

Figure A.2.: Temporal evolution of the maximum scattering intensity, I_{max}, peak position, Q_{peak}, and width, w, of the scattering distribution, $I_{norm}(Q)$ of the $[Co/Pt]_3$ multilayer at negative delay times Δt for a fluence of F_{nIR}^3.

structural modifications particularly likely. Note that, when subjecting the $[Co/Pt]_6$ multilayer (about twice the thickness of $d = 15.2\,nm$ as the $[Co/Pt]_3$ multilayer with $d = 8.6\,nm$) by a similarly high nIR-laser fluence of $F_{nIR} = 13.4\,mJ/cm^2$ in the TR-mSAXS experiment at FERMI, no such alterations in the domain pattern were observed. The combined action of high-fluence nIR-laser and low-fluence FEL pulses, however, was found to induce permanent modifications in a way that might be controlled via the nIR-laser and FEL-pulse temporal overlap (section 6.4.3).

A.2. Impact of High-Fluence FEL Irradiation

A high FEL fluence of $F_{FEL} = (30–35)\,mJ/cm^2$ was used in the TR-mSAXS experiment at FLASH to excite the magnetic maze-domain states of thin Co/Pt multilayers. The impact on the magnetic scattering intensity, $I_{norm}(Q)$, when repeatedly irradiating a fresh membrane window of the $[Co(0.8)/Pt(1.4)_6$-multilayer sample, is shown in Fig. A.3. Upon recording a series of

Table A.1.: Fit parameters from fitting a split Pearson type-VII function to the scattering distributions, $I_{norm}(Q)$, from the $[Co/Pt]_6$ multilayer on a fresh membrane (initial) and after irradiation of multiple FEL pulses with a fluence of $F_{FEL} = (30–35)\,mJ/cm^2$. Also included are the average domain period, $T_{av} = 2\pi/Q_{peak}$, the lateral correlation length, $\xi = 2\pi/w$, and the fraction ξ/T_{av}, which is a measure for the degree of order in the magnetic domain patterns

	Initial	Final
$I_{max}\,(\times 10^{-3}\,a.u.)$	0.610±0.005	0.354±0.003
$Q_{peak}\,(\times 10^{-3}\,nm^{-1})$	13.4±0.1	14.4±0.3
$w\,(\times 10^{-3}\,nm^{-1})$	7.9±0.2	17.4±0.8
$T_{av}\,(nm)$	468±4	436±9
$\xi\,(nm)$	796±19	361±17
ξ/T_{av}	1.70±0.03	0.83±0.04

50 mSAXS images (100 FEL pulse exposures per image), the $I_{norm}(Q)$ changes in intensity and

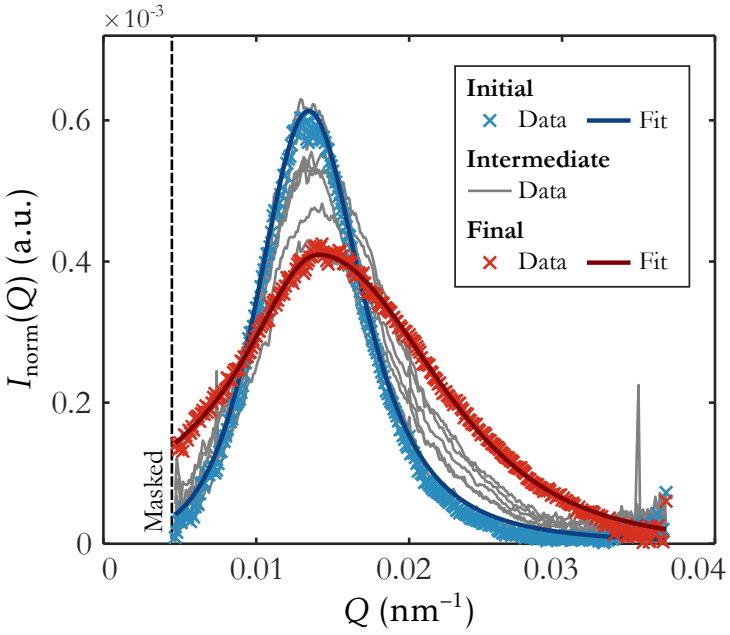

Figure A.3.: Evolution of the magnetic scattering intensity, $I_{norm}(Q)$, obtained from a series of mSAXS images on a fresh membrane window (initial) of the $[Co(0.8)/Pt(1.4)]_6$-multilayer sample using a FEL fluence of $F_{FEL} = (30–35)\,mJ/cm^2$. The high-fluence irradiation results in a reduction of the maximum intensity and a broadening of $I_{norm}(Q)$ from one image to another (100 FEL-pulse exposures per image), shown by examples from a series of 50 consecutive scattering images (intermediate). Eventually, the sample reaches a new equilibrium situation, showing a constant $I_{norm}(Q)$ upon further FEL irradiation (final).

shape, to a peak with about half the maximum intensity and twice the width as the initial $I_{norm}(Q)$. For a photon energy in the XUV regime, a substantial amount of energy is absorbed by the magnetic thin film ($\delta_{XUV} \approx 11\,nm$ in Co), so that thermally activated processes like depinning of domains and domain-wall motion (approximately nanosecond timescale), in general, have to be considered. Permanent alterations at high FEL fluences might, however, also be due to structural changes in the sample, i. e., a growth of the grain size and associated changes in the anisotropy [285], which proceed on even longer timescales. In both cases, the alterations are expected to saturate with the number of FEL-pulse excitations, in agreement with the here-observed effect (new equilibrium configuration after ≈ 50 images, each consisting of 100 FEL-pulse exposures). The alterations are quantified by fitting the $I_{norm}(Q)$ with a split Pearson type-VII function (see section 5.3.1). The fit parameters are summarized in table A.1. Almost the same Q_{peak} and w in the initial state, compared to the values in the TR-mSAXS experiment at FERMI using the very same sample (see $\mu_0 H_z = 0\,mT$ case in table 6.3), shows the feasibility of comparing results from two different FEL facilities. Note that, no such permanent alterations in $I_{norm}(Q)$ by (only!) the FEL pulses are observed in the TR-mSAXS experiment at FERMI, where a much lower FEL fluence of $F_{FEL} = (4.2–7.0)\,mJ/cm^2$ was used. The results show that a low fluence of $F_{FEL} \lesssim 10\,mJ/cm^2$ is desirable for TR-mSAXS experiments on magnetic thin films, in order to avoid such FEL-induced alterations in $I_{norm}(Q)$.

B TR-mSAXS at FLASH: Summarized Fit Parameters Describing Ultrafast Demagnetization

Table B.1.: Overview of the fit-parameters from fitting eq. (5.5) to the femto- to picosecond time evolution of magnetization in the three $[Co/Pt]_x$ multilayers upon excitation by 70 fs-short, **LP** nIR-laser pulses with fluences $F^1_{nIR} = 3.8\,mJ/cm^2$ and $F^2_{nIR} = 9.6\,mJcm^2$. The characteristic decay-time for the slow-recovery of magnetization, τ_0, that is described via a heat diffusion term, is set constant to $\tau_0 = 1000\,ps$

$\mathbf{F^1_{nIR}}$	A_1 (a.u.)	τ_M (ps)	A_2 (a.u.)	τ_E (ps)	δt (ps)
$[Co/Pt]_3$	0.411 ± 0.018	0.099 ± 0.018	0.038 ± 0.007	0.753 ± 0.064	0.031 ± 0.005
$[Co/Pt]_8$	0.275 ± 0.018	0.083 ± 0.027	0.032 ± 0.004	0.678 ± 0.095	0.014 ± 0.009
$[Co/Pt]_6$	0.224 ± 0.017	0.107 ± 0.027	0.033 ± 0.009	0.641 ± 0.090	0.050 ± 0.006
$\mathbf{F^2_{nIR}}$	A_1 (a.u.)	τ_M (ps)	A_2 (a.u.)	τ_E (ps)	δt (ps)
$[Co/Pt]_3$	0.750 ± 0.072	0.160 ± 0.038	0.249 ± 0.013	3.242 ± 0.254	0.041 ± 0.007
$[Co/Pt]_8$	0.841 ± 0.045	0.161 ± 0.026	0.171 ± 0.008	1.229 ± 0.205	0.012 ± 0.006
$[Co/Pt]_6$	0.768 ± 0.035	0.153 ± 0.018	0.103 ± 0.010	0.863 ± 0.094	0.050 ± 0.006

Table B.2.: Overview of the fit-parameters from fitting eq. (5.5) to the femto- to picosecond time evolution of magnetization in the three $[Co/Pt]_x$ multilayers upon excitation by 70 fs-short, **CP** nIR-laser pulses with fluences $F^1_{nIR} = 3.8\,mJ/cm^2$ and $F^2_{nIR} = 9.6\,mJ/cm^2$. The characteristic decay-time for the slow-recovery of magnetization, τ_0, that is described via a heat diffusion term, is set constant to $\tau_0 = 1000\,ps$

$\mathbf{F^1_{nIR}}$	A_1 (a.u.)	τ_M (ps)	A_2 (a.u.)	τ_E (ps)	δt (ps)
$[Co/Pt]_3$	0.512 ± 0.107	0.150 ± 0.053	0.041 ± 0.006	0.735 ± 0.077	0.010 ± 0.003
$[Co/Pt]_8$	0.353 ± 0.102	0.159 ± 0.079	0.043 ± 0.004	0.450 ± 0.133	0.038 ± 0.010
$[Co/Pt]_6$	0.250 ± 0.018	0.101 ± 0.022	0.023 ± 0.009	0.482 ± 0.057	0.046 ± 0.005
$\mathbf{F^2_{nIR}}$	A_1 (a.u.)	τ_M (ps)	A_2 (a.u.)	τ_E (ps)	δt (ps)
$[Co/Pt]_3$	0.828 ± 0.087	0.151 ± 0.025	0.246 ± 0.014	3.747 ± 0.289	0.016 ± 0.006
$[Co/Pt]_8$	0.670 ± 0.108	0.178 ± 0.034	0.166 ± 0.017	1.100 ± 0.157	0.026 ± 0.006
$[Co/Pt]_6$	0.898 ± 0.184	0.135 ± 0.056	0.102 ± 0.015	0.821 ± 0.115	0.014 ± 0.008

Table B.3.: Fit-parameters from fitting eq. (5.5) to the femto- to picosecond time evolution of magnetization in the $[Co/Pt]_6$ multilayer upon excitation by 70 fs and 300 fs-long nIR-laser pulses for linear (LP) and circular (CP) polarizations and a fluence $F^2_{\mathrm{nIR}} = 9.6\,\mathrm{mJ/cm^2}$. The characteristic decay-time for the slow-recovery of magnetization, τ_0, that is described via a heat diffusion term, is set constant to $\tau_0 = 1000\,\mathrm{ps}$

LP	A_1 (a.u.)	τ_{M} (ps)	A_2 (a.u.)	τ_{E} (ps)	δt (ps)
70 fs	0.768 ± 0.035	0.153 ± 0.018	0.103 ± 0.010	0.863 ± 0.094	0.050 ± 0.006
300 fs	0.642 ± 0.059	0.198 ± 0.047	0.094 ± 0.008	0.717 ± 0.105	0.024 ± 0.010
CP	A_1 (a.u.)	τ_{M} (ps)	A_2 (a.u.)	τ_{E} (ps)	δt (ps)
70 fs	0.898 ± 0.184	0.135 ± 0.056	0.102 ± 0.015	0.821 ± 0.115	0.014 ± 0.008
300 fs	0.591 ± 0.038	0.141 ± 0.040	0.107 ± 0.003	0.850 ± 0.100	0.038 ± 0.007

C Re-Evaluated Data from a Previous Collaborative TR-mSAXS Experiment at FLASH

Transient lateral modifications in nanoscopic multi-domain states were first observed in a collaborative TR-mSAXS experiment at FLASH, exciting a $[Co/Pt]_{16}$ multilayer by 70 fs-short nIR-laser pulses with varying fluences from (7.9–14.6) mJ/cm^2 in a single-pulse-like FEL-reference–nIR-pump–XUV-probe mode [32]. The already published data have been re-evaluated as a cross-check for the robustness of the here-developed analysis script. The

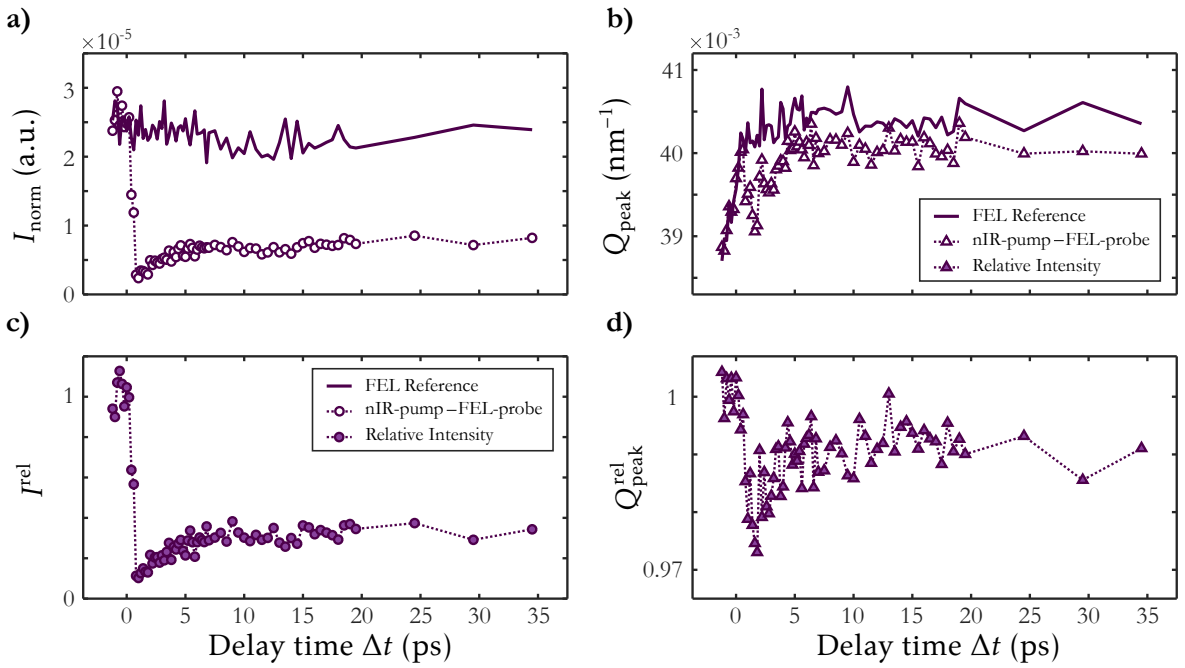

Figure C.1.: Results from a previous collaborative TR-mSAXS experiment at FLASH [32], re-evaluated by the here-developed analysis script. A $[Co/Pt]_{16}$ multilayer was excited by 70 fs-short nIR-laser pulses with a fluence of 14.6 mJ/cm^2 in a single-pulse-like FEL-reference–nIR-pump–XUV-probe mode. a) azimuthally averaged and Q-integrated magnetic scattering intensity normalized to the incoming FEL intensity, I_{norm}. b) fitted position of the first-order magnetic scattering peak, Q_{peak}. c) and d) show the corresponding relative evolutions, i. e., the nIR-pump–XUV-probe data with respect to the FEL-reference data.

resulting time evolution of the magnetic scattering intensity, I_{norm}, and the Q_{peak} position are shown for a selected delay-time scan in Fig. C.1 a) and b), respectively. A constant I_{norm} throughout the acquisition of the delay-time scan shows that the magnetization relaxes back to the initial state at $\Delta t < 0$ after each nIR-pump–XUV-probe event. A steady increase in Q_{peak} at negative delay times indicates heat-induced domain rearrangements, e. g., through (de)pinning. Importantly, a pronounced signature in Q_{peak} at $\Delta t > 0$ was only obtained in the nIR-pump–XUV-probe data, whereas the initial Q_{peak} was measured in the FEL-reference measurements. In combination with the single-pulse-like FEL-reference–nIR-pump–XUV-probe mode, this is a clear indication for an ultrafast nIR-laser induced impact on Q_{peak}. By relating the nIR-pump–XUV-probe data to the FEL-reference data, the mere ultrafast effect can be extracted (Fig. C.1 d)).

Bibliography

[1] J. Stöhr and H. C. Siegmann, *Magnetism: from fundamentals to nanoscale dynamics* (Springer, 2006), ISBN 978-3-540-30282-7.

[2] M. Faraday, *On the magnetization of light and the illumination of magnetic lines of force c. 1* (The Royal Society, 1846), URL https://library.si.edu/digital-library/book/onmagnetizationo01fara.

[3] J. Kerr. *On rotation of the plane of polarization by reflection from the pole of a magnet*, The London, Edinburgh, and Dublin Philosophical Magazine and Journal of Science **3**, 321 (1877), URL https://www.tandfonline.com/doi/full/10.1080/14786447708639245.

[4] D. Strickland and G. Mourou. *Compression of amplified chirped optical pulses*, Optics Communications **56**, 219 (1985), URL https://linkinghub.elsevier.com/retrieve/pii/0030401885901208.

[5] E. Beaurepaire, J.-C. Merle, A. Daunois, and J.-Y. Bigot. *Ultrafast Spin Dynamics in Ferromagnetic Nickel*, Physical Review Letters **76**, 4250 (1996), URL https://link.aps.org/doi/10.1103/PhysRevLett.76.4250.

[6] G. Zhang, W. Hübner, E. Beaurepaire, and J.-Y. Bigot, in *Spin Dynamics in Confined Magnetic Structures I*, edited by B. Hillebrands and K. Ounadjela (Springer, 2002), vol. 83, pp. 245–289, ISBN 978-3-540-41191-8, *Laser-Induced Ultrafast Demagnetization: Femtomagnetism, a New Frontier?*, URL http://link.springer.com/10.1007/3-540-40907-6_8.

[7] A. Kimel, A. Kirilyuk, and T. Rasing. *Femtosecond opto-magnetism: ultrafast laser manipulation of magnetic materials*, Laser & Photonics Reviews **1**, 275 (2007), URL http://doi.wiley.com/10.1002/lpor.200710022.

[8] A. Kirilyuk, A. V. Kimel, and T. Rasing. *Ultrafast optical manipulation of magnetic order*, Reviews of Modern Physics **82**, 2731 (2010), URL https://link.aps.org/doi/10.1103/RevModPhys.82.2731.

[9] J.-Y. Bigot and M. Vomir. *Ultrafast magnetization dynamics of nanostructures*, Annalen der Physik **525**, 2 (2013), URL http://doi.wiley.com/10.1002/andp.201200199.

[10] S. Mathias, C. La-o vorakiat, J. M. Shaw, E. Turgut, P. Grychtol, R. Adam, D. Rudolf, H. T. Nembach, T. J. Silva, M. Aeschlimann, et al. *Ultrafast element-specific magnetization dynamics of complex magnetic materials on a table-top*, Journal of Electron Spectroscopy and Related Phenomena **189**, 164 (2013), URL https://linkinghub.elsevier.com/retrieve/pii/S0368204812001648.

[11] E. Brück, ed., *Handbook of magnetic materials: Volume 26* (North Holland, 2017), 1st ed., ISBN 978-0-444-63927-1.

[12] F. Dalla Longa, J. T. Kohlhepp, W. J. M. de Jonge, and B. Koopmans. *Influence of photon angular momentum on ultrafast demagnetization in nickel*, Physical Review B **75**, 224431 (2007), URL https://link.aps.org/doi/10.1103/PhysRevB.75.224431.

[13] E. Carpene, E. Mancini, C. Dallera, M. Brenna, E. Puppin, and S. De Silvestri. *Dynamics of electron-magnon interaction and ultrafast demagnetization in thin iron films*, Physical Review B **78**, 174422 (2008), URL https://link.aps.org/doi/10.1103/PhysRevB.78.174422.

[14] G. Malinowski, F. Dalla Longa, J. H. H. Rietjens, P. V. Paluskar, R. Huijink, H. J. M. Swagten, and B. Koopmans. *Control of speed and efficiency of ultrafast demagnetization by direct transfer of spin angular momentum*, Nature Physics **4**, 855 (2008), URL http://www.nature.com/articles/nphys1092.

[15] B. Vodungbo, J. Gautier, G. Lambert, A. B. Sardinha, M. Lozano, S. Sebban, M. Ducousso, W. Boutu, K. Li, B. Tudu, et al. *Laser-induced ultrafast demagnetization in the presence of a nanoscale magnetic domain network*, Nature Communications **3**, 999 (2012), URL http://www.nature.com/articles/ncomms2007.

[16] G. P. Zhang and W. Hübner. *Laser-Induced Ultrafast Demagnetization in Ferromagnetic Metals*, Physical Review Letters **85**, 3025 (2000), URL https://link.aps.org/doi/10.1103/PhysRevLett.85.3025.

[17] S. Eich, M. Plötzing, M. Rollinger, S. Emmerich, R. Adam, C. Chen, H. C. Kapteyn, M. M. Murnane, L. Plucinski, D. Steil, et al. *Band structure evolution during the ultrafast ferromagnetic-paramagnetic phase transition in cobalt*, Science Advances **3**, e1602094 (2017), URL http://advances.sciencemag.org/lookup/doi/10.1126/sciadv.1602094.

[18] J. K. Dewhurst, P. Elliott, S. Shallcross, E. K. U. Gross, and S. Sharma. *Laser-Induced Intersite Spin Transfer*, Nano Letters **18**, 1842 (2018), URL http://pubs.acs.org/doi/10.1021/acs.nanolett.7b05118.

[19] M. Hofherr, S. Häuser, J. K. Dewhurst, P. Tengdin, S. Sakshath, H. T. Nembach, S. T. Weber, J. M. Shaw, T. J. Silva, H. C. Kapteyn, et al. *Ultrafast optically induced spin transfer in ferromagnetic alloys*, Science Advances **6**, eaay8717 (2020), URL https://advances.sciencemag.org/lookup/doi/10.1126/sciadv.aay8717.

[20] F. Willems, C. von Korff Schmising, C. Strüber, D. Schick, D. W. Engel, J. K. Dewhurst, P. Elliott, S. Sharma, and S. Eisebitt. *Optical inter-site spin transfer probed by energy and spin-resolved transient absorption spectroscopy*, Nature Communications **11**, 871 (2020), URL http://www.nature.com/articles/s41467-020-14691-5.

[21] E. Golias, I. Kumberg, I. Gelen, S. Thakur, J. Gördes, R. Hosseinifar, Q. Guillet, J. Dewhurst, S. Sharma, C. Schüßler-Langeheine, et al. *Ultrafast Optically Induced Ferromagnetic State in an Elemental Antiferromagnet*, Physical Review Letters **126**, 107202 (2021), URL https://link.aps.org/doi/10.1103/PhysRevLett.126.107202.

[22] C. D. Stanciu, F. Hansteen, A. V. Kimel, A. Kirilyuk, A. Tsukamoto, A. Itoh, and T. Rasing. *All-Optical Magnetic Recording with Circularly Polarized Light*, Physical Review Letters **99**, 047601 (2007), URL https://link.aps.org/doi/10.1103/PhysRevLett.99.047601.

[23] I. Radu, K. Vahaplar, C. Stamm, T. Kachel, N. Pontius, H. A. Dürr, T. A. Ostler, J. Barker, R. F. L. Evans, R. W. Chantrell, et al. *Transient ferromagnetic-like state mediating ultrafast reversal of antiferromagnetically coupled spins*, Nature **472**, 205 (2011), URL http://www.nature.com/articles/nature09901.

[24] C.-H. Lambert, S. Mangin, B. S. D. C. S. Varaprasad, Y. K. Takahashi, M. Hehn, M. Cinchetti, G. Malinowski, K. Hono, Y. Fainman, M. Aeschlimann, et al. *All-optical control of ferromagnetic thin films and nanostructures*, Science **345**, 1337 (2014), URL http://www.sciencemag.org/cgi/doi/10.1126/science.1253493.

[25] M. O. A. Ellis, E. E. Fullerton, and R. W. Chantrell. *All-optical switching in granular ferromagnets caused by magnetic circular dichroism*, Scientific Reports **6**, 30522 (2016), URL http://www.nature.com/articles/srep30522.

[26] Z. Du, C. Chen, F. Cheng, Y. Liu, and L. Pan. *Prediction of Deterministic All-Optical Switching of Ferromagnetic Thin Film by Ultrafast Optothermal and Optomagnetic Couplings*, Scientific Reports **7**, 13513 (2017), URL http://www.nature.com/articles/s41598-017-13568-w.

[27] M. H. Kryder, E. C. Gage, T. W. McDaniel, W. A. Challener, R. E. Rottmayer, G. Ju, Y.-T. Hsia, and M. F. Erden. *Heat Assisted Magnetic Recording*, Proceedings of the IEEE **96**, 1810 (2008), conference Name: Proceedings of the IEEE, URL https://ieeexplore.ieee.org/abstract/document/4694026.

[28] D. Weller, G. Parker, O. Mosendz, A. Lyberatos, D. Mitin, N. Y. Safonova, and M. Albrecht. *Review Article: FePt heat assisted magnetic recording media*, Journal of Vacuum Science & Technology B, Nanotechnology and Microelectronics: Materials, Processing, Measurement, and Phenomena **34**, 060801 (2016), URL http://avs.scitation.org/doi/10.1116/1.4965980.

[29] C. Gutt, L.-M. Stadler, S. Streit-Nierobisch, A. P. Mancuso, A. Schropp, B. Pfau, C. M. Günther, R. Könnecke, J. Gulden, B. Reime, et al. *Resonant magnetic scattering with soft x-ray pulses from a free-electron laser operating at 1.59 nm*, Physical Review B **79**, 212406 (2009), URL https://link.aps.org/doi/10.1103/PhysRevB.79.212406.

[30] C. Gutt, S. Streit-Nierobisch, L.-M. Stadler, B. Pfau, C. M. Günther, R. Könnecke, R. Frömter, A. Kobs, D. Stickler, H. P. Oepen, et al. *Single-pulse resonant magnetic scattering using a soft x-ray free-electron laser*, Physical Review B **81**, 100401(R) (2010), URL https://link.aps.org/doi/10.1103/PhysRevB.81.100401.

[31] T. Wang, D. Zhu, B. Wu, C. Graves, S. Schaffert, T. Rander, L. Müller, B. Vodungbo, C. Baumier, D. P. Bernstein, et al. *Femtosecond Single-Shot Imaging of Nanoscale Ferromagnetic Order in Co / Pd Multilayers Using Resonant X-Ray Holography*, Physical Review Letters **108**, 267403 (2012), URL https://link.aps.org/doi/10.1103/PhysRevLett.108.267403.

[32] B. Pfau, S. Schaffert, L. Müller, C. Gutt, A. Al-Shemmary, F. Büttner, R. Delaunay, S. Düsterer, S. Flewett, R. Frömter, et al. *Ultrafast optical demagnetization manipulates nanoscale spin structure in domain walls*, Nature Communications **3**, 1100 (2012), URL http://www.nature.com/articles/ncomms2108.

[33] L. Müller, C. Gutt, B. Pfau, S. Schaffert, J. Geilhufe, F. Büttner, J. Mohanty, S. Flewett, R. Treusch, S. Düsterer, et al. *Breakdown of the X-Ray Resonant Magnetic Scattering Signal during Intense Pulses of Extreme Ultraviolet Free-Electron-Laser Radiation*, Physical Review Letters **110**, 234801 (2013), URL https://link.aps.org/doi/10.1103/PhysRevLett.110.234801.

[34] C. E. Graves, A. H. Reid, T. Wang, B. Wu, S. de Jong, K. Vahaplar, I. Radu, D. P. Bernstein, M. Messerschmidt, L. Müller, et al. *Nanoscale spin reversal by non-local angular momentum transfer following ultrafast laser excitation in ferrimagnetic GdFeCo*, Nature Materials **12**, 293 (2013), URL https://doi.org/10.1038/nmat3597.

[35] C. von Korff Schmising, B. Pfau, M. Schneider, C. Günther, M. Giovannella, J. Perron, B. Vodungbo, L. Müller, F. Capotondi, E. Pedersoli, et al. *Imaging Ultrafast Demagnetization Dynamics after a Spatially Localized Optical Excitation*, Physical Review Letters **112**, 217203 (2014), URL https://link.aps.org/doi/10.1103/PhysRevLett.112.217203.

[36] N. Bergeard, S. Schaffert, V. López-Flores, N. Jaouen, J. Geilhufe, C. M. Günther, M. Schneider, C. Graves, T. Wang, B. Wu, et al. *Irreversible transformation of ferromagnetic ordered stripe domains in single-shot infrared-pump/resonant-x-ray-scattering-probe experiments*, Physical Review B **91**, 054416 (2015), URL https://link.aps.org/doi/10.1103/PhysRevB.91.054416.

[37] B. Vodungbo, B. Tudu, J. Perron, R. Delaunay, L. Müller, M. H. Berntsen, G. Grübel, G. Malinowski, C. Weier, J. Gautier, et al. *Indirect excitation of ultrafast demagnetization*, Scientific Reports **6**, 18970 (2016), URL http://www.nature.com/articles/srep18970.

[38] D. Weder, C. v. K. Schmising, F. Willems, C. M. Gunther, M. Schneider, B. Pfau, A. E. D. Merhe, E. Jal, B. Vodungbo, J. Luning, et al. *Multi-Color Imaging of Magnetic Co/Pt Multilayers*, IEEE Transactions on Magnetics **53**, 1 (2017), URL https://ieeexplore.ieee.org/document/7931634.

[39] E. Iacocca, T.-M. Liu, A. H. Reid, Z. Fu, S. Ruta, P. W. Granitzka, E. Jal, S. Bonetti, A. X. Gray, C. E. Graves, et al. *Spin-current-mediated rapid magnon localisation and coalescence after ultrafast optical pumping of ferrimagnetic alloys*, Nature Communications **10**, 1756 (2019), URL http://www.nature.com/articles/s41467-019-09577-0.

[40] E. Jal, M. Makita, B. Rösner, C. David, F. Nolting, J. Raabe, T. Savchenko, A. Kleibert, F. Capotondi, E. Pedersoli, et al. *Single-shot time-resolved magnetic x-ray absorption at a free-electron laser*, Physical Review B **99**, 144305 (2019), URL https://link.aps.org/doi/10.1103/PhysRevB.99.144305.

[41] K. Yamamoto, Y. Kubota, M. Suzuki, Y. Hirata, K. Carva, M. Berritta, K. Takubo, Y. Uemura, R. Fukaya, K. Tanaka, et al. *Ultrafast demagnetization of Pt magnetic moment in $L1_0$ -FePt probed by magnetic circular dichroism at a hard x-ray free electron laser*, New Journal of Physics **21**, 123010 (2019), URL https://iopscience.iop.org/article/10.1088/1367-2630/ab5ac2.

[42] P. Maldonado, T. Chase, A. H. Reid, X. Shen, R. K. Li, K. Carva, T. Payer, M. Horn von Hoegen, K. Sokolowski-Tinten, X. J. Wang, et al. *Tracking the ultrafast nonequilibrium energy flow between electronic and lattice degrees of freedom in crystalline nickel*, Physical Review B **101** (2020), URL https://link.aps.org/doi/10.1103/PhysRevB.101.100302.

[43] A. Moser, K. Takano, D. T. Margulies, M. Albrecht, Y. Sonobe, Y. Ikeda, S. Sun, and E. E. Fullerton. *Magnetic recording: advancing into the future*, Journal of Physics D: Applied Physics **35**, R157 (2002), URL https://iopscience.iop.org/article/10.1088/0022-3727/35/19/201.

[44] S. Khizroev and D. Litvinov. *Perpendicular magnetic recording: Writing process*, Journal of Applied Physics **95**, 4521 (2004), URL http://aip.scitation.org/doi/10.1063/1.1695092.

[45] M. N. Baibich, J. M. Broto, A. Fert, F. N. Van Dau, F. Petroff, P. Etienne, G. Creuzet, A. Friederich, and J. Chazelas. *Giant Magnetoresistance of (001)Fe/(001)Cr Magnetic Superlattices*, Physical Review Letters **61**, 2472 (1988), URL https://link.aps.org/doi/10.1103/PhysRevLett.61.2472.

[46] G. Binasch, P. Grünberg, F. Saurenbach, and W. Zinn. *Enhanced magnetoresistance in layered magnetic structures with antiferromagnetic interlayer exchange*, Physical Review B **39**, 4828 (1989), URL https://link.aps.org/doi/10.1103/PhysRevB.39.4828.

[47] J. Daughton, J. Brown, E. Chen, R. Beech, A. Pohm, and W. Kude. *Magnetic field sensors using GMR multilayer*, IEEE Transactions on Magnetics **30**, 4608 (1994), URL https://ieeexplore.ieee.org/document/334164.

[48] H. Richter, A. Dobin, O. Heinonen, K. Gao, R. v.d. Veerdonk, R. Lynch, J. Xue, D. Weller, P. Asselin, M. Erden, et al. *Recording on Bit-Patterned Media at Densities of 1 Tb/in^{2}and Beyond*, IEEE Transactions on Magnetics **42**, 2255 (2006), URL https://ieeexplore.ieee.org/document/1704265.

[49] O. Hellwig, T. Hauet, T. Thomson, E. Dobisz, J. D. Risner-Jamtgaard, D. Yaney, B. D. Terris, and E. E. Fullerton. *Coercivity tuning in Co/Pd multilayer based bit patterned media*, Applied Physics Letters **95**, 232505 (2009), URL http://aip.scitation.org/doi/10.1063/1.3271679.

[50] X. Zhang, G. P. Zhao, H. Fangohr, J. P. Liu, W. X. Xia, J. Xia, and F. J. Morvan. *Skyrmion-skyrmion and skyrmion-edge repulsions in skyrmion-based racetrack memory*, Scientific Reports **5**, 7643 (2015), URL http://www.nature.com/articles/srep07643.

[51] W. Kang, C. Zheng, Y. Huang, X. Zhang, Y. Zhou, W. Lv, and W. Zhao. *Complementary Skyrmion Racetrack Memory With Voltage Manipulation*, IEEE Electron Device Letters **37**, 924 (2016), URL https://ieeexplore.ieee.org/abstract/document/7482654.

[52] R. C. O'Handley, *Modern magnetic materials: principles and applications* (Wiley, 2000), ISBN 978-0-471-15566-9.

[53] I. M. Billas, A. Chatelain, and W. A. de Heer. *Magnetism from the Atom to the Bulk in Iron, Cobalt, and Nickel Clusters*, Science **265**, 1682 (1994), URL https://www.sciencemag.org/lookup/doi/10.1126/science.265.5179.1682.

[54] F. J. Himpsel, P. Heimann, and D. E. Eastman. *Band structure measurements and multi-electron effects (satellites) for nearly-filled d-band metals: Fe, Co, Ni, Cu, Ru, and Pd (invited)*, Journal of Applied Physics **52**, 1658 (1981), URL http://aip.scitation.org/doi/10.1063/1.329671.

[55] E. Kisker, K. Schröder, M. Campagna, and W. Gudat. *Temperature Dependence of the Exchange Splitting of Fe by Spin-Resolved Photoemission Spectroscopy with Synchrotron Radiation*, Physical Review Letters **52**, 2285 (1984), URL https://link.aps.org/doi/10.1103/PhysRevLett.52.2285.

[56] K.-P. Kämper, W. Schmitt, and G. Güntherodt. *Temperature and wave-vector dependence of the spin-split band structure of Ni(111) along the* Γ*- L line*, Physical Review B **42**, 10696 (1990), URL https://link.aps.org/doi/10.1103/PhysRevB.42.10696.

[57] F. Manghi, V. Bellini, J. Osterwalder, T. J. Kreutz, P. Aebi, and C. Arcangeli. *Correlation effects in the low-energy region of nickel photoemission spectra*, Physical Review B **59**, R10409 (1999), URL https://link.aps.org/doi/10.1103/PhysRevB.59.R10409.

[58] R. O. Jones and O. Gunnarsson. *The density functional formalism, its applications and prospects*, Reviews of Modern Physics **61**, 689 (1989), URL https://link.aps.org/doi/10.1103/RevModPhys.61.689.

[59] M. M. Steiner, R. C. Albers, and L. J. Sham. *Quasiparticle properties of Fe, Co, and Ni*, Physical Review B **45**, 13272 (1992), URL https://link.aps.org/doi/10.1103/PhysRevB.45.13272.

[60] J. Kübler, *Theory of Itinerant Electron Magnetism* (Oxford University Press, 2017), ISBN 978-0-19-156542-7.

[61] C. Kittel, *Introduction to Solid State Physics* (Wiley, 1996), ISBN 978-0-471-11181-8.

[62] D. Zusin, Ph.D. thesis, University of Colorado, *Ultrafast Dynamics of Magnetic Multilayer Films: Magneto-Optical Spectroscopy and Resonant Scattering in the Extreme Ultraviolet and Soft X-ray Spectral Regions* (2018), URL https://scholar.colorado.edu/concern/graduate_thesis_or_dissertations/k35694421.

[63] P. Heimann, E. Marschall, H. Neddermeyer, M. Pessa, and H. F. Roloff. *Photoemission and electronic structure of cobalt*, Physical Review B **16**, 2575 (1977), URL https://link.aps.org/doi/10.1103/PhysRevB.16.2575.

[64] E. Du Trémolet de Lacheisserie, D. Gignoux, and M. Schlenker, eds., *Magnetism - Materials and applications*, Selected by Grenoble Sciences (Springer, 2005), ISBN 978-0-387-23000-9.

[65] M. D. Kuz'min. *Shape of Temperature Dependence of Spontaneous Magnetization of Ferromagnets: Quantitative Analysis*, Physical Review Letters **94**, 107204 (2005), URL https://link.aps.org/doi/10.1103/PhysRevLett.94.107204.

[66] A. Liechtenstein, M. Katsnelson, V. Antropov, and V. Gubanov. *Local spin density functional approach to the theory of exchange interactions in ferromagnetic metals and alloys*, Journal of Magnetism and Magnetic Materials **67**, 65 (1987), URL https://www.sciencedirect.com/science/article/pii/0304885387907219.

[67] M. Pajda, J. Kudrnovský, I. Turek, V. Drchal, and P. Bruno. *Ab initio calculations of exchange interactions, spin-wave stiffness constants, and Curie temperatures of Fe, Co, and Ni*, Physical Review B **64**, 174402 (2001), URL https://link.aps.org/doi/10.1103/PhysRevB.64.174402.

[68] V. M. Parakkat, K. R. Ganesh, and P. S. Anil Kumar. *Tailoring Curie temperature and magnetic anisotropy in ultrathin Pt/Co/Pt films*, AIP Advances **6**, 056118 (2016), URL http://aip.scitation.org/doi/10.1063/1.4944343.

[69] P. Bruno, in *Proceedings of Magneto-Optical Recording International Symposium* (The Magnetics Society of Japan, 1991), *Theory of the Curie temperature of Co-based ferromagnetic ultrathin films and multilayers*, vol. 15, pp. 15–20, URL https://www.jstage.jst.go.jp/article/jmsjmag/15/S_1_MORIS_91/15_S_1_MORIS_91_S1_15/_pdf.

[70] S. Hashimoto, Y. Ochiai, and K. Aso. *Ultrathin Co/Pt and Co/Pd multilayered films as magneto-optical recording materials*, Journal of Applied Physics **67**, 2136 (1990), URL http://aip.scitation.org/doi/10.1063/1.345548.

[71] J. Wagner, Ph.D. thesis, Universität Hamburg, *The magnetic properties of ultrathin cobalt multilayers symmetrically and antisymmetrically sandwiched between layers of platinum and iridium* (2018), URL https://ediss.sub.uni-hamburg.de/volltexte/2019/9916/pdf/Dissertation.pdf.

[72] R. Hertel, ed., *Lecture notes of the 40th Spring School 2009: Spintronics - from GMR to quantum information*, no. 10 in Schriften des Forschungszentrums Jülich Reihe Schlüsseltechnologien (Forschungszentrum Jülich, 2009), ISBN 978-3-89336-559-3.

[73] G. Chen, T. Ma, A. T. N'Diaye, H. Kwon, C. Won, Y. Wu, and A. K. Schmid. *Tailoring the chirality of magnetic domain walls by interface engineering*, Nature Communications **4**, 2671 (2013), URL http://www.nature.com/articles/ncomms3671.

[74] A. Hrabec, N. A. Porter, A. Wells, M. J. Benitez, G. Burnell, S. McVitie, D. McGrouther, T. A. Moore, and C. H. Marrows. *Measuring and tailoring the Dzyaloshinskii-Moriya interaction in perpendicularly magnetized thin films*, Physical Review B **90**, 020402 (2014), URL https://link.aps.org/doi/10.1103/PhysRevB.90.020402.

[75] N. Gusev, A. Sadovnikov, S. Nikitov, M. Sapozhnikov, and O. Udalov. *Manipulation of the Dzyaloshinskii–Moriya Interaction in Co/Pt Multilayers with Strain*, Physical Review Letters **124**, 157202 (2020), URL https://link.aps.org/doi/10.1103/PhysRevLett.124.157202.

[76] X.-X. Li, J. Bao, L.-Y. Lu, X.-G. Xu, and Y. Jiang. *Oscillatory antiferromagnetic interlayer coupling in Co/Pt multilayer with perpendicular anisotropy*, Solid State Communications **148**, 209 (2008), URL https://linkinghub.elsevier.com/retrieve/pii/S0038109808004808.

[77] Z. Y. Liu, F. Zhang, H. L. Chen, B. Xu, D. L. Yu, J. L. He, and Y. J. Tian. *Antiferromagnetic interlayer coupling in Pt/Co multilayers with perpendicular anisotropy*, Physical Review B **79**, 024427 (2009), URL https://link.aps.org/doi/10.1103/PhysRevB.79.024427.

[78] S. Blundell, *Magnetism in condensed matter* (Oxford University Press, 2001).

[79] C. Brombacher, H. Schletter, M. Daniel, P. Matthes, N. Jöhrmann, M. Maret, D. Makarov, M. Hietschold, and M. Albrecht. *FePtCu alloy thin films: Morphology, $L1_0$ chemical ordering, and perpendicular magnetic anisotropy*, Journal of Applied Physics **112**, 073912 (2012), URL http://aip.scitation.org/doi/10.1063/1.4757038.

[80] T. Suzuki, D. Weller, C. Chang, R. Savoy, T. Huang, B. A. Gurney, and V. Speriosu. *Magnetic and magneto-optic properties of thick face-centered-cubic Co single-crystal films*, Applied Physics Letters **64**, 2736 (1994), URL http://aip.scitation.org/doi/10.1063/1.111946.

[81] L. Néel. *Anisotropie magnétique superficielle et surstructures d'orientation*, Journal de Physique et le Radium **15**, 225 (1954), URL http://www.edpsciences.org/10.1051/jphysrad:01954001504022500.

[82] A. Kobs, Ph.D. thesis, Universität Hamburg, *Magnetogalvanic effects in ferromagnets of reduced dimensions* (2013), URL https://ediss.sub.uni-hamburg.de/handle/ediss/5113.

[83] P. F. Carcia, A. D. Meinhaldt, and A. Suna. *Perpendicular magnetic anisotropy in Pd/Co thin film layered structures*, Applied Physics Letters **47**, 178 (1985), URL http://aip.scitation.org/doi/10.1063/1.96254.

[84] P. F. Carcia. *Perpendicular magnetic anisotropy in Pd/Co and Pt/Co thin-film layered structures*, Journal of Applied Physics **63**, 5066 (1988), URL http://aip.scitation.org/doi/10.1063/1.340404.

[85] T. Kingetsu. *Molecular-beam-epitaxial growth and magnetic properties of (111)Pt/Co/Ag, Pt/Co, and Ag/Co/Pt superlattices*, Journal of Applied Physics **76**, 4267 (1994), URL http://aip.scitation.org/doi/10.1063/1.357311.

[86] M. T. Johnson, P. J. H. Bloemen, F. J. A. d. Broeder, and J. J. d. Vries. *Magnetic anisotropy in metallic multilayers*, Reports on Progress in Physics **59**, 1409 (1996), URL https://iopscience.iop.org/article/10.1088/0034-4885/59/11/002.

[87] M. Kisielewski, A. Maziewski, M. Tekielak, J. Ferré, S. Lemerle, V. Mathet, and C. Chappert. *Magnetic anisotropy and magnetization reversal processes in Pt/Co/Pt films*, Journal of Magnetism and Magnetic Materials **260**, 231 (2003), URL https://linkinghub.elsevier.com/retrieve/pii/S0304885302013331.

[88] H. Stillrich, C. Menk, R. Frömter, and H. P. Oepen. *Magnetic anisotropy and the cone state in Co/Pt multilayer films*, Journal of Applied Physics **105**, 07C308 (2009), URL http://aip.scitation.org/doi/10.1063/1.3070644.

[89] D. Stickler, R. Frömter, H. Stillrich, C. Menk, H. P. Oepen, C. Gutt, S. Streit-Nierobisch, L.-M. Stadler, G. Grübel, C. Tieg, et al. *Domain size in systems with canted magnetization*, Physical Review B **84**, 104412 (2011), URL https://link.aps.org/doi/10.1103/PhysRevB.84.104412.

[90] A. Hubert and R. Schäfer, *Magnetic Domains - The Analysis of Magnetic Microstructures* (Springer, 1998), ISBN 978-3-540-64108-7.

[91] S. Blundell, *Magnetism in condensed matter*, Oxford master series in condensed matter physics (Oxford University Press, 2001), ISBN 978-0-19-850592-1.

[92] C.-L. Jia, K. W. Urban, M. Alexe, D. Hesse, and I. Vrejoiu. *Direct Observation of Continuous Electric Dipole Rotation in Flux-Closure Domains in Ferroelectric Pb(Zr,Ti)O_3*, Science **331**, 1420 (2011), URL https://www.sciencemag.org/lookup/doi/10.1126/science.1200605.

[93] S. Chikazumi, C. D. Graham, and S. Chikazumi, *Physics of ferromagnetism*, no. 94 in The international series of monographs on physics (Clarendon Press ; Oxford University Press, 1997), ISBN 978-0-19-851776-4.

[94] J. C. Maxwell. *VIII. A dynamical theory of the electromagnetic field*, Philosophical Transactions of the Royal Society of London **155**, 459 (1865), URL https://royalsocietypublishing.org/doi/10.1098/rstl.1865.0008.

[95] J. Stöhr and Y. Wu, in *New Directions in Research with Third-Generation Soft X-Ray Synchrotron Radiation Sources* (Springer, 1994), vol. 254, pp. 221–250, *X-Ray Magnetic Circular Dichroism: Basic Concepts and Theory for 3d Transition Metal Atoms*, URL https://doi.org/10.1007/978-94-011-0868-3_9.

[96] D. J. Griffiths, *Introduction to electrodynamics* (Pearson, 2008), ISBN 978-0-13-919960-8.

[97] J. D. Jackson, *Classical electrodynamics* (Wiley, 1999), ISBN 978-0-471-30932-1.

[98] P. Oppeneer, in *Handbook of Magnetic Materials* (Elsevier, 2001), vol. 13, pp. 229–422, *Magneto-optical kerr spectra (Chapter 3)*, URL https://www.sciencedirect.com/science/article/pii/S1567271901130076.

[99] H. Wijn, ed., *Magnetic Properties of Metals: 3d, 4d and 5d Elements, Alloys and Compounds*, vol. 19a of *Landolt-Börnstein - Group III Condensed Matter* (Springer, 1986), ISBN 978-3-540-15904-9.

[100] W. H. Kleiner. *Space-Time Symmetry of Transport Coefficients*, Physical Review **142**, 318 (1966), URL https://link.aps.org/doi/10.1103/PhysRev.142.318.

[101] I. M. Boswarva, R. E. Howard, A. B. Lidiard, and C. A. Coulson. *Faraday effect in semiconductors*, Proceedings of the Royal Society of London. Series A. Mathematical and Physical Sciences **269**, 125 (1962), URL https://doi.org/10.1098/rspa.1962.0166.

[102] S. Valencia, A. Gaupp, W. Gudat, H.-C. Mertins, P. M. Oppeneer, D. Abramsohn, and C. M. Schneider. *Faraday rotation spectra at shallow core levels: 3p edges of Fe, Co, and Ni*, New Journal of Physics **8**, 254 (2006), URL http://stacks.iop.org/1367-2630/8/i=10/a=254?key=crossref.6502b5923312bf955f4db1815ee7019e.

[103] J. Zak, E. R. Moog, C. Liu, and S. D. Bader. *Magneto-optics of multilayers with arbitrary magnetization directions*, Physical Review B **43**, 6423 (1991), URL https://link.aps.org/doi/10.1103/PhysRevB.43.6423.

[104] S. W. Lovesey and S. P. Collins, *X-ray scattering and absorption by magnetic materials*, Oxford series on synchrotron radiation (Clarendon Press, 1996), ISBN 978-0-19-851737-5.

[105] H. A. Kramers and W. Heisenberg. *Über die Streuung von Strahlung durch Atome*, Zeitschrift für Physik **31**, 681 (1925), URL https://doi.org/10.1007/BF02980624.

[106] P. A. M. Dirac. *The quantum theory of the emission and absorption of radiation*, Proceedings of the Royal Society of London. Series A, Containing Papers of a Mathematical and Physical Character **114**, 243 (1927), URL https://royalsocietypublishing.org/doi/10.1098/rspa.1927.0039.

[107] J. L. Erskine and E. A. Stern. *Calculation of the $M_{2,3}$ magneto-optical absorption spectrum of ferromagnetic nickel*, Physical Review B **12**, 5016 (1975), URL https://link.aps.org/doi/10.1103/PhysRevB.12.5016.

[108] G. Schütz, W. Wagner, W. Wilhelm, P. Kienle, R. Zeller, R. Frahm, and G. Materlik. *Absorption of circularly polarized x rays in iron*, Physical Review Letters **58**, 737 (1987), URL https://link.aps.org/doi/10.1103/PhysRevLett.58.737.

[109] H. Höchst, D. Zhao, and D. L. Huber. *$M_{2,3}$ magnetic circular dichroism (MCD) measurements of Fe, Co and Ni using a newly developed quadruple reflection phase shifter*, Surface Science **352-354**, 998 (1996), URL https://linkinghub.elsevier.com/retrieve/pii/0039602895013156.

[110] L. E. Klebanoff, D. G. Van Campen, and R. J. Pouliot. *Spin-resolved and high-energy-resolution XPS studies of cobalt metal and a cobalt magnetic glass*, Physical Review B **49**, 2047 (1994), URL https://link.aps.org/doi/10.1103/PhysRevB.49.2047.

[111] J. Tobin, K. Goodman, F. Schumann, R. Willis, J. Kortright, J. Denlinger, E. Rotenberg, A. Warwick, and N. Smith. *Direct extraction of exchange splittings from magnetic X-ray dichroism in photoelectron spectroscopy*, Surface Science **395**, L227 (1998), URL https://linkinghub.elsevier.com/retrieve/pii/S0039602897008315.

[112] J. Als-Nielsen and D. McMorrow, *Elements of modern X-ray physics* (Wiley, 2011), ISBN 978-1-119-97015-6.

[113] T. O. Menteş, C. Sánchez-Hanke, and C. C. Kao. *Reconstruction of magnetization density in two-dimensional samples from soft X-ray speckle patterns using the multiple-wavelength anomalous diffraction method*, Journal of Synchrotron Radiation **9**, 90 (2002), URL http://scripts.iucr.org/cgi-bin/paper?S0909049502001310.

[114] K. Chesnel, M. Belakhovsky, S. Landis, J. C. Toussaint, S. P. Collins, G. van der Laan, E. Dudzik, and S. S. Dhesi. *X-ray resonant magnetic scattering study of the magnetic coupling in Co/Pt nanolines and its evolution under magnetic field*, Physical Review B **66**, 024435 (2002), URL https://link.aps.org/doi/10.1103/PhysRevB.66.024435.

[115] J. P. Hannon, G. T. Trammell, M. Blume, and D. Gibbs. *X-Ray Resonance Exchange Scattering*, Physical Review Letters **61**, 1245 (1988), URL https://link.aps.org/doi/10.1103/PhysRevLett.61.1245.

[116] J. B. Kortright. *Resonant soft X-ray and extreme ultraviolet magnetic scattering in nanostructured magnetic materials: Fundamentals and directions*, Journal of Electron Spectroscopy and Related Phenomena **189**, 178 (2013), URL https://linkinghub.elsevier.com/retrieve/pii/S0368204813000212.

[117] J. B. Kortright, S.-K. Kim, G. P. Denbeaux, G. Zeltzer, K. Takano, and E. E. Fullerton. *Soft-x-ray small-angle scattering as a sensitive probe of magnetic and charge heterogeneity*, Physical Review B **64**, 092401 (2001), URL https://link.aps.org/doi/10.1103/PhysRevB.64.092401.

[118] G. Winkler, A. Kobs, A. Chuvilin, D. Lott, A. Schreyer, and H. P. Oepen. *On the variation of magnetic anisotropy in Co/Pt(111) on silicon oxide*, Journal of Applied Physics **117**, 105306 (2015), URL http://aip.scitation.org/doi/10.1063/1.4914039.

[119] O. Hellwig, G. Denbeaux, J. Kortright, and E. E. Fullerton. *X-ray studies of aligned magnetic stripe domains in perpendicular multilayers*, Proceedings of the Seventh International Conference on Surface X-ray and Neutron Scattering **336**, 136 (2003), URL http://www.sciencedirect.com/science/article/pii/S0921452603002825.

[120] J. Miguel, J. F. Peters, O. M. Toulemonde, S. S. Dhesi, N. B. Brookes, and J. B. Goedkoop. *X-ray resonant magnetic scattering study of magnetic stripe domains in a-GdFe thin films*, Physical Review B **74**, 094437 (2006), URL https://link.aps.org/doi/10.1103/PhysRevB.74.094437.

[121] K. Bagschik, Ph.D. thesis, Universität Hamburg, *Coherent soft X-ray magnetic scattering and spatial coherence determination* (2017), URL http://ediss.sub.uni-hamburg.de/volltexte/2017/8800.

[122] T. Kampfrath, R. G. Ulbrich, F. Leuenberger, M. Münzenberg, B. Sass, and W. Felsch. *Ultrafast magneto-optical response of iron thin films*, Physical Review B **65**, 104429 (2002), URL https://link.aps.org/doi/10.1103/PhysRevB.65.104429.

[123] A. B. Schmidt, M. Pickel, M. Donath, P. Buczek, A. Ernst, V. P. Zhukov, P. M. Echenique, L. M. Sandratskii, E. V. Chulkov, and M. Weinelt. *Ultrafast Magnon Generation in an Fe Film on Cu(100)*, Physical Review Letters **105**, 197401 (2010), URL https://link.aps.org/doi/10.1103/PhysRevLett.105.197401.

[124] M. Aeschlimann, M. Bauer, S. Pawlik, W. Weber, R. Burgermeister, D. Oberli, and H. C. Siegmann. *Ultrafast Spin-Dependent Electron Dynamics in fcc Co*, Physical Review Letters **79**, 5158 (1997), URL https://link.aps.org/doi/10.1103/PhysRevLett.79.5158.

[125] U. Conrad, J. Güdde, V. Jähnke, and E. Matthias. *Ultrafast electron and magnetization dynamics of thin Ni and Co films on Cu(001) observed by time-resolved SHG*, Applied Physics B: Lasers and Optics **68**, 511 (1999), URL http://link.springer.com/10.1007/s003400050658.

[126] J. Güdde, U. Conrad, V. Jähnke, J. Hohlfeld, and E. Matthias. *Magnetization dynamics of Ni and Co films on Cu(001) and of bulk nickel surfaces*, Physical Review B **59**, R6608 (1999), URL https://link.aps.org/doi/10.1103/PhysRevB.59.R6608.

[127] A. Comin, M. Rossi, C. Mozzati, F. Parmigiani, and G. P. Banfi. *Femtosecond dynamics of Co thin films on Si support*, Solid State Communications **129**, 227 (2004), URL https://linkinghub.elsevier.com/retrieve/pii/S0038109803009396.

[128] J.-Y. Bigot, M. Vomir, L. Andrade, and E. Beaurepaire. *Ultrafast magnetization dynamics in ferromagnetic cobalt: The role of the anisotropy*, Chemical Physics **318**, 137 (2005), URL https://linkinghub.elsevier.com/retrieve/pii/S030101040500248X.

[129] M. Cinchetti, M. Sánchez Albaneda, D. Hoffmann, T. Roth, J.-P. Wüstenberg, M. Krauß, O. Andreyev, H. C. Schneider, M. Bauer, and M. Aeschlimann. *Spin-Flip Processes and Ultrafast Magnetization Dynamics in Co: Unifying the Microscopic and Macroscopic View of Femtosecond Magnetism*, Physical Review Letters **97**, 177201 (2006), URL https://link.aps.org/doi/10.1103/PhysRevLett.97.177201.

[130] A. Melnikov, J. Güdde, and E. Matthias. *Demagnetization following optical excitation in nickel and permalloy films*, Applied Physics B **74**, 735 (2002), URL http://link.springer.com/10.1007/s00340-002-0927-3.

[131] E. Beaurepaire, M. Maret, V. Halté, J.-C. Merle, A. Daunois, and J.-Y. Bigot. *Spin dynamics in $CoPt_3$ alloy films: A magnetic phase transition in the femtosecond time scale*, Physical Review B **58**, 12134 (1998), URL https://link.aps.org/doi/10.1103/PhysRevB.58.12134.

[132] C. Boeglin, E. Beaurepaire, V. Halté, V. López-Flores, C. Stamm, N. Pontius, H. A. Dürr, and J.-Y. Bigot. *Distinguishing the ultrafast dynamics of spin and orbital moments in solids*, Nature **465**, 458 (2010), URL http://www.nature.com/articles/nature09070.

[133] J. Kimling, J. Kimling, R. B. Wilson, B. Hebler, M. Albrecht, and D. G. Cahill. *Ultrafast demagnetization of FePt:Cu thin films and the role of magnetic heat capacity*, Physical Review B **90**, 224408 (2014), URL https://link.aps.org/doi/10.1103/PhysRevB.90.224408.

[134] R. Wilks, R. J. Hicken, M. Ali, and B. J. Hickey. *Ultrafast demagnetization of $Co_{25}Ni_{75}$/Pt multilayers with perpendicular anisotropy at elevated temperatures*, Journal of Applied Physics **97**, 10A705 (2005), URL http://aip.scitation.org/doi/10.1063/1.1847991.

[135] N. Moisan, G. Malinowski, J. Mauchain, M. Hehn, B. Vodungbo, J. Lüning, S. Mangin, E. E. Fullerton, and A. Thiaville. *Investigating the role of superdiffusive currents in laser induced demagnetization of ferromagnets with nanoscale magnetic domains*, Scientific Reports **4**, 4658 (2015), URL http://www.nature.com/articles/srep04658.

[136] K. C. Kuiper, T. Roth, A. J. Schellekens, O. Schmitt, B. Koopmans, M. Cinchetti, and M. Aeschlimann. *Spin-orbit enhanced demagnetization rate in Co/Pt-multilayers*, Applied Physics Letters **105**, 202402 (2014), URL http://aip.scitation.org/doi/10.1063/1.4902069.

[137] W. Zhang, W. He, L.-C. Peng, Y. Zhang, J.-W. Cai, R. F. L. Evans, X.-Q. Zhang, and Z.-H. Cheng. *The indispensable role of the transversal spin fluctuations mechanism in laser-induced demagnetization of Co/Pt multilayers with nanoscale magnetic domains*, Nanotechnology **29**, 275703 (2018), URL https://iopscience.iop.org/article/10.1088/1361-6528/aabdc9.

[138] L. Pitaevskii. *Electric forces in a transparent dispersive medium*, Soviet Physics JETP **12**, 1008 (1961), URL http://www.jetp.ac.ru/cgi-bin/dn/e_012_05_1008.pdf.

[139] J. P. van der Ziel, P. S. Pershan, and L. D. Malmstrom. *Optically-Induced Magnetization Resulting from the Inverse Faraday Effect*, Physical Review Letters **15**, 190 (1965), URL https://link.aps.org/doi/10.1103/PhysRevLett.15.190.

[140] P. S. Pershan, J. P. van der Ziel, and L. D. Malmstrom. *Theoretical Discussion of the Inverse Faraday Effect, Raman Scattering, and Related Phenomena*, Physical Review **143**, 574 (1966), URL https://link.aps.org/doi/10.1103/PhysRev.143.574.

[141] A. Vaterlaus, T. Beutler, D. Guarisco, M. Lutz, and F. Meier. *Spin-lattice relaxation in ferromagnets studied by time-resolved spin-polarized photoemission*, Physical Review B **46**, 5280 (1992), URL https://link.aps.org/doi/10.1103/PhysRevB.46.5280.

[142] W. Hübner and K. H. Bennemann. *Simple theory for spin-lattice relaxation in metallic rare-earth ferromagnets*, Physical Review B **53**, 3422 (1996), URL https://link.aps.org/doi/10.1103/PhysRevB.53.3422.

[143] J. D. Kmetec, J. J. Macklin, and J. F. Young. *0.5-TW, 125-fs Ti:sapphire laser*, Optics Letters **16**, 1001 (1991), URL https://www.osapublishing.org/abstract.cfm?URI=ol-16-13-1001.

[144] A. Sullivan, H. Hamster, H. C. Kapteyn, S. Gordon, W. White, H. Nathel, R. J. Blair, and R. W. Falcone. *Multiterawatt, 100-fs laser*, Optics Letters **16**, 1406 (1991), URL https://www.osapublishing.org/abstract.cfm?URI=ol-16-18-1406.

[145] B. Koopmans, *Handbook of magnetism and advanced magnetic materials*, vol. 3 of *Novel Techniques for Characterizing and Preparing Samples* (John Wiley & Sons, 2007), ISBN 978-0-470-02217-7.

[146] J.-H. Shim, A. A. Syed, J.-I. Kim, H.-G. Piao, S.-H. Lee, S.-Y. Park, Y. S. Choi, K. M. Lee, H.-J. Kim, J.-R. Jeong, et al. *Role of non-thermal electrons in ultrafast spin dynamics of ferromagnetic multilayer*, Scientific Reports **10**, 6355 (2020), URL http://www.nature.com/articles/s41598-020-63452-3.

[147] F. Dalla Longa, Ph.D. thesis, Technische Universiteit Eindhoven, *Laser-induced magnetization dynamics: an ultrafast journey among spins and light pulses* (2008), URL https://research.tue.nl/en/publications/laser-induced-magnetization-dynamics-an-ultrafast-journey-among-s.

[148] B. I. Cho, K. Engelhorn, A. A. Correa, T. Ogitsu, C. P. Weber, H. J. Lee, J. Feng, P. A. Ni, Y. Ping, A. J. Nelson, et al. *Electronic Structure of Warm Dense Copper Studied by Ultrafast X-Ray Absorption Spectroscopy*, Physical Review Letters **106**, 167601 (2011), URL https://link.aps.org/doi/10.1103/PhysRevLett.106.167601.

[149] A. M. Brown, R. Sundararaman, P. Narang, W. A. Goddard, and H. A. Atwater. *Ab initio phonon coupling and optical response of hot electrons in plasmonic metals*, Physical Review B **94**, 075120 (2016), URL https://link.aps.org/doi/10.1103/PhysRevB.94.075120.

[150] L. Waldecker, R. Bertoni, R. Ernstorfer, and J. Vorberger. *Electron-Phonon Coupling and Energy Flow in a Simple Metal beyond the Two-Temperature Approximation*, Physical Review X **6**, 021003 (2016), URL https://link.aps.org/doi/10.1103/PhysRevX.6.021003.

[151] M. van Kampen, J. T. Kohlhepp, W. J. M. d. Jonge, B. Koopmans, and R. Coehoorn. *Sub-picosecond electron and phonon dynamics in nickel*, Journal of Physics: Condensed Matter **17**, 6823 (2005), URL https://iopscience.iop.org/article/10.1088/0953-8984/17/43/004.

[152] L. Guidoni, E. Beaurepaire, and J.-Y. Bigot. *Magneto-optics in the Ultrafast Regime: Thermalization of Spin Populations in Ferromagnetic Films*, Physical Review Letters **89**, 017401 (2002), URL https://link.aps.org/doi/10.1103/PhysRevLett.89.017401.

[153] J.-Y. Bigot, M. Vomir, and E. Beaurepaire. *Coherent ultrafast magnetism induced by femtosecond laser pulses*, Nature Physics **5**, 515 (2009), URL http://www.nature.com/articles/nphys1285.

[154] J. Hohlfeld, T. Gerrits, M. Bilderbeek, T. Rasing, H. Awano, and N. Ohta. *Fast magnetization reversal of GdFeCo induced by femtosecond laser pulses*, Physical Review B **65** (2001), URL https://link.aps.org/doi/10.1103/PhysRevB.65.012413.

[155] C. Stamm, T. Kachel, N. Pontius, R. Mitzner, T. Quast, K. Holldack, S. Khan, C. Lupulescu, E. F. Aziz, M. Wietstruk, et al. *Femtosecond modification of electron localization and transfer of angular momentum in nickel*, Nature Materials **6**, 740 (2007), URL http://www.nature.com/articles/nmat1985.

[156] B. Koopmans, J. J. M. Ruigrok, F. D. Longa, and W. J. M. de Jonge. *Unifying Ultrafast Magnetization Dynamics*, Physical Review Letters **95**, 267207 (2005), URL https://link.aps.org/doi/10.1103/PhysRevLett.95.267207.

[157] B. Koopmans, G. Malinowski, F. Dalla Longa, D. Steiauf, M. Fähnle, T. Roth, M. Cinchetti, and M. Aeschlimann. *Explaining the paradoxical diversity of ultrafast laser-induced demagnetization*, Nature Materials **9**, 259 (2010), URL http://www.nature.com/articles/nmat2593.

[158] A. Vaterlaus, T. Beutler, and F. Meier. *Spin-lattice relaxation time of ferromagnetic gadolinium determined with time-resolved spin-polarized photoemission*, Physical Review Letters **67**, 3314 (1991), URL https://link.aps.org/doi/10.1103/PhysRevLett.67.3314.

[159] M. Wietstruk, A. Melnikov, C. Stamm, T. Kachel, N. Pontius, M. Sultan, C. Gahl, M. Weinelt, H. A. Dürr, and U. Bovensiepen. *Hot-Electron-Driven Enhancement of Spin-Lattice Coupling in Gd and Tb 4f Ferromagnets Observed by Femtosecond X-Ray Magnetic Circular Dichroism*, Physical Review Letters **106**, 127401 (2011), URL https://link.aps.org/doi/10.1103/PhysRevLett.106.127401.

[160] T. Roth, A. J. Schellekens, S. Alebrand, O. Schmitt, D. Steil, B. Koopmans, M. Cinchetti, and M. Aeschlimann. *Temperature Dependence of Laser-Induced Demagnetization in Ni: A Key for Identifying the Underlying Mechanism*, Physical Review X **2**, 021006 (2012), URL https://link.aps.org/doi/10.1103/PhysRevX.2.021006.

[161] D. Steiauf and M. Fähnle. *Elliott-Yafet mechanism and the discussion of femtosecond magnetization dynamics*, Physical Review B **79**, 140401(R) (2009), URL https://link.aps.org/doi/10.1103/PhysRevB.79.140401.

[162] M. Pickel, A. B. Schmidt, F. Giesen, J. Braun, J. Minár, H. Ebert, M. Donath, and M. Weinelt. *Spin-Orbit Hybridization Points in the Face-Centered-Cubic Cobalt Band Structure*, Physical Review Letters **101**, 066402 (2008), URL https://link.aps.org/doi/10.1103/PhysRevLett.101.066402.

[163] F. Beuneu and P. Monod. *The Elliott relation in pure metals*, Physical Review B **18**, 2422 (1978), URL https://link.aps.org/doi/10.1103/PhysRevB.18.2422.

[164] E. Turgut, C. La-o vorakiat, J. M. Shaw, P. Grychtol, H. T. Nembach, D. Rudolf, R. Adam, M. Aeschlimann, C. M. Schneider, T. J. Silva, et al. *Controlling the Competition between Optically Induced Ultrafast Spin-Flip Scattering and Spin Transport in Magnetic Multilayers*, Physical Review Letters **110** (2013), URL https://link.aps.org/doi/10.1103/PhysRevLett.110.197201.

[165] R. Decker, A. Born, R. Büchner, K. Ruotsalainen, C. Stråhlman, S. Neppl, R. Haverkamp, A. Pietzsch, and A. Föhlisch. *Measuring the atomic spin-flip scattering rate by x-ray emission spectroscopy*, Scientific Reports **9**, 8977 (2019), URL http://www.nature.com/articles/s41598-019-45242-8.

[166] Y. Yafet. *g-Factors and Spin-Lattice Relaxation of Conduction Electrons*, Solid State Physics **14**, 1 (1963), URL https://www.sciencedirect.com/science/article/pii/S0081194708602593.

[167] M. Lisowski, P. A. Loukakos, A. Melnikov, I. Radu, L. Ungureanu, M. Wolf, and U. Bovensiepen. *Femtosecond Electron and Spin Dynamics in Gd(0001) Studied by Time-Resolved Photoemission and Magneto-optics*, Physical Review Letters **95**, 137402 (2005), URL https://link.aps.org/doi/10.1103/PhysRevLett.95.137402.

[168] E. Turgut, D. Zusin, D. Legut, K. Carva, R. Knut, J. M. Shaw, C. Chen, Z. Tao, H. T. Nembach, T. J. Silva, et al. *Stoner versus Heisenberg: Ultrafast exchange reduction and magnon generation during laser-induced demagnetization*, Physical Review B **94**, 220408(R) (2016), URL https://link.aps.org/doi/10.1103/PhysRevB.94.220408.

[169] D. Zusin, P. M. Tengdin, M. Gopalakrishnan, C. Gentry, A. Blonsky, M. Gerrity, D. Legut, J. M. Shaw, H. T. Nembach, T. J. Silva, et al. *Direct measurement of the static and transient magneto-optical permittivity of cobalt across the entire M-edge in reflection geometry by use of polarization scanning*, Physical Review B **97**, 024433 (2018), URL https://link.aps.org/doi/10.1103/PhysRevB.97.024433.

[170] M. Battiato, K. Carva, and P. M. Oppeneer. *Superdiffusive Spin Transport as a Mechanism of Ultrafast Demagnetization*, Physical Review Letters **105**, 027203 (2010), URL https://link.aps.org/doi/10.1103/PhysRevLett.105.027203.

[171] M. Aeschlimann, R. Burgermeister, S. Pawlik, M. Bauer, D. Oberli, and W. Weber. *Spin-dependent electron dynamics investigated by means of time- and spin-resolved photoemission*, Journal of Electron Spectroscopy and Related Phenomena **88-91**, 179 (1998), URL https://linkinghub.elsevier.com/retrieve/pii/S0368204897001102.

[172] V. P. Zhukov, E. V. Chulkov, and P. M. Echenique. *Lifetimes and inelastic mean free path of low-energy excited electrons in Fe, Ni, Pt, and Au: Ab initio GW + T calculations*, Physical Review B **73**, 125105 (2006), URL https://link.aps.org/doi/10.1103/PhysRevB.73.125105.

[173] D. Rudolf, C. La-O-Vorakiat, M. Battiato, R. Adam, J. M. Shaw, E. Turgut, P. Maldonado, S. Mathias, P. Grychtol, H. T. Nembach, et al. *Ultrafast magnetization enhancement in metallic multilayers driven by superdiffusive spin current*, Nature Communications **3**, 1037 (2012), URL http://www.nature.com/articles/ncomms2029.

[174] A. Eschenlohr, L. Persichetti, T. Kachel, M. Gabureac, P. Gambardella, and C. Stamm. *Spin currents during ultrafast demagnetization of ferromagnetic bilayers*, Journal of Physics: Condensed Matter **29**, 384002 (2017), URL http://stacks.iop.org/0953-8984/29/i=38/a=384002?key=crossref.0b546cb37e9b5bd60c6923d3c6b46064.

[175] U. Atxitia, O. Chubykalo-Fesenko, J. Walowski, A. Mann, and M. Münzenberg. *Evidence for thermal mechanisms in laser-induced femtosecond spin dynamics*, Physical Review B **81**, 174401 (2010), URL https://link.aps.org/doi/10.1103/PhysRevB.81.174401.

[176] P. Tengdin, W. You, C. Chen, X. Shi, D. Zusin, Y. Zhang, C. Gentry, A. Blonsky, M. Keller, P. M. Oppeneer, et al. *Critical behavior within 20 fs drives the out-of-equilibrium laser-induced magnetic phase transition in nickel*, Science Advances **4**, eaap9744 (2018), URL https://www.ncbi.nlm.nih.gov/pmc/articles/PMC5834307/.

[177] M. Djordjevic and M. Münzenberg. *Connecting the timescales in picosecond remagnetization experiments*, Physical Review B **75**, 012404 (2007), URL https://link.aps.org/doi/10.1103/PhysRevB.75.012404.

[178] N. Kazantseva, U. Nowak, R. W. Chantrell, J. Hohlfeld, and A. Rebei. *Slow recovery of the magnetisation after a sub-picosecond heat pulse*, EPL (Europhysics Letters) **81**, 27004 (2008), URL https://iopscience.iop.org/article/10.1209/0295-5075/81/27004.

[179] P. J. Meschter, J. W. Wright, C. R. Brooks, and T. G. Kollie. *Physical contributions to the heat capacity of nickel*, Journal of Physics and Chemistry of Solids **42**, 861 (1981), URL https://linkinghub.elsevier.com/retrieve/pii/0022369781901748.

[180] A. Manchon, Q. Li, L. Xu, and S. Zhang. *Theory of laser-induced demagnetization at high temperatures*, Physical Review B **85**, 064408 (2012), URL https://link.aps.org/doi/10.1103/PhysRevB.85.064408.

[181] U. Atxitia, O. Chubykalo-Fesenko, N. Kazantseva, D. Hinzke, U. Nowak, and R. W. Chantrell. *Micromagnetic modeling of laser-induced magnetization dynamics using the*

Landau-Lifshitz-Bloch equation, Applied Physics Letters **91**, 232507 (2007), URL http://aip.scitation.org/doi/10.1063/1.2822807.

[182] K. C. Kuiper, G. Malinowski, F. D. Longa, and B. Koopmans. *Nonlocal ultrafast magnetization dynamics in the high fluence limit*, Journal of Applied Physics **109**, 07D316 (2011), URL http://aip.scitation.org/doi/10.1063/1.3540681.

[183] D. Cheskis, A. Porat, L. Szapiro, O. Potashnik, and S. Bar-Ad. *Saturation of the ultrafast laser-induced demagnetization in nickel*, Physical Review B **72**, 014437 (2005), URL https://link.aps.org/doi/10.1103/PhysRevB.72.014437.

[184] S. Alebrand, A. Hassdenteufel, D. Steil, M. Cinchetti, and M. Aeschlimann. *Interplay of heating and helicity in all-optical magnetization switching*, Physical Review B **85**, 092401 (2012), URL https://link.aps.org/doi/10.1103/PhysRevB.85.092401.

[185] A. Hassdenteufel, B. Hebler, C. Schubert, A. Liebig, M. Teich, M. Helm, M. Aeschlimann, M. Albrecht, and R. Bratschitsch. *Thermally Assisted All-Optical Helicity Dependent Magnetic Switching in Amorphous $Fe_{100-x}Tb_x$ Alloy Films*, Advanced Materials **25**, 3122 (2013), URL https://doi.org/10.1002/adma.201300176.

[186] R. F. L. Evans, T. A. Ostler, R. W. Chantrell, I. Radu, and T. Rasing. *Ultrafast thermally induced magnetic switching in synthetic ferrimagnets*, Applied Physics Letters **104**, 082410 (2014), URL http://aip.scitation.org/doi/10.1063/1.4867015.

[187] K. Vahaplar, A. M. Kalashnikova, A. V. Kimel, S. Gerlach, D. Hinzke, U. Nowak, R. Chantrell, A. Tsukamoto, A. Itoh, A. Kirilyuk, et al. *All-optical magnetization reversal by circularly polarized laser pulses: Experiment and multiscale modeling*, Physical Review B **85**, 104402 (2012), URL https://link.aps.org/doi/10.1103/PhysRevB.85.104402.

[188] A. R. Khorsand, M. Savoini, A. Kirilyuk, A. V. Kimel, A. Tsukamoto, A. Itoh, and T. Rasing. *Role of Magnetic Circular Dichroism in All-Optical Magnetic Recording*, Physical Review Letters **108**, 127205 (2012), URL https://link.aps.org/doi/10.1103/PhysRevLett.108.127205.

[189] M. Berritta, R. Mondal, K. Carva, and P. M. Oppeneer. *Ab Initio Theory of Coherent Laser-Induced Magnetization in Metals*, Physical Review Letters **117**, 137203 (2016), URL https://link.aps.org/doi/10.1103/PhysRevLett.117.137203.

[190] I. Radu, K. Vahaplar, C. Stamm, T. Kachel, N. Pontius, H. A. Dürr, T. A. Ostler, J. Barker, R. F. L. Evans, R. W. Chantrell, et al. *Transient ferromagnetic-like state mediating ultrafast reversal of antiferromagnetically coupled spins*, Nature **472**, 205 (2011).

[191] D. J. Higley, K. Hirsch, G. L. Dakovski, E. Jal, E. Yuan, T. Liu, A. A. Lutman, J. P. MacArthur, E. Arenholz, Z. Chen, et al. *Femtosecond X-ray magnetic circular dichroism absorption spectroscopy at an X-ray free electron laser*, Review of Scientific Instruments **87**, 033110 (2016), URL http://aip.scitation.org/doi/10.1063/1.4944410.

[192] S. Yamamoto, M. Taguchi, T. Someya, Y. Kubota, S. Ito, H. Wadati, M. Fujisawa, F. Capotondi, E. Pedersoli, M. Manfredda, et al. *Ultrafast spin-switching of a ferrimagnetic alloy at room temperature traced by resonant magneto-optical Kerr effect using a seeded free electron laser*, Review of Scientific Instruments **86**, 083901 (2015), URL http://aip.scitation.org/doi/10.1063/1.4927828.

[193] T. Ostler, J. Barker, R. Evans, R. Chantrell, U. Atxitia, O. Chubykalo-Fesenko, S. El Moussaoui, L. Le Guyader, E. Mengotti, L. Heyderman, et al. *Ultrafast heating as a sufficient stimulus for magnetization reversal in a ferrimagnet*, Nature Communications **3**, 666 (2012), URL http://www.nature.com/articles/ncomms1666.

[194] D. Steil, S. Alebrand, A. Hassdenteufel, M. Cinchetti, and M. Aeschlimann. *All-optical magnetization recording by tailoring optical excitation parameters*, Physical Review B **84**, 224408 (2011), URL https://link.aps.org/doi/10.1103/PhysRevB.84.224408.

[195] R. Medapalli, D. Afanasiev, D. K. Kim, Y. Quessab, S. Manna, S. A. Montoya, A. Kirilyuk, T. Rasing, A. V. Kimel, and E. E. Fullerton. *Multiscale dynamics of helicity-dependent all-optical magnetization reversal in ferromagnetic Co/Pt multilayers*, Physical Review B **96**, 224421 (2017), URL https://link.aps.org/doi/10.1103/PhysRevB.96.224421.

[196] T. D. Cornelissen, R. Córdoba, and B. Koopmans. *Microscopic model for all optical switching in ferromagnets*, Applied Physics Letters **108**, 142405 (2016), URL http://aip.scitation.org/doi/10.1063/1.4945660.

[197] V. Raposo, E. Martínez, A. Hernández, and M. Zazo. *Micromagnetic Modeling of All-Optical Switching*, IEEE Transactions on Magnetics **55**, 1 (2019), URL https://ieeexplore.ieee.org/document/8611312.

[198] J. Gorchon, Y. Yang, and J. Bokor. *Model for multishot all-thermal all-optical switching in ferromagnets*, Physical Review B **94**, 020409 (2016), URL https://link.aps.org/doi/10.1103/PhysRevB.94.020409.

[199] Y. Takahashi, R. Medapalli, S. Kasai, J. Wang, K. Ishioka, S. Wee, O. Hellwig, K. Hono, and E. Fullerton. *Accumulative Magnetic Switching of Ultrahigh-Density Recording Media by Circularly Polarized Light*, Physical Review Applied **6**, 054004 (2016), URL https://link.aps.org/doi/10.1103/PhysRevApplied.6.054004.

[200] R. John, M. Berritta, D. Hinzke, C. Mueller, T. Santos, H. Ulrichs, P. Nieves, J. Walowski, R. Mondal, O. Chubykalo-Fesenko, et al. *Magnetisation switching of FePt nanoparticle recording medium by femtosecond laser pulses*, Scientific Reports **7**, 4114 (2017), URL https://www.nature.com/articles/s41598-017-04167-w.

[201] P. Asselin, R. F. L. Evans, J. Barker, R. W. Chantrell, R. Yanes, O. Chubykalo-Fesenko, D. Hinzke, and U. Nowak. *Constrained Monte Carlo method and calculation of the temperature dependence of magnetic anisotropy*, Physical Review B **82**, 054415 (2010), URL https://link.aps.org/doi/10.1103/PhysRevB.82.054415.

[202] D. Hinzke and U. Nowak. *Domain Wall Motion by the Magnonic Spin Seebeck Effect*, Physical Review Letters **107**, 027205 (2011), URL https://link.aps.org/doi/10.1103/PhysRevLett.107.027205.

[203] V. Raposo, R. Guedas, F. García-Sánchez, M. A. Hernández, M. Zazo, and E. Martínez. *Micromagnetic Modeling of All Optical Switching of Ferromagnetic Thin Films: The Role of Inverse Faraday Effect and Magnetic Circular Dichroism*, Applied Sciences **10**, 1307 (2020), URL https://www.mdpi.com/2076-3417/10/4/1307.

[204] Y. Tsema, G. Kichin, O. Hellwig, V. Mehta, A. V. Kimel, A. Kirilyuk, and T. Rasing. *Helicity and field dependent magnetization dynamics of ferromagnetic Co/Pt multilayers*, Applied Physics Letters **109**, 072405 (2016), URL http://aip.scitation.org/doi/10.1063/1.4961246.

[205] J. Gorchon, C.-H. Lambert, Y. Yang, A. Pattabi, R. B. Wilson, S. Salahuddin, and J. Bokor. *Single shot ultrafast all optical magnetization switching of ferromagnetic Co/Pt multilayers*, Applied Physics Letters **111**, 042401 (2017), URL http://aip.scitation.org/doi/10.1063/1.4994802.

[206] M. S. El Hadri, P. Pirro, C.-H. Lambert, S. Petit-Watelot, Y. Quessab, M. Hehn, F. Montaigne, G. Malinowski, and S. Mangin. *Two types of all-optical magnetization switching mechanisms using femtosecond laser pulses*, Physical Review B **94**, 064412 (2016), URL https://link.aps.org/doi/10.1103/PhysRevB.94.064412.

[207] M. Vomir, M. Albrecht, and J.-Y. Bigot. *Single shot all optical switching of intrinsic micron size magnetic domains of a Pt/Co/Pt ferromagnetic stack*, Applied Physics Letters **111**, 242404 (2017), URL http://aip.scitation.org/doi/10.1063/1.5010915.

[208] J.-H. Shim, A. Ali Syed, C.-H. Kim, K. M. Lee, S.-Y. Park, J.-R. Jeong, D.-H. Kim, and D. Eon Kim. *Ultrafast giant magnetic cooling effect in ferromagnetic Co/Pt multilayers*, Nature Communications **8**, 796 (2017), URL http://www.nature.com/articles/s41467-017-00816-w.

[209] W. B. Zeper, F. J. A. M. Greidanus, P. F. Carcia, and C. R. Fincher. *Perpendicular magnetic anisotropy and magneto-optical Kerr effect of vapor-deposited Co/Pt-layered structures*, Journal of Applied Physics **65**, 4971 (1989), URL http://aip.scitation.org/doi/10.1063/1.343189.

[210] C.-J. Lin and H. Do. *Magneto-optical recording on evaporated Co/Pt multilayer films*, IEEE Transactions on Magnetics **26**, 1700 (1990), URL http://ieeexplore.ieee.org/document/104497/.

[211] C.-J. Lin, G. Gorman, C. Lee, R. Farrow, E. Marinero, H. Do, H. Notarys, and C. Chien. *Magnetic and structural properties of Co/Pt multilayers*, Journal of Magnetism and Magnetic Materials **93**, 194 (1991), URL https://linkinghub.elsevier.com/retrieve/pii/0304885391903299.

[212] H. van Kesteren and W. Zeper. *Controlling the Curie temperature of Co/Pt multilayer magneto-optical recording media*, Journal of Magnetism and Magnetic Materials **120**, 271 (1993), URL https://linkinghub.elsevier.com/retrieve/pii/0304885393913399.

[213] H. Stillrich, C. Menk, R. Frömter, and H. P. Oepen. *Magnetic anisotropy and spin reorientation in Co/Pt multilayers: Influence of preparation*, Proceedings of the Joint European Magnetic Symposia **322**, 1353 (2010), URL http://www.sciencedirect.com/science/article/pii/S0304885309009366.

[214] O. Ermolaeva, N. Gusev, E. Skorohodov, Y. Petrov, M. Sapozhnikov, and V. Mironov. *Magnetic Force Microscopy of Nanostructured Co/Pt Multilayer Films with Perpendicular Magnetization*, Materials **10**, 1034 (2017), URL http://www.mdpi.com/1996-1944/10/9/1034.

[215] K. Bagschik, R. Frömter, J. Bach, B. Beyersdorff, L. Müller, S. Schleitzer, M. H. Berntsen, C. Weier, R. Adam, J. Viefhaus, et al. *Employing soft x-ray resonant magnetic scattering to study domain sizes and anisotropy in Co/Pd multilayers*, Physical Review B **94**, 134413 (2016), URL https://link.aps.org/doi/10.1103/PhysRevB.94.134413.

[216] A. Kobs, S. Heße, W. Kreuzpaintner, G. Winkler, D. Lott, P. Weinberger, A. Schreyer, and H. P. Oepen. *Anisotropic Interface Magnetoresistance in Pt / Co / Pt Sandwiches*, Physical Review Letters **106**, 217207 (2011), URL https://link.aps.org/doi/10.1103/PhysRevLett.106.217207.

[217] P. Johnson and R. Christy. *Optical constants of transition metals: Ti, V, Cr, Mn, Fe, Co, Ni, and Pd*, Physical Review B **9**, 5056 (1974), URL https://link.aps.org/doi/10.1103/PhysRevB.9.5056.

[218] D. L. Windt, W. C. Cash, M. Scott, P. Arendt, B. Newnam, R. F. Fisher, and A. B. Swartzlander. *Optical constants for thin films of Ti, Zr, Nb, Mo, Ru, Rh, Pd, Ag, Hf, Ta, W, Re, Ir, Os, Pt, and Au from 24 Å to 1216 Å*, Applied Optics **27**, 246 (1988), URL https://www.osapublishing.org/abstract.cfm?URI=ao-27-2-246.

[219] C. Tieg, R. Frömter, D. Stickler, S. Hankemeier, A. Kobs, S. Streit-Nierobisch, C. Gutt, G. Grübel, and H. P. Oepen. *Imaging the in-plane magnetization in a Co microstructure by Fourier transform holography*, Optics Express **18**, 27251 (2010), URL https://www.osapublishing.org/oe/abstract.cfm?uri=oe-18-26-27251.

[220] E. Beaurepaire, H. Bulou, L. Joly, and F. Scheurer, eds., *Magnetism and Synchrotron Radiation: Towards the Fourth Generation Light Sources: Proceedings of the 6th International School "Synchrotron Radiation and Magnetism"* (Springer, 2013), ISBN 978-3-319-03031-9, URL http://link.springer.com/10.1007/978-3-319-03032-6.

[221] K. Tiedtke, A. Azima, N. von Bargen, L. Bittner, S. Bonfigt, S. Düsterer, B. Faatz, U. Frühling, M. Gensch, C. Gerth, et al. *The soft x-ray free-electron laser FLASH at DESY: beamlines, diagnostics and end-stations*, New Journal of Physics **11**, 023029 (2009), URL http://stacks.iop.org/1367-2630/11/i=2/a=023029?key=crossref.993e502c88b3e19a361aef99ff69d450.

[222] M. Zangrando, A. Abrami, D. Bacescu, I. Cudin, C. Fava, F. Frassetto, A. Galimberti, R. Godnig, D. Giuressi, L. Poletto, et al. *The photon analysis, delivery, and reduction system at the FERMI@Elettra free electron laser user facility*, Review of Scientific Instruments **80**, 113110 (2009), URL http://aip.scitation.org/doi/10.1063/1.3262502.

[223] G. Geloni, E. Saldin, L. Samoylova, E. Schneidmiller, H. Sinn, T. Tschentscher, and M. Yurkov. *Coherence properties of the European XFEL*, New Journal of Physics **12**, 035021 (2010), URL http://stacks.iop.org/1367-2630/12/i=3/a=035021?key=crossref.dc630f0aee0300bd75259fe9df796b02.

[224] H. Franz, O. Leupold, R. Röhlsberger, S. Roth, O. Seeck, J. Spengler, J. Strempfer, M. Tischer, J. Viefhaus, E. Weckert, et al. *Technical Report: PETRA III: DESY's New High Brilliance Third Generation Synchrotron Radiation Source*, Synchrotron Radiation News **19**, 25 (2006), URL http://www.tandfonline.com/doi/abs/10.1080/08940880601064984.

[225] S. Khan, K. Holldack, T. Kachel, R. Mitzner, and T. Quast. *Femtosecond Undulator Radiation from Sliced Electron Bunches*, Physical Review Letters **97** (2006), URL https://link.aps.org/doi/10.1103/PhysRevLett.97.074801.

[226] J. Andruszkow, B. Aune, V. Ayvazyan, N. Baboi, R. Bakker, V. Balakin, D. Barni, A. Bazhan, M. Bernard, A. Bosotti, et al. *First Observation of Self-Amplified Spontaneous*

Emission in a Free-Electron Laser at 109 nm Wavelength, Physical Review Letters **85**, 3825 (2000), URL https://link.aps.org/doi/10.1103/PhysRevLett.85.3825.

[227] L.-H. Yu. *High-Gain Harmonic-Generation Free-Electron Laser*, Science **289**, 932 (2000), URL https://www.sciencemag.org/lookup/doi/10.1126/science.289.5481.932.

[228] L. H. Yu, L. DiMauro, A. Doyuran, W. S. Graves, E. D. Johnson, R. Heese, S. Krinsky, H. Loos, J. B. Murphy, G. Rakowsky, et al. *First Ultraviolet High-Gain Harmonic-Generation Free-Electron Laser*, Physical Review Letters **91**, 074801 (2003), URL https://link.aps.org/doi/10.1103/PhysRevLett.91.074801.

[229] E. Allaria, C. Callegari, D. Cocco, W. M. Fawley, M. Kiskinova, C. Masciovecchio, and F. Parmigiani. *The FERMI@Elettra free-electron-laser source for coherent x-ray physics: photon properties, beam transport system and applications*, New Journal of Physics **12**, 075002 (2010), URL https://iopscience.iop.org/article/10.1088/1367-2630/12/7/075002.

[230] P. Finetti, H. Höppner, E. Allaria, C. Callegari, F. Capotondi, P. Cinquegrana, M. Coreno, R. Cucini, M. B. Danailov, A. Demidovich, et al. *Pulse Duration of Seeded Free-Electron Lasers*, Physical Review X **7**, 021043 (2017), URL http://link.aps.org/doi/10.1103/PhysRevX.7.021043.

[231] R. Ivanov, J. Liu, G. Brenner, M. Brachmanski, and S. Düsterer. *FLASH free-electron laser single-shot temporal diagnostic: terahertz-field-driven streaking*, Journal of Synchrotron Radiation **25**, 26 (2018), URL http://scripts.iucr.org/cgi-bin/paper?S160057751701253X.

[232] S. Toleikis, in *Proceedings of the 13th International Conference on Synchrotron Radiation Instrumentation - SRI2018* (Taipei, 2019), *The FLASH facility current status in 2018 and future upgrade plans*, p. 030015, URL http://aip.scitation.org/doi/abs/10.1063/1.5084578.

[233] P. Schmüser, M. Dohlus, J. Rossbach, and C. Behrens, *Free-Electron Lasers in the Ultraviolet and X-Ray Regime*, vol. 258 of *Springer Tracts in Modern Physics* (Springer, 2014), ISBN 978-3-319-04080-6, URL http://link.springer.com/10.1007/978-3-319-04081-3.

[234] A. Shabalin, Ph.D. thesis, Universität Hamburg, *Coherent X-ray diffraction studies of mesoscopic materials* (2015), URL https://ediss.sub.uni-hamburg.de/handle/ediss/6576?mode=full.

[235] G. Geloni, Z. Huang, and C. Pellegrini, in *Energy and Environment Series*, edited by U. Bergmann, V. Yachandra, and J. Yano (Royal Society of Chemistry, 2017), pp. 1–44,

ISBN 978-1-84973-100-3, *The Physics and Status of X-ray Free-electron Lasers*, URL http://ebook.rsc.org/?DOI=10.1039/9781782624097-00001.

[236] E. Allaria, L. Badano, S. Bassanese, F. Capotondi, D. Castronovo, P. Cinquegrana, M. B. Danailov, G. D'Auria, A. Demidovich, R. De Monte, et al. *The FERMI free-electron lasers*, Journal of Synchrotron Radiation **22**, 485 (2015), URL http://scripts.iucr.org/cgi-bin/paper?ig5031.

[237] V. Ayvazyan, N. Baboi, I. Bohnet, R. Brinkmann, M. Castellano, P. Castro, L. Catani, S. Choroba, A. Cianchi, M. Dohlus, et al. *Generation of GW Radiation Pulses from a VUV Free-Electron Laser Operating in the Femtosecond Regime*, Physical Review Letters **88**, 104802 (2002), URL https://link.aps.org/doi/10.1103/PhysRevLett.88.104802.

[238] R. Mitzner, B. Siemer, M. Neeb, T. Noll, F. Siewert, S. Roling, M. Rutkowski, A. A. Sorokin, M. Richter, P. Juranic, et al. *Spatio-temporal coherence of free electron laser pulses in the soft x-ray regime*, Optics Express **16**, 19909 (2008), URL https://www.osapublishing.org/oe/abstract.cfm?uri=oe-16-24-19909.

[239] P. Cinquegrana, S. Cleva, A. Demidovich, G. Gaio, R. Ivanov, G. Kurdi, I. Nikolov, P. Sigalotti, and M. Danailov. *Optical beam transport to a remote location for low jitter pump-probe experiments with a free electron laser*, Physical Review Special Topics - Accelerators and Beams **17**, 040702 (2014), URL https://link.aps.org/doi/10.1103/PhysRevSTAB.17.040702.

[240] M. B. Danailov, F. Bencivenga, F. Capotondi, F. Casolari, P. Cinquegrana, A. Demidovich, E. Giangrisostomi, M. P. Kiskinova, G. Kurdi, M. Manfredda, et al. *Towards jitter-free pump-probe measurements at seeded free electron laser facilities*, Optics Express **22**, 12869 (2014), URL https://www.osapublishing.org/abstract.cfm?URI=oe-22-11-12869.

[241] S. Schulz, M. K. Czwalinna, M. Felber, P. Prędki, S. Schefer, H. Schlarb, and U. Wegner, in *Advances in X-ray Free Electron Lasers II: Instrumentation*, edited by T. Tschentscher and K. Tiedtke (Prague, 2013), *Femtosecond-precision synchronization of the pump-probe optical laser for user experiments at FLASH*, p. 87780R, URL http://proceedings.spiedigitallibrary.org/proceeding.aspx?doi=10.1117/12.2021572.

[242] J. W. Goodman, *Statistical optics*, Wiley classics library (Wiley, 2000), ISBN 978-0-471-39916-2.

[243] D. Paterson, B. Allman, P. McMahon, J. Lin, N. Moldovan, K. Nugent, I. McNulty, C. Chantler, C. Retsch, T. Irving, et al. *Spatial coherence measurement of X-ray undulator*

radiation, Optics Communications **195**, 79 (2001), URL https://linkinghub.elsevier.com/retrieve/pii/S0030401801012767.

[244] F. Lehmkühler, C. Gutt, B. Fischer, M. A. Schroer, M. Sikorski, S. Song, W. Roseker, J. Glownia, M. Chollet, S. Nelson, et al. *Single Shot Coherence Properties of the Free-Electron Laser SACLA in the Hard X-ray Regime*, Scientific Reports **4**, 5234 (2015), URL http://www.nature.com/articles/srep05234.

[245] M. Sikorski, S. Song, A. Schropp, F. Seiboth, Y. Feng, R. Alonso-Mori, M. Chollet, H. T. Lemke, D. Sokaras, T.-C. Weng, et al. *Focus characterization at an X-ray free-electron laser by coherent scattering and speckle analysis*, Journal of Synchrotron Radiation **22**, 599 (2015), URL http://scripts.iucr.org/cgi-bin/paper?S1600577515004361.

[246] S. Bajt. *Improved reflectance and stability of Mo-Si multilayers*, Optical Engineering **41**, 1797 (2002), URL http://opticalengineering.spiedigitallibrary.org/article.aspx?doi=10.1117/1.1489426.

[247] S. Bajt, H. N. Chapman, N. Nguyen, J. Alameda, J. C. Robinson, M. Malinowski, E. Gullikson, A. Aquila, C. Tarrio, and S. Grantham. *Design and performance of capping layers for extreme-ultraviolet multilayer mirrors*, Applied Optics **42**, 5750 (2003), URL https://www.osapublishing.org/abstract.cfm?URI=ao-42-28-5750.

[248] H. Redlin, A. Al-Shemmary, A. Azima, N. Stojanovic, F. Tavella, I. Will, and S. Düsterer. *The FLASH pump–probe laser system: Setup, characterization and optical beamlines*, Nuclear Instruments and Methods in Physics Research Section A: Accelerators, Spectrometers, Detectors and Associated Equipment **635**, S88 (2011), URL https://linkinghub.elsevier.com/retrieve/pii/S0168900210021935.

[249] E. Allaria, A. Battistoni, F. Bencivenga, R. Borghes, C. Callegari, F. Capotondi, D. Castronovo, P. Cinquegrana, D. Cocco, M. Coreno, et al. *Tunability experiments at the FERMI@Elettra free-electron laser*, New Journal of Physics **14**, 113009 (2012), URL https://iopscience.iop.org/article/10.1088/1367-2630/14/11/113009.

[250] F. Capotondi, E. Pedersoli, F. Bencivenga, M. Manfredda, N. Mahne, L. Raimondi, C. Svetina, M. Zangrando, A. Demidovich, I. Nikolov, et al. *Multipurpose end-station for coherent diffraction imaging and scattering at FERMI@Elettra free-electron laser facility*, Journal of Synchrotron Radiation **22**, 544 (2015), URL http://scripts.iucr.org/cgi-bin/paper?S1600577515004919.

[251] F. Capotondi, E. Pedersoli, N. Mahne, R. H. Menk, G. Passos, L. Raimondi, C. Svetina, G. Sandrin, M. Zangrando, M. Kiskinova, et al. *Invited Article: Coherent imaging using seeded free-electron laser pulses with variable polarization: First results and research*

opportunities, Review of Scientific Instruments **84**, 051301 (2013), URL http://aip.scitation.org/doi/10.1063/1.4807157.

[252] E. Abbe. *Beiträge zur Theorie des Mikroskops und der mikroskopischen Wahrnehmung*, Archiv für Mikroskopische Anatomie **9**, 413 (1873), URL http://link.springer.com/10.1007/BF02956173.

[253] H. Hopster and H. P. Oepen, eds., *Magnetic microscopy of nanostructures*, no. 1434-4904 in Nanoscience and technology (Springer, 2004), ISBN 978-3-540-40186-5.

[254] D.-H. Kim, P. Fischer, W. Chao, E. Anderson, M.-Y. Im, S.-C. Shin, and S.-B. Choe. *Magnetic soft x-ray microscopy at 15 nm resolution probing nanoscale local magnetic hysteresis (invited)*, Journal of Applied Physics **99**, 08H303 (2006), URL http://aip.scitation.org/doi/10.1063/1.2167060.

[255] A. Tripathi, J. Mohanty, S. H. Dietze, O. G. Shpyrko, E. Shipton, E. E. Fullerton, S. S. Kim, and I. McNulty. *Dichroic coherent diffractive imaging*, Proceedings of the National Academy of Sciences **108**, 13393 (2011), URL http://www.pnas.org/cgi/doi/10.1073/pnas.1104304108.

[256] S. Flewett, S. Schaffert, J. Mohanty, E. Guehrs, J. Geilhufe, C. M. Günther, B. Pfau, and S. Eisebitt. *Method for Single-Shot Coherent Diffractive Imaging of Magnetic Domains*, Physical Review Letters **108**, 223902 (2012), URL https://link.aps.org/doi/10.1103/PhysRevLett.108.223902.

[257] X. Shi, P. Fischer, V. Neu, D. Elefant, J. C. T. Lee, D. A. Shapiro, M. Farmand, T. Tyliszczak, H.-W. Shiu, S. Marchesini, et al. *Soft x-ray ptychography studies of nanoscale magnetic and structural correlations in thin $SmCo_5$ films*, Applied Physics Letters **108**, 094103 (2016), URL http://aip.scitation.org/doi/10.1063/1.4942776.

[258] J. Gräfe, M. Skripnik, G. Dieterle, F. Haering, M. Weigand, I. Bykova, N. Träger, H. Stoll, T. Tyliszczak, D. Vine, et al. *Ptychographic imaging and micromagnetic modeling of thermal melting of nanoscale magnetic domains in antidot lattices*, AIP Advances **10**, 125122 (2020), URL http://aip.scitation.org/doi/10.1063/5.0025784.

[259] A. Scherz, W. F. Schlotter, K. Chen, R. Rick, J. Stöhr, J. Lüning, I. McNulty, C. Günther, F. Radu, W. Eberhardt, et al. *Phase imaging of magnetic nanostructures using resonant soft x-ray holography*, Physical Review B **76**, 214410 (2007), URL https://link.aps.org/doi/10.1103/PhysRevB.76.214410.

[260] S. Streit-Nierobisch, D. Stickler, C. Gutt, L.-M. Stadler, H. Stillrich, C. Menk, R. Frömter, C. Tieg, O. Leupold, H. P. Oepen, et al. *Magnetic soft x-ray holography study of focused ion*

beam-patterned Co/Pt multilayers, Journal of Applied Physics **106**, 083909 (2009), URL http://aip.scitation.org/doi/10.1063/1.3246724.

[261] R. L. Sandberg, D. A. Raymondson, C. La-o vorakiat, A. Paul, K. S. Raines, J. Miao, M. M. Murnane, H. C. Kapteyn, and W. F. Schlotter. *Tabletop soft-x-ray Fourier transform holography with 50 nm resolution*, Optics Letters **34**, 1618 (2009), URL https://www.osapublishing.org/abstract.cfm?URI=ol-34-11-1618.

[262] S. Schaffert, B. Pfau, J. Geilhufe, C. M. Günther, M. Schneider, C. v. Korff Schmising, and S. Eisebitt. *High-resolution magnetic-domain imaging by Fourier transform holography at 21 nm wavelength*, New Journal of Physics **15**, 093042 (2013), URL https://iopscience.iop.org/article/10.1088/1367-2630/15/9/093042.

[263] S. Eisebitt, J. Lüning, W. F. Schlotter, M. Lörgen, O. Hellwig, W. Eberhardt, and J. Stöhr. *Lensless imaging of magnetic nanostructures by X-ray spectro-holography*, Nature **432**, 885 (2004), URL http://www.nature.com/articles/nature03139.

[264] D. Stickler, R. Frömter, H. Stillrich, C. Menk, C. Tieg, S. Streit-Nierobisch, M. Sprung, C. Gutt, L.-M. Stadler, O. Leupold, et al. *Soft x-ray holographic microscopy*, Applied Physics Letters **96**, 042501 (2010), URL http://aip.scitation.org/doi/10.1063/1.3291942.

[265] J. Viefhaus, F. Scholz, S. Deinert, L. Glaser, M. Ilchen, J. Seltmann, P. Walter, and F. Siewert. *The Variable Polarization XUV Beamline P04 at PETRA III: Optics, mechanics and their performance*, The 4th international workshop on Metrology for X-ray Optics, Mirror Design, and Fabrication **710**, 151 (2013), URL http://www.sciencedirect.com/science/article/pii/S0168900212012831.

[266] L. Müller, G. Hartmann, S. Schleitzer, M. H. Berntsen, M. Walther, R. Rysov, W. Roseker, F. Scholz, J. Seltmann, L. Glaser, et al. *Soft X-ray transmission polarizer based on ferromagnetic thin films*, Review of Scientific Instruments **89**, 036103 (2018), URL https://doi.org/10.1063/1.5018396.

[267] K. Bagschik, J. Wagner, R. Buß, M. Riepp, A. Philippi-Kobs, L. Müller, J. Buck, F. Trinter, R. Frömter, J. Viefhaus, et al. *Direct 2D spatial-coherence determination using the Fourier-analysis method: multi-parameter characterization of the P04 beamline at PETRA III*, Optics Express **28**, 7282 (2020), URL https://www.osapublishing.org/abstract.cfm?URI=oe-28-5-7282.

[268] T. Wang, Ph.D. thesis, Stanford University, *Nanoscale and Ultrafast Imaging of Magnetic Materials with Resonant Soft X-Rays* (2013), URL https://www-ssrl.slac.stanford.edu/stohr/.

[269] B. Pfau, Ph.D. thesis, Technische Universität Berlin, *Imaging magnetic nanostructures using soft x-ray Fourier transform holography* (2013), URL http://dx.doi.org/10.14279/depositonce-3854.

[270] S. Schaffert, Ph.D. thesis, Technische Universität Berlin, *Holographic Imaging and Time-Resolved X-ray Scattering on Magnetic-Domain Sysems* (2014), URL https://depositonce.tu-berlin.de/handle/11303/4524.

[271] S. Yamamoto and I. Matsuda. *Measurement of the Resonant Magneto-Optical Kerr Effect Using a Free Electron Laser*, Applied Sciences **7**, 662 (2017), URL https://www.mdpi.com/2076-3417/7/7/662.

[272] V. López-Flores, J. Arabski, C. Stamm, V. Halté, N. Pontius, E. Beaurepaire, and C. Boeglin. *Time-resolved x-ray magnetic circular dichroism study of ultrafast demagnetization in a CoPd ferromagnetic film excited by circularly polarized laser pulse*, Physical Review B **86**, 014424 (2012), URL https://link.aps.org/doi/10.1103/PhysRevB.86.014424.

[273] M. Baidakova, R. Carley, R. Gort, G. Grübel, L. Le Guyader, E. Jal, E. Lobanova, L. Mercadier, G. Mercurio, S. Molodtsov, et al., in *2020 International Conference Laser Optics (ICLO)* (Saint Petersburg, 2020), *Ultrafast dynamics of spatial magnetic fluctuations in Co/Pt multilayers studied at European XFEL*, pp. 1–1, ISBN 978-1-72815-232-5 978-1-72815-233-2, URL https://ieeexplore.ieee.org/document/9285794/.

[274] M. M. Hall Jr., V. G. Veeraraghavan, H. Rubin, and P. G. Winchell. *The approximation of symmetric X-ray peaks by Pearson type Vll distributions*, Journal of Applied Crystallography **10**, 66 (1977), URL https://scripts.iucr.org/cgi-bin/paper?a15317.

[275] M. D. Kuz'min, M. Richter, and A. N. Yaresko. *Factors determining the shape of the temperature dependence of the spontaneous magnetization of a ferromagnet*, Physical Review B **73**, 100401(R) (2006), URL https://link.aps.org/doi/10.1103/PhysRevB.73.100401.

[276] D. Halliday, R. Resnick, J. Walker, and S. W. Koch, *Physik* (Wiley, 2009), ISBN 978-3-527-40645-6.

[277] J. W. Arblaster. *The Thermodynamic Properties of Platinum*, Platinum Metals Review **49**, 141 (2005), URL http://www.ingentaselect.com/rpsv/cgi-bin/cgi?ini=xref&body=linker&reqdoi=10.1595/147106705X54262.

[278] X. Luo. *Subwavelength Artificial Structures: Opening a New Era for Engineering Optics*, Advanced Materials **31**, 1804680 (2019), _eprint: https://onlinelibrary.wiley.com/doi/pdf/10.1002/adma.201804680, URL https://onlinelibrary.wiley.com/doi/abs/10.1002/adma.201804680.

[279] Z. Lin, L. V. Zhigilei, and V. Celli. *Electron-phonon coupling and electron heat capacity of metals under conditions of strong electron-phonon nonequilibrium*, Physical Review B **77** (2008), URL https://link.aps.org/doi/10.1103/PhysRevB.77.075133.

[280] D. Zahn, F. Jakobs, Y. W. Windsor, H. Seiler, T. Vasileiadis, T. A. Butcher, Y. Qi, D. Engel, U. Atxitia, J. Vorberger, et al. *Lattice dynamics and ultrafast energy flow between electrons, spins, and phonons in a 3d ferromagnet*, Physical Review Research **3**, 023032 (2021), URL https://link.aps.org/doi/10.1103/PhysRevResearch.3.023032.

[281] M. S. Si and G. P. Zhang. *Resolving photon-shortage mystery in femtosecond magnetism*, Journal of Physics: Condensed Matter **22**, 076005 (2010), URL https://iopscience.iop.org/article/10.1088/0953-8984/22/7/076005.

[282] G. P. Zhang, G. Lefkidis, W. Hübner, and Y. Bai. *Ultrafast demagnetization in ferromagnets and magnetic switching in nanoclusters when the number of photons is kept fixed*, Journal of Applied Physics **109**, 07D303 (2011), URL http://aip.scitation.org/doi/10.1063/1.3533255.

[283] J. E. Davies, O. Hellwig, E. E. Fullerton, G. Denbeaux, J. B. Kortright, and K. Liu. *Magnetization reversal of CoPt multilayers: Microscopic origin of high-field magnetic irreversibility*, Physical Review B **70**, 224434 (2004), URL https://link.aps.org/doi/10.1103/PhysRevB.70.224434.

[284] V. López-Flores, M.-A. Mawass, J. Herrero-Albillos, A. A. Uenal, S. Valencia, F. Kronast, and C. Boeglin. *A local view of the laser induced magnetic domain dynamics in CoPd stripe domains at the picosecond time scale*, Journal of Physics: Condensed Matter **32**, 465801 (2020), URL https://iopscience.iop.org/article/10.1088/1361-648X/aba1ac.

[285] L. Müller, S. Schleitzer, C. Gutt, B. Pfau, S. Schaffert, J. Geilhufe, C. von Korff Schmising, M. Schneider, C. M. Günther, F. Büttner, et al. *Ultrafast Dynamics of Magnetic Domain Structures Probed by Coherent Free-Electron Laser Light*, Synchrotron Radiation News **26**, 27 (2013), URL http://www.tandfonline.com/doi/abs/10.1080/08940886.2013.850384.

Publications And Conference Contributions

First-Author Contributions:

- M. Riepp, L. Müller, A. Philippi-Kobs, W. Roseker, R. Rysov, M. Walther, K. Bagschik, R. Frömter, H. P. Oepen, T. Golz, N. Stojanovic, D. Naumenko, E. Pedersoli, F. Capotondi, M. Kiskinova, and G. Grübel, in *FEL19 - 39th International Free-Electron Laser Conference* (Hamburg, 2019), *Ultrafast Magnetisation Dynamics at the Low-Fluence Limit Supported by External Magnetic Fields*, pp. 574–577, ISBN 978-3-95450-210-3, URL https://fel2019.vrws.de/papers/proceed.pdf.
- M. Riepp, *Pump-probe holographic imaging of nanoscale magnetic domains*, talk at spring meeting of the German Physical Society (Dresden, 2017).
- M. Riepp, *Structural and magnetic properties of FePt-Mn thin films*, poster at the spring meeting of the German Physical Society (Dresden, 2017).
- M. Riepp, *Ultrafast demagnetization in Co/Pt multilayers studied at the Co L_3 edge*, talk at the spring meeting of the German Physical Society (Berlin, 2018).
- M. Riepp, *Ultrafast magnetisation dynamics at the low-fluence limit supported by external magnetic fields*, talk at FEL19 - 39th international free-electron laser conference (Hamburg, 2019).

Co-Author Contributions:

- M. Baidakova, R. Carley, R. Gort, G. Grübel, L. Le Guyader, E. Jal, E. Lobanova, L. Mercadier, G. Mercurio, S. Molodtsov, L. Müller, A. Philippi-Kobs, D. Potorochin, M. Riepp, W. Roseker, A. Scherz, J. Schlappa, S. M. Suturin, B. van Kuiken, A. Yaroslavtsev, I. I. Pronin, in *2020 International Conference Laser Optics (ICLO)* (Saint Petersburg, 2020), *Ultrafast dynamics of spatial magnetic fluctuations in Co/Pt multilayers studied at European XFEL*, pp. 1–1, ISBN 978-1-72815-232-5, URL https://ieeexplore.ieee.org/document/9285794/.
- K. Bagschik, J. Wagner, R. Buß, M. Riepp, A. Philippi-Kobs, L. Müller, J. Buck, F. Trinter, F. Scholz, J. Seltmann, M. Hoesch, J. Viefhaus, G. Grübel, H. P. Oepen, R. Frömter, *Direct*

2D spatial-coherence determination using the Fourier-analysis method: multi-parameter characterization of the P04 beamline at PETRA III, Optics Express 28 , 7282 (2020), URL https://www.osapublishing.org/abstract.cfm?URI=oe-28-5-7282.

- K. Bagschik, M. Schneider, J. Wagner, R. Buß, M. Riepp, A. Philippi-Kobs, L. Müller, W. Roseker, F. Trinter, M. Hoesch, J. Viefhaus, S. Eisebitt, G. Grübel, H. P. Oepen, R. Frömter, *Enabling time-resolved 2D spatial-coherence measurements using the Fourier-analysis method with an integrated curved-grating beam monitor*, Optics Letters 45 , 5591 (2020), URL https://www.osapublishing.org/abstract.cfm?URI=ol-45-19-5591.

- A. Philippi-Kobs, M. H. Berntsen, L. Müller, W. Roseker, M. Riepp, K. Bagschik, J. Wagner, R. Frömter, M. Danilov, E. Pedersoli, F. Capotondi, M. Manfredda, M. Kiskinova, B. Ziaja, H. P. Oepen, G. Grübel, *Ultrafast demagnetization by extreme ultraviolet light*, (submitted).

Acknowledgement

First of all, I would like to thank Prof. Gerhard Grübel for supervision of this PhD project. You opened the exciting world of ultrafast magnetism at FELs for me and gave me the opportunity to meet and work with scientists from all over the world. I would like to thank you for continuously supporting and believing in me as well as your patience regarding my thesis.

I would like to thank Prof. Ralf Röhlsberger for being the second assessor of this thesis.

I also want to gratefully acknowledge the co-supervision of Prof. Wilfried Wurth in the beginning of this project. His sudden death in 2019 came as a shock for the scientific community, especially for his colleagues at DESY. As lead scientist and director of FLASH, Wilfried Wurth played an important role for advancing in the field of ultrafast sciences at FEL facilities. As Professor of experimental physics at the University of Hamburg he was popular with students due to his calm temper and unconventional thinking. For me as a young scientist working with FELs for the first time, he was a great motivator and personality to look up to.

I would like to thank the whole FS-CXS group at DESY under the lead of Prof. Gerhard Grübel. It was and is a great pleasure to work in such an open-minded and creative environment. Especially, I would like to thank Wojciech Roseker, Leonard Müller and André Philippi-Kobs for their guidance through the past five years, assistance in preparing and conducting the experiments, help with data analysis and interpretation, many fruitful discussions and support for this thesis. I will happily remember our after-work games of squash and football as well as BBQs at Wojciech's. I'm thankful for the help of Michael Walther for designing and engineering the equipment for the experiments, such as the magnet system, and helping set up the experiments. Last but not least I thank Rustam Rysov and Simon Marotzke for their support in the experiments and help with sample characterization. I will never forget the various beamtimes we all had together here in Hamburg, Italy and Japan and the memories we share from the following travels.

This thesis would not have been possible without the help of many scientists from various places. In particular, the long-year collaboration with the former group of Prof. Hans Peter Oepen at the University of Hamburg was of great importance for this PhD project. I would like to say

thank you to Sonja Hesselmann for her help with preparing the Co/Pt-multilayer samples. I also feel very thankful for the support by Robert Frömter, Jochen Wagner, Kai Bagschik and Ralph Buß who not only were supporting the TR-mSAXS experiment at FLASH but also leading the FTH experiment at PETRA III.

At large-scale facilities like PETRA III, FLASH or FERMI, it requires local support from experienced teams to run and control the experiments. Your dedication deserves extra credit and I would like to thank all of you who contributed to making the experiments a success, especially:

FTH and mSAXS at the P04 beamline at PETRA III
Jens Buck, Frank Scholz and Jens Viefhaus.

TR-mSAXS at the BL3 beamline at FLASH
Rui Pan, Torsten Golz, Bastian Manschwetus, Mark Temme, Sven Toleikis, Rolf Treusch and Nicola Stojanovic.

TR-mSAXS at the DiProI beamline at FERMI
Flavio Capotondi, Emmanuele Pedersoli, Dennys Naumenko, Ignacio Lopez Quintas, Marco Zangrando, Miltcho Boyanov Danailov and Maja Kiskinova.

Hiermit erkläre ich an Eides statt, dass ich die vorliegende Dissertationsschrift selbst verfasst und keine anderen als die angegebenen Quellen und Hilfsmittel benutzt habe.

Die eingereichte schriftliche Fassung entspricht der auf dem elektronischen Speichermedium. Die Dissertation wurde in der vorgelegten oder einer ähnlichen Form nicht schon einmal in einem früheren Promotionsverfahren angenommen oder als ungenügend beurteilt.

Ort, Datum

Unterschrift